STRUCTURES IN THE SOLAR WIND AND THEIR INFLUENCE IN INNER HELIOSPHERE

THESIS

SUBMITTED FOR THE AWARD OF THE DEGREE OF

Doctor of Philosophy

IN

PHYSICS

BY

ANAND KUMAR

UNDER THE SUPERVISION OF

PROF. BADRUDDIN

DEPARTMENT OF PHYSICS
ALIGARH MUSLIM UNIVERSITY
ALIGARH (INDIA)

2015

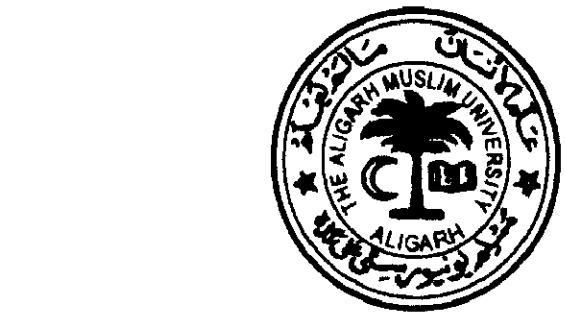

Dedicated to

My Dear Family

&

Respected Teachers

CANDIDATE'S DECLARATION

I, **Anand Kumar**, Department of **Physics** certify that the work embodied in this Ph.D. thesis is my own bonafide work carried out by me under the supervision of **Prof. Badruddin** at Aligarh Muslim University, Aligarh. The matter embodied in this Ph.D. thesis has not been submitted for the award of any other degree.

I declare that I have faithfully acknowledged, given credit to and referred to the research workers wherever their works have been cited in the text and the body of the thesis. I further certify that I have not willfully lifted up some other's work, para, text, results, etc. reported in the journals, books, magazines, reports, dissertations, theses, etc., or available at web-sites and included them in this Ph.D. thesis and cited as my own work.

Date: 07/07/2015

Anand Kumar

(Signature of the candidate)

Anand Kumar

(Name of the candidate)

CERTIFICATE FROM THE SUPERVISOR

This is to certify that the above statement made by the candidate is correct to the best of my/our knowledge.

Signature of the Supervisor:

Name & Designation: Dr. Badruddin
(Professor)

Department: Physics

(Signature of the Chairman of the Department with seal)

Chairperson
Department of Physics
A.M.U., Aligarh

COURSE WORK/COMPREHENSIVE EXAMINATION/PRE-SUBMISSION SEMINAR COMPLETION CERTIFICATE

This is to certify that **Mr. Anand Kumar**, Department of **Physics** has satisfactorily completed the course work/comprehensive examination and pre-submission seminar requirement, which is part of his Ph.D. programme.

Date: 7.7.2015

(Signature of the Chairman of the Department)
Chairperson
Department of Physics
A.M.U., Aligarh

COPYRIGHT TRANSFER CERTIFICATE

Title of the Thesis: Structures in the solar wind and their influence in inner heliosphere

Candidate's Name: Anand Kumar

COPYRIGHT TRANSFER

The undersigned hereby assigns to the Aligarh Muslim University, Aligarh copyright that may exist in and for the above thesis submitted for the award of the Ph.D. degree.

Anand Kumar

Signature of the candidate

Note: However, the author may reproduce or authorize others to reproduce material extracted verbatim from the thesis or derivative of the thesis for author's personal use provide that the University's copyright notice are indicated.

Acknowledgments

First and foremost, I praise God, the Almighty, providing me this opportunity and granting me the capability to complete this research work successfully. This thesis appears in its current form due to the assistance and guidance of several people during this hard time, but a very fruitful period of new experiences. I would therefore like to offer my sincere thanks to all of them.

It is my pleasure to express my deep respect, immense gratitude and indebtedness to my supervisor Prof. Badruddin for his valuable suggestions, continued interest, encouragement and support throughout the completion of this work. I highly appreciate the way he encouraged me to work hard as well as the way he refined my aptitude for research. His excellent guidance, advice towards the structure of this thesis is very much appreciated. I have always felt privileged and honoured to work under his guidance. It has always been a pleasure working with him. To be honest I was extremely impressed by his personality and teaching methods during my B.Sc. (Hons) and M.Sc. There was no need of any second thought for me to join him to pursue my PhD. I would like to thank him for giving me the opportunity to do research.

I express my thanks to Prof. Rahimullah Khan, Chairperson, Department of Physics and Dean Faculty of Science, AMU, Aligarh for providing me all necessary facilities and academic environment during the course of this work. I am also grateful to Prof. W. Haider, Prof. M. Zafar, Former Chairman, Department of Physics, AMU, Aligarh, for their valuable support and encouragements. I am also sincerely thankful to all my respected teachers specially Dr. I.A. Ansari, Prof. A. Qaiyum, Prof. M.A. Ansari, Prof. I.A. Rizvi, Dr. A.R. Khan, Dr. S. Ahmad, Dr. S.M. Afzal and Dr. S. Husain, Department of Physics AMU, Aligarh, for their inspiration, innovation and kind help to learn the subject in a quite scholarly way. I thank to the Departmental office for their cooperation in providing the required official assistance, and seminar library and Maulana Azad Library of AMU, Aligarh for providing the valuable literatures. Many thanks to the staff members of the workshop and computer lab of the Department for help in maintaining the things in working conditions in my Research lab with no delay. The house keeping staff members of the Department are also appreciated for making my research lab and the Department neat and clean.

I would like to express my heartfelt and warm gratitude towards my very loving parents for their love, prayers, caring. They have seen very hard day in and day out and sacrificed their joys of life for educating and preparing me for this goal of my life. I am extremely thankful to my elder sisters (Mrs. Krishna, Mrs. Sangeeta, and Mrs. Rajani), brother in laws (Mr. R.P. Tiwari, Mr. P.K. Bhardwaj, and Mr. R. Pathak) and all my relatives for their continuous support, endless patience, blessings and moral supports. I always found my elder sister Mrs. Sangeeta as so supportive as my local guardian here at Aligarh. I feel very grateful to Mrs. Arti, Mrs. Jyoti, and Mrs. Ratna for their very kind support to me as my real sisters. Special thanks to my beloved younger brother (Mr. Chitra Kumar) and sister (Miss. Upasana) for their prayers, help and boosting me in tough time with their unbounded love. Special thanks also go to my little nieces and nephews (Deeksha, Vivechana, Himanshi, Aadrika, Govind, Vivek, Nishant, and Pawan) to make me feel refreshed, energetic and smiley with their sweet chirpings and talkative activities. A great thank to my elder cousin (Mr. S.K. Trivedi) who was always ready to cooperate me in travel

arrangements for attending conferences in India and abroad as well. Special thank to his sweet wife (Mrs. Ujala) also for their kind caring and having keen interest in completion of my PhD thesis.

Let me not forget to express my profound sense of gratitude to my very dear and respected Shri G.S. Shrama and Shri R.P. Singh for their contributions by giving their precious time, blessings, love, encouragements and financial help in the adverse times of my life to make my education easy and my PhD experience more productive and stimulating. I always got their support as my guardians. I always remember them for extending their liberal hands whenever and wherever I needed. It would not have been possible to complete this work without their constant support. I am also highly thankful to my college teacher Shri M. Rajauria for his motivational and contagious conversations to encouraging me all the time. His unwavering support and love have always been a reason to smile to me.

I am very much thankful to my lab mates Mrs. F. Mustajab, Mr. O.P.M. Aslam, and Miss. Z. Falak and colleagues Mr. Harish Kumar, Dr. M. Jane Alam, Mr. Alamgir for their generous help throughout the duration of the research work. It was a very nice and memorable association with all the research scholars of the departments. I wish to give them special thanks for their constant support and help. A big thank to Dr. Y.P. Singh, Dr. M. Singh, Dr. (Mrs.) Mukti Sharma, Dr. Irfan, Dr. Yashpal. S. Raghav, Dr. Shamsher Khan, Mrs. Sanghmitra, Er. Manish. D. Sharma for their creative suggestions and help in improving my understanding of the Physics, Computer Applications and Statistics behind the data I was analyzing. I owe special thanks to my dear friends specially Mr. Suneel, Mr. Prateek, Mr. Shekhar, Mr. Ashish, Mr. Anirudha, Miss. Divya, Mr. Nekase Lal, Mrs. Yasha, Mr. Afaq, Mr. Lokesh, Mr. Arvind, Mr. Tanveer Ali, Mr. Zeeshan, and Mr. Danish for their moral support which they extended with their humorous and good-natured approach to life. The conversations with them was really fruitful and a source of inspiration to me. Hostel life at V.M. Hall in AMUC was also so enjoyable with few hostel shifting. It was really very nice to have Mr. S. Afzal Ali, Mr. Rashid, Mr. Nishar, Mr. Anant Ashthana as my room partners time to time, who took care of me as my family member.

UGC, New Delhi and DST-PURSE are gratefully acknowledged for providing me the fellowship during my research work.

Last but not the least; I thank each and every one who has helped me directly or indirectly at some stage or the other in making this thesis possible. Thanks

Anand Kumar

Abstract

Large-scale structures in the solar-wind *i.e.* interplanetary coronal mass ejections, interplanetary shocks, magnetic clouds, corotating interaction regions etc, have been identified in the inner heliosphere near-Earth space using space-based and ground-based observations. Continuous observations of these structures and solar-wind plasma/field parameters are available at least for solar cycle 23 (1995 – 2009) and later periods. Simultaneous ground-based cosmic ray data by neutron monitors (NMs) located at different latitudes and longitudes is also being recorded world wide. In this work, we concentrate on the study of large-scale structures in the inner heliosphere and their effects on the cosmic-ray intensity and simultaneously on solar-wind parameters.

In the heliosphere, the large-scale structure of the solar wind is dominated by two types of interplanetary disturbances: transient and corotating disturbances. Corotating disturbances, associated with spatial variability and solar rotation, occur in response to the interaction of fast and slow solar winds. Transient disturbances, due to episodic solar eruptions, expand outward from the Sun into interplanetary space. Interplanetary structures such as shocks, sheaths, interplanetary counterparts of coronal mass ejections (ICMEs), magnetic clouds, and corotating interaction regions (CIRs) are of special interest for the study of the transient modulation of galactic cosmic rays (GCRs). Depending on their associated features, the ICMEs identified in near-Earth space are grouped into the different classes; *i.e.* ICMEs may or may not be associated with shock/sheath, bidirectional superthermal electron event (BDE), magnetic-cloud (MC) structures, and halo CME structure. Further, BDE-ICMEs are divided on the basis of their occurrence with bidirectional energetic ion flows (BIF) and without BIF signatures. These structures modulate the GCR intensity with varying amplitude and recovery-time profiles. This classification into different groups lead us to study in detail the relative GCR-effectiveness (*i.e.* ability to depress GCR intensity) of different structures/features associated/not-associated with ICMEs. It will help us not only in identifying the structures/features of importance but also to understand the physical mechanisms playing important roles in transient modulation of galactic cosmic rays. A Forbush decrease is characterized by rapid reduction in cosmic-ray intensity within one to two days followed by a slow recovery typically lasting several

days. It is known that ICMEs are mainly responsible for Forbush decreases in GCR intensity. However, not all of the ICMEs produce such decreases in GCR intensity.

For the statistical study of the GCR-response to these ICMEs, based on the degree of their "effectiveness" (we call it "GCR effectiveness" more precisely) in producing depressions in GCR intensity, we have divided ICME "GCR-effectiveness" in five groups on the basis of their decrease in GCR intensity in percent, ΔI (%) using Kiel neutron monitor data, *i.e.* quiet ($\Delta I \approx 0.0$), small ($\Delta I \approx -0.01$ to -0.49 %); moderate ($\Delta I \approx -0.50$ to -1.49 %); large ($\Delta I \approx -1.50$ to -2.99 %); and very large (ΔI larger than -3.00 %) depression groups. Such a wide range in GCR effectiveness of ICMEs motivated us to look for the distinctions, if any, in the properties of average interplanetary plasma and field behavior during the passage of ICMEs responsible for the depressions of different range (small, moderate, large, and very large). We utilize GCR intensity data recorded by neutron monitors and solar-wind plasma/field data during the passage of ICMEs with different features and structures, and perform a superposed-epoch analysis of the data. We also adopt the best-fit approach with suitable functions to interpret the observed similarities and differences in various parameters. Using the GCR-effectiveness as a measure of cosmic-ray response to the passage of ICMEs, about half of the ICMEs identified during 1996 – 2009 are found to produce moderate to very large intensity depressions in GCR intensity. ICMEs associated with shocks/BDEs/MCs/halo-CMEs are more GCR-effective than ICMEs not associated with these structures/features. Each group (BDE/MC/halo) was subdivided into shock/no shock cases. A large difference in their GCR-effectiveness is observed; shock/sheath associated BDE/MC/halo ICMEs are much more GCR-effective than those not associated with any shock/sheath region. This difference is most prominent in case of shock/sheath associated ICMEs rather than those not associated with shock/sheath region. This emphasizes the role of the shock/sheath region in producing larger depressions in GCR intensity. Further, the characteristic recovery time of GCR intensity due to shock/BDE/MC/halo-CME-associated ICMEs is larger than those due to ICMEs not associated with these structures/features. *This work has been published in Solar Physics in 2014.*

As mentioned earlier ICMEs and CIRs are the two main large-scale structures in the heliosphere. Heliosphere is the region of space around the Sun in which the solar wind dominates. Next we compare the cosmic-ray response of ICMEs and CIRs

during their passage in near-Earth space. We study the relative importance of various structures/features identified during the passage of ICMEs and CIRs observed during solar cycle 23 (1995 – 2009). As the plasma and field properties are different during the passage of different structures, both in ICMEs and CIRs, we systematically vary epoch time in our superposed-epoch analysis one by one. In this way, we study the role and effects of each identified individual structures/features during the passage of ICMEs and CIRs. The average amplitude of GCR intensity depression for ICMEs is ~ 1.5 % as compared for CIRs which is ~ 0.5 %. The ratio of GCR depressions for ICMEs with shock to ICMEs without shock is ~2.5, and the ratio of intensity depression due to shock-associated CIRs to non-shock CIRs is also nearly the same. From the average plots obtained from superposed-epoch analysis, the time variation of GCR intensity due to ICMEs, during the main (decrease) phase, is found to be better correlated with time variation of magnetic field vector. However time variation of solar-wind velocity better correlates with GCR intensity during this phase, in case of decrease due to CIRs. The temporal variation of GCR intensity is found to be better correlated with simultaneous variations in solar-wind velocity, during the recovery of decrease (recovery phase) both due to ICMEs as well CIRs. *This work has been submitted for publication in Solar Physics.*

The continuous flow of the ambient solar wind is often overlaid by faster streams, as is evident from observations of the solar plasma in space. These so called high-speed solar-wind streams (HSS) are recognized as those ejected from solar active regions during coronal mass ejections (CMEs) and those coming from diverging and unipolar-field regions called coronal holes (CH). As a consequence, there are two classes of interplanetary structures related to two types of magnetic-field topology on the Sun, *i.e.* interplanetary coronal mass ejections (ICMEs) and corotating interaction region (CIRs). Both the ICMEs and the CIRs are capable of driving shocks in the interplanetary space due to interaction between high-speed CME/CH-streams and ambient solar wind. These HSS, as observed in near-Earth space, may be associated to different solar sources, *e.g.* i) a coronal hole, ii) a CME, iii) multiple coronal holes, iv) multiple CMEs, or v) compound streams due to coronal hole(s) and CME(s). The streams of i) different speed, ii) different duration, and iii) associated with different solar/interplanetary structures are likely to exhibit different responses in cosmic-ray intensity variations, both in amplitude and time profile. So we have also studied the

modulation of galactic cosmic rays (GCR) due to high-speed streams (HSS) identified in the solar wind. We compare the GCR modulation due to i) streams with different speed, ii) streams of different duration, and iii) streams from different solar sources. We also investigate the solar sources, interplanetary causes, and physical mechanisms responsible for GCR-intensity decreases of different amplitude, duration, and time profile, such as the so-called Forbush decreases, corotating decreases, long-lived, and multiple-dip cosmic-ray decreases.

On the average, GCR-intensity decreases at the arrival of the stream. HSS of higher speed and/or higher duration produce more depressions in GCR intensity. Multiple CME streams are found to be most, and single CH streams are least effective in modulating the GCR intensity. The rate of intensity decrease with increase in solar-wind velocity during the decreasing phase is highest for multiple CME streams and lowest for single CH streams. We observe that the intensity depression is strongest when the shock occurred both at the start of the HSS and in between the start and the end of the HSS. *This work has been published in Solar Physics in 2014.*

****

LIST OF PUBLICATIONS

Papers published in peer refereed journals

1. **Anand Kumar** and Badruddin, 2014 – Interplanetary coronal mass ejections, associated features, and transient modulation of galactic cosmic rays, *Solar Phys.* **289**, 2177 – 2205. doi: 10.1007/s11207-013-0465-7.
2. **Anand Kumar** and Badruddin, 2014 – cosmic-ray modulation due to high-speed solar-wind streams of different sources, speed, and duration, *Solar Phys.* **289**, 4267 – 4296. doi: 10.1007/s11207-014-0565-z.
3. Badruddin and **Anand Kumar**, 2015 – Study of the Forbush decreases, geomagnetic storms, and ground-level enhancements in selected intervals and their space weather implications, *Solar Phys.* **290**, 1271 – 1283. doi: 10.1007/s11207-015-0665-4.
4. **Anand Kumar** and Badruddin, 2015 – Study of the cosmic-ray modulation during the passage of ICMEs and CIRs, *Solar Phys.* (submitted). SOLA-D-14-00235.

Papers published in the proceedings of the international/national proceedings

1. Badruddin and **Anand Kumar**, 2013 – Interplanetary coronal mass ejections, their associated features, related plasma/field variations and transient modulation of cosmic rays, International Symposium on Solar Terrestrial Physics, *ASI Conference Series*, **10**, 107 – 110.
2. **Anand Kumar**, Aslam, O. P. M., and Badruddin, 2014 – Solar sources of high-speed streams and their influence on cosmic-ray intensity, Proceedings on National Seminar on Solar Plasma Processes & Cosmic Ray Modulation, Govt. New Science College, Rewa (M.P.) 5 – 8, ISBN - 13: 978-81-928063-5-8.

Papers presented at international/national conferences

1. Relative geo-effectiveness of coronal mass ejections with distinct features in

interplanetary space - Badruddin, Mustajab, F., and **Anand Kumar**, 39th international committee on space research (COSPAR) scientific assembly, July 14 - 22, 2012, Mysore, India.

2. Interplanetary coronal mass ejections, their associated features, related plasma/field variations and transient modulation of cosmic rays – Badruddin and **Anand Kumar**, International Symposium on Solar-Terrestrial Physics, Novmber 6 – 9, 2012, IISER, Pune.
3. Solar sources of high-speed streams and their influence on cosmic- ray intensity – **Anand Kumar**, Aslam, O.P.M., and Badruddin, National Seminar on Solar Plasma Processes and Cosmic-Ray Modulation, 8 – 9 February, 2014, Rewa, M.P.
4. Geomagnetic storms and transient depressions in cosmic rays due to coronal mass ejections and corotating interaction regions: a comparative study – **Anand Kumar** and Badruddin, 40th International Committee on Space Research (COSPAR) Scientific Assembly, August 02 – 10, 2014, Moscow, Russia.
5. Relative geo-effectiveness of high-speed solar-wind streams associated with different plasma and field characteristics: 1996 – 2013 – Badruddin, Aslam, O.P.M, and **Anand Kumar**, 40th International Committee on Space Research (COSPAR) Scientific Assembly, August 02-10, 2014, Moscow, Russia.

****

Contents

List of Figures

Figure 2.14 Exponential fit and characteristic recovery time [τ, hours] during recovery of GCR-intensity depressions due to ICMEs associated/not associated with magnetic cloud (MC) and halo CMEs.

Figure 2.15 Linear-regression plot between V_{max} [km s^{-1}] and GCR-intensity recovery time (hours), obtained from superposed-epoch plots, due to ICMEs with different GCR effectiveness and ICMEs associated/not associated with different structures/features.

Figure 3.1 The superposed-epoch plots of hourly data of galactic cosmic ray (GCR) intensity at Oulu NM $[\Delta I/I]_O$ (%), GCR intensity at Newark NM $[\Delta I/I]_N$ (%), solar-wind velocity [V], IMF vector [F], standard deviation in IMF vector [σ_F], the derivatives FV and FV^2 due to ICMEs and CIRs observed during 1995 – 2009; zero hour (epoch) corresponds to arrival time (hour) of ICMEs and CIRs. N stands for number of events.

Figure 3.2 The superposed-epoch plots of hourly data of galactic cosmic ray (GCR) intensity at Oulu NM $[\Delta I/I]_O$ (%), GCR intensity at Newark NM $[\Delta I/I]_N$ (%), plasma/field parameters [V, F, σ_F, FV, and FV^2] due to ICMEs and CIRs associated with shocks observed during 1995 – 2009; zero hour (epoch) corresponds to arrival time (hour) of ICMEs and CIRs with shocks. N stands for number of events.

Figure 3.3 The superposed-epoch plots of hourly data of galactic cosmic ray (GCR) intensity at Oulu NM $[\Delta I/I]_O$ (%), GCR intensity at Newark NM $[\Delta I/I]_N$ (%), plasma/field parameters [V, F, σ_F, FV, and FV^2] due to ICMEs associated with/without shocks observed during 1995 – 2009; zero hour (epoch) corresponds to arrival time (hour) of ICMEs associated with/without shocks. N stands for number of events.

Figure 3.4 Frequency distribution of i) maximum speed, [V_{max}, km s^{-1}], ii) maximum IMF vector, [F_{max}, nT], iii) maximum electric field, [FV_{max}, mV m^{-1}], iv) maximum standard deviation in IMF vector, [σ_{Fmax}, nT], iv) maximum [FV^2_{max}, mV s^{-1}], and (vi) CR decrease observed during the passage of ICMEs associated/not associated with shocks. Gaussian best fit curves representing the distribution of ICMEs are also shown in the first five panel of figure. The central peak values x_c, and full width

at half maxima w_c obtained from the fits are also given. N stands for number of events considered for each histrogram.

Figure 3.5 The superposed-epoch plots of hourly data of galactic cosmic ray (GCR) intensity at Oulu NM $[\Delta I/I]_O$ (%), GCR intensity at Newark NM $[\Delta I/I]_N$ (%), plasma/field parameters [V, F, σ_F, FV, and FV^2] due to ICMEs associated with shocks observed during 1995 – 2009; zero hour (epoch) corresponds to time (hour) of shock arriving at same/different time as Magnetic Obstacle (ejecta). N stands for number of events.

Figure 3.6 The superposed-epoch plots of hourly data of galactic cosmic ray (GCR) intensity at Oulu NM $[\Delta I/I]_O$ (%), GCR intensity at Newark NM $[\Delta I/I]_N$ (%), plasma/field parameters [V, F, σ_F, FV, and FV^2] due to ICMEs associated with shocks observed during 1995 – 2009; zero hour (epoch) corresponds to time (hour) of Magnetic Obstacle (ejecta) arriving at same/different time as shocks. N stands for number of events.

Figure 3.7 The superposed-epoch plots of hourly data of galactic cosmic ray (GCR) intensity at Oulu NM $[\Delta I/I]_O$ (%), GCR intensity at Newark NM $[\Delta I/I]_O$ (%), plasma/field parameters [V, F, σ_F, FV, and FV^2] due to ICMEs associated with/without shocks observed during 1995 – 2009; zero hour (epoch) corresponds to end time (hour) of ICMEs associated with/without shocks. N stands for number of events.

Figure 3.8 The superposed-epoch plots of hourly data of galactic cosmic ray (GCR) intensity at Oulu NM $[\Delta I/I]_O$ (%), GCR intensity at Newark NM $[\Delta I/I]_N$ (%), plasma/field parameters [V, F, σ_F, FV, and FV^2] due to CIRs associated with/without shocks observed during 1995 – 2009; zero hour (epoch) corresponds to arrival time (hour) of CIRs associated with/without shocks. N stands for number of events.

Figure 3.9 Frequency distribution of i) maximum speed, [V_{max}, km s^{-1}], ii) maximum IMF vector, [F_{max}, nT], iii) maximum electric field, [FV_{max}, mV m^{-1}], iv) standard deviation in IMF vector, [σ_{Fmax}, nT], and v) maximum [FV^2max, mV s^{-1}] observed during the passage of CIRs associated/not associated with shocks. Gaussian best fit curves representing the distribution of CIRs are also shown in the figure. The

central peak values x_c, and full width at half maxima w_c obtained from the fits are also given. N stands for number of events considered for each histograms.

Figure 3.10 The superposed-epoch plots of hourly data of galactic cosmic ray (GCR) intensity at Oulu NM $[\Delta I/I]_O$ (%), GCR intensity at Newark NM $[\Delta I/I]_N$ (%), plasma/field parameters [V, F, σ_F, FV, and FV^2] due to CIRs associated with/without shocks observed during 1995 - 2009; zero hour (epoch) corresponds to stream interface (SI) time (hour) of CIRs associated with/without shocks. N stands for number of events.

Figure 3.11 The superposed-epoch plots of hourly data of galactic cosmic ray (GCR) intensity at Oulu NM $[\Delta I/I]_O$ (%), GCR intensity at Newark NM $[\Delta I/I]_N$ (%), plasma/field parameters [V, F, σ_F, FV, and FV^2] due to CIRs associated with/without shocks observed during 1995 - 2009; zero hour (epoch) corresponds to end time (hour) of CIRs associated with/without shocks. N stands for number of events.

Figure 4.1 A typical compound high-speed stream caused by two coronal–hole associated streams (C) and a CME associated stream (E) observed between UT: 14:00, 20 July 2010 to UT 14:00, 12 August 2010. The dotted vertical lines on the left and right are the start and end times of the stream. We plot the temporal variation of various parameters: GCR-intensity variation recorded by Oulu neutron monitor $[\Delta I/I]_O$ (%), and Hermanus neutron monitor $[\Delta I/I]_H$ (%), the solar-wind velocity [V, km s^{-1}], plasma density [N, n cm^{-3}], plasma temperature [T, 10^5 K], interplanetary magnetic field [B, nT], standard deviation in field vector [σ_F, nT], and the electric field [E, mV m^{-1}] from 15 July 2010 to 14 August 2010.

Figure 4.2 Superposed-epoch analysis results of the GCR-intensity variation recorded at Oulu NM $[\Delta I/I]_O$ (%), at Hermanus NM $[\Delta I/I]_H$ (%), the solar-wind velocity [V, km s^{-1}], interplanetary magnetic field vector [F, nT], standard deviation of magnetic field [σ_F, nT], electric field [E, mV m^{-1}], plasma density [N, n cm^{-3}], and the plasma temperature [T, 10^5 K] plotted for the arrival times of high-speed streams (zero hour) of the five categories based on the speed.

Figure 4.3 Relationship between the averaged temporal variation of the solar-wind velocity and the GCR-intensity depressions during the main phase of the intensity decrease caused by the five stream categories based on speed.

Figure 4.4 Superposed-epoch analysis results of the GCR-intensity variation recorded at Oulu NM $[\Delta I/I]_O$ (%), at Hermanus NM $[\Delta I/I]_H$ (%), the solar-wind velocity [V, km s^{-1}], interplanetary magnetic field vector [F, nT], standard deviation of magnetic field [σ_F, nT], electric field [E, mV m^{-1}], plasma density [N, n cm^{-3}], and the plasma temperature [T, 10^5 K] plotted for the arrival times of high-speed streams (zero hour) of the five categories based on the duration.

Figure 4.5 Relationship between the averaged temporal variation of the solar-wind velocity and the GCR-intensity depressions during the main phase of the intensity decrease caused by the five stream categories based on duration.

Figure 4.6 Superposed-epoch analysis results of the GCR-intensity variation recorded at Oulu NM $[\Delta I/I]_O$ (%), at Hermanus NM $[\Delta I/I]_H$ (%), the solar-wind velocity [V, km s^{-1}], interplanetary magnetic field vector [F, nT], standard deviation of magnetic field [σ_F, nT], electric field [E, mV m^{-1}], plasma density [N, n cm^{-3}], and the plasma temperature [T, 10^5 K] plotted for the arrival times of the high-speed streams (zero hour) of the five categories based on the stream sources.

Figure 4.7 Relationship between the averaged temporal variation of the solar-wind velocity and the GCR-intensity depressions during the main phase of the intensity decrease caused by the five stream categories based on sources.

Figure 4.8 Superposed-epoch analysis results of the GCR-intensity variation recorded at Oulu NM $[\Delta I/I]_O$ (%), at Hermanus NM $[\Delta I/I]_H$ (%), the solar-wind velocity [V, km s^{-1}], interplanetary magnetic field vector [F, nT], standard deviation of magnetic field [σ_F, nT], electric field [E, mV m^{-1}], plasma density [N, n cm^{-3}], and the plasma temperature [T, 10^5 K] plotted for the arrival times of high-speed streams (zero hour) associated or not associated with a shock.

List of Tables

Chapter 1

INTRODUCTION AND LITERATURE SURVEY

This chapter describes an overview of basic idea and history that are discussed in this thesis, starting with a short introduction of the Sun, its interior and atmosphere. This is followed by a description of the solar wind, interplanetary magnetic field, and the heliosphere. The large-scale structures of the solar wind in the heliosphere i.e. interplanetary counterparts of coronal mass ejections (ICMEs) and corotating interaction regions (CIRs), their origin, and the shock waves driven by these structures are addressed. A special class of coronal mass ejection, called magnetic cloud is also described. Finally, a brief review of the concepts in galactic cosmic-ray modulation and different mechanisms responsible for modulation are presented. This chapter also envelops the results of earlier studies on transient and corotating decreases in cosmic-ray intensity, mainly due to ICMEs and CIRs.

1.1 The Sun

The Sun is our nearest star and at the centre of the solar system. It is the most important source of energy for life on the Earth. The Sun is a nearly spherical ball of hot plasma, with internal convective motion that generates a magnetic field via a dynamo process (Charbonneau, 2014). The Sun has a total luminosity L = 3.86 × 10^{26} W, the mean density is 1.4 g cm^{-3} and radius $R = 6.96 \times 10^8$ m which is about 109 times that of Earth, and it has a mass M = 1.99 × 10^{30} kg, which is about 330,000 times that of Earth, accounting for about 99.86 % of the total mass of the solar system (Woolfson, 2000). Chemically, about three quarters of the Sun's mass consists of hydrogen, whereas the rest is mostly helium, and much smaller quantities of heavier elements, including oxygen, carbon, neon and iron (Basu and Antia, 2008). The Sun is a G-type main-sequence star (G2V) based on spectral class which was formed about five billion years ago from the gravitational collapse of matter within a region of large molecular cloud (Connelly *et al.*, 2012). Most of the matter gathered in the centre, whereas the rest flattened into an orbiting disk that became the solar system. The central mass became increasingly hot and dense, eventually initiating thermonuclear fusion in its core. The entire energy emitted by the Sun is produced by 'hydrogen fusion' reactions. The Sun has an absolute magnitude of +4.83 and visual brightness –26.74. This is now estimated to be brighter than about 85 % of the stars in the Milky Way (Lada, 2006). The Sun is roughly in middle age and will continue to maintain this stable state for about another five billion years before entering the red giant phase.

1.1.1 Solar Interior

The solar interior is separated into four regions by the different processes that occur there as shown in Figure 1.1. The core is the central part of the Sun, where nuclear fusion takes place. The temperatures in the core are around 1.5×10^7 K and the pressure exceeds 2.5×10^{11} atm which is high enough for the fusion reaction to occur. The core is about to $0.3R_\odot$ in radius, where $R_\odot$ is the radius of the Sun. The core is surrounded by a $0.44R_\odot$ wide shell, called the radiative core or radiative zone. In radiative zone, energy is transported by radiation. The next outer layer of the Sun (0.74 – 1.0 $R_\odot$) is the convection zone, in which energy is transported by convection. The temperature of the convection zone is lower than that in the radiative zone and

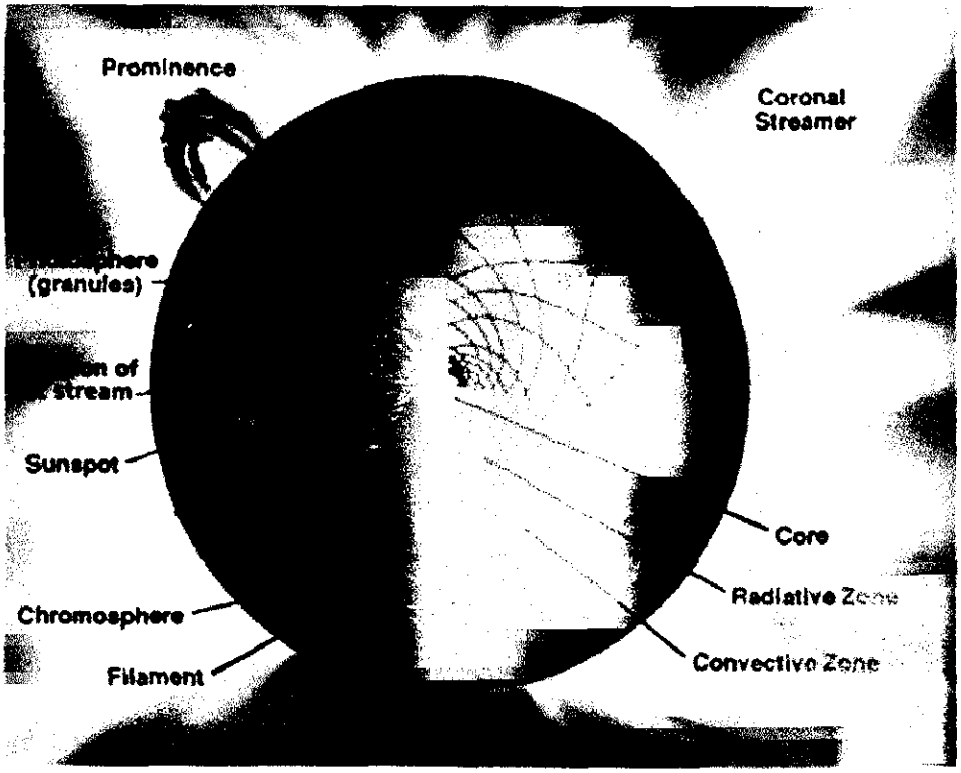

Figure 1.1 Different layers of the Sun and its atmosphere.

heavier atoms are not fully ionized. The density of the gases in this zone is low enough to have convective currents. The interface layer lies between the radiative zone and the convective zone. This is a region where the sharp regime change between the uniform rotation of the radiative zone and the differential rotation of the convection zone results in a large shear—a condition where successive horizontal layers slide past one another (Tobias, 2005). The fluid motions found in the convection zone above, slowly disappear from the top of this layer to its bottom, matching the calm characteristics of the radiative zone on the bottom. It is now believed that the Sun's magnetic field is generated by a magnetic dynamo in this layer. The changes in fluid flow velocities across the layer (shear flows) can stretch magnetic field lines of force and make them stronger. This change in flow velocity gives this layer its alternative name – the tachocline. There also appears to be sudden changes in chemical composition across this layer. The top of the convection zone is the photosphere, the visible surface of the Sun. It is called the visible surface because here most of the visible light is emitted. Below the photosphere the Sun becomes opaque to visible light (Abhayankar, 1977) and above the photosphere

visible sunlight is free to propagate into space, and its energy escapes the Sun entirely. The convective motions themselves are visible at this surface as granules and supergranules. A number of features can be observed in the photosphere such as the dark sunspots, the bright faculae, granules and supergranules as well as large scale flows and a pattern of waves and oscillations. From the centre of the core to the photosphere, the density decreases by more than ten orders of magnitude, and the temperature decreases by a factor of 3000.

1.1.2 The Solar Atmosphere

The Sun's atmosphere typically refers to all the regions above the photosphere (Abhayankar, 1977). Based on their temperature, density, and composition, the solar atmosphere consists of three layers: the chromosphere, the transition region, and the corona (see Figure 1.1).

The chromosphere is an irregular layer above the photosphere where the temperature rises from ~ 4500 K to about ~ 20,000 K with increasing height. It is about 2000 km thick with a density of about 10^{16} m^{-3} dominated by a spectrum of emission and absorption lines. At these higher temperatures hydrogen emits light that gives off a reddish color (H-alpha emission). This colorful emission can be seen in prominences that project above the limb of the Sun during total solar eclipses. The features that appear on this layer include the chromospheric network of magnetic field elements, bright plages around sunspots, dark filaments across the disk and prominences above the limb (Gallagher *et al.*, 1999). The chromosphere is the surface of activity also. Changes in solar flares, prominence and filament eruptions, and the flow of material in post-flare loops can all be seen over the duration of just a few minutes.

The transition region is a thin (about 200 km) and very irregular layer of the Sun's atmosphere that separates the hot corona from the much cooler chromosphere. Heat flows down from the corona into the chromosphere and produces this thin region where the temperature changes rapidly from 10^6 K down to about 20,000 K (Erdelyi and Ballai, 2007). The transition region does not occur at a well-defined altitude. In this region, hydrogen is ionised so instead of hydrogen, the light emitted by the transition region is dominated by such ions as carbon, oxygen, and silicon each with three electrons stripped off. These ions emit light in the ultraviolet region of the solar

spectrum that is not easily visible from Earth's surface but is readily observable from space.

The corona is the Sun's outer atmosphere. It can be seen during a solar eclipse as a structured, irregular ring of rays around the solar disk. Its structure and extent vary with the solar cycle. However, the corona does not have a sharp outer boundary, but instead shows structures which extend into different heights and then fade into background. Temperature of this region is about 10^6 K and has a particle density around 10^{15}– 10^{16} m^{-3} (Hansteen, Leer, and Halzer, 1997). Radiations from the corona are recorded continuously by an instrument called coronagraph. The coronal light may be divided into three components: i) The K-corona. Here K denotes continuous radiation resulting from the photospheric radiation that is Thomson-scattered by free electrons in the corona. ii) The F-corona (or false corona). This is photospheric radiation diffracted by interplanetary dust. This is not physically connected with the corona but needs to be determined to separate it from the desired K-corona. iii) The E or L-corona. This is the total light of coronal emission lines (optical region), such as the green coronal line (5303 Å due to Fe XIV) and yellow line (5694 Å due to Ca XV). Helmet streamers (coronal streamers), polar plumes, coronal loops, and coronal holes are various coronal features.

1.2 Solar Wind, Interplanetary Magnetic Field, and the Heliosphere

The name "solar wind" was introduced by Parker (1958) and its confirmation came with the advent of the Soviet probes Lunik 2 and 3 in 1960, after they left the magnetosphere. The probe Mariner, in 1962, during its 4 months around the planet Venus, have also confirmed the existence of a continuous flow of plasma from the Sun (Synder and Neugebaur, 1963). The solar wind is now considered as a continuous flux of mixture of solar particles found in the solar plasma, such as ionized hydrogen (protons and electrons), helium (alpha particles), and trace amounts of heavy ions and atomic nuclei: C, N, O, Ne, Mg, Si, S, and Fe streaming away by heating of the Sun's outer atmosphere, *i.e.* corona (Feldman *et al.*, 1998) through the solar system at a temperature of 1 million degrees (Celsius). Thus, Solar wind is the expansion of solar corona out into the heliosphere, carrying the coronal magnetic field along, forming the interplanetary magnetic field (Parker, 1958; Hundhausen, 1972).

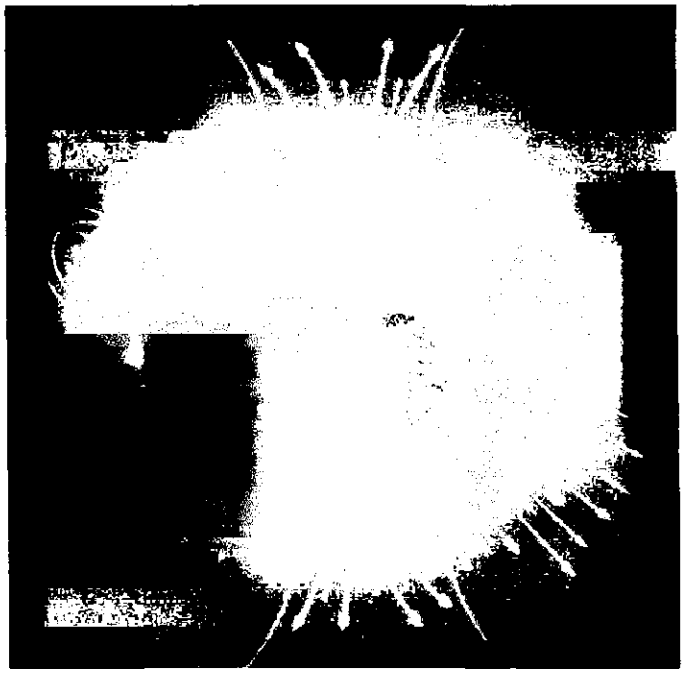

Figure 1.2 Fast and slow solar winds, open and closed magnetic field lines.

In Figure 1.2, the solar atmosphere, or corona, threaded with magnetic fields is shown by yellow lines. Regions with open magnetic fields, known as coronal holes, give rise to fast, low density, solar-wind streams are represented by long, solid red arrows. Areas with closed magnetic fields yield the slow, dense wind are shown by short, dashed red arrows. This image representing Figure 1.2 was taken on 11 September 2003, with Extreme-Ultraviolet Imaging Telescope (EIT), aboard the Solar and Heliospheric Observatory (SOHO).

The formation of the solar wind is closely linked to the hot corona. Recent in situ measurements at the Earth's orbit and remote observations at the UV wavelengths by SOHO spacecraft have provided clues for the heating of ions by the ion-cyclotron waves. The generation of wave energy may be continuous or episodic. In the open field corona, the energy is carried by the solar wind in the form of kinetic energy, which is the work done against the gravity of the Sun.

Parker (1958) prediction is that the open corona cannot exist in hydrostatic equilibrium with respect to the local interstellar medium and can only be balanced by the continuous outward expansion of the corona into space. Since the rarefied corona is good thermal conductor (Parker, 1964), its temperature can be maintained nearly at the same level even at sufficiently large distance from the Sun (*i.e.*, the temperature

gradient is very small). However, the decreasing density with increasing heliocentric distance produce by the gravity of the Sun causes a steep gradient in the gas pressure. As a result, the hydrostatic equilibrium cannot be maintained in the corona and the pressure gradient aids to push the coronal material outward and solar wind flows radially outward in all directions and fills the whole interplanetary space. At certain distances, some of the features of the solar wind, particularly in the case of the high speed streams (HSS) (Krieger, Timothy, Roelof, 1973), can be identified with features of the large-scale corona, the so-called coronal holes (CHs). CHs are usually located above inactive parts of the Sun, where "open" magnetic field lines prevail, *e.g.*, at the polar caps around activity minima.

Two basic classes of plasma flows are observed in the interplanetary medium as the fast and the slow solar wind. Ulysses and Helios missions both contributed to the confirmation of the existence of these two different types of solar wind. The fast solar wind originates in the coronal holes, the dark parts of the corona dominated by open field lines are representatives of the inactive or "quiet" Sun. Feldman *et al.* (1976) first proposed this nomenclature, which caused a major paradigm change. Ulysses orbited over the solar poles and observed faster solar wind. On the other hand, Helios with its orbit mostly in the ecliptic plane detected the features of the slow solar wind commonly found in the equatorial region. In fact, the existence of sharp boundaries between solar-wind streams (in longitude and in latitude) has already been noticed by Rosenbauer *et al.*, 1977. These two types of solar wind differ markedly in their main properties and by the location and magnetic topology of their sources in the corona. The fast solar-wind streams are often stable over a long time period and variations from one stream to another are small. This solar wind has flow speeds between 400 km s^{-1} and 800 km s^{-1}, the average density is low *i.e.* about 3 ion cm^{-3} at 1 AU. The average particle flux is about 2×10^{12} s^{-1} m^{-2}, implying a total particle loss from the Sun of about 1.3×10^{31} s^{-1}. The proton temperature is about 2×10^{5} K and the electron temperature is about 1×10^{5} K. The slow solar wind has lower speeds between 250 km s^{-1} and 400 km s^{-1}. Its density is about 8 ions cm^{-3}at 1AU, and the flux density is about twice as large as that in the fast solar wind. During solar minimum the slow solar wind originates from regions close to the current sheet at the heliomagnetic equator. During solar maximum the slow solar wind are most often associated with closed magnetic structures, such as bipolar loop systems and above the more active

regions in the streamer. Compared with the fast solar wind, it is highly variable and turbulent, often containing large-scale structures such as magnetic clouds or shocks. The proton temperatures are markedly lower, about 3×10^4 K, while the ion temperatures are similar to fast solar wind. The field lines of slow solar wind are more curved than faster one (Kallenrode, 1998). These two solar winds are probably distinct in relation to their acceleration mechanism. Figure 1.3 shows the radial dependence of the solar wind speed for different coronal temperatures. For a coronal density of about 2×10^8 cm^{-3} and temperature of one million Kelvin, the critical point is about 6 $R_\odot$. The solar wind then accelerates upto about 40 $R_\odot$, afterwards propagating at a nearly constant speed of 500 km s^{-1}.

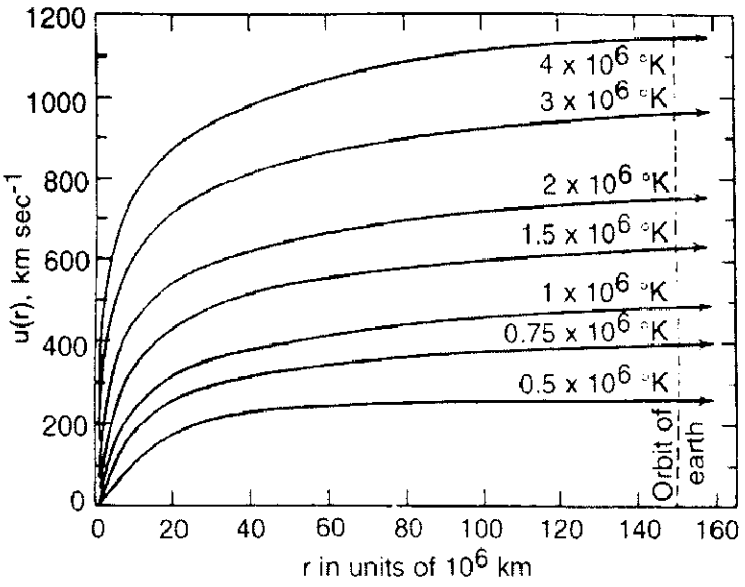

Figure 1.3 Acceleration of the solar wind according to Parker's theory.

Since the conductivity of the solar wind plasma is high, the Sun's magnetic field is frozen into the plasma and is carried along with the plasma flow out into the interplanetary space (Kallenrode, 1998; Owens and Forsyth, 2013), is called the interplanetary magnetic field (IMF). The frozen-in IMF takes the shape of the Archimedian spiral pattern (Figure 1.4), because of the radial out flow of the solar wind, the rotation of the Sun, and the azimuthal symmetry of the solar wind with respect to the rotation axis of the Sun. The angle φ between the spiral magnetic field and the Sun-Earth radial vector (spiral angle) can be given by equation, $tan\ \varphi = B\varphi/B_r$

$= -\omega r/V$, where ω is the angular velocity of the solar rotation, r is the distance from the Sun, and V is the solar wind velocity.

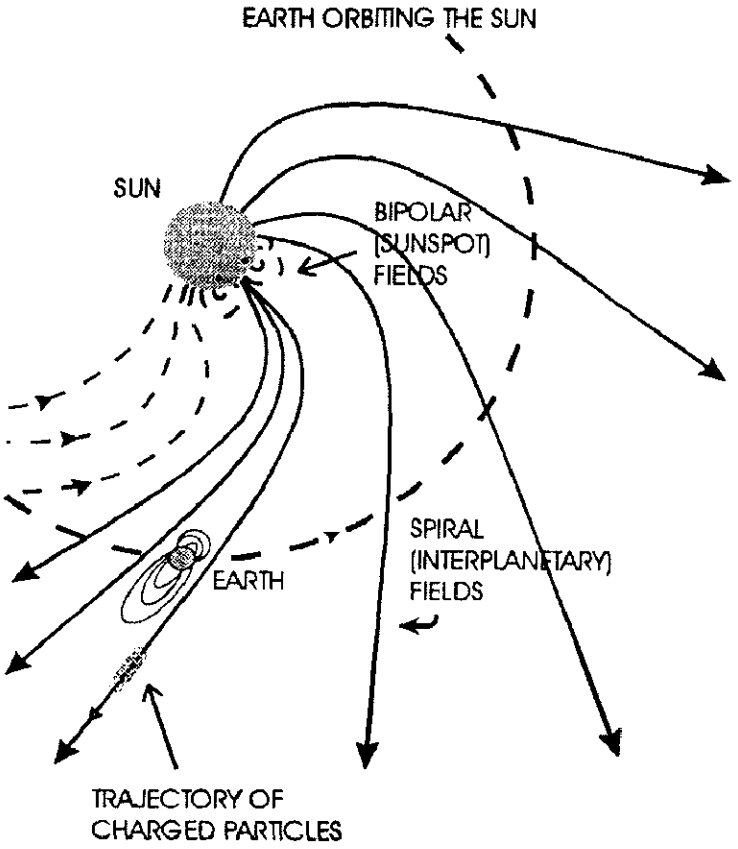

Figure 1.4 The spiral structure of the interplanetary magnetic field.

The radial component of the field, B_r varies as $B_r \sim r^{-2}$ and at large distance, it merges with the azimuthal component $B\varphi$, which falls of linearly with distance, $B\varphi \sim r^{-1}$ (Patzold *et al.*, 1987). At the orbit of the Earth, a solar-wind speed of ~ 400 km s^{-1} gives a spiral angle φ of approximately 45° with respect to the radial flow direction. With increasing distance from the Sun, φ increases and becomes nearly 90° near the Jupiter and the magnetic field becomes more and more toroidal. The IMF has a sector with fields of positive (anti-sunward) and negative (sun-ward) polarities that alternate at cycles almost coinciding with the Sun's rotational period of 27 days. The region at which the polarity changes from positive to negative is called sector boundary. The IMF effectively shapes the three–dimensional view of the interplanetary medium.

Heliosphere is the region of space directly influenced by the Sun and its magnetic field. The magnetic field of the Sun is enormous and is carried throughout space by solar wind. The solar wind streams off out of the Sun at a speed of several hundred km s^{-1}, creating a magnetized bubble of hot plasma around the Sun. This bubble is called the heliosphere, and it is separated from the interstellar gas by heliopause. The heliopause is believed to be ~150 AU away from the Sun, *i.e.*, all planets are located within it (Venkatesan and Badruddin, 1990). The point where the solar wind slows down is the termination shock; the point where the interstellar medium and solar wind pressures balance is called the heliopause; the point where the interstellar medium, travelling in the opposite direction, slows down as it collides with the heliosphere is the bow shock (Figure. 1.5).

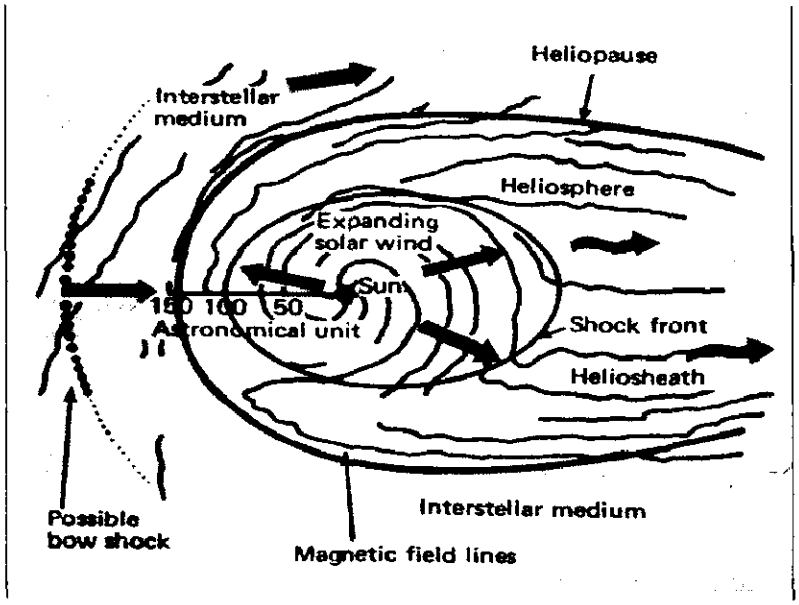

Figure 1.5 A schematic view of the heliosphere and its interaction with the interstellar medium. The out flow of solar wind and IMF lines are also shown here (Venkatesan and Badruddin, 1990).

In 2002, Voyager 1 and Voyager 2 were cruising near 85 AU and 67 AU, respectively and Voyager 1 crossed the termination shock at 94 AU in December 2004 and Voyager 2 crossed at 84 AU in August 2007. In 2008, Voyager 1 was about 106.26 AU from the Sun. Currently, as of May 2015, Voyager 1 was at a distance of

131.51 AU from the Sun and Voyager 2 at a distance 108.11 AU. Voyager 1 is escaping the solar system at a speed of about 3.6 AU per year, 35 degrees out of the ecliptic plane to the north, in the general direction of the Solar Apex (the direction of the Sun's motion relative to nearby stars). Voyager 2 is also escaping the solar system at a speed of about 3.3 AU per year, 48 degrees out of the ecliptic plane to the south. The ultimate goal is of reaching and studying the heliopause, which is the known boundary of our stellar system. The Voyagers should cross the heliopause 10 to 20 years after reaching the termination shock. The Voyagers have enough electrical power and thrusters' fuel to operate at least until 2020 (see *http://voyager.jpl.nasa.gov*).

1.3 Large-Scale Structures in the Heliosphere:

1.3.1 Coronal Mass Ejections and Their Propagation in the Interplanetary Medium

The idea of plasma clouds propagating from the Sun to the Earth was proposed as a cause of geomagnetic storms even before the existence of the solar wind was contemplated (Lindermann, 1919). Such plasma clouds are now known as coronal mass ejections (CMEs) and are routinely observed in the solar wind. As a consequence of the frozen-in property of magnetic fields in fully ionized plasma, a beam of plasma from the Sun carries along the solar magnetic field. The CMEs are large-scale structure expelled through the solar corona. The observations of CMEs are possible with coronagraphs, which artificially occult the solar disk, or during a solar eclipse and enable imaging of the solar corona.

At the time of the first observations, the corona was considered very quiet, almost static, with a very slow evolution in its appearance over the 11-years solar activity cycle. With the advent of the new technologies and the improvement on the observation techniques, the corona was recognized by its very dynamic behaviour, with activity occurring over a wide range of temporal and spatial scales. Only after the advent of the first coronagraph 7th Orbiting Solar Observatory (OSO-7) and with Skylab/ATM and P78-1 at the beginning of the 1970's came the first observation of a CME at the solar surface. The white light that appeared in the coronagraph images onboard OSO-7 gave birth to the knowledge of a new type of solar eruption (Tousey

et al., 1973), later denominated coronal mass ejections (Gosling *et al.*, 1975; Burlaga *et al.*, 1982). Hundhausen *et al.* (1984) defined a CME as "an observable change in coronal structure that 1) occurs on a time scale of a few minutes and several hours and 2) involves the appearance (and outward motion) of a new, discrete, bright, white light feature in the coronagraph field of view". Although CMEs often exhibit a three part structure which consists of a bright front followed by a dark cavity and bright core as clearly seen in Figure 1.6. The difficulties to understand the mechanisms involved in their acceleration, as well as the mechanism related to the generation of these structures, reveal that there is still a lot to be investigated about CMEs. It is observed that around 30 % of the CMEs have associated to their sources an enormous eruptive prominence (Wang and Zhang, 2008) whose features can be observed even after the eruption. The plasma behaviour is very different when CMEs are involved once we deal with densities in general higher than the typical solar-wind density.

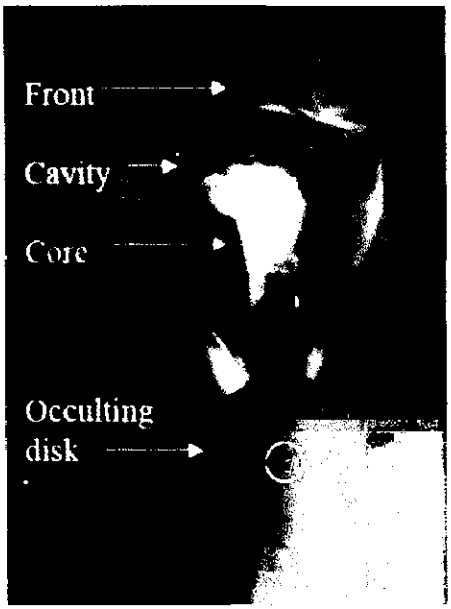

Figure 1.6 The typical parts of a normal CME observed by the LASCO coronagraph on SOHO spacecraft. The white circle marks the solar limb.

By using images from Large Angle Spectrographic Coronagraph (LASCO), Cremades, Bothmer, and Tripathi (2006) found that CMEs' central position angles (PAs) have been sorted in two categories: eastern PAs (0 – 180°) and western PAs

(180 – 360°). The PA is an angular attribute of a feature projected in the plane of the sky, measured counter clockwise from the solar north.

Because of their position in the solar disc and the place they are ejected in the field of view of the coronagraph, CMEs may be classified as limbs, halos or partial halos. The so-called "halo" CMEs extend themselves over the full solar disc and their brightening occurs simultaneously all around the coronagraph occulting disk (Howard *et al.*, 1982; Webb and Howard, 2013). Halos can be front-sided or back-sided, which can be distinguished by obtaining simultaneous disk observations. Partial halos are CMEs with apparent width between 120° and 360° and the Limb CMEs occur above the limb and have an angular width less than120°. However, this difference in appearance is mainly because of the projection effect. A typical CME seen above the limb with an angular width of 60° would appear as a halo or a partial halo CME depending upon whether it is oriented along the Sun-Earth direction or 40^0 away from the Sun-Earth direction, respectively.

Cremades and Bothmer (2004) have corrected the effect of CME's projection for 200 events observed between years 1996 and 2002 by determining their real latitudinal centers. During solar minimum the solar equator was pointed out as the center of the ejections. They found that the CME sources were centred in two belts around 25° latitude North and South. Furthermore, the deflection on the structured CME was mostly caused by the fast solar wind from the CHs in the solar poles. The CHs block the CME expansion to higher latitudes; however, this has dependence on the solar cycle and on the complexity of the corona. For instance, when larger CHs are absent, the CMEs would not suffer such deflection. The combination of observations from LASCO and the EIT allowed the determination of the origin of the CME, whether it is in the far side or in the visible disk (earthward). In addition to the images obtained from the instruments onboard the satellites, magnetic field and plasma data complement the understanding of the relations between the interplanetary structures and their solar sources. When propagating in the interplanetary medium, together with the solar wind that constantly flows from the solar atmosphere, the CMEs are named Interplanetary Coronal Mass Ejections (ICMEs).

The frequency of their occurrence is a function of the 11-years solar activity cycle. Perhaps the most spectacular manifestations of the coronal activity are the CMEs. During the maximum of the solar activity the frequency is higher than 6 CMEs per

day, while in the minimum this frequency decreases to 0.5 CMEs per day (Gopalswamy, 2006). This is not so surprising because in general CMEs observed in connection with filaments and also with flares which both depends upon solar cycle. Gopalswamy *et al.* (2003) studied the solar cycle variations of various properties of CMEs for cycle 23 (1996 – 2002) and they found an increase of the mean and median speeds of CMEs from minimum to maximum by a factor of 2.

Observations of CMEs have not only led to study of morphological properties but also their physical and kinematical properties on a statistical basis. The projected widths of CMEs show a distribution of an average of about 46° and a median is of 42°. CMEs smaller than 20° and greater than 60° are rarely found. The angular extent is found more than 120°. The width of CMEs found independent of solar cycle. During a CME between 2×10^{14} g and 4×10^{16} g coronal material is ejected outward into interplanetary space from the Sun; the kinetic energy contained in a CME is in between 10^{22} J and 10^{24} J (Kallenrode, 1998). Ejection speed range from less than 50 km s^{-1} in some of the slower events to greater than 2000 km s^{-1} in some of the faster ones (Gopalswamy, 2004). CMEs are gigantic plasma clouds ejected from the Sun to the interplanetary space that normally are associated to high propagation speeds. This later property leads to large scale shock waves generated due to the difference between the speed of the medium and the speed of the CME.

1.3.2 Interplanetary Shocks

Interplanetary shocks are identified by characteristic changes in the plasma and field parameters, in particular a sudden increase in the plasma density, speed, and temperature, and a jump in the magnetic field strength.

The properties of interplanetary shocks are highly variable. Between 0.3 AU and 1 AU, the basic characteristics are as follows:

1. The compression ratio varies between 1 and 8 with an average close to 2.
2. The magnetic compression (ratio between the upstream and downstream magnetic field strengths) varies between 1 and 7 with an average at 1.9.
3. Shock speeds in the laboratory frame vary between 300 km s^{-1} and 700 km s^{-1} with an average about 600 km s^{-1}, occasionally shock speeds above 200 km s^{-1} can be observed. Shocks with speeds only slightly above 300 km s^{-1} can be observed in very slow solar wind streams only.

4. The angular extend of the shock varies between a few tens of degree and up to 180°, the shock is always wider than the driving CME.
5. The Alfven Mach number is between 1 and 13 with an average at 1.7.

The shock parameters, of course, are related to the properties of the CME, such as speed, angular extent, and total energy released. An interplanetary shock is a disturbance propagating into the expanding solar wind. The shock should develop absolutely because it expands, too, and also relative to the ambient medium as the latter ones expands differently. In particular, the expansion of the shock leads to decrease in the plasma and magnetic flux densities. Thus the energy density also decreases. But the latter decreases not only because of shocks expansion: turbulence created in the wake of the shock and particles accelerated at the shock front also reduce the shock's energy.

Two extreme cases can be distinguished. If a shock is very fast close to the Sun (with CME speeds above 1000 km s^{-1}), it is likely to decelerate in interplanetary space. On the other hand, shocks that are rather slow on the Sun do not decelerate but propagate at roughly constant speed. The faster shocks in general tend to be more efficient particle accelerators, and thus part of the shock's kinetic energy is converted into kinetic energy of particles. In some sense, this relates to the different speed characteristics of the CMEs and to the conversion of shock kinetic energy into particle energy (Kallenrode, 1998).

When the Magnetohydrodynamic (MHD) theory is taken into account, three possible speeds are present: the sound, Alfv'en, and magnetoacoustic speeds (Burlaga, 1971). Consequently there are six possible types of shocks: the fast, the slow, and four other types of intermediate shocks (Wu, 1990). However, based on the shock's evolutionary condition of ideal MHD, Taniuti (1962) argued that the MHD intermediate shocks are not structurally stable and are physically unrealizable. However, theoretical study and numerical simulations showed that the MHD intermediate shocks are admissible and can be formed by the steepening of nonlinear MHD waves (*e.g.*, Kennel, Blandford, Coppi, 1989).

The type of shock is dependent on the propagation speed of the surface in relation to the characteristic speeds of the medium (Burlaga, 1995, and references therein). In space, the most likely type is the fast one, characterized by an increase in the IMF strength, while the slow one is characterized by a decrease in the IMF strength. Both

fast and slow shocks that move radially away from the Sun are so called forward shocks, and the ones that move toward the Sun relatively to the solar wind are named reverse shocks. In the interplanetary space, the forward shocks are normally formed as a consequence of the propagation of structures such as CMEs and identified by the sensors onboard satellites in orbit. In general, when a mass flux through the shock is observed and subsequently the solar-wind parameters and the entropy of the system increase abruptly, a shock wave is identified.

Interplanetary shock waves involve non-linear processes that take place in the interplanetary space with non-collisional plasmas. Collisionless shock waves in the solar wind result from the interaction of plasma flows of different velocities, densities, and temperatures. They are formed when the difference between the speeds of the interacting plasma flows is greater than the characteristic velocity at which information about dissipation processes propagates. In the classical view of MHD shock waves, when two plasmas interact, this takes place over a very short distance, and at a sufficient distance away from the shock surface (Balogh *et al.*, 1995).

Through a closer examination one can see that shock waves involve a wide variety of complex plasma phenomena with wave-particle interactions. Such interaction can have a significant spatial extent, affecting the properties of the upstream, as well as the downstream solar wind flow. Depending on the geometry of the magnetic field in relation to the shock surface, it can play an important role in determining the type of dissipation process that will take place. The angle between the shock normal and the upstream magnetic field is used to classify the shocks in the upstream region.

The existence of shock waves in collisionless plasmas has been debated over many decades. The first prediction of a shock wave formed in front of Earth's magnetosphere was done by Axford (1962). The confirmation came with spacecraft observations in 1963. The shock formed in front of the dayside magnetopause is due to the continuous supersonic solar wind flow that finds an obstacle in its path. The interaction and the difference between the speed of the solar wind and the obstacle speed in the medium forms a shock wave in the interplanetary space that represents an important feature of the solar wind. With the advent of the probe Interplanetary Monitoring Platform 1 (IMP-1)/Explorer 18, the so-called bow shock was reported for the first time (Sonett *et al.*, 1964).

In the same manner as the steady-state shocks, which are formed due to interaction between the solar wind and planets, shocks involving collisions can be formed in the interplanetary space. The presence of electromagnetic fields may alter the dissipation process of the charged particles leading to collisions among them. Finally, these long-range interactions result in collective effects that, among others, form shock waves and other plasma modes. In general, shock waves are easily identifiable phenomena by the observation of the local plasma and magnetic field "in situ" measurements. Despite this fact, there is a size distribution of weak shock waves whose identification is not always trivial, but most parts of time questionable because of the difficulty on distinguishing it from a pressure pulse signature (Balogh *et al.*, 1995).

Despite the type of shock, there is always a surface associated to this shock that provides the direction of propagation of the wave, as well as the region of the lower entropy. Such surface is defined by the normal vector that forms an angle with the upstream magnetic field. By using the kinetic theory, one has more information about the details of these shock surfaces. However, the MHD theory gives enough information about the plasma before (upstream) and after (downstream) the shock surface that enables us to describe the shock.

1.3.3 Shock associated ICMEs

Only about the one-third of the CMEs in space drive an interplanetary shock (Gosling, 1992), while apparently all travelling interplanetary shocks are driven by CMEs. The CME driven shocks can play a significant role in the acceleration of solar energetic particles and producing transient decreases in galactic cosmic rays (Gosling, 1990). Transient shocks are often formed during the passage of large-scale structures, such as the ICMEs, in the interplanetary medium (Sheeley Jr. *et al.*, 1985). The interplanetary shock is the result of the difference between the propagating structure (upstream) and the medium (downstream) speeds. Normally, ICMEs are associated to speeds higher than the magnetosonic speed of the solar wind, resulting in shock waves from ICMEs. An important feature to identify shocks is the fact that, as they propagate in a medium, there will be a mass flux through their surfaces. However, this is not a sufficient condition to identify a shock because the rotational discontinuities and other non-linear waves can also propagate in this medium and they are not considered shock waves. A necessary condition to identify a shock is that there is an entropy

increase through the propagating surface. The 3D structure of an ICME and upstream shock, relating magnetic field, and plasma is presented in Figure 1.7.

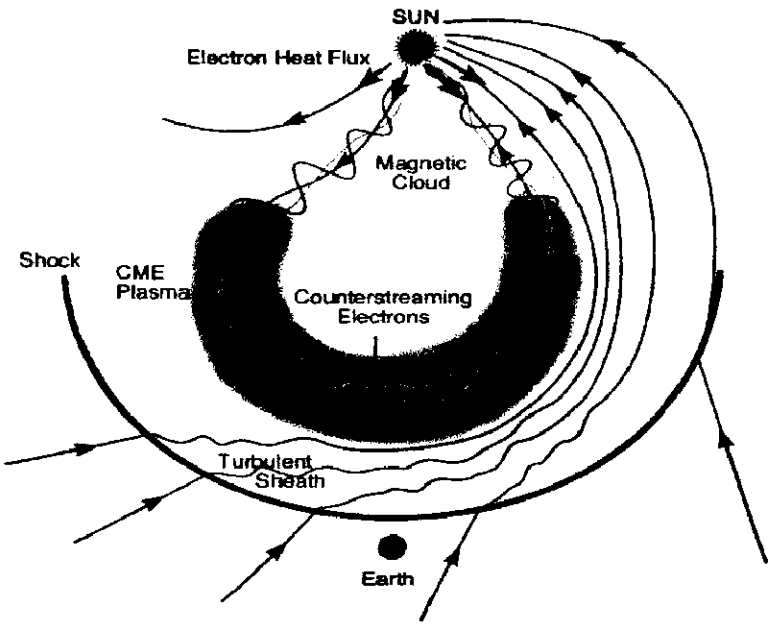

Figure 1.7 Schematic diagram of the 3D structure of an ICME and upstream shock, relating magnetic field, and plasma (Richardson and Cane, 2010).

The fast CMEs often drive large-scale density waves out into space, which eventually steepen to form shock waves, similar to bow shocks in front of the Earth's magnetosphere. The shock wave is the outer boundary of a plasma sheath that results from compression, deflection and heating of the ambient solar wind by the ejecta. The sheath may contain substantial distortions of the interplanetary magnetic field due to field line draping (McComas *et al.*, 1988) around the ejecta cloud pressing from behind.

The ejecta themselves have properties that differ radically from those of the ambient solar wind. At first, the ejecta are often separated from sheath plasma by a tangential discontinuity. Their very different origin is discernible from their different elemental composition, ionization state, temperature depression, cosmic-ray intensity decreases, the appearance of bidirectional distributions of energetic protons and cosmic rays and superthermal electrons (*e.g.* see Schwenn, 2006, and references there in).

1.3.4 Magnetic Cloud

The term Magnetic Cloud (MC) was first used by Morrison (1954) referring to plasma and magnetic field ejections from solar active regions (Klein and Burlaga, 1982). Magnetic clouds are localized regions in interplanetary space with a simple magnetic field topology as is typical for flux ropes. They are characterized by enhanced magnetic field strength, lower proton temperature than the background solar wind and a large-scale large-angle smooth rotation of the magnetic field vector (Burlaga *et al.*, 1981). The ratio between the two pressures (thermal and magnetic) is represented by the plasma beta (β). Plasma beta is characteristically low (lower or equal to 0.1) in MCs due to the dominance of the magnetic field and the low proton temperature and the non-enhanced proton density, typical of MCs. About 30 % of the ICMEs at 1AU exhibited magnetic flux ropes (Gosling, 1990). However, it was suggested that all ICMEs contain a well defined flux rope close to the Sun (Murubashi, 1997), but that some flux rope signature have weakened as the ICME evolves on its way to 1AU (*e.g.* Oshervich and Burlaga, 1997). Alternatively, ICMEs may continue to contain identifiable flux ropes out to 1AU, but some of them are traversed far from the central flux rope where the flux rope can not be defined (see Jian *et al.*, 2006a). Because of their high magnetic field strength and large plasma bulk velocity MCs often (but not always) drive interplanetary shocks. However, in case of a magnetic cloud preceded by a shock wave, there is usually a turbulent sheath between the shock and the magnetic cloud. This difference in the level of magnetic turbulence during the passage of magnetic clouds and sheath regions has been very useful in the study of transient (Forbush) decrease in cosmic-ray intensity (*e.g.* Badruddin, Yadav, and Yadav, 1986; Zhang and Burlaga, 1988; Badruddin,Venkatesan, and Zhu, 1991; Ananth and Venkatesan, 1993; Cane, 1993; Singh and Badruddin, 2007a). In a statistical study of relationship between magnetic clouds and Forbush decreases, it is necessary to distinguish between a magnetic cloud which is preceded by a shock and a magnetic cloud which is not preceded by a shock. However, a MC is not necessary for a Forbush decrease. Any ejection moving fast enough to produce a shock might produce a Forbush decrease (Cane, 2000). Burlaga *et al.* (1981), Klein and Burlaga (1982) identified magnetic clouds in the solar wind, that have a characteristic size of the order of 0.25 AU at 1 AU. Additionally, Burlaga *et al.*, (1982) identifed a magnetic cloud that could be associated with coronal mass ejection, and Wilson and

Hildner (1984, 1986) have found additional evidence supportive of an association between MCs and ICMEs. Every observed MC is believed to have a solar origin, not only because of their large sizes, but also for numerous other reasons including their often apparently successful direct linkage to solar events (Marubashi, 1986; Gosling, 1990).

For about one third of all shocks driven in interplanetary CMEs, the succeeding plasma exhibits to an observer the topology of `magnetic clouds' (Burlaga *et al.*, 1981; Gosling, 1990). However, Cane, Richardson, and Wibberenz (1997) suggest that the ratio might be more like 50% and furthermore that the cloud geometry may be a consequence of intercepting an ejecta near its centre. These ejecta with magnetic cloud or magnetic flux rope geometry are of particular interest to theoreticians, because such structures can be easily modeled, Further, these ejeta have a magnetic enhancement which shows a clear rotation in direction and are therefore easy to identify.

Extensive analysis of solar and interplanetary sources of geomagnetic storms (Zhao and Webb, 2003; Mustajab and Badruddin, 2013) has indicated that CMEs and MCs frequently trigger major geomagnetic activity. Echer, Gonzalez, Alives (2006) determined that combinations of interplanetary structures rather than isolated structures, and specifically interplanetary shocks driven by MCs, are most geo effective (Watermann *et al.*, 2009; Kim, *et al.*, 2013) their geomagnetic effectiveness depends on whether the field at the leading edge has a strong northward or southward component.

MCs were early on associated with either, shocks, stream interfaces, CMEs or disappearing filaments (Burlaga *et al.*, 1981; Lepping, Berdichevsky, and Wu, 2006) and are now a day's considered to be contained in ICMEs as a special subset (Gopalswamy *et al.*, 1998; Lepping, Berdichevsky, and Wu, 2006). They are a relatively common phenomenon (Klein and Burlaga, 1982) about 25% of all ICMEs were reported to fulfil the criteria for MCs (Cane and Richardson, 2003).

1.3.5 Corotating Interaction Regions

Corotating interaction regions (CIRs) are long lasting large-scale plasma structures generated in low and middle latitude regions of the heliosphere where streams of stable fast solar wind and the surrounding slow solar wind collide and interact with

each other. CIRs are detected by solar wind monitor such as the Advanced Composition Explorer (ACE) and *WIND* satellite.

From Helios and Pioneer measurements it can be seen that regions of fast and slow solar wind are separated by sharp boundaries, leading to strong longitudinal speed gradients (Hundhausen and Gosling, 1976). Fast and slow wind steams originate on the Sun while these streams propagate outward, the frozen-in magnetic field is wound up to Archimedean spirals (Gosling and Pizzo, 1990). However, if a slow moving stream is followed by a fast moving stream the faster moving material will catch-up to the slower material and plow into it, this forms an interaction region (compression on the rising-speed portion of the slow stream and a rarefaction on the trailing edge of the fast stream), as indicated in Figure 1.8 (Sarabhai, 1963; Hundausen, 1972).

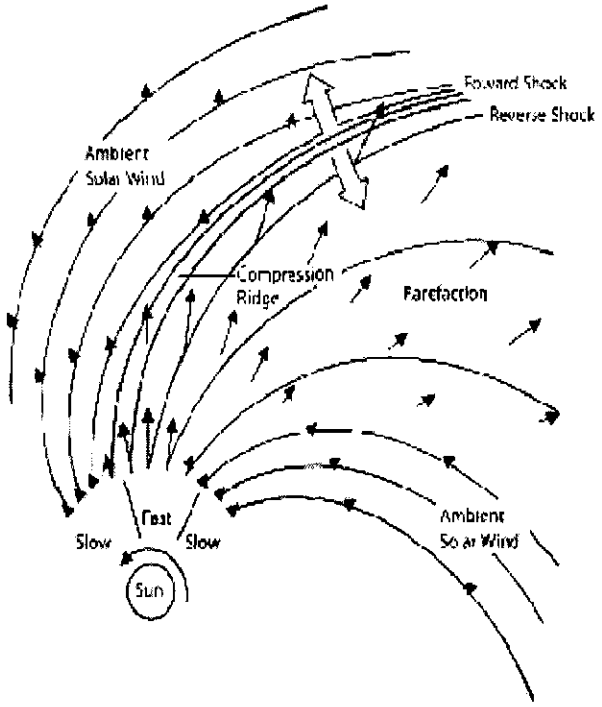

Figure 1.8 Schematic of the formation of corotating interaction regions (CIRs) between slow and fast solar winds. The compression of plasma and magnetic field are also shown (Pizzo, 1978).

If the structure is stable for several solar rotations, an observer in space sees these interaction regions again during the following solar rotations and therefore called a corotating interaction region. This interaction produces shock waves that can accelerate particles to very high speeds. In a stationary frame of reference the source

of the radially expanding HSS rotates with the Sun and thus induces spirally shaped regions of compressions and rarefactions because of the fact that where the high speed material overtakes the slow plasma it forms a compression wave. The non-radial components of the evolving pressure gradients drive secondary non-radial motions (Fahr and Fichtner, 1991).

The interaction between fast and slow streams starts in the inner heliosphere and interaction region broadens with increasing heliocentric distance (Jian *et al.*, 2006b). With increasing distance from the Sun, the characteristic propagation speeds, which are the sound and Alfven speeds decrease. At some distance between 2 and 3 AU, the density gradient on both sides of the compression region becomes too large and a shock pair develops, propagating away from the interface. The shock propagating into the slow wind ahead is called the forward shock. Typical signatures are step like increases of the solar-wind speed, density and magnetic field strength. The boundary separating the originally these two solar-wind streams is termed as stream interface (SI) (Gosling *et al.*, 1978). Typical signatures are the change in entropy, density and abundant ratio of different solar-wind elements (Wimmer-Schweingruber, von Steiger, and Paerli, 1999). Plasma pressure within a CIR peaks in the vicinity of the SI, where there is a large shear in the flow. CIRs tend to distort or even destroy all small-scale fluctuations and disturbance propagating outward from the Sun. In the outer heliosphere, the magnetic field and the shock fronts are more azimuthally aligned, sometimes extending around the entire Sun (Kallenrode, 1998). The corotating shocks at CIRs were first identified between 1 and 5 AU by the probes Pioneer 10 and 11 through the magnetic field and plasma data collected by them during their operation. After the launch of Helios mission, important information related to the features of such structures in the inner heliosphere were available. From these data, it was possible to compare two different regions in the heliosphere, the inner and the outer heliosphere. The observations made by Helios served as a link between what was known about CIRs at distances between 1 and 5 AU, and their evolution in the inner heliosphere.

1.4 Solar Modulation of Cosmic Rays: Basic Concepts

Galactic cosmic rays (GCRs) are high energy charged particles, originating in outer space, distributed throughout our Milky Way galaxy, that travel at nearly the speed of

light and are incident on the solar system isotropically and constantly. It basically consists of hydrogen, helium, and electrons, but also heavier ions such as C, O, and Fe. Most GCRs have energies between 100 MeV and 10 GeV; however ions of energies upto ~ 10^{21} eV have been found in cosmic rays but with decreasing flux.

GCRs encounter a turbulent solar wind with an embedded heliospheric magnetic field when entering the heliosphere. This leads to significant global and temporal variations in their intensity and in their energy as a function of position inside the heliosphere, *i.e.* at energy below a few GeV per nucleon, the intensities of the galactic cosmic radiation show a strong dependence on solar activity with a maximum during the solar mimimum. This effect or process is called solar modulation of cosmic rays. With increasing solar activity, the maximum of the energy spectrum shifts towards higher energies. At proton energies of about 100 MeV the modulation is maximal, while at energies of about 4 GeV the modulation is only 15 % – 20 %. Up to about 10 GeV galactic electrons show a spectrum similar to the protrons. They also show a modulation with solar activity in the energy range 0.1 to 1 GeV (Kallenrode, 1998). Interplanetary structures such as shocks, sheaths, interplanetary counterparts of coronal mass ejections (ICMEs), magnetic clouds, and CIRs are of special interest for the study of the transient modulation of galactic cosmic rays. These structures modulate the GCR intensity with varying amplitude and recovery-time profiles.

The modulation of the galactic cosmic radiation at some GeV is shown in Figure 1.9 (upper panel) together with the sunspot number as an indicator of solar activity (lower panel). In both panels, the solar rotation averages are used. From the figure the anticorrelation is clearly visible. On a longer time scale, the cosmic-ray intensity variations in anti-phase with solar activity having ≈ 11-year cyclicity is well known and has been studied extensively, (*e.g.*, see Venkatesan and Badruddin 1990; Sabbah and Rybansky, 2006; Ma, Han, and Yin, 2009; Chowdhury, Dwivedi, and Ray, 2011; Kudela, 2012; Bazilevskaya *et al.*, 2014). In addition, the ≈ 22-year modulation cycle in cosmic-ray flux due to solar magnetic-field polarity reversals is observed and modeled (*e.g.* Webber and Lockwood, 1988; Potgieter, 1995; Cliver and Ling, 2001; Laurenza *et al.*, 2012; Potgieter, 2013). However, in order to understand these phenomena, it is important to understand how cosmic-ray transport and propagation vary with solar activity and solar magnetic polarity (Heber, 2013).

Cosmic-ray transport in the heliosphere is described by the Parker transport equation (Parker, 1965). If $f(r,P,t)$ is the cosmic-ray distribution with respect to particle rigidity [P], then the cosmic-ray variation with time [t] and position [r] is

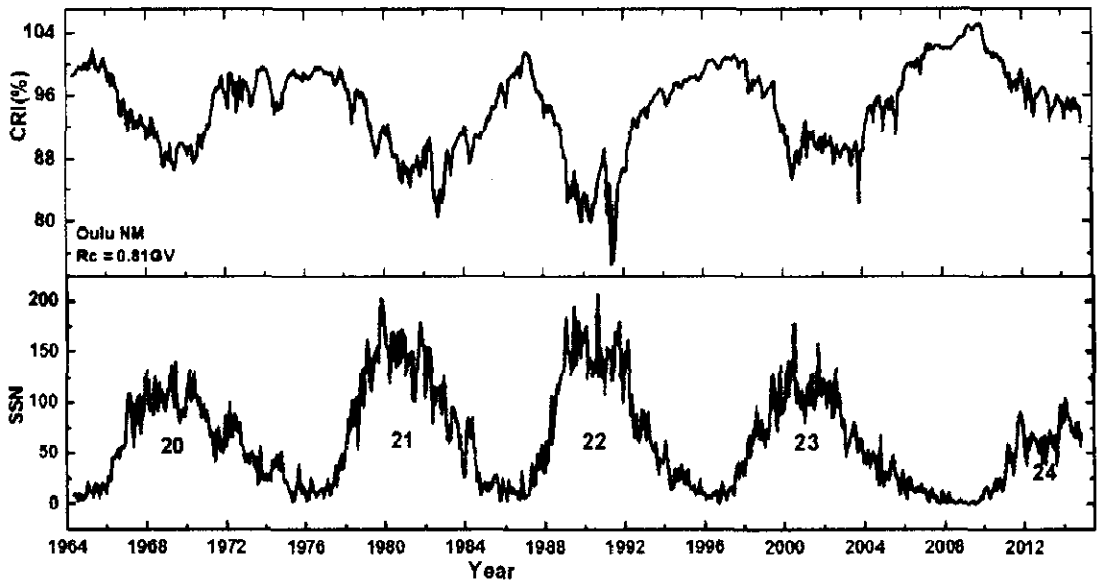

Figure 1.9 The variation of relative cosmic-ray intensity, CRI (%) (upper panel) and solar activity (sunspot numbers, SSN) (lower panel) at the resolution of 27-day average from April 1964 to November, 2014. Solar cycle number (20, 21, 22, 23, and 24) is also shown in the lower panel. The cosmic-ray intensity is in anticorrelation with the sunspot activity.

given by equation:

$$\frac{\partial f}{\partial t} = -\mathbf{V}\cdot\nabla f - < v_D > \cdot \nabla f + \nabla\cdot(k_s\cdot\nabla f) + \frac{1}{3}\nabla\cdot\mathbf{V})\frac{\partial f}{\partial lnP} \qquad (1)$$

The first term on the right-hand side represents an outward convection caused by the solar wind velocity [V]. The second term represents the gradient and curvature drifts in the global heliospheric magnetic field (Jokipii *et al.*, 1977). The drift velocity for weak scattering is given by

$$< v_D >= f_s \frac{vpc}{3q}\nabla \times \frac{B}{B^2} \qquad (2)$$

The third term represents the diffusion caused by turbulent irregularities in the background heliospheric magnetic field [B]. The last term describes the adiabatic energy change depending on the sign of the divergence of solar-wind velocity [V]. Thus we see that in each of the four terms, directly or indirectly, either solar-wind velocity [V] or heliospheric magnetic field [B] is involved (see, *e.g.*, reviews by Strauss, Potgieter, and Ferreira, 2012; Heber, 2013; Kota, 2013, and references therein).

GCR modulation in the heliosphere has been studied soundly over the last ~ 50 years. Still there are some open questions, especially on the relative roles of different solar polarity and activity phases (Alanko *et al.*, 2007; Potgieter, 2014; Aslam and Badruddin, 2014).

The current theory for cosmic-ray behavior in the heliosphere was developed almost 50 years ago (Parker, 1965) and has been studied extensively since then (Gleeson and Axford, 1968; Jokipii and Parker, 1970; Kota and Jokipii, 1983; Boella *et al.*, 2001; Alanko *et al.*, 2007 also see reviews by Hall, Duldig, Humble, 1996; Potgieter, 1998; Heber and Potgieter, 2006, Heber, Fichner, and Scherer, 2006; and references therein). The basic ideas behind this theory can be stated relatively simply. The solar wind moves out almost radially from the Sun in all directions. It carries with it a magnetic field. The cosmic ray particles are charged and thus interact with the magnetic field. The rotation of the Sun gives the magnetic field the form of a three dimensional Archimedean spiral, known as the Parker spiral. The solar wind, then, tends to sweep GCRs out of the heliosphere, or equivalently the cosmic rays must fight their way upstream against the outward flow of the wind. Not all the cosmic rays successfully make this trek, with the result that the cosmic ray flux seen in the inner heliosphere is lower than that in the interstellar medium. And if we vary conditions in the heliosphere the cosmic ray flux will change in time. Fisk (1996) pointed out that a different correction needs to be made to the Parker spiral model for the simple reason that the Sun does not rotate rigidly but differentially, with the solar poles rotating ~ 20 % slower than the solar equator.

The four physical processes which are believed to be important for modulation of galactic cosmic rays: diffusion, effects associated with the large-sale magnetic field, convection, and energy change (*e.g.* Fisk, 1980).

i) *Diffusion*: The magnetic field in the solar wind contains small-scale irregularities. There are Alfven waves, perhaps some magnetosonic waves, and other fluctuations. In some cases these irregularities have scale sizes comparable to the gyroradii of the cosmic rays, with the result that the cosmic rays are scattered. Their pitch angle or equivalently their velocity parallel to the mean magnetic field changes randomly with time. It is also possible for the particles to be scattered or to propagate by other means, in a random fashion, in a direction normal to the mean magnetic field (Jokipii and Parker, 1969). We normally describe the effects of this scattering as a diffusion process.

ii) Effects due to the large-scale magnetic field: We expect simply from the orientation of the mean magnetic field that cosmic rays should have an easier access to the inner heliosphere over the south poles than they do near the equatorial plane. The effect associated with the global heliospheric magnetic field, is gradient and curvature drift. The orientation and magnitude of the magnetic field varies with radial distance and latitude. Thus, particles may undergo systematic drifts in this field, which among other effects should result in a significant transport of particles in latitude. This process has been studied in detail (*e.g.*, Jokipii, Levy, and Hubbard, 1977).

The direction in which particles drift depends on the polarity of the magnetic field; if the polarity is reversed, particles drift in the opposite direction. At least in solar-minimum conditions, the heliospheric magnetic field appears to be divided into two regions of relatively uniform polarity (Smith, Tsurutani, and Rosenberg, 1978). The northern hemisphere of the heliosphere has the same polarity as the north pole of the Sun; the southern hemisphere the polarity of the southern solar pole. The two regions are divided by a wraped current sheet that lies near the solar equatorial plane. However, the polarity of the solar magnetic field changes approximately every 11 years, and with it the polarity of the heliospheric field and direction of the particle drifts. We might expect, then, as a result of drift effects, that the overall behavior of the modulation in the heliosphere could be substantially different in succeeding solar cycles.

iii) Convection: The third physical effect that is important for modulation, and probably the simplest, is convection. The speeds of the waves which scatter the particles and cause them to diffuse are very much less than the solar-wind speed. The

waves are thus convected outward with the solar wind, and in turn tend to convect the cosmic rays out of the heliosphere.

iv) Energy change: Another effect of importance for the modulation is particle energy changes. The magnetic field irregularities which scatter the particles are being convected outward with the solar wind, and thus are moving. The particles, then, are interacting with moving irregularities, and they suffer energy changes in the process.

This energy change process is one of the more subtle effects in modulation theory because we can think of it in two seemingly contradictory ways (Fisk, 1980). The cosmic rays, as far as the solar wind is concerned, are a highly mobile gas which exerts a pressure. And since there are more cosmic rays in the interstellar medium than in the inner heliosphere, this pressure has a positive gradient. The solar wind, then, which blows outward, does work against this pressure gradient and imparts energy to the cosmic rays. However, as far as the cosmic rays are concerned, they find themselves in an expanding medium. The solar wind blows radially from the Sun, and thus diverges or expands as it goes outward. The cosmic rays, which are rattling around in the wind, will expand along with it, and they are adiabatically cooled (Parker, 1965).

In short, cosmic rays enter the heliosphere due to random motions, and diffuse inward toward the Sun, gyrating around the interplanetary magnetic field and scattering at irregularities in the field. They will also experience curvature drifts and will be convected back toward the boundary by the solar wind and lose energy through adiabatic cooling, although the latter process is only important below a few GeV and does not affect ground-based observations. The combined effect of these processes is the modulation of the cosmic ray distribution in the heliosphere (Forman and Gleeson, 1975).

The discovery of cosmic rays by Victor Hess, in 1912 took place in a historic balloon flight. Subsequently Scott E. Forbush identified three time-varying features of cosmic ray intensity: the solar flare effect, the Forbush decrease and the long-term variation of cosmic ray intensity, negatively correlated with solar activity as represented by sunspot numbers. All these significant variations along with the daily variation of cosmic ray intensity have clearly demonstrated the solar control of the interplanetary electromagnetic state through the owing solar wind plasma with the embedded solar magnetic field.

Galactic cosmic ray particles which enter the heliosphere are affected by the large-scale IMF and its small-scale irregularities whose scale sizes are comparable to their Larmor radius and their motions are like a random walk. Intensity of cosmic rays is modulated by the condition of the interplanetary medium. Conversely, the understanding to the modulation process can be used for diagnosing the interplanetary condition through the observation of cosmic rays (Storini, 1990).

Cosmic ray intensity variations in different magnetic conditions are of interest. As cosmic rays respond to both local and large-scale solar wind structures in the heliosphere and, consequently, they are significantly affected by the interplanetary structure. Thus cosmic ray variation studies provide a valuable probe for both local and large-scale solar wind structure in the heliosphere. Thus, the subject of cosmic rays in the heliosphere brings together several areas of active research like solar wind, structure of the IMF, variation of cosmic rays over short and long-term time scales, solar-terrestrial interactions etc.

1.5 Forbush Decreases and Corotating Decreases

Decreases in cosmic-ray intensity which last typically for about a week, were first observed by Forbush (1937) and Hess and Demmelmair (1937) using ionisation chambers. The transient decreases in the GCR intensity observed at the Earth are called Forbush decreases (FDs) which are named after their discoverer.

These shorter term decreases in the cosmic-ray intensity exhibit a sudden decrease and a gradual recovery. Initially it was assumed that these variations were produced, either directly or indirectly, by geomagnetic disturbances such as perturbation of geomagnetic field during geomagnetic storms and these variations were thought to be of terrestrial origin. It was in the early 1950s, when work of Simpson using neutron monitors (Simpson, 1954) showed that the origin of these decreases was in the interplanetary medium. They concluded that these variations are not related with the terrestrial activity but with solar activity. Various configuration of solar activity (*e.g.* see Burlaga, 1983; Lockwood, 1971; Iucci, *et al.*, 1989, Venkatesan and Badruddin, 1990; Badruddin, 2000; Cane 2000; Belov, *et al.*, 2014) have been suggested as the possible cause of FDs. FDs are generally correlated with Earth-directed CMEs from the Sun.

There are two general types of decreases: The first one is 'Non-recurrent decreases' also called Forbush decreases, are caused by transient interplanetary events which are related to coronal mass ejections from the Sun. These have the characteristics of a sudden onset, reach maximum depression within about a day and have a more gradual recovery. The second types are 'Recurrent decreases', also called corotating decreases (Lockwood, 1971) which have a more gradual onset, and are more symmetric in profile. These are well associated with corotating high-speed solar-wind streams (*e.g.*, Iucci *et al.* 1979b). Historically, all short term decreases have been called 'Forbush decreases'.

Since their discovery (Forbush, 1937), FDs have been extensively studied and many features have been clarified. It has been a basic problem in cosmic ray study to identify the physical mechanism responsible for FD. Early theoretical work on FDs suggested various mechanisms to explain this phenomenon and had established in the process all the important mechanism of solar modulation of galactic cosmic rays (*i.e.*, convection, diffusion, drift and adiabatic energy change). Morrison (1956) was the first to suggest that FDs could be caused by turbulent magnetic clouds ejected from the solar active regions. Laster *et al.* (1962) proposed cosmic rays temporarily trapped in an expanding turbulent magnetic cloud being adiabatically cooled. The ambient interplanetary magnetic field would be compressed and distorted by a shock wave, forming a shell of intense magnetic fields which could act as a shield against incoming cosmic rays. He also considered the additional effects of diffusion and large-scale gradient drifts. All these and other mechanisms were later combined by Parker (1965) in the well known fundamental transport equation of cosmic rays in the heliosphere (equation 1). Later the continued coverage of the solar wind properties and cosmic ray intensities at various positions in or near the equatorial plane has, however, led to renewed interest in finding the dominating mechanism of FDs amongst the existing ones.

Although idea of FDs caused by enhanced scattering in distorted magnetic fields in the vicinity of shock has been invoked in models (*e.g.* Nishida, 1982; Lockwood, Webber, and Jokipii, 1986) the experimental evidence is not conclusive. On the one hand there are those who favour enhanced scattering (*e.g.* Badruddin, Yadav, and Yadav, 1986; Zhang and Burlaga, 1988), while others (*e.g.* Sarris, Dodopoulos, and Venkatesan, 1989; Cheng, Sarris, and Dadopoulos, 1990) favour for drift caused by

gradient in the relatively large-scale fields of propagating solar wind disturbances as driving mechanism of FDs.

At 1 AU, temporal variations in cosmic-ray intensity on the time scale of the order of days are related to the passage of corotating stream and transient flows (*e.g.* see reviewers by Lockwood, 1971; Rao, 1972; Burlaga, 1983; Venkatesan and Badruddin, 1990; Cane, 2000; Richardson, 2004). For both types of flows the correlation between cosmic ray count rate and strength of the magnetic field is reported to be strong; intensity decreases when the region of enhanced magnetic field moves past the detector (Barouch and Burlaga, 1975; Burlaga *et al.*, 1985). Region of enhanced magnetic field were classified as (Burlaga and King, 1979) corotating interaction (which occur ahead of corotating streams), post-shock flows (including both sheath flows and ejecta) and cold magnetic enhancements (which include magnetic clouds). The largest decreases in cosmic-ray intensity, Forbush decreases, are usually associated with shock and post-shock flows. Long-lasting FDs are sometimes observed at 1 AU (Lockwood, 1971), and these are related to the passage of a series of shock-associated transient flows (Barouch and Burlaga, 1975).

CMEs are plasma eruptions from the solar atmosphere involving previously closed field regions which are expelled into the interplanetary medium. Such regions, and the shocks which they may generate, have pronounced effects on cosmic ray densities both locally and at some distance away (Cane, 2000). These energetic particle effects can often be used to identify CMEs in the interplanetary medium, where they are usually called 'ejecta'. When both the ejecta and shock effects are present the resulting cosmic ray event is called a 'classical, two-step' Forbush decrease. It is known that ICMEs are mainly responsible for FDs in GCR intensity. However, not all of the ICMEs produce such decreases in GCR intensity. Figure 1.10 shows the time variation of cosmic ray decrease of two steps. It is believed that the first step of the Forbush decrease is most likely due to the different scattering conditions upstream and downstream of the shock or, in case of a CIR, in the fast and slow solar wind streams. The second step associated with the arrival of the ejecta seems to be influenced by different scattering conditions too, which regulate the filling of the ejecta originally void of energetic particles. The duration of cosmic-ray intensity to reach from its start of decrease to minimum level is called main phase duration, and the duration cosmic-ray intensity reaches its pre decrease level from its minimum

level is called recovery phase (see Figure 1.10). In general, decreases due to CMEs were earlier attributed to solar flares (*e.g.* Lockwood, 1971; Iucci *et al.*, 1979b). However, Duggal and Pomerantz (1978) suggested that majority of cosmic ray decreases cannot be uniquely assigned to specific solar flares. Kane (1977) and Kudela and Brenkus (2004) have shown that FDs and major geomagnetic storms are well associated. It is now known that largest geomagnetic storms are caused by CMEs and associated shocks (Gosling, 1993).

Thus CME-related cosmic-ray decreases are of three basic types; those caused by a shock and ejecta, those caused by a shock only and those caused by an ejecta only. The majority (>80 %) of short-term decreases greater than 4 % are of the two steps (shock plus ejecta) type (Cane, Richardson, and von Rosenvinge, 1996). Only very energetic CMEs create shocks which are strong enough on their flanks to cause significant cosmic-ray decreases for observers who detect the shocks beyond the azimuthal extent of the 'driver' CMEs (*i.e.* shock-only decreases). In such cases the shocks also generate major solar energetic particle increases with profiles characteristic of events originating far from central meridian (Cane, Reames, and von Rosenvinge, 1988). The energetic particles allow one to be sure that the cosmic-ray decrease was caused by a CME-driven shock intercepted on its flank and not by a co-rotating stream.

The largest FDs have magnitudes in the range 10 – 25 % for neutron monitors. Because of anisotropies present in neutron monitor data, the size reported for an FD will vary from one station to another. Also the sizes will be smaller if daily averages are used rather than hourly averages. At the lower rigidities accessible via spacecraft observations, FDs are larger. FDs are most common near solar maximum but occur throughout the solar cycle. There are fewer than 10 FDs greater than 10 % per cycle and they occur around sunspot maximum but notably not in the year or so just after solar maximum (Cane, Richardson, and von Rosenvinge, 1996). The rigidity (P) dependence of the amplitude of FDs is approximately equal to $P^{-\gamma}$ (Lockwood, 1971; Venkatesan, Shukla, and Agrawal, 1982), where γ ranges from about 0.4 – 1.2. A number of researchers have found that the rigidity dependence of FDs does not vary with the Sun's polarity (see, *e.g.*, Morishita *et al.*, 1990).

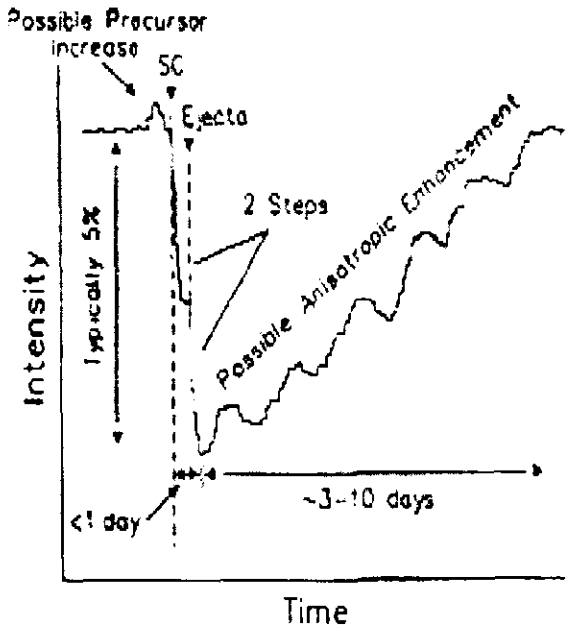

Figure 1.10 Classical two step Forbush decrease.

In isolated single FDs the recovery can be described as exponential with an average recovery time of about 5 days but ranging from ~ 3 to ~ 10 days (Lockwood, Webber, and Jokipii, 1986). Kumar and Badruddin (2014a) state that the characteristic recovery time of galactic cosmic ray is larger for shock-associated CMEs as compared to those not associated with shocks. Badruddin, Yadav, and Yadav, (1986); Zhang and Burlaga (1988) discussed FDs associated with shocks and magnetic clouds and concluded that magnetic clouds are not very effective in producing the maximum depression of a Forbush decrease. However, Ananth and Venkatesan (1993), and Sanderson *et al.*, (1990) found that the maximum depression observed in many cases only after the arrival of magnetic clouds.

This it can be seen from the above discussion of cosmic-ray decreases that this field of research is complex and needs further advanced studies in this regard.

1.6 Objectives and Scope of the Present Work

As discussed before in this chapter, **Chapter 1** gives an overview of the Sun, its internal structure and atmosphere, solar wind, the heliosphere. Large-scale structures in the interplanetary medium (*i.e.* ICMEs, CIRs) relevant for modulation studies in the heliopshere is also discussed. A brief and basic idea of solar modulation of

galactic cosmic ray is also presented. We also describe the FDs and corotating decreases with the previous results of these decreases in cosmic-ray intensity.

Chapter 2 deals with the detail study of transient modulation of cosmic-ray intensity associated with solar cycle 23 ICMEs and its various features. Depending upon associated features of ICMEs, a set of ICMEs identified in near-Earth space were grouped in different group of events such as ICMEs associated/not associated with shocks, bidirectional electron events (BDEs), MC, and halo CMEs. We study the response of these different groups of ICMEs on GCR-intensity changes (decreases) as recorded by two ground-based neutron monitors. We also analyse the simultaneous solar-wind plasma/field data (solar-wind velocity V, interplanetary magnetic-field vector F, standard deviation in field vector σ_F, the ratio σ_F/F, Plasma β and interplanetary electric field E) during the passage of ICMEs with different features and structures, and we perform a superposed-epoch analysis of the data. We also adopt the best-fit approach with suitable functions to interpret the observed similarities and differences in various parameters. For the statistical study of the GCR-response to these ICMEs, based on the degree of their "effectiveness" in producing depressions in GCR intensity, we have divided ICME "GCR-effectiveness" in five groups using Kiel data *i.e.* quiet ($\Delta I \approx 0.0$), small ($\Delta I \approx -0.01$ to -0.49 %); moderate ($\Delta I \approx -0.50$ to -1.49 %); large ($\Delta I \approx -1.50$ to -2.99 %); and very large (ΔI larger than -3.00 %) depressions, here I is the cosmic-ray counts per minute. The characteristic recovery time of GCR intensity due to shock/BDE/MC/halo-CME-associated ICMEs and those due to ICMEs not associated with these structures/features also studied.

Chapter 3 describes the study of cosmic-ray modulation during the passage of ICMEs and CIRs. We compare the cosmic-ray response of ICMEs and CIRs during their passage in near-Earth space. We study the relative importance of various structures/features identified during the passage of ICMEs and CIRs observed during solar cycle 23 (1995 – 2009). The identified ICME structures are the shock front, the sheath, and the CME ejecta. We isolate shock arrival time, passage of the sheath region, arrival of ejecta and the end time of its passage. Similarly, we isolate the CIR arrival, associated forward shock, the SI and the reverse shock during the passage of CIR. For the cosmic-ray intensity, we utilize the data from two high counting rate neutron monitors. In addition to neutron monitor data, we utilize near-simultaneous

and same time-resolution data of interplanetary plasma and field. Relating the properties of various structures and corresponding variations in plasma and field parameters to changes of cosmic-ray intensity, we identify the relative importance of plasma/field parameters in influencing the amplitude and time profiles of cosmic-ray intensity variations during the passage of ICMEs and CIRs.

In Chapter 4, we discuss the study and results of cosmic-ray modulation due to high-speed solar-wind streams of different sources, speed, and duration which are identified in the solar wind. We apply the method of superposed-epoch analysis to analyze the interplanetary plasma and field parameters during the passage of streams with distinct plasma and field characteristics. We utilize the plasma/field characteristics to distinguish various features of solar sources and interplanetary structures, and discuss the observed differences in the cosmic-ray response. We study the influence of speed, duration, and solar sources of the streams on the GCR modulation. We discuss the relative importance of different solar-wind parameters in the modulation process. We also study the influence of individual streams in modulating the GCR intensity by grouping them into suitable GCR-effective groups of increasing range of GCR-intensity depressions produced by them.

The final chapter of this thesis, **Chapter 5**, we summarize our results of the over all thesis.

****

Chapter 2

TRANSIENT MODULATION OF COSMIC-RAY INTENSITY ASSOCIATED WITH INTERPLANERATY CORONAL MASS EJECTIONS AND ITS VARIOUS FEATURES

In this chapter, the detailed description of transient modulation of cosmic-ray intensity associated with interplanetary coronal mass ejections (ICMEs) and its various features is presented. Depending upon associated features of ICMEs, a set of ICMEs identified in near-earth space were grouped in different categories of events such as ICMEs associated/not associated with shocks, bidirectional electron events (BDEs), magnetic clouds, and halo-CMEs. We analyses 14 years (1996 – 2009) of ICME data and study their response in GCR-intensity changes (decreases) as recorded by ground-based neutron monitors.

2.1 Introduction

In the heliosphere, the large-scale structure of the solar wind is dominated by two types of interplanetary disturbances: transient and corotating disturbances. Corotating disturbances, associated with spatial variability and solar rotation, occur in response to the interaction of fast and slow solar winds. Transient disturbances, due to episodic solar eruptions, expand outward from the Sun into interplanetary space (Gosling, 1996).

The galactic cosmic-ray (GCR) intensity is modulated by long-term effects such as ≈ 11-year solar-activity cycle and ≈ 22 year solar magnetic cycle as well as by short-term effects such as passage of corotating flows (high-speed streams) and transient disturbances (*e.g.* interplanetary coronal mass ejections). Recurrent depressions in GCR intensity due to corotating fields and flows and Forbush decreases due to transient disturbances have been studied in the past (see, *e.g.* Lockwood, 1971; Rao, 1972; Iucci *et al.*, 1989; Venkatesan and Badruddin, 1990; Cane, 2000; Kudela *et al.*, 2000; Gupta and Badruddin, 2009; Oh and Yi, 2009; Kane, 2010; Wawrzynczak and Alania, 2010; Abbrescia *et al.*, 2011; Modzelewska and Alania, 2012; Sabbah and Kudela, 2011, and references therein).

Short-term transient depression caused generally by ICMEs and particularly by magnetic clouds have been studied extensively and many features of resulting depressions in GCR intensity, including their recovery characteristics, have been clarified (see, *e.g.* Badruddin, Yadav, and Yadav, 1986; Zhang and Burlaga, 1988; Nagashima *et al.*, 1990; Kahler and Reames, 1991; Lockwood, Webber, and Debrunner, 1991; Cane, 1993; Mavromichalaki *et al.*, 2003; Dorotovic *et al.*, 2008; Usoskin *et al.*, 2008; Richardson and Cane, 2011, and references therein). However, important features of fields and flows, their magnetic structure, and the physical processes playing the dominant role are yet to be clearly identified (see, *e.g.* Jordan *et al.*, 2011; Richardson and Cane, 2011; Dumbovic *et al.*, 2012; Kudela, 2012).

Forbush decreases are characterized by rapid reduction in cosmic-ray intensity within one to two days followed by a slow recovery typically lasting several days. After their discovery (Forbush, 1937), the search began for their solar sources, responsible interplanetary structures, and physical mechanisms playing an important role. Simpson (1954) related these decreases to solar activity, and individual

decreases were generally attributed to solar flares before the beginning of space age or even after (see reviews, *e.g.* Lockwood, 1971; Venkatesan and Badruddin, 1990). However, with the advent of space coronagraphs in the 1970s and subsequent observations of coronal mass ejections (CMEs) and their interplanetary counterparts (ICMEs), it was realized that CMEs instead of solar flares may be the solar cause of Forbush decreases. It is known that only some of the observed ICMEs produce the Forbush decrease in GCR intensity. Cane (2000) states that the maximum of the depression is about 25 % for neutron monitors.

ICMEs with speed from about 300 km s^{-1} up to about 1000 km s^{-1} have been observed. The field enhancements in the ICMEs may have values from a few nT up to about 40 nT (Richardson and Cane, 2010). It is also observed that ICMEs observed in near-Earth space may or may not be associated with shock/sheath (Cane and Richardson, 2003), bidirectional superthermal electron events (Gosling *et al.*, 1987), and magnetic-cloud structures (Gosling, 1990; Richardson and Cane, 2010). Furthermore, the CMEs may have halo structure or not (*e.g.* Gopalswamy, Yashiro, and Akiyama, 2007), where halo CMEs are those with an apparent width of 360 degrees. In this work, we analyze the ground-based neutron-monitor data together with the interplanetary plasma and field data during the passage of ICMEs associated with different features and structures in interplanetary space.

Burlaga *et al.*, (1981) and Klein and Burlaga (1982) identified magnetic clouds, a subset of CMEs, in the interplanetary plasma and field data obtained from space-based observations. Subsequently, the role of magnetic clouds and their associated structures (shock/sheath) in producing Forbush decreases were studied extensively (*e.g.* Badruddin *et al.*, 1985; Badruddin, Yadav, and Yadav, 1986; Zhang and Burlaga, 1988; Iucci *et al.*, 1989; Badruddin, Venkatesan, and Zhu, 1991; Lepping *et al.*, 1991; Lockwood, Webber, and Debrunner, 1991; Venkatesan *et al.*, 1992; Ananth and Venkatesan, 1993; Cane, 1993; Cane, Richardson and von Resenvinge, 1996; Cane, Richardson and Wibberenz, 1997). These and many other such studies have lead to the suggestion that ICMEs cause Forbush decreases (Cane, 2000). Subsequent studies of the effect of ICME related interplanetary disturbances on cosmic rays (*e.g.* Badruddin, 2002; Singh and Badruddin, 2007a; Quenby *et al.*, 2008; Subramanian *et al.*, 2009; Yu *et al.*, 2010; Jordan *et al.*, 2011; Richardson and Cane, 2011; Dumbovic

et al., 2011, 2012; Augusto *et al.*, 2012; Oh and Yi, 2012; Arunbabu *et al.*, 2013; Blanco *et al.*, 2013) have utilized solar, interplanetary, and ground-based observations and provided further insight about Forbush decreases, *e.g.* their solar sources, interplanetary structures, important plasma/field parameters, and physical mechanisms playing an important role in deciding the amplitude and recovery characteristics of these decreases. However, regarding the relative importance of shock/sheath, ICME/MC (see, *e.g.* Badruddin, Yadav, and Yadav, 1986; Cane, 1993; Arunbabu *et al.*, 2013; Blanco *et al.*, 2013), one-step/two-step decrease (see, *e.g.* Cane, 2000; Jordan *et al.*, 2011), open/closed-field topology (Reames, Kahler, and Tylka, 2009; Richardson and Cane 2011), and field turbulence/strength (Badruddin, Venkatesan, and Zhu, 1991; LeRoux and Potgieter, 1991; Wibberenz *et al.*, 1998; Dumbovic *et al.*, 2012), some questions still remain open.

It is important, therefore, to identify GCR effective ICMEs and study their plasma/field properties, related features, and structures in relation to the Forbush decreases produced by them.

2.2 Data Analysis

Using spacecraft data, useful catalogues of ICMEs have been prepared and published for various durations: e.g. 1996 – 2002 (Cane and Richardson, 2003), 1996 – 2000 (Gopalswamy *et al.*, 2001), 1995 – 2004 (Jian *et al.*, 2006a), and 1996 – 2009 (Richardson and Cane, 2010). The catalogue by Richardson and Cane (2010) covers the whole of solar cycle 23 and gives a large amount of information and data as regards near-Earth ICME. The information as regards ≈ 300 ICMEs regarding their timing, associated structures/features, and some other related data formed the basis of this work. Furthermore, interplanetary plasma and field data were utilized from the NASA OMNI Web data base. Neutron-monitor data for cosmic-ray intensity were used from two locations: Kiel and Calgary. Data for two neutron-monitor stations were utilized to confirm that the observed changes in intensity are real and not due to any instrumental problem or any local effect. These data are analyzed by the method of superposed epoch (Chree) analysis (Chree, 1912; Singh and Badruddin, 2006).

We utilize 14 years (1996 – 2009) of ICME data and study their response in GCR-

intensity changes (decreases) as recorded by ground-based neutron monitors. For this statistical study of the GCR-response to these ICMEs, based on the degree of their "effectiveness" in producing depressions in GCR intensity, we have divided ICME "GCR-effectiveness" in five groups using Kiel data. In partial analogy with the so-called "geo-effectiveness", we name and divide the "GCR-effectiveness" of ICMEs into five groups and call them, on the basis of their effects in modulating GCR intensity [I: counts per minute]: quiet ($\Delta I \approx 0.0$), small ($\Delta I \approx -0.01$ to -0.49 %); moderate ($\Delta I \approx -0.50$ to -1.49 %); large ($\Delta I \approx -1.50$ to -2.99 %); and very large (ΔI larger than -3.00 %) depressions. For calculating ΔI, the intensity data are first normalized to the 6 May 1997 value. Then the difference ΔI [%] is obtained from plots corresponding to each ICME event, *i.e.* change in intensity ΔI [%] after the arrival of each ICME is found from these plots. We find that nearly half (48.4 %) of the ICMEs either did not produce any depression in GCR intensity at all (17.3 %) or small depressions of less than 0.5 % (31.1 %). The rest of the ICMEs produce either the so-called moderate (27.3 %), large (11.8 %), and or very large (12.5 %) intensity depressions. Such a wide range in GCR effectiveness of ICMEs motivated us to look for the distinctions, if any, in the properties of average interplanetary plasma and field behavior during the passage of ICMEs responsible for the depressions of different range (small, moderate, large, and very large).

2.2.1 Method of Superposed-Epoch Analysis

Superposed-epoch method (Chree, 1912; Forbush *et al.*, 1983; Singh and Badruddin, 2006) is a statistical analysis technique which is often used to demonstrate an effect or a periodicity. With the help of this method, we study the effects of various solar/interplanetary phenomena on cosmic-ray intensity. Firstly we selected the events with particular criteria. Having defined the criteria of an event, data of specifically designed interval (48 hours before and 264 hours after the start of an event) were extracted from the full data base. Then, the hourly data of selected time interval were superposed on each other taking the zero time as the start time of events. These data were averaged for each hour from −48 to +264 hours and plotted. The results so obtained are expected to reveal dynamic component of the response.

2.2.2 Correlation Analysis

Simple Pearson correlation analysis is used to determine the changes in a physical variable, which are associated with changes in another physical quantity. The data for a correlation analysis consists two input columns and each column contained values for one of the variable. Here one is cosmic ray intensity decrease [%] and other column values are of any one of the interplanetary parameters used for the analysis. From the value of correlation coefficient (R), we can say that dependence between two parameters is strong or weak.

2.3 Results and Discussion

2.3.1 Average Plasma/Field Properties during Passage of ICMEs of Different GCR Effectiveness: Superposed-Epoch Analysis

We have selected several interplanetary plasma/field parameters together with GCR intensity as measured by two neutron monitors located at different positions on the Earth. The velocity of the solar wind and magnitude of the magnetic field are two important parameters for modulation of galactic cosmic rays. In addition to these two parameters, solar-wind velocity [V, km s^{-1}] and interplanetary magnetic-field vector [F, nT], we have selected, for our analysis, standard deviation in field vector [σ_F, nT] and the ratio σ_F/F as measures of fluctuations in magnetic-field vector. Plasma β is also selected, as it provides information as regards the ratio of thermal [nkT] to magnetic [$B^2/2\mu_0$] pressures during the passage of ICME structures. The interplanetary electric field [E, mV m^{-1}] is also utilized as it is considered as an important modulation parameter. As a measure of GCR intensity at the Earth, we have utilized neutron-monitor data recorded at two stations: Calgary (latitude = 51.05 N, longitude = 114.08 W, cut-off rigidity R_c = 1.09 GV) and Kiel (latitude = 54.30 N, longitude = 10.10 E, cut-off rigidity R_c = 2.36 GV). The superposed-epoch analysis results with respect to arrival time (zero hour) of ICME disturbances of the five groups of ICMEs are shown in Figure 2.1a – 2.1e. These show the average amplitude and temporal profile of various parameters before the arrival, during, and after the passage of each group of ICMEs.

We observe that the GCR depression, in four (Figure 2.1b – 2.1e) out of five cases

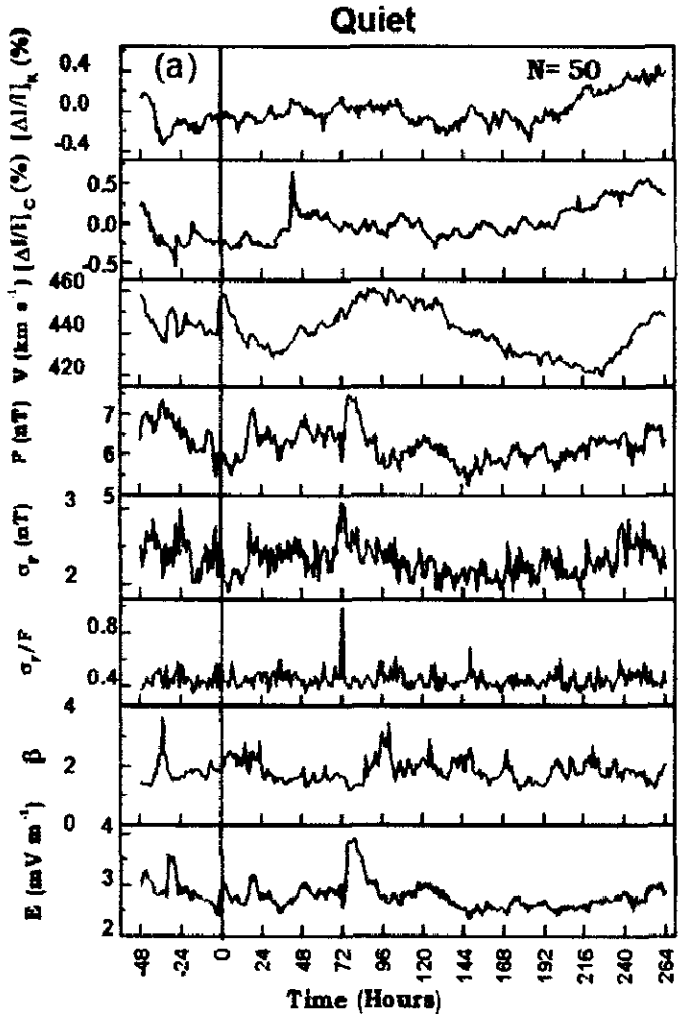

Figure 2.1 Superposed-epoch analysis of GCR intensity of neutron monitors at Kiel and Calgary and interplanetary-plasma field parameters; velocity [*V*], magnetic-field vector [*F*], standard deviation of field vector [σ_F], ratio [σ_F/F], plasma β, and electric field [*E*] with respect to arrival time (zero hour) of ICME disturbances producing depressions in GCR intensity of different range; (a) quiet, (b) small, (c) moderate, (d) large, and (e) very large depressions. N stands for number of events.

(see Figure 2.1a – 2.1e) starts [A] near zero hour [arrival time of ICME-related disturbance], a sharper decrease at first up to a few hours [B], a slower decrease until minimum intensity [C], and then recovery to pre-decrease level [D] taking a much longer time. These timings are shown by vertical lines [A, B, C and D] respectively, in these figures. However, as shown in Figure 2.1a for the "quiet" group of ICMEs, there is essentially no decrease in GCR intensity after zero hour: *i.e.* arrival of the ICME. In this case, as evident from superposed results, the enhancements in *V*, *F*, and *E* as well as the level of σ_F are very small. Differences in amplitudes (Table 2.1) and time profiles (Figure 2.1a – 2.1e) can be seen.

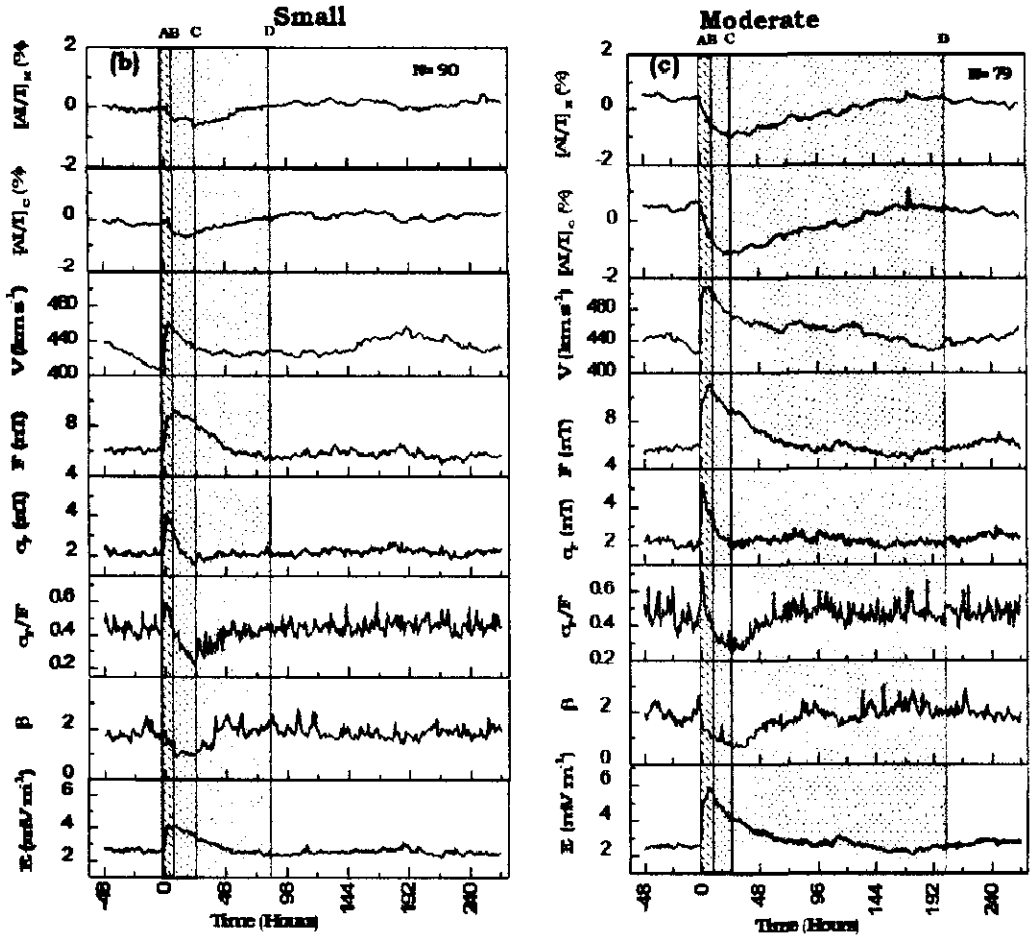

Figure 2.1 *(Continued)*

The parameters V, F, and E increase sharply and reach to its maximum level during the first few hours duration (≈ six – ten hours) of the passage of ICME structures. During this period σ_F and σ_F/F are also enhanced, indicating the dominance of the passage of the magnetically turbulent region. This period [AB] corresponds to a relatively faster rate of depression in GCR (see Figure 2.1b – 2.1e). During the period of subsequent slower decrease in GCR intensity up to lowest level [BC], although still high, the trend in V, F, and E is a decreasing one. Further, during this period, values of σ_F, σ_F/F, and the plasma β are very low, indicating the passage of a magnetically quiet but high-field region. This region [BC] probably corresponds to the passage of the CME/magnetic-cloud structure. Then the GCR recovery starts [C] and recovers during the period marked CD. During this period V, F, and E are decreasing but σ_F, σ_F/F, and β have almost stabilized to the pre-event level [before A].

It is known that the magnetic field is enhanced during the passage of shock/sheath

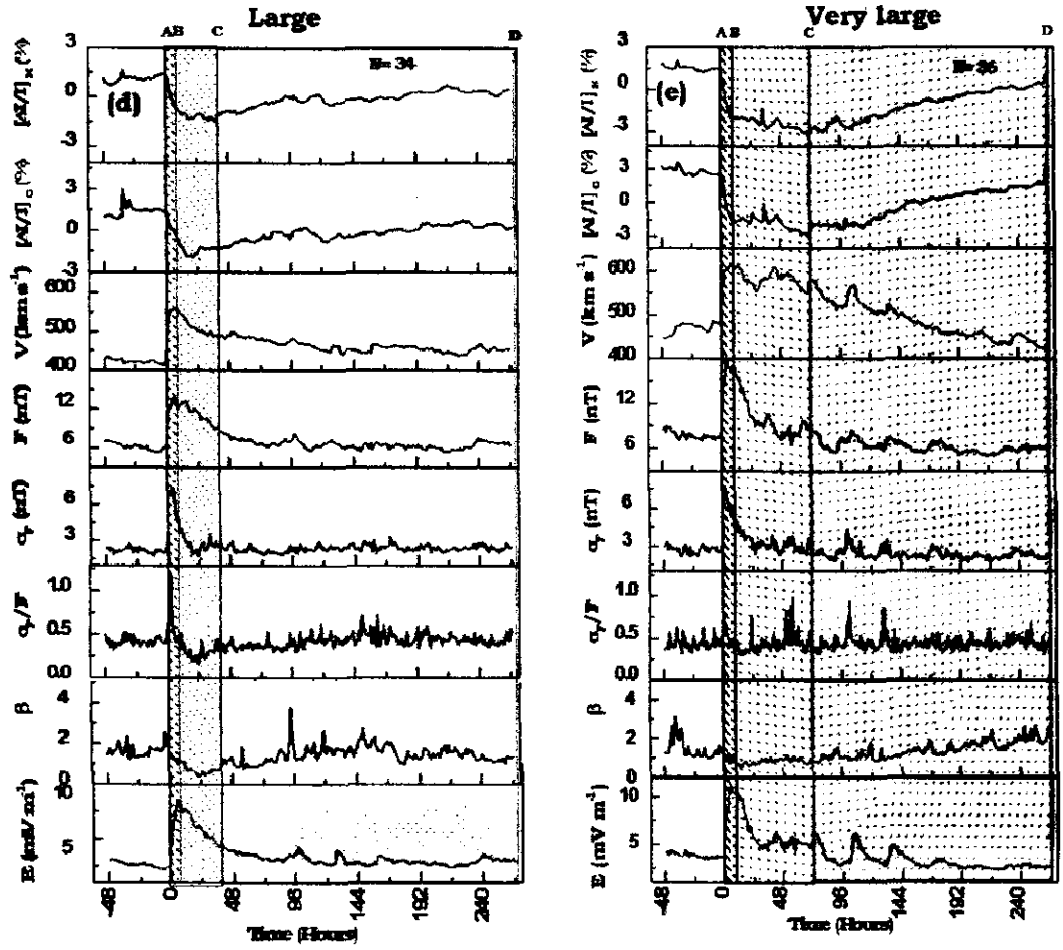

Figure 2.1 (*Continued*)

regions (if and when developed ahead of CMEs) as well as in the following CME/ magnetic cloud structures (*e.g.* Klein and Burlaga, 1982; Badruddin, Yadav, and Yadav, 1986; Gosling, 1990; Venkatesan *et al.*, 1992; Badruddin and Singh, 2009). However the field is likely to be turbulent inside the sheath region, while high-field ICME/magnetic-cloud structures are, in general magnetically "quiet" (Zhang and Burlaga, 1988; Badruddin, Venkatesan, and Zhu, 1991; Liu *et al.*, 2006; Yu *et al.*, 2010). The initial step of fast decreasing intensity [AB] appears to coincide with the passage of magnetically turbulent high-field region (*e.g.* shock/sheath); the next step of slow decrease in intensity [BC] is likely to take place during the passage of the magnetically quiet high-field region (*e.g.* CME/magnetic cloud), and recovery is likely to start after the passage of this region and the recovery time [CD] may be influenced by the solar-wind speed profile. This is consistent with the hypothesis made by Badruddin, Venkatesan, and Zhu (1991) (see also Yu *et al.*, 2010). Another

point to be mentioned here is that the last group, with maximum amplitude and duration of decrease, appears to be influenced by multiple ICME events passing one after the other. In Figure 2.1e, the substructures in plasma/field data, especially *V* and *F*, can be seen by multiple jumps after the start of GCR intensity both during the decreasing and recovery phase. It is worth mentioning here that multiple ICMEs may also produce geomagnetic storms of larger intensity (see, *e.g.* Farrugia and Berdichevsky, 2004; Gopalswamy, Yashiro, and Akiyama, 2007; Zhang *et al.* 2007).

2.3.2 Distribution of Plasma/Field Parameters for ICMEs with Different GCR Effectiveness

Having studied the average plasma and field properties associated with ICMEs producing depressions of different range in GCR intensity, it will be useful to look for the differences in the distribution of some important plasma/field parameters (*e.g.* speed, magnetic field, and electric field) during the passage of ICMEs of different GCR effectiveness. These distributions for the peak values of speed [km s^{-1}], vector magnetic field [nT], and electric field [mV m^{-1}] producing different ranges (groups) of depressions in GCR intensity are shown, respectively, in Figures 2.2a, 2.2b, and 2.2c. To see the quantitative differences in different values and the spread in the distribution, the Gaussian $[y = y_0 + (A/w\sqrt{\pi/2})\ \exp(-2(x-x_c)^2/w^2)]$ fitted curves are also shown over the respective histograms. From these plots we observe that, in general,

i) the frequency distribution shifts towards higher ranges of V_{max}, F_{max}, and E_{max} from the first group (quiet) towards the last group (very large) of ICMEs, producing GCR effectiveness of increasing range,

ii) the peak values of these parameters systematically shift towards higher values, and

iii) the spread in frequency distributions (full width at half maximum, $w_c = w\sqrt{\ln 4}$) is also larger for higher groups.

These values for different groups of GCR-effective ICMEs are tabulated in Tables 2.2, 2.3, and 2.4.

2.3.3 GCR Effectiveness of ICMEs associated with Different Structures/Features: Superposed-Epoch Analysis

We study the average plasma/field parameters and GCR effectiveness of ICMEs by dividing them into different groups based on their effectiveness in modulating GCR intensity, without consideration of any distinction in their types and/or associated features/structures. However, differences have been reported in plasma/field properties and the geomagnetic/ionosphere/cosmic-ray response of halo and non-halo CMEs (*e.g.* Gopalswamy, Yashiro, and Akiyama, 2007), magnetic-cloud/non-magnetic-cloud structure ICMEs (Marcz, 1992; Badruddin, 1998; Badruddin and Singh, 2009; Alves, Echer, and Ganzalez, 2011), ICMEs observed with bidirectional electron flows (BDEs) and without BDEs (Gosling *et al.*, 1987) and ICMEs driving a shock/sheath structures and those not associated with shock/sheath region (*e.g.* Badruddin 2002, Oh and Yi, 2012). Therefore, it is important to study in detail the relative GCR effectiveness of different structures/features associated/not-associated with ICMEs. It will help us not only in identifying the structures/features of importance but also to understand the physical mechanisms playing important roles in the transient modulation of galactic cosmic rays.

We have performed a superposed-epoch analysis of GCR-intensity and interplanetary plasma/field parameters with respect to ICMEs associated with shocks (see Figure 2.3a) and those not associated with any shock (Figure 2.3b). It is observed that there is a large difference between the amplitude and time profiles of GCR-intensity depressions in the two cases; the depression due to shock/sheath associated ICMEs is a Forbush-decrease type with a much stronger decrease, while it is only a small depression in case of ICMEs without shocks. The average GCR effectiveness of shock-associated ICMEs is about three times higher than those not associated with shock/sheath regions (see Table 2.5). The difference in enhancements of various parameters during the passage of shock-associated ICMEs and ICMEs without shocks can be seen in Figures 2.3a and 2.3b; enhancements in various parameters (V, F, σ_F, σ_F/F, and E) are larger during shock-associated ICMEs than ICMEs not associated with shocks. To quantify it, the ratio of the averaged peak values (*e.g.* V_{max}) and enhancements (*e.g.* ΔV) in various interplanetary plasma/field parameters during ICMEs with and without shock have also been calculated (see Table 2.5). This ratio in peak values of various parameters [V_{max}, F_{max}, σ_{Fmax}, and E_{max}] is about 1.2 to 2. However, the enhancements in individual parameters [ΔV, ΔF, $\Delta\sigma_F$, ΔE] are

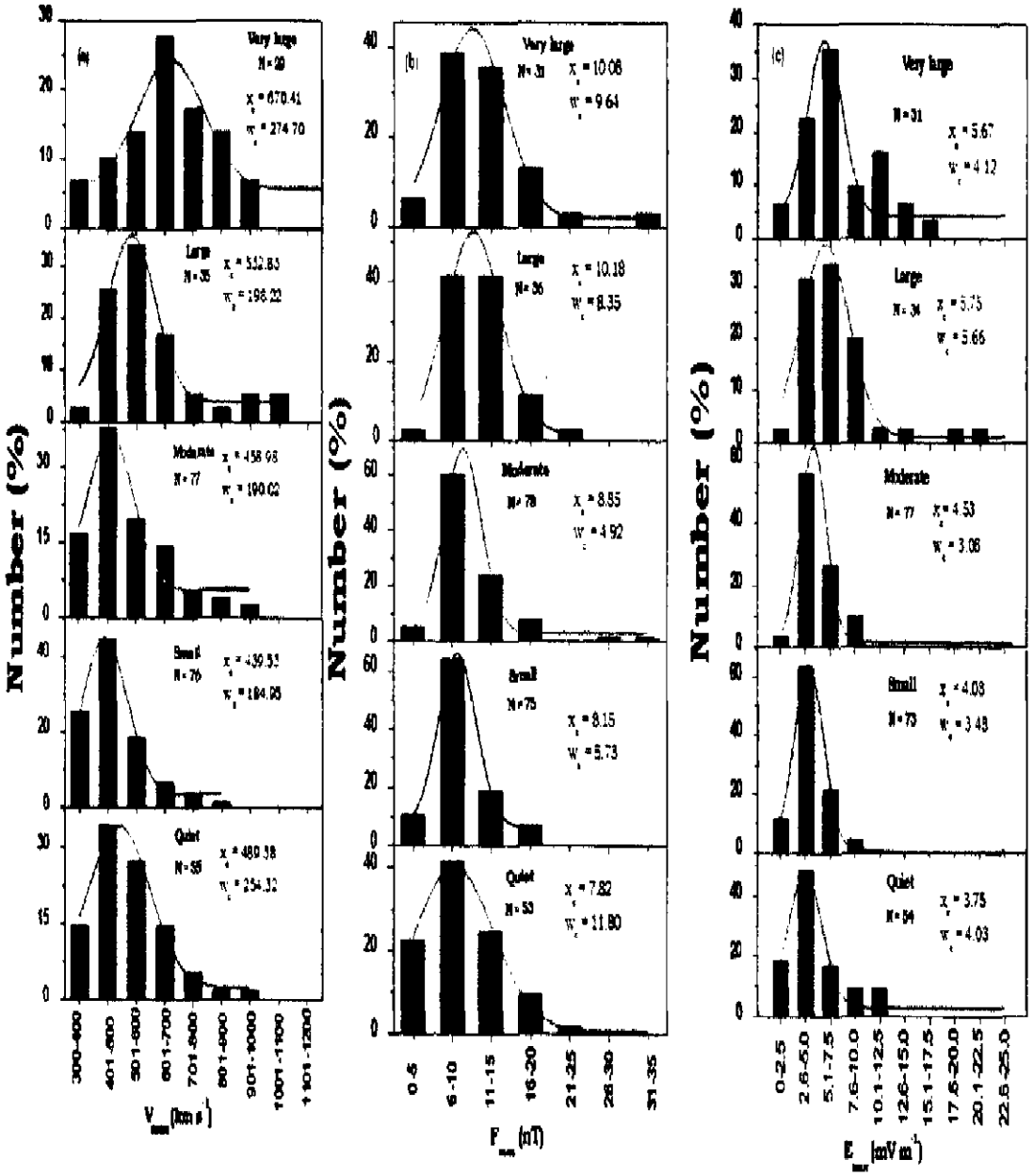

Figure 2.2 Frequency distribution and Gaussian-fitted curves for (a) V_{max} [km s^{-1}], (b) F_{max} [nT], and (c) E_{max} [mV m^{-1}], during the passage of ICMEs producing GCR-intensity depression of different range (quiet, small, moderate, large, and very large).

Table 2.2 Gaussian-fit parameters for the distribution of maximum solar-wind velocity [V_{max}], central-peak value of V_{max} [x_c], width [w], full width at half maximum [w_c], and the product $x_c w_c$ during the passage of ICMEs of different GCR effectiveness.

Group	Gaussian-fit parameters for V_{max}				
	R^2	x_c	w	w_c	$x_c w_c$ [10^4]
Small	0.99	439.53 ± 4.99	157.08 ± 10.59	184.95	8.13
Moderate	0.93	458.98 ± 14.96	161.39 ± 31.42	190.02	8.72
Large	0.97	532.83 ± 8.51	168.35 ± 19.20	198.22	10.56
Very large	0.89	670.41 ± 20.30	233.31 ± 56.43	274.70	18.42

Table 2.3 Gaussian-fit parameters for the distribution of maximum magnetic field [F_{max}], central-peak value of F_{max} [x_c], width [w], full width at half maximum [w_c], and the product $x_c w_c$ during the passage of ICMEs of different GCR effectiveness.

Group	Gaussian-fit parameters for F_{max}				
	R^2	x_c	w	w_c	$x_c w_c$
Small	0.99	8.15 ± 0.00	4.87 ± 0.00	5.73	46.70
Moderate	0.99	8.85 ± 0.55	4.81 ± 1.18	5.66	50.09
Large	0.98	10.18 ± 0.46	7.09 ± 2.12	8.35	85.00
Very large	0.98	10.08 ± 0.36	8.19 ± 0.99	9.64	97.17

Table 2.4 Gaussian-fit parameters for the distribution of maximum electric field [E_{max}], central-peak value of E_{max} [x_c], width [w], full width at half maximum [w_c], and the product $x_c w_c$ during the passage of ICMEs of different GCR effectiveness.

Group	Gaussia- fit parameters for E_{max}				
	R^2	x_c	w	w_c	$x_c w_c$
Small	0.99	4.08 ± 0.06	2.96 ± 0.09	3.49	14.24
Moderate	0.97	4.53 ± 0.20	2.62 ± 0.47	3.08	13.95
Large	0.96	5.75 ± 0.23	4.81 ± 0.52	5.66	32.54
Very large	0.84	5.67 ± 0.40	3.50 ± 0.89	4.12	23.36

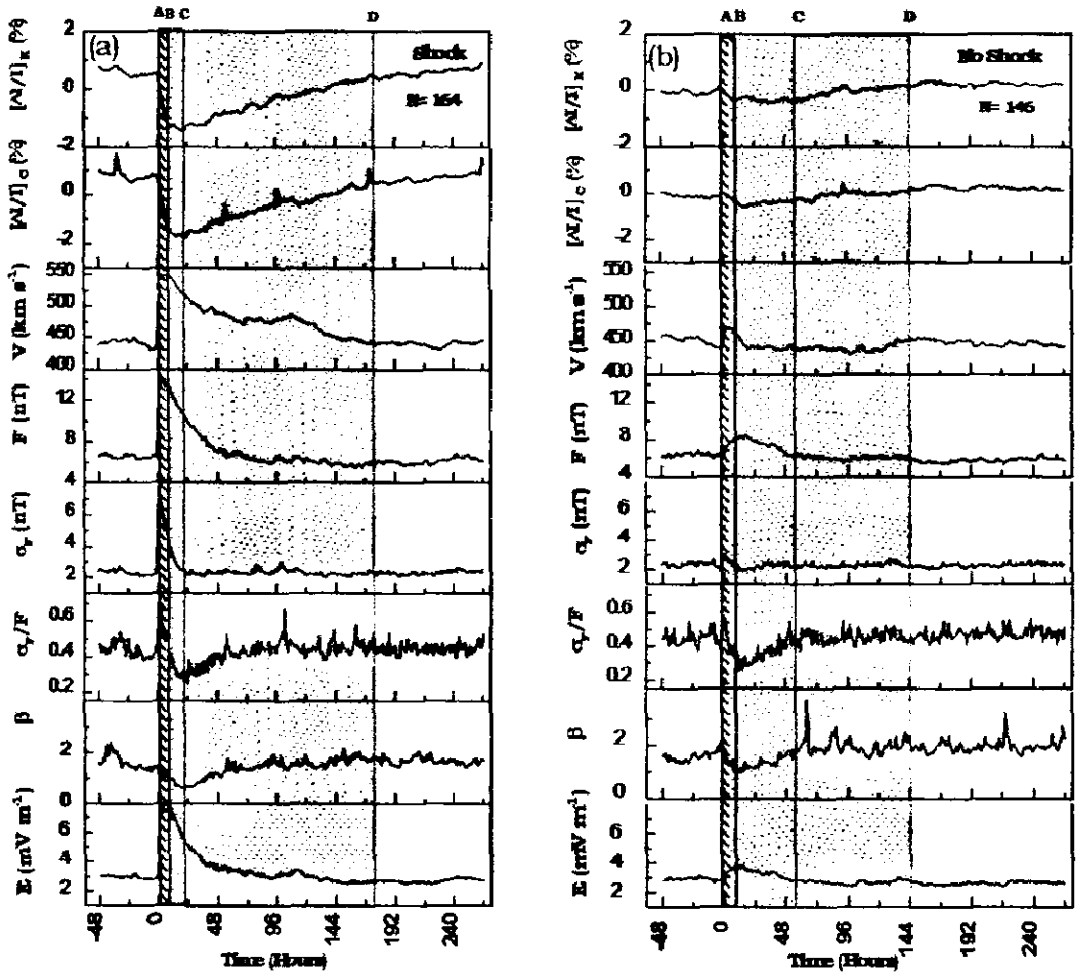

Figure 2.3 Superposed-epoch analysis results of GCR intensity and interplanetary plasma and field parameters; velocity [*V*], magnetic-field vector [*F*], standard deviation of field vector [σ_F], ratio [σ_F/F], plasma β, and electric field [*E*] with respect to passage of ICMEs associated with, (a) shock/sheath and (b) ICMEs not associated with shock/sheath region. N stands for number of events.

3 to 6 times larger in case of shock-associated ICMEs than ICMEs without shocks.

Similar analyses have been performed by dividing the solar cycle 23 ICMEs in two groups:

i) those associated with bidirectional superthermal electron events (BDEs) and

ii) those not showing a BDE signature.

The superposed-epoch plots of GCR-intensity and plasma/field parameters with respect to ICMEs with BDE and those not with BDE signature are shown in Figures 2.4a and 2.4b, respectively. Differences in amplitudes and time profiles in the GCR-intensity as well as interplanetary parameters are evident from these two figures. The GCR effectiveness of BDE-ICMEs as compared to non-BDE ICMEs is about 3.5

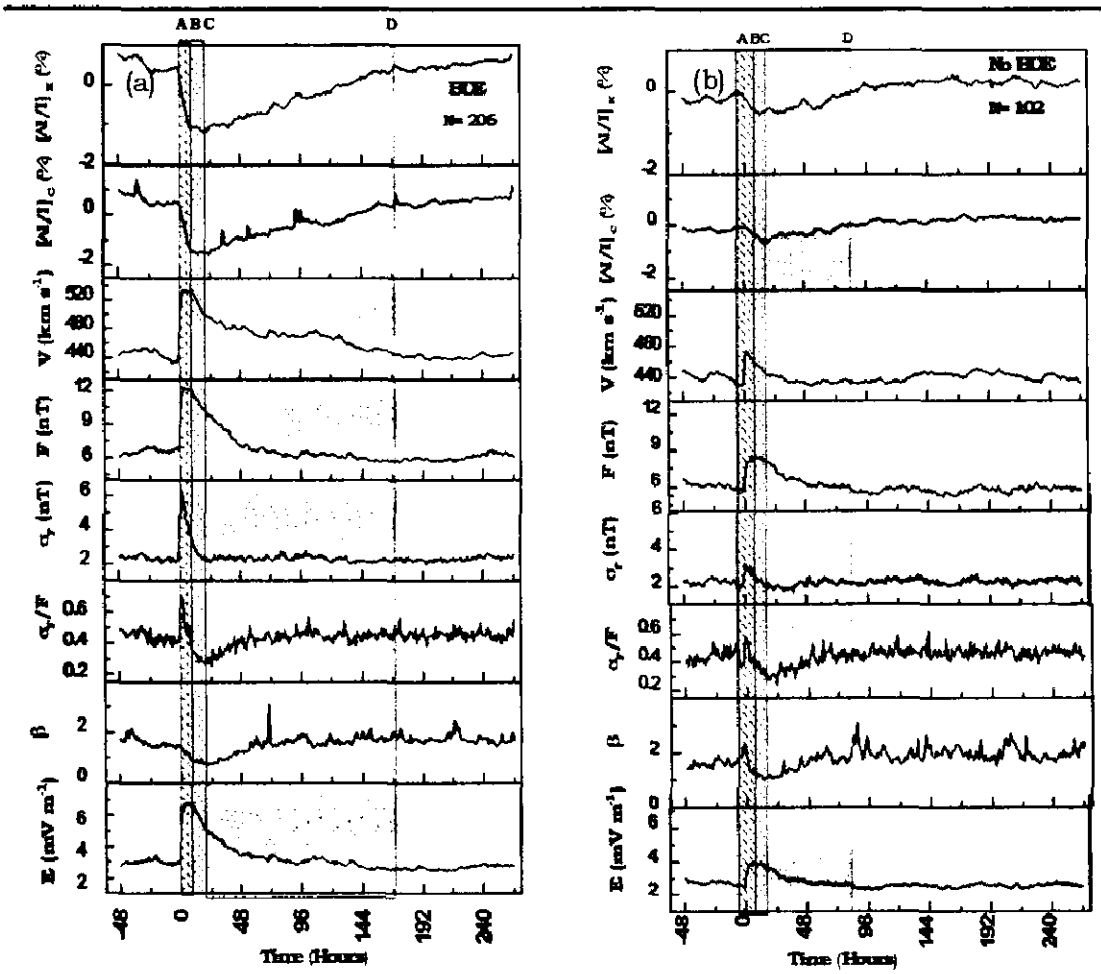

Figure 2.4 Superposed-epoch analysis results of GCR intensity and interplanetary plasma and field parameters; velocity [V], magnetic-field vector [F], standard deviation of field vector [σ_F], ratio [σ_F/F], plasma β, and electric field [E] due to ICMEs, (a) with bidirectional superthermal electron flows (BDEs), and (b) without BDEs. N stands for number of events.

times larger, on the average (see Table 2.5). The enhancements in peak values of various parameters (V_{max}, F_{max}, σ_{Fmax}, E_{max}) are about 1.2 to 2 times higher in case of BDE-ICMEs than non-BDE ICMEs. However, the ratio of enhancements in various parameters (ΔV, ΔF, $\Delta\sigma_F$, ΔE) is about 2 to 3 times larger for BDE-ICMEs than non-BDE ICMEs; these values are tabulated in Table 2.5. However, when BDE-ICMEs. were divided on the basis of their occurrence with bidirectional energetic ion flows (BIF) and without BIF signatures, and superposed-epoch analysis of GCR-intensity and solar-wind parameters were performed with respect to arrival of BDE-ICME with and without BIFs, no great difference in their GCR effectiveness was found except some difference in temporal profiles (see Figures 2.5a, 2.5b, and Table 2.5). Similarly the changes in solar plasma and field parameters, considered here, are not very differ-

Table 2.5 Average GCR intensity depression ΔI [%] at the Kiel and Calgary neutron monitors, peak values of interplanetary plasma/field parameters [V_{max}, F_{max}, σ_{Fmax}, σ_F/F_{max}, β_{max}, and E_{max}], and enhancements in these parameters [ΔV, ΔF, $\Delta\sigma_F$, $\Delta(\sigma_F/F)$, and ΔE] due to ICMEs associated with/without shocks, BDEs, BDE- BIF, magnetic cloud, and halo structures. The calculated ratios of the values of different parameters due to ICME with/without particular structure are also given

ICME Structure	ΔI [%] (Kiel) NM	ΔI [%] Calgary NM	V_{max} [km s^{-1}]	ΔV [km s^{-1}]	F_{max} [nT]	ΔF [nT]	σ_{Fmax} [nT]	$\Delta\sigma_F$ [nT]	$(\sigma_F/F)_{max}$	$\Delta(\sigma_F/F)$	β_{max}	E_{max} [mV m^{-1}]	ΔE [mV m^{-1}]
Shock	-1.92	-2.50	546	117	13.95	7.32	7.31	5.25	0.70	0.31	1.50	7.95	5.18
No Shock	-0.56	-0.62	471	31	8.42	2.33	2.97	0.89	0.59	0.32	2.04	3.78	1.08
Ratio	**3.43**	**4.03**	**1.16**	**3.77**	**1.66**	**3.14**	**2.46**	**5.90**	**1.19**	**0.97**	**0.73**	**2.10**	**4.80**
BDE	-1.63	-2.08	533	100	12.27	5.53	6.30	4.00	0.70	0.30	1.54	6.90	3.97
No BDE	-0.48	-0.61	472	42	8.55	2.95	3.33	1.46	0.58	0.22	2.27	3.98	1.56
Ratio	**3.40**	**3.41**	**1.13**	**2.38**	**1.43**	**1.87**	**1.89**	**2.74**	**1.21**	**1.36**	**0.68**	**1.73**	**2.54**
BDE – BIF	-2.12	-2.50	538	113	13.31	6.09	7.42	5.10	0.79	0.42	1.52	7.39	4.37
BDE - No BIF	-2.20	-3.40	562	119	15.68	9.91	7.97	6.01	1.13	0.72	1.77	10.04	7.36
Ratio	**0.96**	**0.73**	**0.96**	**0.95**	**0.85**	**0.61**	**0.93**	**0.85**	**0.70**	**0.58**	**0.86**	**0.74**	**0.59**
MC	-1.84	-2.50	512	98	13.96	7.82	6.40	4.40	0.84	0.63	2.49	7.67	5.14
No MC	-1.16	-1.24	526	86	10.39	3.85	4.85	2.60	0.68	0.27	1.45	5.59	2.75
Ratio	**1.59**	**2.02**	**0.97**	**1.14**	**1.34**	**2.03**	**1.32**	**1.69**	**1.23**	**2.33**	**1.72**	**1.37**	**1.87**
Halo	-2.31	-2.81	568	127	15.60	8.55	7.69	5.41	0.84	0.44	1.78	9.07	6.06
No Halo	-1.34	-1.84	535	87	11.03	4.44	5.19	2.94	0.68	0.35	1.76	6.03	3.11
Ratio	**1.72**	**1.53**	**1.06**	**1.46**	**1.41**	**1.92**	**1.48**	**1.84**	**1.23**	**1.26**	**1.01**	**1.50**	**1.95**

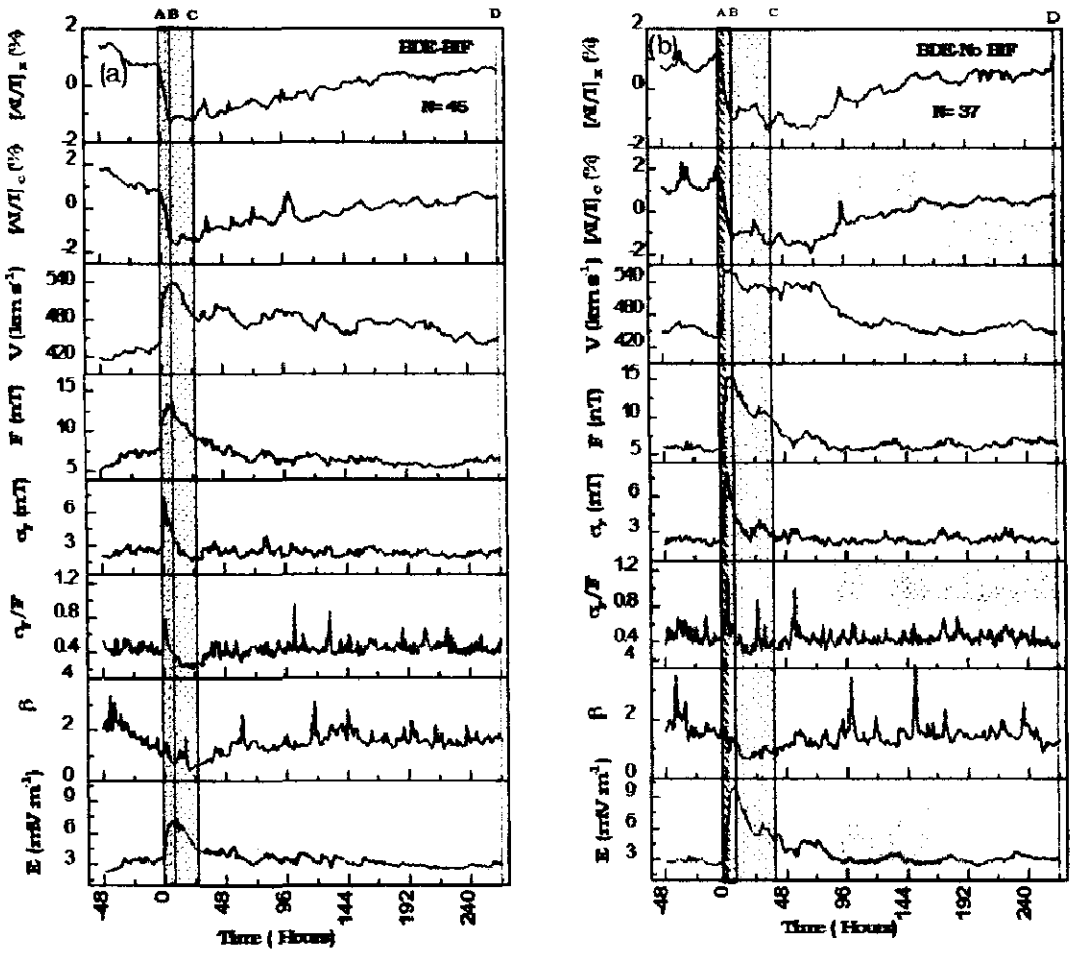

Figure 2.5 Superposed-epoch analysis results of GCR intensity and interplanetary plasma and field parameters; velocity [V], magnetic-field vector [F], standard deviation of field vector [σ_F], ratio [σ_F/F], plasma β, and electric field [E] with respect to (a) ICMEs with bidirectional superthermal electron flows (BDEs) as well as bidirectional energetic ion flows (BIFs), and (b) ICMEs with BDEs but without BIFs. N stands for number of events.

-ent in the two cases.

We have considered two sets of solar cycle 23 ICMEs:

i) those reported as magnetic clouds and

ii) those whole plasma and field properties are not similar to those of magnetic clouds.

To see whether magnetic clouds are more GCR effective than non-magnetic cloud ICMEs or not, we have adopted a similar approach as to that used in earlier cases, and we performed superposed-epoch analysis of GCR-intensity and plasma/field parameters with reference to

i) ICMEs with magnetic cloud structures and

ii) ICMEs not showing magnetic cloud features.

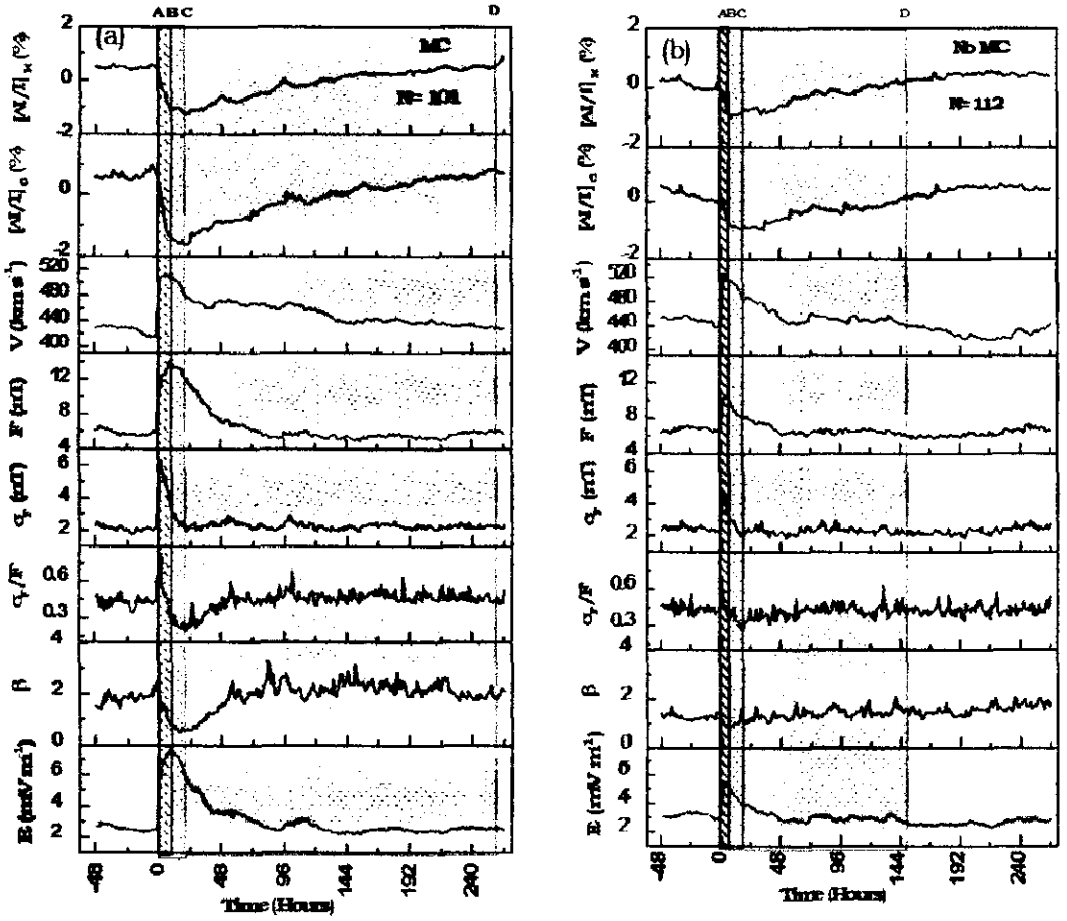

Figure 2.6 Superposed-epoch analysis results of GCR intensity and interplanetary plasma and field parameters; velocity [V], magnetic-field vector [F], standard deviation of field vector [σ_F], ratio [σ_F/F], plasma β, and electric field [E] with respect to (a) ICMEs reported to be magnetic clouds (MC) and (b) ICMEs not showing magnetic cloud structure (non-MC). N stands for number of events.

It is found (see Figures 2.6a and 2.6b) that magnetic clouds are, on average, about twice as GCR-effective as non-magnetic cloud ICMEs. As regards the differences in variations in plasma/field parameters, it is observed that, although the average speed and enhancement in it is almost same in two cases, the vector magnetic-field and electric-field enhancement in the case of magnetic clouds is almost twice as large as in the case of non-magnetic cloud ICMEs (see Table 2.5).

A superposed-epoch analysis with respect to ICMEs related to halo CMEs and non-halo CMEs also shows a difference in the GCR effectiveness of two type of CMEs; halo CMEs are more GCR-effective than non-halo CMEs; the relative GCR-effectiveness is about 1.5 times larger for halo CME as than non-halo CMEs. Differences in solar-wind speed, IMF strength, and electric fields are also observed (see Figures 2.7a, 2.7b, and Table 2.5).

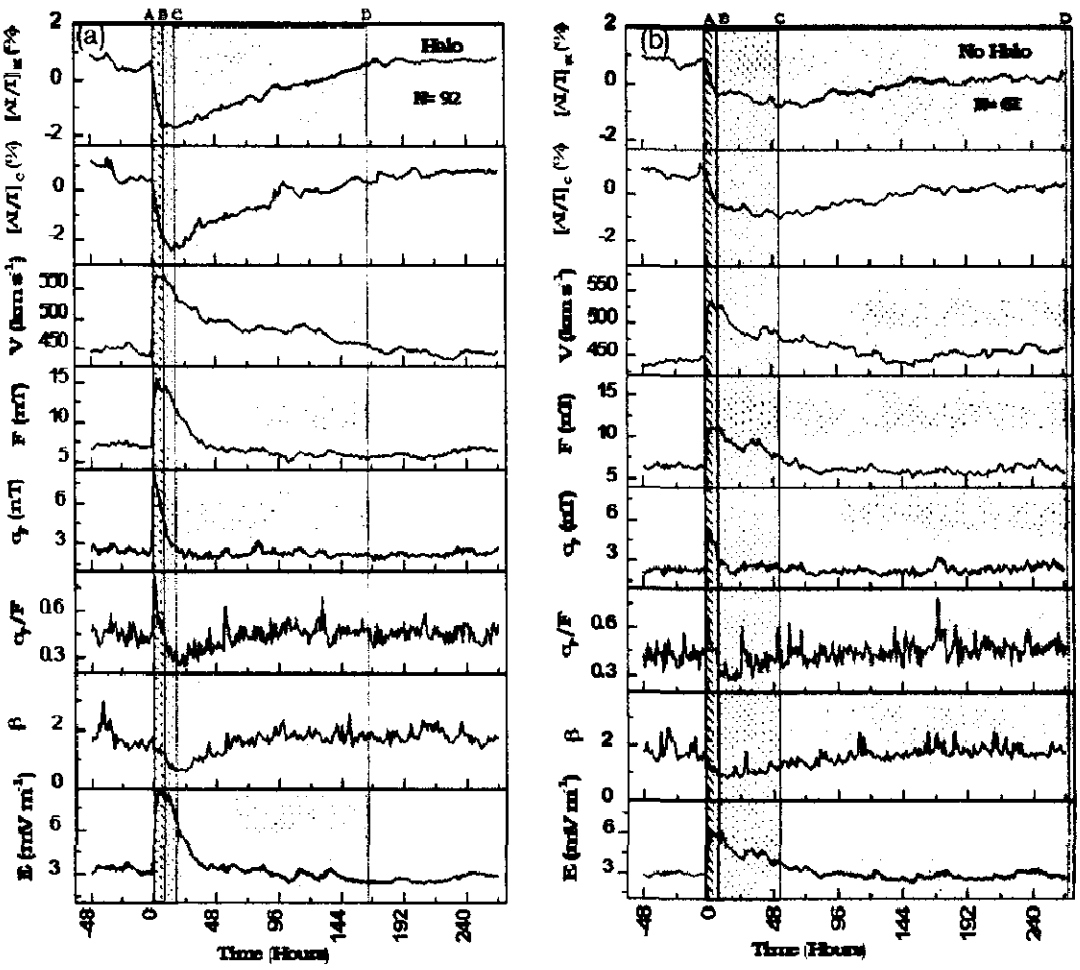

Figure 2.7 Superposed-epoch analysis results of GCR intensity and interplanetary plasma and field parameters: velocity [V], magnetic-field vector [F], standard deviation of field vector [σ_F], ratio [σ_F/F], plasma β, and electric field [E] for ICME structures due to (a) halo CMEs and (b) for ICME structures other than halo CMEs (non-halo). N stands for number of events.

From the above discussions it is clear that the ICMEs associated with shocks/BDEs/MCs/halo-CMEs are more GCR-effective than ICMEs not associated with these structures/features. Each group (BDE/MC/halo) was subdivided into shock/no shock cases. A large difference in their GCR-effectiveness is observed; shock/sheath associated BDE/MC/halo ICMEs are much more GCR-effective than those not associated with any shock/sheath region, (see Table 2.6). This result again emphasizes the role of magnetic turbulence in sheath regions as is evident from the ratios of $\Delta\sigma_F$ (see also Badruddin, Venkatesan, and Zhu, 1991; Yu *et al.*, 2010, Dumbovic *et al.*, 2011).

We have shown that the GCR effectiveness of ICMEs associated/not associated

Table 2.6 Average GCR intensity depression [%] at the Kiel and Calgary neutron monitors, peak values of interplanetary plasma-field parameters [V_{max}, F_{max}, σ_{Fmax}, $(\sigma_F/F)_{max}$, β_{max} and E_{max}] and enhancements in these parameters [ΔV, ΔF, $\Delta\sigma_F$, $\Delta(\sigma_F/F)$, and ΔE] due to BDE ICMEs associated with/without shock, magnetic clouds with/without shock, halo CMEs with/without shock structures. The calculated ratios of different parameters due to ICME of different features with/without shock are also given.

ICME Structure	ΔI [%] (Kiel) NM	ΔI [%] Calgary NM	V_{max} [$km\,s^{-1}$]	ΔV [$km\,s^{-1}$]	F_{max} [nT]	ΔF [nT]	$\sigma_{F\,max}$ [nT]	$\Delta\sigma_F$ [nT]	$(\sigma_F/F)_{max}$	$\Delta(\sigma_F/F)$	β_{max}	E_{max} [$mV\,m^{-1}$]	ΔE [$mV\,m^{-1}$]
BDE with shock	-2.28	-2.82	556	132	14.93	8.18	7.56	5.44	0.76	0.36	1.37	8.39	5.46
BDE without shock	-0.87	-1.26	501	51	9.52	2.96	4.48	2.26	0.76	0.35	1.78	5.17	2.18
Ratio	**2.62**	**2.23**	**1.11**	**2.59**	**1.57**	**2.76**	**1.69**	**2.41**	**1.00**	**1.03**	**0.77**	**1.62**	**2.50**
MC with shock	-2.69	-3.59	555	134	16.20	10.07	8.06	5.92	1.01	0.45	1.91	8.85	6.24
MC without shock	-0.60	-0.83	441	44	11.23	6.22	3.27	1.55	0.81	0.43	6.45	3.68	1.65
Ratio	**4.48**	**4.32**	**1.26**	**3.04**	**1.44**	**1.62**	**2.46**	**3.82**	**1.25**	**1.05**	**0.30**	**2.40**	**3.78**
Halo with shock	-3.02	-3.61	585	156	17.30	11.01	9.07	6.81	0.85	0.42	1.43	10.08	7.38
Halo without shock	-1.27	-1.41	551	90	11.45	4.06	5.23	2.93	0.84	0.51	2.78	6.62	3.06
Ratio	**2.38**	**2.56**	**1.06**	**1.73**	**1.51**	**2.71**	**1.73**	**2.32**	**1.01**	**0.82**	**0.51**	**1.52**	**2.41**

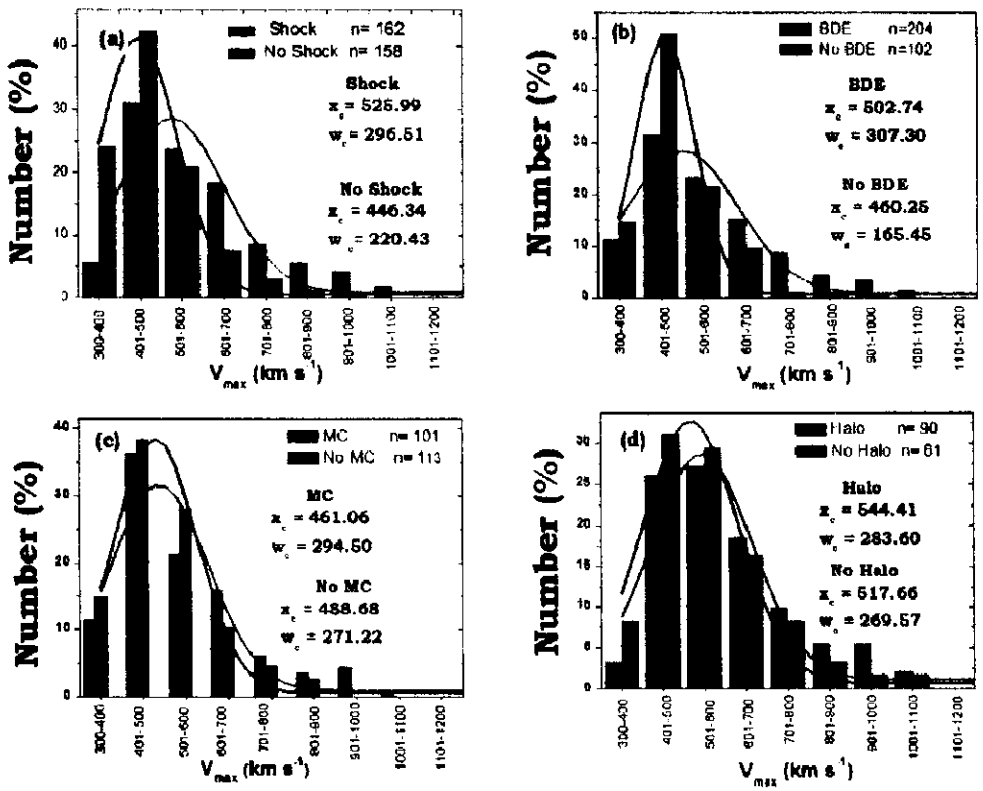

Figure 2.8 Frequency distribution of maximum speed, [V_{max}, km s^{-1}] observed during the passage of ICMEs associated/not associated with (a) shocks, (b) BDEs, (c) magnetic clouds, and (d) halo CMEs. Gaussian best-fit curves representing the distribution of ICMEs are also shown in the figure. The central-peak values [x_c] and full widths at half maximum [ω_c] obtained from the fits. n stands for number of events, considered for each histogram.

with different structures/features is not similar, and there are distinctions in the distribution of different ranges of GCR depressions from quiet, small, moderate, large, up to very large depressions. Therefore, it is important to look for the distribution of various plasma/field parameters. We have studied these distributions for three parameters [V_{max}, F_{max}, and E_{max}] by dividing these parameters into suitable bins. These distributions for V_{max} are shown for shock/non-shock ICMEs, BDE/non-BDE ICMEs, magnetic cloud/non-magnetic cloud ICMEs, and halo/non-halo ICMEs (Figure 2.8). Similar distributions for F_{max} (Figure 2.9) and E_{max} (Figure 2.10) are also plotted. Central peak values [x_c], full width at half maximum [w_c], and the product [$x_c w_c$] are also calculated for each structure and the parameters after fitting a Gaussian function (see Tables 2.7, 2.8, and 2.9). A clear difference in the values of frequency distributions [x_c, w_c, and $x_c w_c$] for different parameters [V_{max}, F_{max}, and E_{max}]

due to shock/no-shock, BDE/non-BDE, magnetic cloud/non-magnetic cloud and halo/non-halo ICMEs can be seen (see Figures 2.8, 2.9, 2.10, and Tables 2.7, 2.8, 2.9).

2.3.4 GCR Effectiveness of ICMEs with Different Structures/Features: Statistical Results

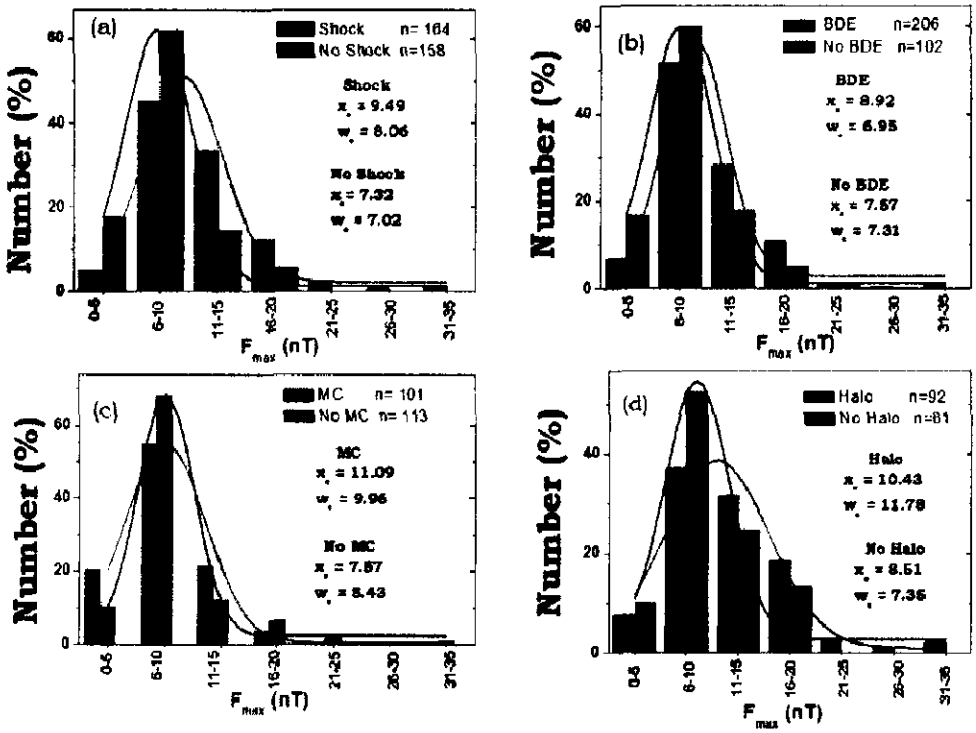

Figure 2.9 Frequency distribution of maximum magnetic-field vector, [F_{max}, nT] observed during the passage of ICMEs associated/not associated with (a) shocks, (b) BDEs, (c) magnetic clouds, and (d) halo CMEs. Gaussian best-fit curves representing the distribution of ICMEs are also shown in the figure. The central-peak values [x_c] and full widths at half maximum [w_c] obtained from the fits. n stands for number of events, considered for each histogram.

As discussed in Section 2.3.1, we have divided the GCR effectiveness of ICMEs into five convenient groups, on the basis of their effects in modulating GCR intensity:

i) quiet ($\Delta I \approx 0.0$);

ii) small ($\Delta I \approx -0.01$ to -0.49 %);

iii) moderate ($\Delta I \approx -0.50$ to -1.49 %)

iv) large ($\Delta I \approx -1.50$ to -2.99 %), and,

v) very large (ΔI larger than -3.00 %) depressions.

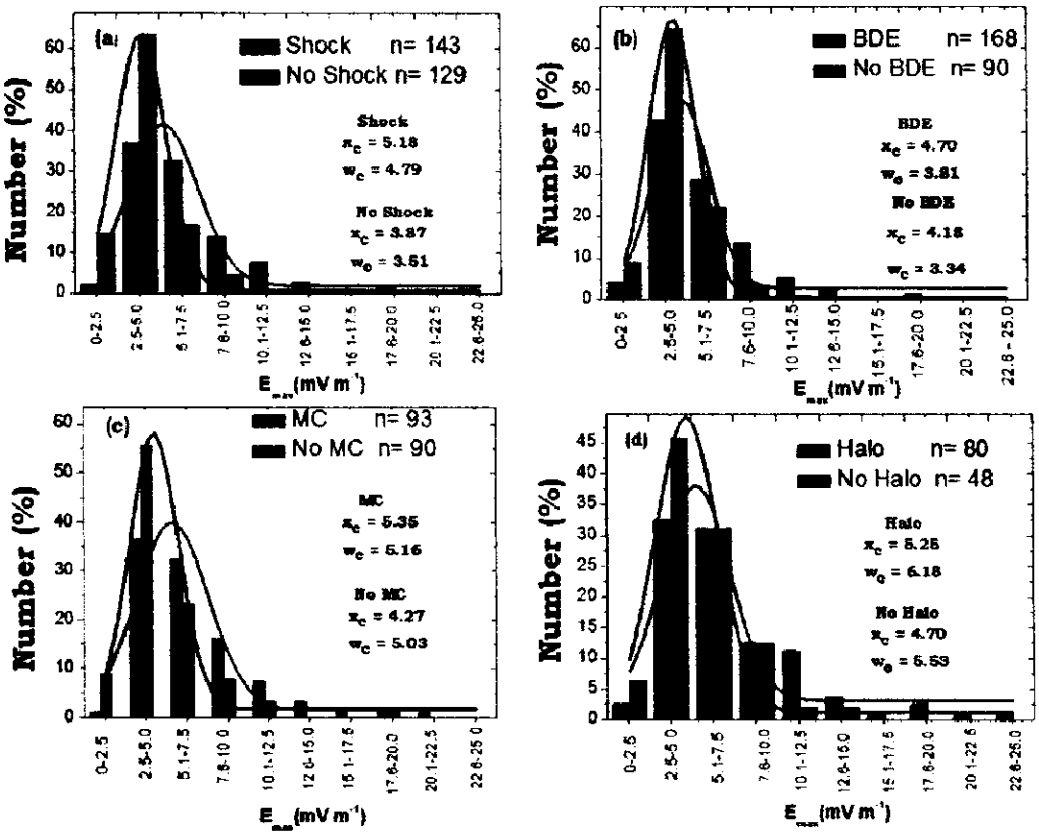

Figure 2.10 Frequency distribution of maximum electric field, [E_{max}, mV m^{-1}] observed during the passage of ICMEs associated/not associated with (a) shocks, (b) BDEs, (c) magnetic clouds, and (d) halo CMEs. Gaussian best-fit curves representing the distribution of ICMEs are also shown in the figure. The central-peak values [x_c] and full widths at half maximum [w_c] obtained from the fits. n stands for number of events, considered for each histogram.

The contributions of ICMEs associated/not associated with different structures/features to the different groups of depressions (quiet, small, moderate, large and very large) are given for shock/no-shock ICMEs, BDE/No-BDE ICMEs, BDE-BIF/BDE-no-BIF, magnetic cloud/non magnetic cloud, and halo/non-halo ICMEs (see Table 2.10). It can be seen from this table that, in general, shock/BDE/MC/halo ICMEs are more often associated with "large" and "very large" GCR effectiveness than the no-shock/no-BDE/no-C/no-halo ICMEs. This difference is most prominent in case of shock/sheath associated ICMEs rather than those not associated with shock/sheath region. This again emphasizes the role of the shock/sheath region in producing larger depressions in GCR intensity (see also Zhang and Burlaga, 1988; Badruddin, Venkatesan, and Zhu, 1991; Lockwood, Webber, and Debrunner, 1991; Oh, Yi, and Kim, 2008; Yu *et al.*, 2010, Dumbovic *et al.*, 2012).

Table 2.7 Gaussian-fit parameters for the distribution of maximum solar-wind velocity [V_{max}], central peak value of V_{max} [x_c], width [w], full width at half maximum [w_c], and the product $x_c w_c$ during the passage of ICMEs with different structures/features

ICME Structure	Gaussian-fit parameters for V_{max}				
	R^2	x_c	w	w_c	$x_c w_c$ [10^4]
Shock	0.90	526.00 ± 14.84	251.83 ± 33.31	296.51	15.60
No Shock	0.99	446.34 ± 3.72	187.22 ± 8.23	220.43	09.84
BDE	0.94	502.74 ± 12.13	261.00 ± 28.17	307.30	15.45
No BDE	0.98	460.25 ± 4.52	140.52 ± 7.67	165.45	07.61
MC	0.93	461.06 ± 14.18	250.12 ± 33.72	294.50	13.58
No MC	0.91	488.68 ± 13.42	230.35 ± 30.58	271.22	13.25
Halo	0.93	544.41 ± 12.05	240.86 ± 26.52	283.60	15.44
No Halo	0.97	517.66 ± 7.37	228.95 ± 16.29	269.57	13.95

Table 2.8 Gaussian-fit parameters for the distribution of maximum magnetic field [F_{max}], central-peak value of F_{max} [x_c], width [w], full width at half maximum [w_c], and the product $x_c w_c$ during the passage of ICMEs with different structures/features.

ICME Structure	Gaussian-fit parameters for F_{max}				
	R^2	x_c	w	w_c	$x_c w_c$
Shock	0.96	9.49 ± 0.42	6.85 ± 1.39	8.06	76.49
No Shock	0.99	7.32 ± 0.23	5.96 ± 0.34	7.02	51.40
BDE	0.97	8.92 ± 0.44	5.90 ± 1.10	6.95	61.99
No BDE	0.99	7.57 ± 0.18	6.21 ± 0.28	7.31	55.34
MC	0.98	11.09 ± 0.39	8.46 ± 0.98	9.96	110.46
No MC	0.99	7.57 ± 0.11	7.16 ± 0.19	8.43	63.82
Halo	0.95	10.43 ± 0.67	10.01 ± 1.72	11.78	122.86
No Halo	0.95	8.51 ± 0.59	6.24 ± 0.17	7.35	62.55

Table 2.9 Gaussian-fit parameters for the distribution of electric field [E_{max}], central-peak value of E_{max} [x_c], width [w], full width at half maximum [w_c], and the product $x_c w_c$ during the passage of ICMEs with different structures/features.

ICME Structure	Gaussian-fit parameters for E_{max}				
	R^2	x_c	w	w_c	$x_c w_c$
Shock	0.94	5.18 ± 0.26	4.07 ± 0.64	4.79	24.81
No Shock	0.99	3.87 ± 0.07	2.98 ± 0.09	3.51	13.58
BDE	0.93	4.70 ± 0.22	3.24 ± 0.66	3.81	17.91
No BDE	0.99	4.18 ± 0.05	2.84 ± 0.07	3.34	13.96
MC	0.92	5.35 ± 0.32	4.38 ± 0.73	5.16	27.61
No MC	0.98	4.27 ± 0.14	2.95 ± 0.24	5.03	21.48
Halo	0.91	5.25 ± 0.29	3.95 ± 0.75	6.18	32.44
No Halo	0.96	4.70 ± 0.18	3.65 ± 0.46	5.53	25.99

Table 2.10 Comparative distribution of relative GCR effectiveness (quiet, small, moderate, large, and very large) due to ICMEs associated/not associated with different structures.

Number (%)					
ICME Structure	Quiet $\Delta I \approx 0.0$	Small $-0.01 \geq \Delta I \geq -0.49$ [%]	Moderate $-0.50 \geq \Delta I \geq -1.49$ [%]	**Large $-1.50 \geq \Delta I \geq -2.99$ [%]**	Very large $\Delta I \leq -3.00$ **[%]**
Shock	14.8	18.3	29.6	19.7	**17.6**
No Shock	22.2	37.3	28.6	6.3	**5.6**
BDE	**14.8**	24.8	30.2	**14.8**	**15.4**
No BDE	25.9	25.9	32.9	11.8	**3.5**
MC	14.0	21.5	35.5	14.0	**15.0**
No MC	20.2	28.1	23.6	15.7	**12.4**
Halo	**24.7**	**14.8**	23.5	21.0	**16.0**
No Halo	10.4	20.8	37.5	12.5	**18.8**

2.3.5 Decrease Amplitude and Its Dependence on Interplanetary Parameters: Quantitative Relationship

In Tables 2.1 and 2.5, 2.6, we have tabulated the amplitudes/enhancements in various parameters including GCR intensity obtained from superposed plots. Using the values given in these tables, we obtained the linear relationship between the GCR-intensity depression ΔI [%] at Kiel and other tabulated parameters. The linear-correlation coefficients so obtained and the rate of change of GCR intensity with various parameters are given in Table 2.11. Scatter plots and best-fit linear curves with magnetic and electric fields are also plotted in Figures 2.11a and b. However, it should be noted that the linear fit is obtained from the averages, which are not independent, as the same events are present in various classes of data points. On the basis of these fits, using averaged values of parameters, the GCR intensity is found to decrease at a rate of –0.37 % per unit increase in vector magnetic field [nT] and –0.48 % per unit increase in electric field [mV m^{-1}] during the passage of ICMEs.

2.3.6 Recovery Characteristics of Depressions in GCR-Intensity due to ICMEs

We have studied the recovery characteristics of GCR-intensity depression for the averaged recovery profiles obtained due to depressions of different GCR effectiveness (small, moderate, large, and very large depressions) and due to ICMEs with different features/structures (shock/no-shock, BDE/no-BDE, magnetic cloud/no-magnetic cloud, halo/non-halo ICMEs). We have also fitted an exponential [$y = y_0 + Ae^{(-x/\tau)}$] to these recovery profiles (see Figure 2.12, 2.13, and 2.14 and Table 2.12). The characteristic recovery time [τ] increases with GCR-effectiveness (Table 2.12); it is larger for the shock-associated ICMEs than for those not associated with shocks. A similar trend in differences in characteristic time can be seen in the case of BDE/non-BDE ICME, and halo/non-halo ICMEs. The characteristic recovery time [τ] is larger for BDE-ICMEs than for non-BDE-ICMEs and it is larger for halo ICMEs than for non-halo ICMEs (Table 2.12).

We have also tried to search for the parameter out of those considered here [V, F, σ_F, σ_F/F, β, and E] that best correlates with the rate of change in the intensity of GCR during its recovery. Out of these parameters, we find that, during recovery, it is better correlated with solar-wind speed (even better than F and E), at least during recovery

Table 2.11 Correlation coefficient [R] and slope from the best-fit linear curve between average GCR-intensity change and various parameters obtained from superposed-epoch analysis during the passage of ICMEs with different GCR effectiveness and associated/not associated with different structures/features.

Serial No.	Parameters	ΔI [%]	
		Linear fit	
		R	Slope
1	V_{max} [km s^{-1}]	− 0.91	− 0.02 ± 0.00
2	ΔV [km s^{-1}]	− 0.95	− 0.02 ± 0.00
3	F_{max} [nT]	− 0.96	− 0.37 ± 0.03
4	ΔF [nT]	− 0.94	− 0.37 ± 0.03
5	$\sigma_{F\,max}$ [nT]	− 0.95	− 0.57 ± 0.04
6	$\Delta\sigma_F$ [nT]	− 0.95	− 0.60 ± 0.05
7	$(\sigma_F/F)_{max}$	− 0.65	− 4.52 ± 1.27
8	$\Delta(\sigma_F/F)$	− 0.50	− 3.92 ± 1.65
9	E_{max} [mV m^{-1}]	− 0.97	− 0.48 ± 0.03
10	ΔE [mV m^{-1}]	− 0.98	− 0.52 ± 0.02
11	β_{max}	0.41	0.42 ± 0.22

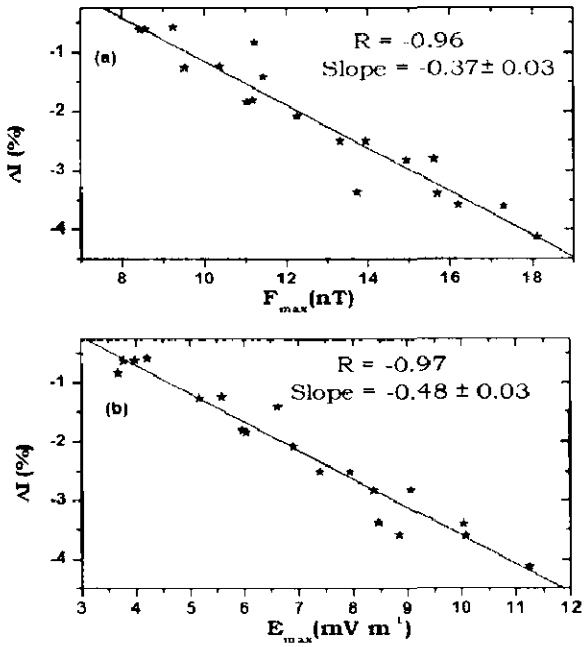

Figure 2.11 Best fit linear curve between averaged GCR-intensity depression [ΔI, %] and (a) magnetic-field amplitude [F_{max}, nT] (b) electric-field amplitude [E_{max}, mV m^{-1}] due to ICMEs with different GCR-effectiveness and ICMEs associated/not associated with different structures/features.

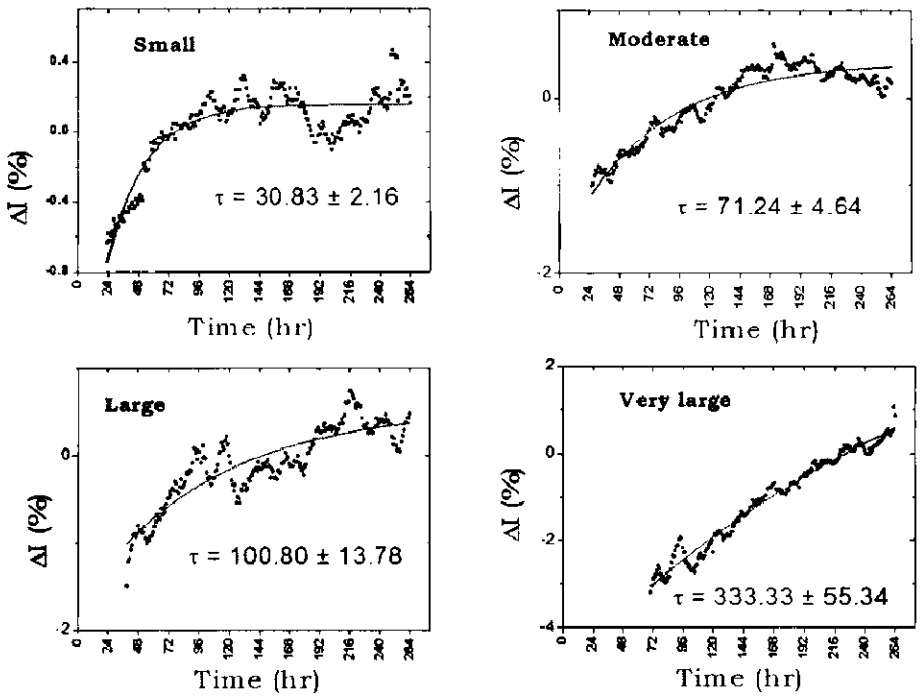

Figure 2.12 Exponential fit and characteristic recovery time [τ, hours] during recovery of GCR-intensity depressions due to ICMEs of different GCR-effectiveness.

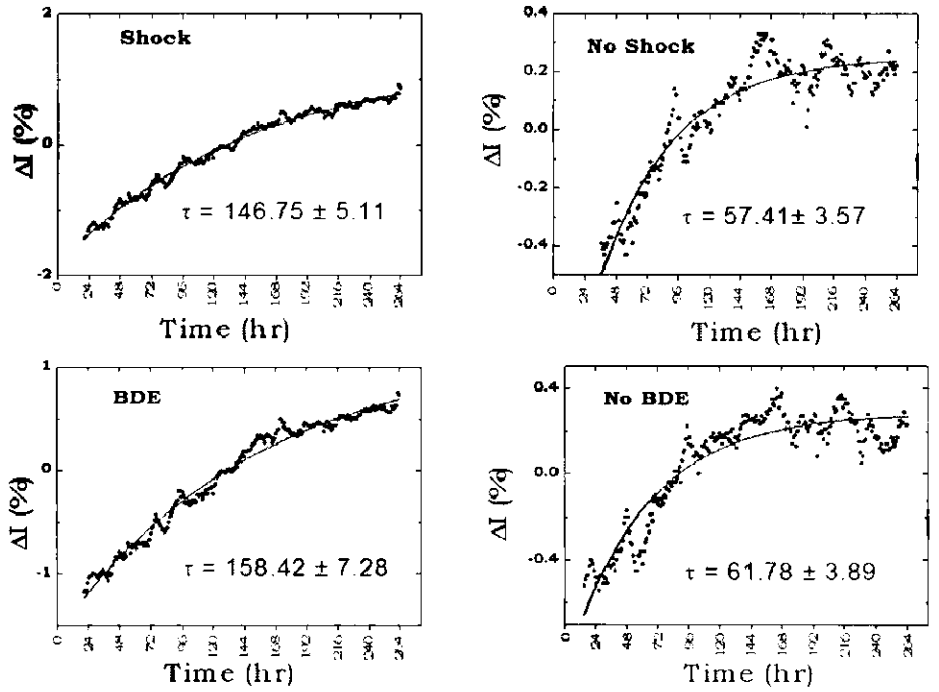

Figure 2.13 Exponential fit and characteristic recovery time [τ, hours] during recovery of GCR-intensity depressions due to ICMEs associated/not associated with shocks and bidirectional superthermal electron events (BDEs).

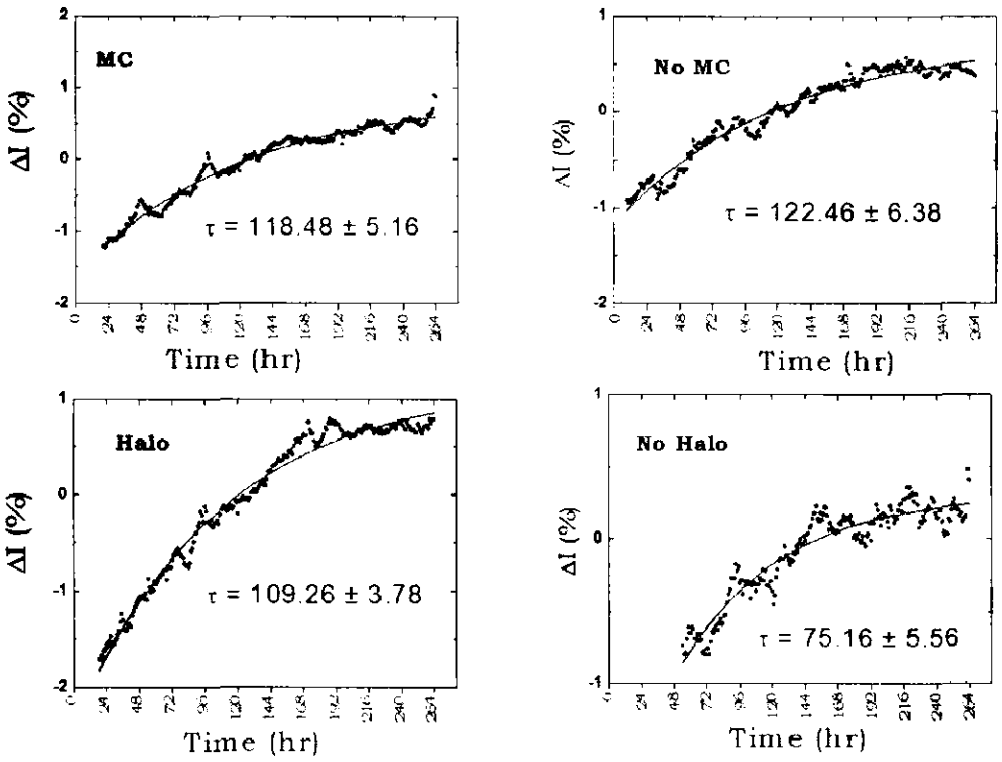

Figure 2.14 Exponential fit and characteristic recovery time [τ, hours] during recovery of GCR-intensity depressions due to ICMEs associated/not associated with magnetic cloud (MC) and halo CMEs.

after passage of shock/sheath associated ICMEs, BDE-associated ICMEs and halo-CMEs (see Table 2.13).

From our averaged plots, we have also attempted to find whether the speed of the ICME disturbance during its passage to Earth is related to recovery time (*i.e.* the time period from the minimum of the depression to the point of GCR intensity returning to the pre-decrease value) of the GCR-intensity depression or not. A linear-regression plot (Figure 2.15) between V_{max} and the recovery time of the depression shows that the speed the ICME-related disturbance may influence the recovery time after the depression.

2.4 Summary and Conclusions

From the statistical and superposed epoch analysis presented in this article, we summarize our conclusions:

- Nearly half (48.4 %) of the ICMEs identified in the near-Earth interplanetary plasma/field data near the Earth either do not produce any depression in GCR-

Table 2.12 Characteristic recovery time [τ, hours] of GCR intensity with determination coefficient [R^2] due to ICMEs of different GCR-effectiveness, ICMEs associated/not associated with different structures/features and different ICMEs with/without shocks.

GROUP/ ICME Structure	Recovery Phase	
	Exponential fit	
	R^2	τ [hours]
Small	**0.79**	30.83 ± 2.16
Moderate	**0.89**	71.24 ± 4.64
Large	**0.78**	100.80 ± 13.78
Very large	**0.97**	333.33 ± 55.34
Shock	**0.99**	146.75 ± 5.11
No Shock	**0.89**	57.41 ± 3.57
BDE	**0.98**	158.42 ± 7.28
No BDE	**0.87**	61.78 ± 3.89
MC	**0.97**	118.48 ± 5.16
No MC	**0.96**	122.46 ± 6.38
Halo	**0.98**	109.26 ± 3.78
No Halo	**0.91**	75.16 ± 5.56
BDE with Shock	0.98	173.13 ± 7.63
BDE without Shock	*0.91*	*163.28 ± 16.46*
MC with Shock	0.98	144.71 ± 6.92
MC without Shock	0.52	36.40 ± 5.18
Halo with Shock	0.98	112.18 ± 3.70
Halo without Shock	0.86	58.36 ± 4.24

Table 2.13 Correlation coefficients between the rate of change in the GCR intensity during the recovery phase and various parameters for ICMEs associated with different structures and different GCR effectiveness.

ICME Structure	Recovery Phase					
	Correlation [R] between ΔI and different parameters during recovery					
	V	F	σ_F	σ_F/F	β	E
Shock	– 0.94	– 0.80	– 0.13	0.58	0.82	-0.87
No- Shock	– 0.62	– 0.65	0.28	0.50	0.45	-0.67
BDE	– 0.93	– 0.82	– 0.37	0.60	0.70	-0.87

Table 2.13 (*continued*)

No-BDE	– 0.47	– 0.67	0.51	0.03	0.64	– 0.66
MC	–0.92	– 0.75	– 0.24	0.54	0.58	– 0.84
No-MC	– 0.75	– 0.72	0.07	0.47	0.56	– 0.67
Halo	– 0.92	– 0.78	– 0.01	0.61	0.77	– 0.82
No-Halo	– 0.59	– 0.32	0.25	0.33	0.59	– 0.53
Small	– 0.33	– 0.92	0.52	0.72	0.58	– 0.91
Moderate	– 0.82	– 0.87	– 0.32	0.51	0.76	–0.89
Large	– 0.72	– 0.73	0.02	0.38	0.45	– 0.69
Very large	– 0.95	– 0.64	– 0.36	– 0.05	0.75	– 0.67

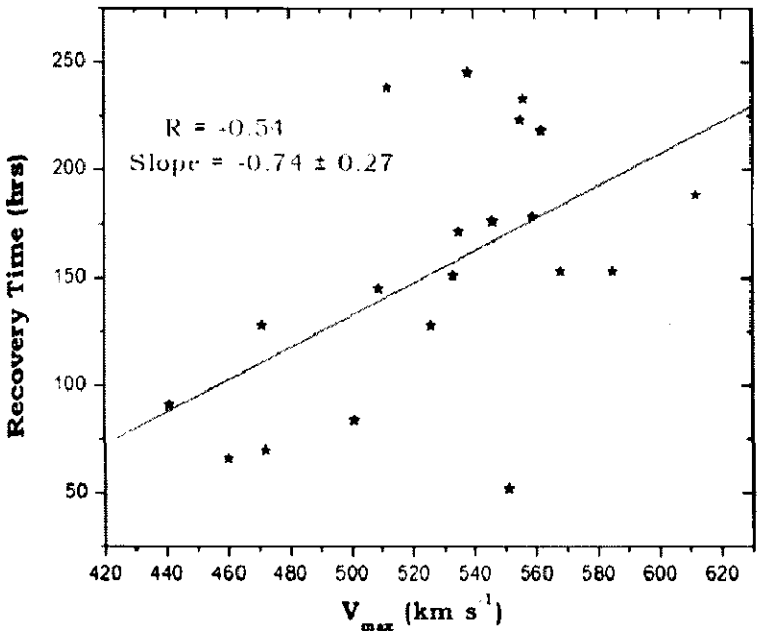

Figure 2.15 Linear-regression plot between V_{max} [km s^{-1}] and GCR-intensity recovery time [hours], obtained from superposed-epoch plots, due to ICMEs with different GCR effectiveness and ICMEs associated/not associated with different structures/features.

intensity (17.3 %) or produce small depressions of less than 0.5 % (31.1 %). The rest of the ICMEs either produce the so-called moderate (27.3 %), large (11.8 %), or very large (12.5 %) depressions in GCR intensity.

- The average GCR-intensity depression profile due to the four groups of GCR effective ICMEs (small, moderate, large, and very large) with successively increasing depressions start at the arrival of ICME-related disturbance, with a relatively sharper decrease at first up to a few hours, followed by a slower decrease until minimum intensity is reached. Subsequently recovery starts, reaching the pre-decrease level in a much longer time (a few days).
- It is found from the frequency distribution of plasma/field parameter (speed, magnetic-field vector, and electric fields) that the distribution of these parameters, their peak values, and the spread of frequency distribution shift successively towards the higher side from the quiet, small, moderate, large, to very large group of GCR effective ICMEs.
- Based on the superposed-epoch analysis, we found that the GCR effectiveness of shock-associated ICMEs, on average, is about three times larger than that of those not associated with a shock/sheath region. Similar analyses also reveal that the ICMEs with bidirectional superthermal electron (BDE) signatures are about 3.5 times more geo-effective than ICMEs not associated with BDEs. Further, ICMEs with a magnetic-cloud structure are about twice as GCR effective as ICMEs observed to have non-magnetic cloud structures. The ICMEs due to halo-CMEs are found to be about 1.5 times more GCR-effective than those due to non-halo CMEs. Enhancements in various plasma and field parameters are also found to be larger due to ICMEs associated with shocks/BDEs/MCs/halo-CMEs than those not associated with these structures/features.
- From statistical analysis of five groups of GCR-effective ICMEs (quiet, small, moderate, large, and very large) associated/not associated with different structures/features, we found that "large" and "very large" depressions together are much larger (37.3 %) due to shock-associated ICMEs than those not associated with shocks (11.9 %). Similarly a larger number of large and very large depressions in GCR intensity are associated with ICMEs with BDE rather than to non-BDE ICMEs, magnetic clouds rather than to ICMEs having another than the magnetic-cloud structure, and ICMEs due to halo ICMEs rather than due to non-halo ICMEs.

- The central peak values, full width at half maximum, and their products obtained from Gaussian fits to distributions of different parameters [V_{max}, F_{max}, and E_{max}] due to shock, BDE, MC, and halo ICMEs are larger than those not associated with these structures/features.
- From the best-fit linear relation between averaged GCR-intensity depressions [%] and maximum values of magnetic [F_{max}] and electric fields [E_{max}], we found that GCR intensity decreases at the rate of ≈ 0.40 % per unit increase in vector magnetic field [nT] and ≈ 0.50 % per unit increase in electric field [mV m^{-1}].
- An exponential fit to the recovery of GCR intensity reveals that the characteristic recovery time is much larger for shock/BDE/MC/halo-CME-associated ICMEs than those not associated with these structures/features.
- During recovery, the temporal variation of GCR intensity is found to be better correlated with simultaneous variation in solar-wind speed than other parameters [*e.g.* F and E].
- Speed of ICME-related disturbances appears to be influential in deciding the total recovery time of the depressions.

****

Chapter 3

COSMIC-RAY MODULATION DURING THE PASSAGE OF COROTATING INTERACTION REGIONS (CIRs) AND INTERPLANETARY CORONAL MASS EJECTIONS (ICMEs) AND THEIR COMPARISON

The present chapter deals with the study of cosmic-ray modulation during the passage of ICMEs and corotating interaction regions (CIRs). We compare the cosmic-ray response of ICMEs and CIRs during their passage in near-Earth space. We study the relative importance of various structures/features identified during the passage of ICMEs and CIRs observed during solar cycle 23 (1995 – 2009).

3.1 Introduction

Interplanetary counterparts of coronal mass ejections (ICMEs) and corotating interaction regions (CIRs) are two important large-scale structures in the interplanetary space. During the passage of these structures, decrease in galactic cosmic-ray intensity has been observed both by space borne and ground based cosmic ray instruments with varying amplitudes and time profiles (*e.g.* see reviews, Lockwood, 1971; Iucci *et al.*, 1989; Venkatesan and Badruddin, 1990; Cane, 2000; Kudela, 2013, and references therein).

The ICMEs passing through near-earth space may be associated with a well developed shock and sheath regions in the front or they may be only a flux rope structure moving with different speed. Many studies have been done to understand and model the cosmic-ray decreases during the passage of ICMEs (*e.g.* Badruddin, Yadav, and Yadav, 1986; Iucci *et al.*, 1989; Badruddin, Venketasan, and Zhu, 1991; LeRoux and Potgieter, 1991; Lockwood, Webber, and Debrunner, 1991; Cane and Richardson, 2003; Mavromichalaki *et al.*, 2003; Kudela and Storini, 2005; Singh and Badruddin, 2007a; Usoskin *et al*; 2008; Oh, Yi, and Kim, 2008; Kane, 2010; Yu *et al.*, 2010; Dumbovic *et al.*, 2011; Richardson and Cane, 2011; Arunbabu *et al.*, 2013; Kumar and Badruddin, 2014a).

The CIRs are formed due to interaction of high-speed stream with the slower ambient solar wind. These structures propagating with high speed in space may or may not have a forward shock associated with them. The cosmic-ray depressions during the passage of high-speed streams/CIRs too have been studied experimentally and modelled by researchers from the last many years (*e.g.* Iucci *et al.*, 1979b; Badruddin, 1997; Sabbah, 2000; Singh and Badruddin, 2007b; Dumbovic *et al.*, 2012; Modzelewska and Alania, 2012; Kumar and Badruddin, 2014b).

Most of the earlier studies have been confined to study the nature and sources of transient/Forbush decreases due to ICMEs and corotating depression in cosmic-ray intensity due to CIRs and high-speed solar-wind streams. There have been many efforts to understand the role of individual structures within ICMEs and CIRs, however, there is still lack in the understanding of the underlying physical processes. Since the plasma/field properties at the arrival and during the passage of these distinct structures in ICMEs and CIRs might not be similar, it will be interesting to study the role of these distinct structures in ICMEs and CIRs in influencing the GCR intensity.

The *in situ* plasma and field observations from Advanced Composition Explorer (ACE) and *Wind* spacecraft have been extensively utilized to identify near-Earth ICMEs and CIRs for a continuous period spanning the whole solar cycle 23 (Richardson and Cane, 2010; Jian, Russell, and Luhmann, 2011). A survey of ICMEs and CIRs provides selection criteria and the timings of various distinct features and structures observed during the passage of ICMEs and CIRs (Jian *et al.*, 2006a, b).

The aim of this study is two fold. Firstly, to compare the GCR-effectiveness *i.e.* the ability to depress the GCR intensity (see Kumar and Badruddin, 2014a) of ICMEs and CIRs detected during 1995 – 2009. Secondly, we study the relative importance of various distinct features/structures in ICMEs and in CIRs in influencing the magnitude and time profile of resulting decreases in cosmic-ray intensity. The distinct features/structures identified in shock-associated ICMEs are, the shock/discontinuity followed by the sheath region formed due to compression of ambient plasma and field by the magnetic obstacle, which is basically the CME ejecta which might or might not show the flux rope characteristics depending on the spacecraft trajectory through the ICME (Jian *et al.*, 2006a; Jian, Russell, and Luhmann, 2011). In case of CIRs, the start time, the time of stream interface (formed due to compression of slow wind by high-speed solar wind) as well as end of CIR have been identified. The information is also available whether a CIR is associated with a forward shock or not. Similarly it is also known whether a CIR is associated with reverse shock or not. Discontinuity time, in general coincides with the forward shock time if such shock is associated with CIR. However, in the interplanetary data, sometimes stream interface is also seen as discontinuity (see Jian *et al.*, 2006a, b). We study the influence of CIR as a whole on its arrival, forward shock (when associated), stream interface and the end (passage) of CIR on the amplitude and time profile of GCR intensity depression. In addition, we also search for the interplanetary plasma field parameter(s) that play(s) important role in influencing the amplitude and the time profile of GCR intensity variation during the passage of ICMEs and CIRs.

3.2 Data and Method

We have applied the method of superposed-epoch analysis as discussed in section 2.2.1 of Chapter 2, on cosmic ray as well as interplanetary plasma and field data

utilizing the start time of different ICME/CIR structures as epochs in our analysis. By systematically changing the epochs, one by one, and analyzing the hourly data of GCR intensity and near-simultaneous solar-wind plasma/field data, we have tried to study their role in affecting the GCR intensity on their arrival and during the passage of different regions of distinct plasma/field properties. For ICMEs and CIR data, compiled catalogues of ICMEs and CIRs surveys were utilized (*http://www-ssc.igpp.ucla.edu/~jlan/ACE/Level3/*). The start/end time of various structures/features in ICMEs, such as start of ICME, magnetic obstacle, end time of ICME as well as the time of discontinuity is given in ICME catalogue. In the (Stream Interaction Region) SIR catalogue, start and end time of CIR as well as discontinuity and stream interface timings are given (see Jian *et al.*, 2006a, b for details). We analysed 291 events of ICMEs, out of which 181 are associated with shock. Out of total 416 CIRs events, 76 are associated with forward shock. For cosmic-ray intensity, we have used the neutron monitor data of two locations on the Earth: Oulu (Latitude = 64.05 N, Longitude = 25.47 E, cut-off rigidity R_c = 0.81 GV) and Newark (Latitude = 39.7 N, Longitude = 75.7 W, cut-off rigidity R_c = 2.09 GV). Data for two neutron-monitor stations were utilized to ensure that the observed variations in GCR intensity are not due to any local effects but they are real, with almost similar temporal profiles that differ in amplitude due to different cut-off rigidity of the two locations. The OMNI Web based data (omniweb.gsfc.nasa.gov) of plasma/field parameters, namely, solar-wind velocity [V, km s^{-1}], IMF vector [F, nT], standard deviation of IMF vector [σ_F, nT], the product [FV, mV m^{-1}] which has the dimension of electric field, and [FV^2, mV s^{-1}] which has the dimension of time variation of electric potential, have been utilized in this analysis.

3.3 Results and Discussion

3.3.1 ICMEs and CIRs: Comparison of Cosmic-ray and Plasma/Field Variations

Figure 3.1 shows the superposed-epoch plots of hourly data of galactic cosmic ray (GCR) intensity [$\Delta I/I$, %], solar-wind velocity [V], interplanetary magnetic field (IMF) vector [F], standard deviation of IMF vector [σ_F], the product [FV], and FV^2. These plots show the variations of these parameters 3 days before and 15 days after the start of disturbance due to ICMEs and CIRs observed during 1995 – 2009; zero

hour (epoch) corresponds to arrival time (hour) of ICMEs and CIRs. For comparison, the time variation of different parameters due to ICMEs and CIRs are plotted in the same panel on the same scale. It is observed that there is a large difference in the amplitude and time profiles of GCR-intensity depressions in the two structures; the depression due to ICMEs is much larger compared to the CIRs. Thus the ICMEs are much more GCR-effective than the CIRs (see, Table 3.1). In both the cases, GCR depression starts near the zero hour *i.e.* start time of the associated disturbance. The decrease is faster due to ICMEs than the CIRs. Although GCR intensity recovered to pre-decrease level after few days in case of ICMEs, however, the depression persists for longer time in case of CIRs. These results supports the earlier such studies with smaller data sets (*e.g.* Iucci *et al.*, 1979a; Venkatesan, Shukla, and Agrawal, 1982; Badruddin, 1997; Sabbah, 2000; Singh and Badruddin, 2007b; Kumar and Badruddin, 2014a). Differences in time profiles and amplitudes in various solar-wind parameters, along with GCR intensity are obvious, due to ICMEs and CIRs. Although the enhancements in parameters [F, σ_F] and the derivatives [FV, FV^2] are larger for ICMEs as compared to CIRs, the enhancement in the solar-wind velocity [ΔV] is much higher during the passage of CIRs as compared to ICMEs (Table 3.1). However, the change/increase in velocity in case of ICMEs is sudden at the start of ICME disturbance while the velocity increases slowly to its maximum in case of CIR associated disturbances.

It is known that the ICMEs and CIRs both may or may not be associated with a forward shock. The importance of shocks in the transient modulation of galactic cosmic rays has been highlighted in many earlier studies (*e.g.* see Badruddin, Yadav, and Yadav, 1986; Zhang and Burlaga, 1988; Lockwood, Webber, and Debrunner, 1991; Kudela and Brenkus, 2004; Richardsan and Cane 2011; Kane, 2014; Kumar and Badruddin, 2014a). Therefore, we have compared the effectiveness of ICMEs and CIRs associated with shocks in depressing the GCR intensity with the help of superposed-epoch analysis with respect to arrival of these two groups of interplanetary structures. The results of superposed analysis of GCR intensity and simultaneous interplanetary plasma and field parameters [V, F, σ_F, FV, and FV^2] are plotted in Figure 3.2. We observe that, similar to Figure 3.1, the shock associated ICMEs are much more GCR-effective than the shock-associated CIRs; however,

respective amplitudes in this case are larger as compared to those plotted in Figure 3.1.

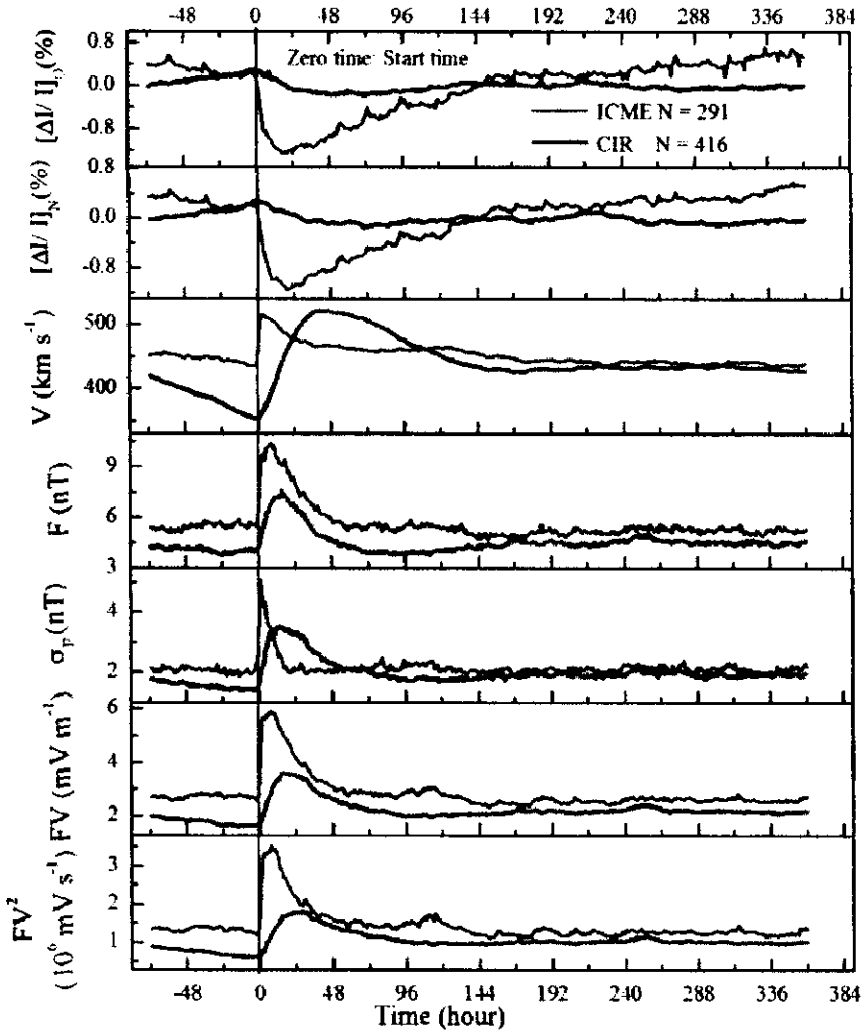

Figure 3.1 The superposed-epoch plots of hourly data of galactic cosmic ray (GCR) intensity at Oulu NM $[\Delta I/I]_O$ (%), GCR intensity at Newark NM $[\Delta I/I]_N$ (%), solar-wind velocity $[V]$, IMF vector $[F]$, standard deviation in IMF vector $[\sigma_F]$, the derivatives $[FV]$ and $[FV^2]$ due to ICMEs and CIRs observed during 1995 – 2009; zero hour (epoch) corresponds to arrival time (hour) of ICMEs and CIRs. N stands for number of events.

The amplitudes of most of the plasma/field parameters [F_{max}, σ_{Fmax}, $(FV)_{max}$, and $(FV^2)_{max}$] are much larger during the shock-associated ICMEs than shock-associated CIRs (see, Table 3.1). We note that most of the initial depression in GCR intensity takes place during first ~ 15 hours for shock-associated ICMEs, where σ_F is also enhanced. This shows the importance of turbulent field region in depressing the GCR intensity, in agreement with previous studies (see, *e.g.* Badruddin, Yadav, and Yadav,

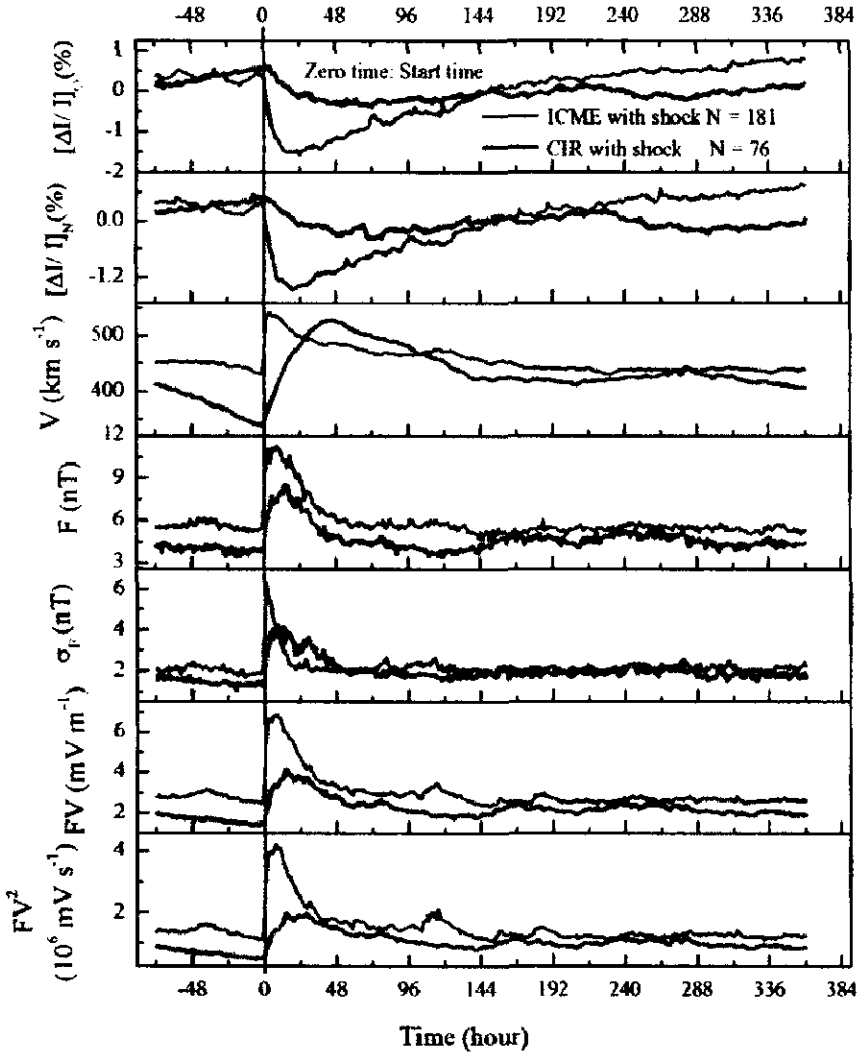

Figure 3.2 The superposed-epoch plots of hourly data of galactic cosmic ray (GCR) intensity at Oulu NM $[\Delta I/I]_O$ (%), GCR intensity at Newark NM $[\Delta I/I]_N$ (%), plasma/field parameters [*V*, *F*, σ_F, *FV*, and FV^2] due to ICMEs and CIRs associated with shocks observed during 1995 – 2009; zero hour (epoch) corresponds to arrival time (hour) of ICMEs and CIRs with shocks. N stands for number of events.

1986; Zhang and Burlaga, 1988; Lockwood, Webber, and Debrunner, 1991; Yu *et al.*, 2010; Kumar and Badruddin, 2014a).

3.3.2 Structures within ICMEs and their Influence

We next study the transient modulation due to ICMEs associated and not-associated with shocks. Considering the start time of these two groups of ICMEs, detected between 1995 and 2009, we perform the superposed-epoch analysis of cosmic-ray intensity data for two neutron monitors, Oulu, and Newark, as well as simultaneous plasma/field parameters (Figure 3.3). The figure shows that shock-associated ICMEs

are more GCR-effective than those not associated with shocks. These results concur with the earlier findings (see, *e.g.* Kumar and Badruddin, 2014a, and references therein) emphasizing the importance of shock/sheath region in modulating the GCR intensity. As expected, the amplitude of GCR-intensity decrease is smaller due to ICMEs without shocks. As regards the time profiles, there is similarity in both the cases. However, the initial start due to no-shock ICMEs is expected to be more gradual. This observed time behaviour is probably a statistical effect. Enhancements in various parameters [V, F, σ_F, FV, and FV^2] are much larger due to shock-associated

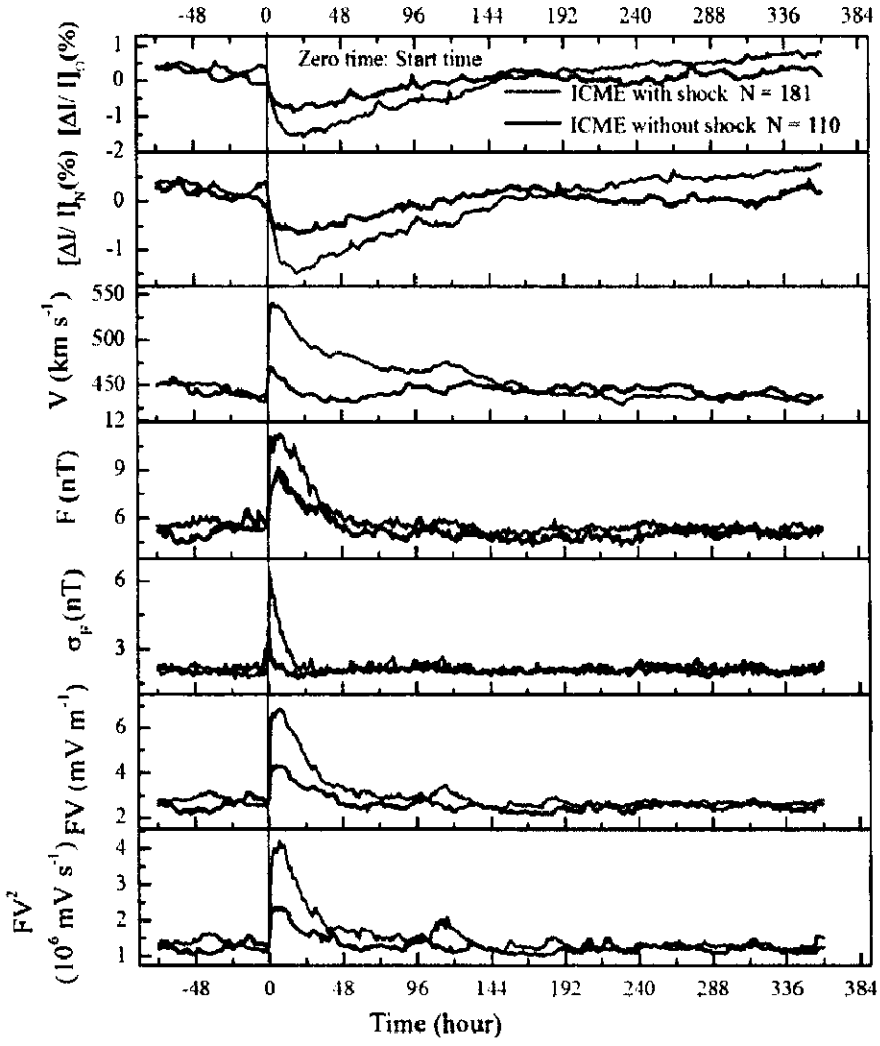

Figure 3.3 The superposed-epoch plots of hourly data of galactic cosmic ray (GCR) intensity at Oulu NM $[\Delta I/I]_O$ (%), GCR intensity at Newark NM $[\Delta I/I]_N$ (%), plasma/field parameters [V, F, σ_F, FV, and FV^2] due to ICMEs associated with/without shocks observed during 1995 – 2009; zero hour (epoch) corresponds to arrival time (hour) of ICMEs associated with/without shocks. N stands for number of events.

Table 3.1 Average GCR intensity decrease [ΔI, %] at Oulu and Newark neutron monitors, peak values of plasma/field parameters [V_{max}, F_{max}, $(\sigma_F)_{max}$, $(FV)_{max}$, and $(FV^2)_{max}$] and enhancements in these parameters [ΔV, ΔF, $\Delta\sigma_F$, $\Delta(FV)$, and $\Delta(FV^2)$] due to ICMEs and CIRs detected during 1995 – 2009. Zero hour corresponds to start time of particular event.

Interplanetary structure/group	No	ΔI (Oulu) [%]	ΔI (Newark) [%]	V_{max} [km s^{-1}]	ΔV [km s^{-1}]	F_{max} [nT]	ΔF [nT]	$(\sigma_F)_{max}$ [nT]	$\Delta\sigma_F$ [nT]	$(FV)_{max}$ [mVm^{-1}]	$\Delta(FV)$ [mV m^{-1}]	$(FV^2)_{max}$ [mV s^{-1}]	$\Delta(FV^2)$ [mV s^{-1}]
ICMEs	291	1.49	1.37	514	79	10.42	4.94	5.09	3.09	5.90	3.36	3.54	2.38
CIRs	416	0.48	0.45	520	168	7.61	3.67	3.54	2.18	3.61	2.02	1.80	1.21
ICME with shocks	181	2.07	1.90	542	110	11.31	6.10	6.36	4.52	6.87	4.40	4.24	3.13
CIR with shocks	76	0.99	0.89	527	188	8.56	4.85	4.23	3.00	4.15	2.77	1.98	1.47
ICMEs with shocks	181	2.07	1.90	542	110	11.31	6.10	6.36	4.52	6.87	4.40	4.24	3.13
ICMEs without shocks	110	0.91	0.80	470	34	9.19	3.74	3.90	1.89	4.31	1.68	2.39	1.19
Shock-associated ICMEs with start time and MO time same	22	1.80	2.18	509	62	12.78	8.39	4.62	2.96	6.98	4.25	3.88	2.70
Shock-associated ICMEs with time and MO time different	87	2.32	1.82	551	124	12.51	7.60	6.80	5.07	7.90	5.58	5.14	4.10
CIR with forward shocks	76	0.99	0.89	527	188	8.56	4.85	4.23	3.00	4.15	2.77	1.98	1.47
CIR without forward shocks	296	0.41	0.37	514	158	7.42	3.42	3.43	2.05	3.49	1.84	1.78	1.16

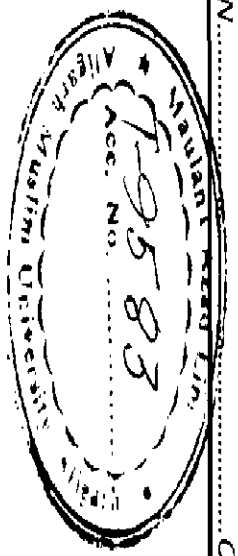

ICMEs than those not associated with shocks (Table 3.1). These are the average values of plasma/field parameters obtained from the superposed plots in Figure 3.3. To confirm that the difference between ICMEs associated with and without shocks observed with superposed-epoch analysis is not due to some extreme events, but rather come from the general behavior of ICMEs associated/not associated with shocks, we have studied the frequency distribution of these plasma/field parameters (*e.g.* V_{max}, F_{max}, σ_{Fmax}, $(FV)_{max}$, $(FV^2)_{max}$, and cosmic-ray decrease (Forbush decrease) during the passage of ICMEs associated/not associated with shocks, by making suitable groups of amplitudes of various parameters. We also applied the Gaussian fit over the histograms to see quantitative differences in central peak values and the spread in the distribution. For each parameter we use equidistant bins of suitable range so that all the distributions consist of comparable number of bins (7 to 10 bins). We use equidistant bins of 100 km s^{-1} for speed, 5 nT for IMF, 1 nT for SD of IMF, 2.5 mV m^{-1} for FV, 2 mV s^{-1} for FV^2, and 0.5 % for GCR intensity decrease. These distribution for the amplitude, i) V_{max}, ii) F_{max}, iii) $(FV)_{max}$, iv) $(\sigma_F)_{max}$, v) $(FV^2)_{max}$, and vi) GCR-intensity decrease are plotted in Figure 3.4. Difference between distributions of shock-associated ICMEs and those not associated with a shock, for all parameters, can be seen from these plots; the distribution for shock-associated ICMEs is shifted towards higher values in almost all these distributions. Further, the shift in peaks of Gaussian fitted curves in these plots, toward higher values for shock-associated ICMEs is also seen.

Having confirmed the importance of shock-associated ICMEs, we next consider only these ICMEs. From the ICME survey/catalogues we note that for some of the shock-associated ICMEs, magnetic obstacle (*i.e.* ejecta) and ICME start time is same while in some others ICME start time is earlier than magnetic obstacle (MO) arrival time (see Jian *et al.*, 2006a for details about 'magnetic obstacle' and its identification). The former category of ICMEs appear to have forward shock just in front of MO without sheath region while the later category of ICMEs have forward shock followed by a sheath region and then the MO or ejecta.

To study the differences in the GCR-effectiveness of these two groups of ICMEs, *i.e.*, (a) when start time and MO time is same and (b) when start time and MO time is different, we have plotted the superposed-epoch plots with respect to start time of these two groups of ICMEs (Figure 3.5). We observe that in case of both groups of

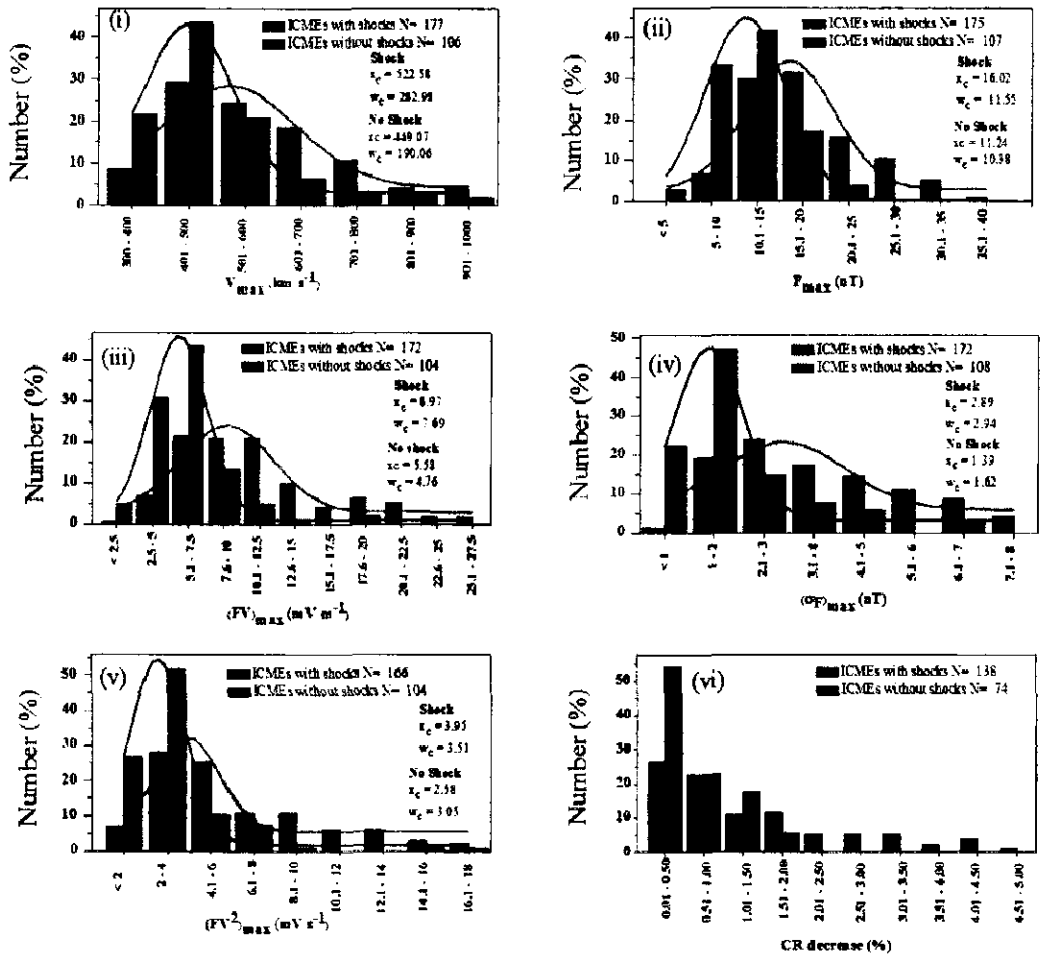

Figure 3.4 Frequency distribution of i) maximum speed, [V_{max}, km s^{-1}], ii) maximum IMF vector, [F_{max}, nT], iii) maximum electric field, [FV_{max}, mV m^{-1}], iv) maximum standard deviation in IMF vector, [σ_{Fmax}, nT], iv) maximum [FV^2_{max}, mV s^{-1}], and (vi) CR decrease observed during the passage of ICMEs associated/not associated with shocks. Gaussian best fit curves representing the distribution of ICMEs are also shown in the first five panel of figure. The central peak values x_c, and full width at half maxima w_c obtained from the fits are also given. N stands for number of events considered for each histogram.

ICMEs the GCR intensity decrease starts at the start time but, in case of later group (b) ICMEs, the amplitude is larger (see Table 3.1), the initial decrease is faster, and the minimum GCR intensity is observed earlier as compared in case of group (a) ICMEs. However, somewhat higher amplitude at Newark as compared to that at Oulu due to group (a) ICMEs is unexpected, as Newark cut-off rigidity is higher. Next we set MO time as the zero (epoch) in the superposed plots of GCR intensity and plasma/field parameters in both the cases *i.e.* when (a) the ICME start time is same as that of magnetic obstacle, and (b) when start of disturbance and magnetic obstacle

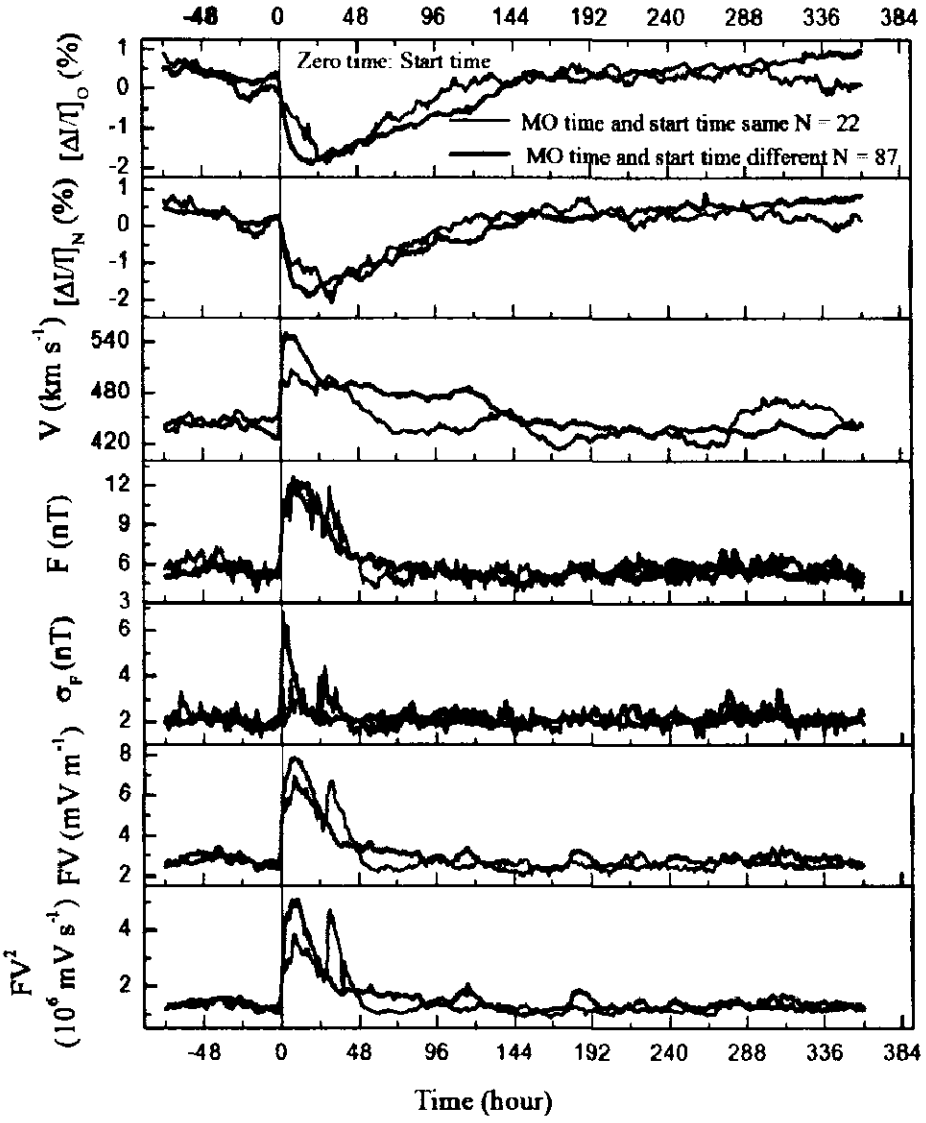

Figure 3.5 The superposed-epoch plots of hourly data of galactic cosmic ray (GCR) intensity at Oulu NM $[\Delta I/I]_O$ (%), GCR intensity at Newark NM $[\Delta I/I]_N$ (%), plasma/field parameters [V, F, σ_F, FV, and FV^2] due to ICMEs associated with shocks observed during 1995 - 2009; zero hour (epoch) corresponds to time (hour) of shock arriving at same/different time as Magnetic Obstacle (ejecta). N stands for number of events.

time is different. These plots are shown in Figure 3.6. We see that due to the later group of shock associated ICMEs depression starts before the arrival of MO (ejecta) and two-step decreases may be due to such ICMEs, the second step likely to take place at the time of MO (ejecta) and the first step during passage of shock/sheath region (see, Cane, 2000). The time profiles of F and σ_F support this conclusion; F and

σ_F both are high during the passage of shock/sheath region while only F is enhanced for several hours after the MO time.

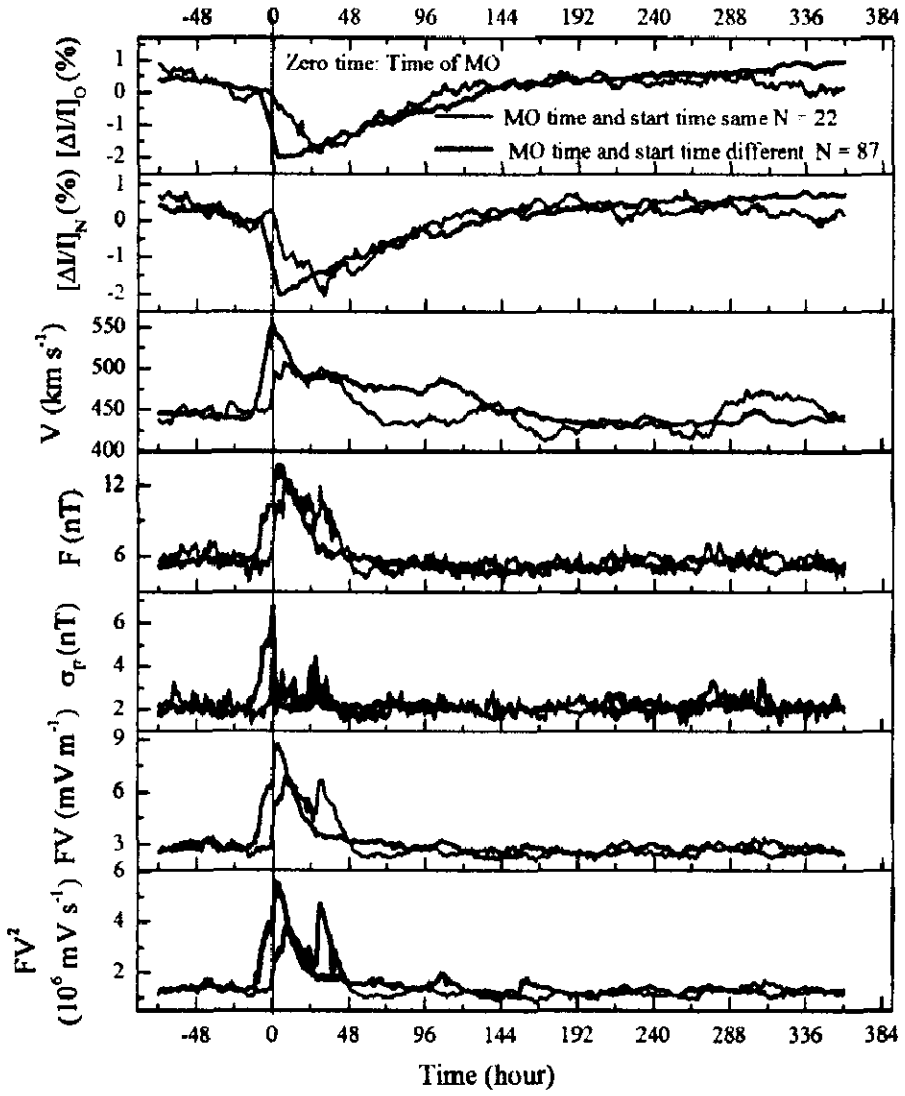

Figure 3.6 The superposed-epoch plots of hourly data of galactic cosmic ray (GCR) intensity at Oulu NM $[\Delta I/I]_O$ (%), GCR intensity at Newark NM $[\Delta I/I]_N$ (%), plasma/field parameters [V, F, σ_F, FV, and FV^2] due to ICMEs associated with shocks observed during 1995 – 2009; zero hour (epoch) corresponds to time (hour) of Magnetic Obstacle (ejecta) arriving at same/different time as shocks. N stands for number of events.

The next observable feature in ICMEs is the end time of ICME, both in the ICMEs associated and those not associated with the shocks. We are interested to see whether GCR recovery starts at the end of ICME structure or at some later/earlier time. To study this, we have taken the end time of ICMEs as the epoch (zero hour) for the two ICME groups, (a) associated and (b) not associated with shocks. We observe (see

Figure 3.7) that the recovery generally starts few hours before the passage of the rear part of ICMEs.

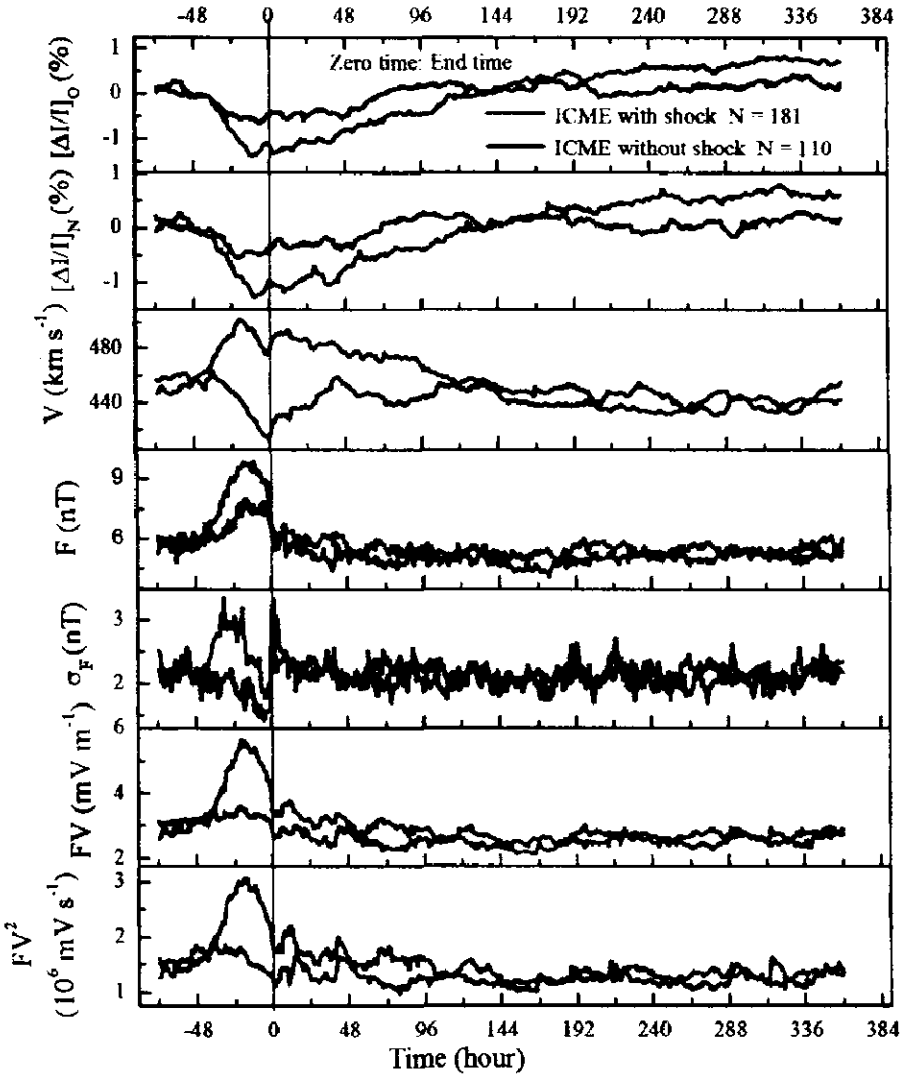

Figure 3.7 The superposed-epoch plots of hourly data of galactic cosmic ray (GCR) intensity at Oulu NM $[\Delta I/I]_O$ (%), GCR intensity at Newark NM $[\Delta I/I]_O$ (%), plasma/field parameters [V, F, σ_F, FV, and FV^2] due to ICMEs associated with/without shocks observed during 1995 - 2009; zero hour (epoch) corresponds to end time (hour) of ICMEs associated with/without shocks. N stands for number of events.

It may, however, be noted that apart from its usefulness in several areas of space research and other disciplines (see, Singh and Badruddin, 2006), superposed-epoch analysis has its limitation also. The fine substructures will be smeared out unless one chooses zero epoch wisely. For example, we can study the start of the shock/sheath region by choosing its timing as zero epoch, however, then the information about

ejecta start is lost. On the other hand, if we choose the ejecta start as the zero epoch, we can look at the ejecta substructure separately.

3.3.3 Structures within CIRs and their Influence

We have studied the effects of two groups of CIRs *i.e.* (a) CIRs with forward shock, and (b) CIRs without forward shock. We performed superposed-epoch analysis of GCR intensity and plasma/field parameters [V, F, σ_F, FV, and FV^2] with respect to start time of these two groups of CIRs (Figure 3.8). We find a large difference in amplitude of depression in GCR intensity (Table 3.1) due to CIRs with shock and CIRs without shocks; the former group of CIRs being more GCR effective than the later group although the recovery time profile in both the cases is almost similar.

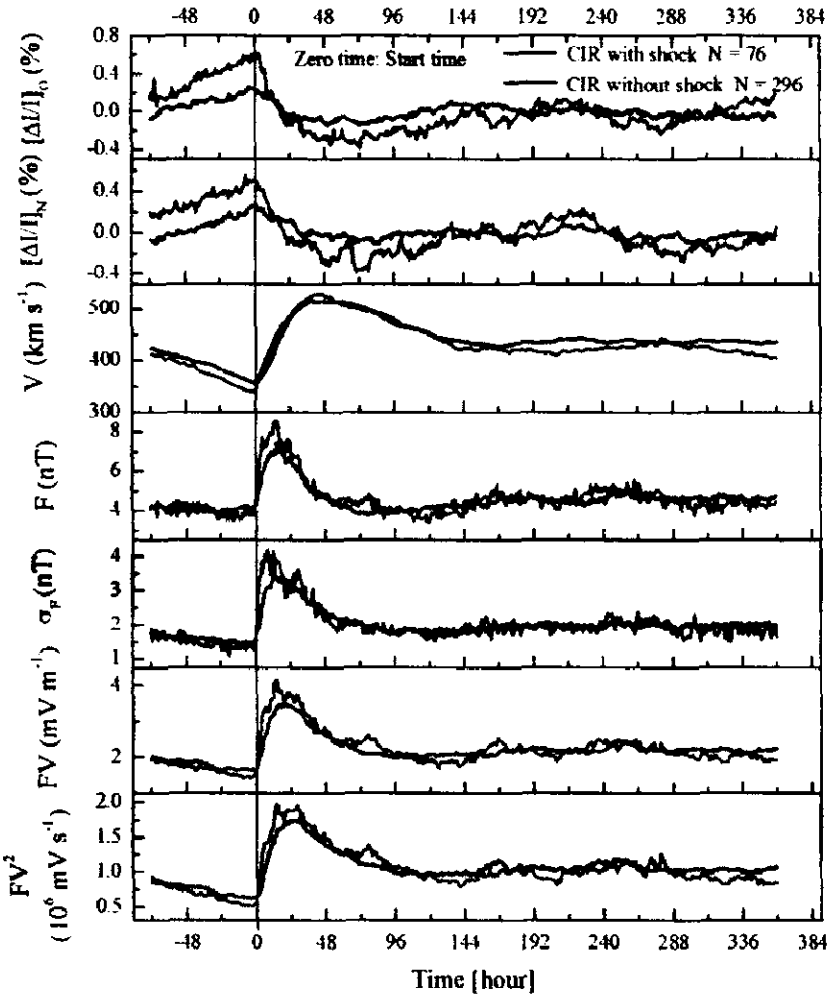

Figure 3.8 The superposed-epoch plots of hourly data of galactic cosmic ray (GCR) intensity at Oulu NM $[\Delta I/I]_O$ (%), GCR intensity at Newark NM $[\Delta I/I]_N$ (%), plasma/field parameters [V, F, σ_F, FV, and FV^2] due to CIRs associated with/without shocks observed during 1995 - 2009; zero hour (epoch) corresponds to arrival time (hour) of CIRs associated with/without shocks. N stands for number of events.

Enhancements in the average plasma/field parameters are somewhat larger (Table 3.1) and more fluctuating in case of CIRs with shocks (see Figure 3.8).

In addition, we also studied the distribution of parameters [V_{max}, F_{max}, $(FV)_{max}$, $(\sigma_F)_{max}$, and $(FV^2)_{max}$] during the passage of these two types of CIRs (Figure 3.9). Although the distributions in two cases look similar, the Guassian fitted central peak values (x_c) are higher specially for F_{max}, $(FV)_{max}$, and $(\sigma_F)_{max}$ in case of CIRs with shocks (see the values of x_c given in Figure 3.9).

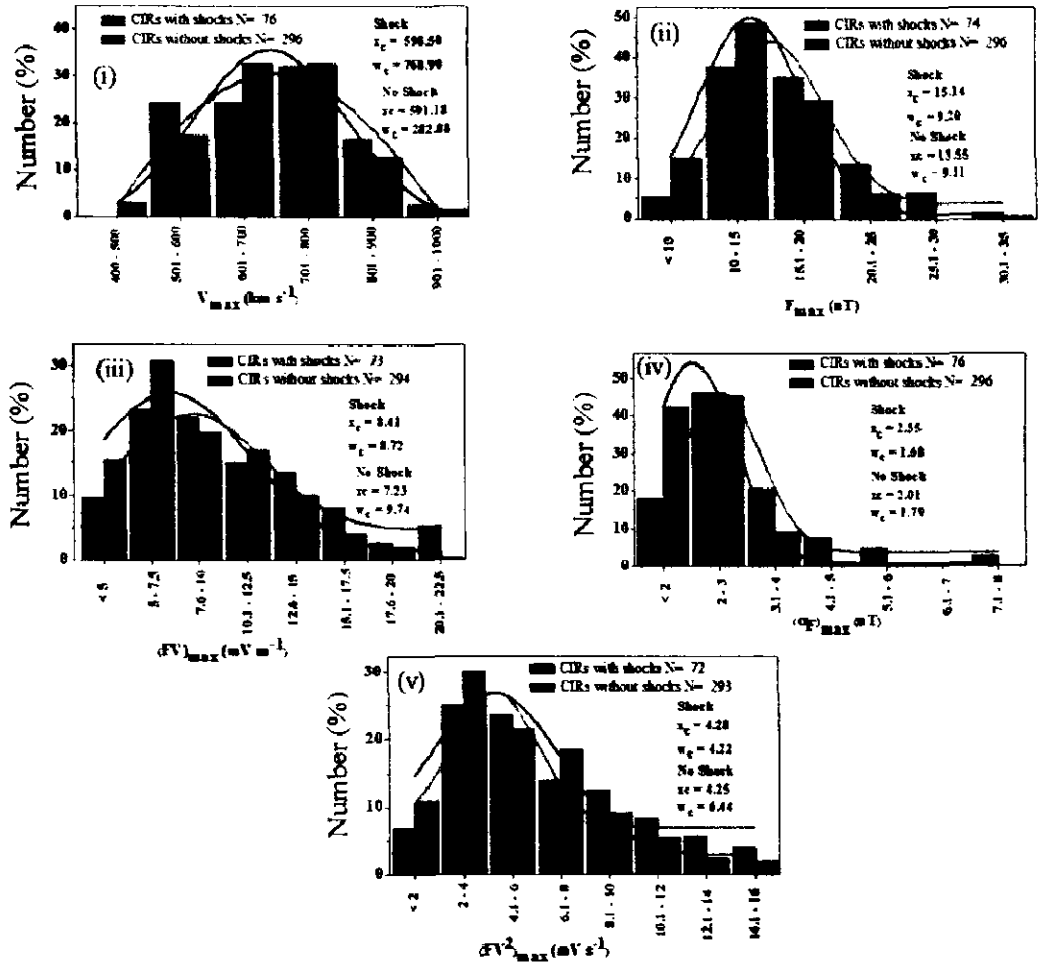

Figure 3.9 Frequency distribution of i) maximum speed, [V_{max}, km s^{-1}], ii) maximum IMF vector, [F_{max}, nT], iii) maximum electric field, [FV_{max}, mV m^{-1}], iv) standard deviation in IMF vector, [σ_{Fmax}, nT], and v) maximum [FV^2_{max}, mV s^{-1}] observed during the passage of CIRs associated/not associated with shocks. Gaussian best fit curves representing the distribution of CIRs are also shown in the figure. The central peak values x_c, and full width at half maxima ω_c obtained from the fits are also given. N stands for number of events considered for each histogram.

A stream interface (SI) can be identified within CIRs. At the SI, field fluctuations are expected to be high. Therefore, it will be interesting to search for the role of SI in influencing the GCR-intensity time profile. For this purpose, we first divided the CIRs, into two groups, (i) CIRs with shocks and (ii) CIRs without shock and then applied the method of superposed- epoch analysis to cosmic ray and plasma/field data with reference to SI time, separately for two groups of CIRs. We note that the depression in GCR intensity starts earlier than zero time, and reaches the minimum value after the SI arrival. The enhancements in interplanetary parameters at this time are also visible in superposed plots (Figure 3.10).

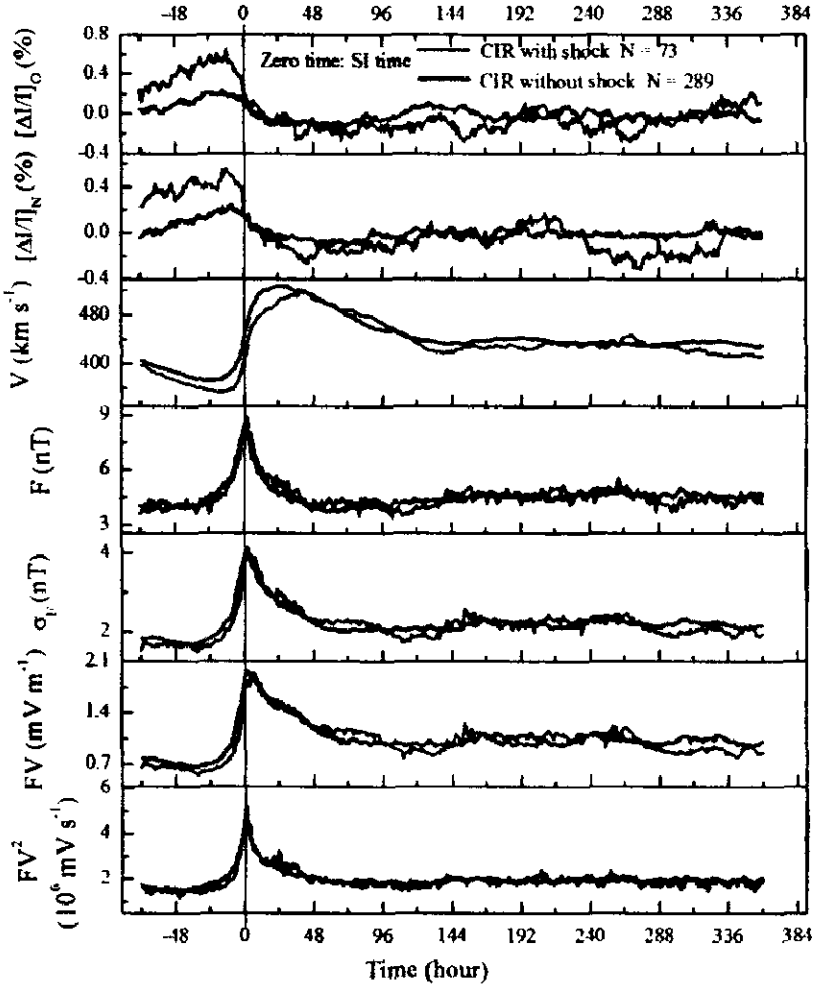

Figure 3.10 The superposed-epoch plots of hourly data of galactic cosmic ray (GCR) intensity at Oulu NM $[\Delta I/I]_O$ (%), GCR intensity at Newark NM $[\Delta I/I]_N$ (%), plasma/field parameters [V, F, σ_F, FV, and FV^2] due to CIRs associated with/without shocks observed during 1995 - 2009; zero hour (epoch) corresponds to stream interface (SI) time (hour) of CIRs associated with/without shocks. N stands for number of events.

It indicates that the SI contributes to the modulation of galactic cosmic rays during the passage of CIRs, although the depression starts earlier at the arrival of CIRs.

To see if the depression in GCR intensity that usually starts at the arrival of CIR persists after its passage for some time or it starts recovering, we have considered two groups of CIRs *i.e.* CIRs with forward shock and CIRs without forward shocks. Then the superposed-epoch analysis is done by arranging the data with respect to end time of two groups of CIRs separately (see Figure 3.11). We observe that in both the cases, the GCR recovery starts a few hours after passage of CIRs, although slowly, especially in the case of CIR, with forward shock.

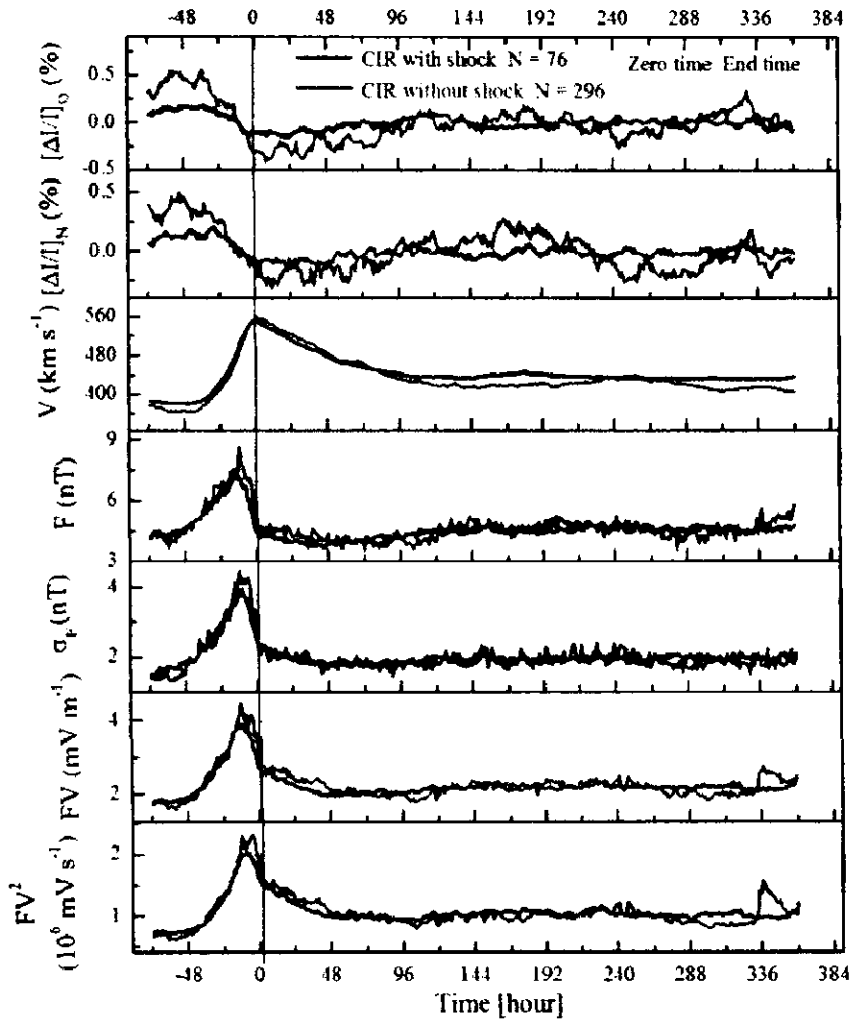

Figure 3.11 The superposed-epoch plots of hourly data of galactic cosmic ray (GCR) intensity at Oulu NM $[\Delta I/I]_O$ (%), GCR intensity at Newark NM $[\Delta I/I]_N$ (%), plasma/field parameters [*V*, *F*, σ_F, *FV*, and FV^2] due to CIRs associated with/without shocks observed during 1995 - 2009; zero hour (epoch) corresponds to end time (hour) of CIRs associated with/without shocks. N stands for number of events.

From the superposed-epoch plots of various parameters shown in some of the plotted figures (Figures, 3.1, 3.2, 3.3, and 3.8), we have determined the durations of main phases and recovery phases (Table 3.2). From these averaged plots, the duration of main phases (start to minimum) due to, (a) shock-associated ICMEs is 18 hours, (b) ICMEs without shocks (20 hours), (c) CIRs with shock (52 hours), (d) CIRs without shocks (56 hours). The corresponding duration of recovery phase is 172 hour (~ 7 days) for ICME with shock and 95 hours (~ 4 days) for ICMEs without shock. However, in case of CIRs, both with and without shocks, the exact duration of recovery phase could not be determined since the intensity does not recover to its pre-decrease level within the chosen time-interval. Although the main phase durations of individual Forbush decreases (FDs) may vary, average main phase duration of FDs was estimated to be 13 ± 4.5 hours (Oh, Yi, and Kim, 2008). Superposed-epoch analysis of cosmic-ray data with respect to magnetic clouds has shown the main phase duration to be ~ 21 – 24 hours (Singh and Badruddin, 2007b). Results of our superposed-epoch analysis regarding main phase durations *i.e.* 18 hours for shock-associated ICMEs and 20 hours for no-shock ICMEs are in reasonable agreement with these earlier findings. The recovery of FDs may also vary (~ 3 to ~10 days) with an average time of ~ 5 days (*e.g.* Lockwood, Webber, and Jokipii, 1986; Cane, Richardson, and von Rosenvinge, 1996; Cane, 2000). The results of our study based on the superposed-epoch analysis compliment these findings. It further indicates that recovery duration may be, in general, shorter due to ICMEs not associated with shocks and larger due to shock-associated ICMEs. Depressions due to CIRs are, in general, slower and take longer time than those due to ICMEs. Most of the earlier studies are limited to the study of individual/average depressions due to CIRs/high-speed streams and obtained many interesting results about their time history, their association with plasma/field parameters (*e.g.* see Richardson, 2004, and references therein). However, we study these aspects by separating them into two groups *i.e.* those associated and not associated with shocks and studied differences in their effects.

In addition to differences in durations and time profiles of main phase due to ICMEs and CIRs, we observe, on the average basis, that the GCR-intensity depression due to ICMEs with shock is ~ 2.5 times higher than that due to ICMEs without

shocks. Similarly CIRs with shocks produced ~ 2.4 times more depression in GCR intensity than CIRs without shocks. When we compare shock effects in ICMEs and CIRs, we observe that ICMEs with shocks are twice as GCR-effective as compared to shock-associated CIRs. The same ratio approximately holds for no shock ICMEs and CIRs. Thus it appears that the shock/sheath effect is not similarly GCR-effective for both ICMEs and CIRs. Richardson and Cane (2011) compared the shock effect to the total depression in GCR intensity. They observed that, although there are large event-to-event variations in the shock and ICME contributions to total depression, however, on the average the size of shock effect in ICMEs is ~ 55% of the total change. It implies that the shock and the ICME effects are almost equal on the average. Our results concur with these results, which show that the shock-associated ICMEs are about twice as GCR-effective as compared the ICMEs without shocks.

From these averaged (superposed epoch) plots, we have tried to find the plasma/field parameters whose time variation best correlates with the time variation of GCR intensity, separately during main and recovery phases due to ICMEs and CIRs. Table 3.2 shows the value of simple Pearson's correlation coefficients [R]. We find that out of the parameters considered, the time variation of IMF vector [F] best correlates the GCR intensity during main phase while it is the time variation of velocity [V] that best correlates the time variation of GCR intensity during recovery, due to ICMEs with shock as well as ICMEs without shock. However, it is the time variation of velocity [V] that best correlates with the time variation of GCR intensity both during main as well as recovery phases due to CIRs with and without shocks (see Table 3.2).

Depression in GCR intensity during Forbush decreases being correlated with magnetic field strength have been reported earlier also (*e.g.* Cane, 1993; Dumbovic *et al.*, 2011; Kumar and Badruddin, 2014a). Cane (1993) reported a good correlation between FD amplitude and maximum magnetic field in magnetic clouds. Dumbovic *et al.* (2011) concluded that the field strength B strongly influences FD. Kumar and Badruddin (2014a) have found that depression in GCR intensity is related to amplitude of the interplanetary field vector during passage of ICMEs with different features. The modulation of cosmic-ray intensity in CIR associated high-speed solar wind streams related to the solar-wind speed increase have been reported (*e.g.* Iucci *et*

Table 3.2 Linear simple Pearson correlation coefficients [R] obtained from the linear fit between the temporal variation of decrease in the GCR intensity and related plasma/field parameters [V, F, σ_F, FV, and FV^2] during the main and recovery phases of intensity-depression due to ICMEs and CIRs associated with/without shocks. Durations of the main phase and recovery phase are also given.

Interplanetary structure/group	Duration of main phase [hrs]	Duration of recovery phase [hrs]	Value of Correlation coefficients [R] between GCR intensity and various parameters									
			During main phase					During recovery phase				
			V	F	σ_F	FV	FV^2	V	F	σ_F	FV	FV^2
ICMEs	19	153	-0.59	-0.75	0.41	-0.68	-0.65	-0.87	-0.80	-0.02	-0.83	-0.82
CIRs	51	-	-0.98	0.26	0.03	-0.35	-0.72	-0.77	0.39	-0.25	-0.24	-0.61
ICME with shock	18	215	-0.64	-0.68	0.20	-0.61	-0.55	-0.97	-0.72	-0.19	-0.84	-0.83
ICME without shock	20	95	-0.66	-0.71	0.26	-0.68	-0.65	-0.93	-0.76	0.29	-0.78	-0.73
CIR with shock	52	-	-0.97	0.58	0.68	0.12	-0.47	-0.87	0.20	-0.03	-0.39	-0.66
CIR without Shock	56	-	-0.98	0.03	-0.27	-0.51	-0.78	-0.82	0.45	-0.49	-0.31	-0.56

al., 1979b; Badruddin, 1997; Richardson, Wibberenz, and Cane, 1996; Richardson, Cane, and Wibberenz, 1999; Kumar and Badruddin, 2014b). Iucci *et al.* (1979b) reported that these depressions follow the changes in the solar-wind velocity. Richardson, Wibberenz, and Cane (1996) also found that high-speed streams are accompanied by depressions in GCR intensity and tend to be anti-correlated with the solar-wind speed (see also, Richardsan, Cane, and Wibberenz, 1999; Singh and Badruddin 2007b; Kumar and Badruddin, 2014b). Although these studies were able to clarify many aspects of modulation due to CIRs and high-speed streams, this chapter studies the effects of CIRs with larger data base by separating them in two groups *i.e.* those associated and non-associated with forward shock. We have also studied the role of different features of CIRs, *e.g.* forward shocks and stream interaction regions on the amplitude and time profile of GCR intensity depression.

3.4 Summary and Conclusions

Based on our analysis of the cosmic-ray intensity together with interplanetary plasma and field parameters during the passage of ICMEs and CIRs of solar cycle 23 (1995 – 2009), a summary of our conclusions is given below.

- In agreement with earlier findings, ICMEs are found to be more effective in modulating the GCR intensity as compared to CIRs, even though the enhancements in solar-wind velocity due to CIRs is larger than the enhance ements in solar-wind velocity due to CIRs is larger than the enhancement due to ICMEs. However, the average amplitudes of interplanetary magnetic and electric field vectors are larger during the passage of ICMEs. In addition to amplitudes, the time profiles of GCR intensity depressions are also different due to these two interplanetary structures in agreement with earlier findings.
- The average amplitude of GCR intensity depression for ICMEs is ~ 1.5% as compared for CIRs which is ~ 0.5%. The ratio of GCR depressions for ICMEs with shock to ICMEs without shock is about 2.5, and the ratio of intensity depression due to shock-associated CIRs to non-shock CIRs is also nearly the same.

- The GCR intensity depression in general starts at the arrival of ICMEs, whether associated with shocks or not; however depression is much larger due to shock-associated ICMEs in agreement with previous studies, emphasizing the importance of shock/sheath region in transient modulation of GCRs.
- The GCR recovery, after initial phase of intensity decrease, starts before the passage of the rear part of the ICME.
- The CIRs with forward shock are more effective in depressing the GCR intensity than those not associated with shock although the time profiles of GCR intensity in two cases are almost similar; slow depression to a minimum and a long and slow recovery.
- At the arrival of stream interface within CIRs, a further decrease in GCR intensity generally to takes place.
- From the average plots obtained from superposed-epoch analysis, the time variation of GCR intensity due to ICMEs, during the main (decrease) phase, is found to be better correlated with time variation of magnetic field vector. However time variation of solar-wind velocity better correlates with GCR intensity during this phase, in case of decrease due to CIRs. During the recovery phase, the temporal variation of GCR intensity is found to be better correlated with simultaneous variations in solar-wind velocity, during the recovery of decrease both due to ICMEs as well CIRs. These results provide further support to earlier results who reported good correlation between amplitude of GCR intensity decrease and interplanetary magnetic field strength during Forbush decreases. Further it also concurs with the decrease in intensity associated with increase in solar-wind velocity during corotating depression in GCR intensity
- The amplitude of depression is maximum for the case of shock-associated ICMEs, a fast-decrease starts at the start and minimum intensity is reached within ~ 18 hours. Sudden enhancement in F and σ_F at start time and σ_F remaining enhanced till about the same duration emphasizing the important role of enhanced and turbulent magnetic field in such decreases through the scattering of cosmic rays by the enhanced and turbulent field region.

****

Chapter 4

SHORT TERM MODULATION OF COSMIC-RAY INTENSITY ASSOCIATED WITH HIGH-SPEED SOLAR-WIND STREAMS

This chapter puts forward the results of cosmic-ray modulation due to high-speed solar-wind streams of different sources, speed, and duration which are identified in the solar wind. The influence of speed, duration, and solar sources of the streams on the GCR modulation is presented. The relative importance of different solar-wind parameters in the modulation process is also discussed in this chapter. We also studied the influence of individual streams in modulating the GCR intensity by grouping them into suitable GCR-effective groups of increasing range of GCR-intensity depressions produced by them.

4.1 Introduction

The continuous flow of the ambient solar wind is often overlaid by faster streams, as is evident from observations of the solar plasma in space. These so called high-speed solar-wind streams are recognized as those ejected from solar active regions during coronal mass ejections (CMEs) and those coming from diverging and unipolar-field regions called coronal holes (CH). As a consequence, there are two classes of interplanetary structures related to two types of magnetic-field topology on the Sun, *i.e.* interplanetary coronal mass ejections (ICMEs) and corotating interaction region (CIRs) (*e.g.* Gosling, 1996; Gopalswamy, 2006; Jian *et al.*, 2006a, 2006b). Both the ICMEs and the CIRs are capable of driving shocks in the interplanetary space due to interaction between high-speed CME/CH-streams and ambient solar wind.

Solar-terrestrial effects due to interplanetary structures and streams associated with ICMEs and CH have been a subject of considerable interest and studied extensively. In particular, corotating depressions (*e.g.* Iucci *et al.*, 1979b; Badruddin, 1997; Richardson, Cane, and Wibberenz 1999; Singh and Badruddin, 2007a; Gupta and Badruddin, 2009; Sabhah and Kudela, 2011; Modzelevska and Alania, 2012, and references therein) and Forbush decreases in cosmic-ray intensity (*e.g.* Lockwood, 1971; Badruddin, Yadav, and Yadav, 1986; Badruddin, Venkatesan, and Zhu, 1991; Venkatesan and Badruddin, 1990; LeRoux and Potgieter, 1995; Lockwood, Webber and Debrunner, 1991; Cane, 2000; Kudela and Storini, 2005; Singh and Badruddin, 2007b; Oh, Yi, and Kim, 2008; Subramanian *et al.*, 2009; Yu *et al.*, 2010; Richardson and Cane, 2011; Dumbovic *et al.*, 2012; Kumar and Badruddin, 2014a, and references therein) have been studied extensively in the past. However, in addition to isolated Forbush decreases and corotating depressions in cosmic-ray intensity, long-lived and multiple-step cosmic-ray depressions (*e.g.* Kane, 1977; Kudela and Brenkus, 2004; Badruddin, 2006) have also been observed in ground-based cosmic-ray intensity measurements. It is, therefore, important to search for solar sources, interplanetary causes, and physical mechanisms responsible for depressions in GCR intensity with different shape, size, and time profile.

It is recognized that the variations in cosmic-ray intensity observed on the ground and in the interplanetary space, at various time scales, are due to fields and flows coming from the Sun. However, these flows and fields, especially those with high speed ($\geq$ 400 km s^{-1}) as observed in near-Earth and interplanetary space, have a wide

range of speeds extending up to more than 1000 km s^{-1}. The duration of these flows and fields varies from ≈ 2 to 20 days. These streams may be due to different solar sources, *e.g.* i) a coronal hole, ii) a CME, iii) multiple coronal holes, iv) multiple CMEs, or v) compound streams due to coronal hole(s) and CME(s). The streams of i) different speed, ii) different duration, and iii) associated with different solar/interplanetary structures are likely to exhibit different responses in cosmic-ray intensity variations, both in amplitude and time profile.

Thus, in this chapter, we study the response of high-speed solar-wind streams of different speed, duration, and sources on the modulation of galactic cosmic rays. We also investigate the solar sources, interplanetary causes, and physical mechanisms responsible for GCR-intensity decreases of different amplitude, duration, and time profile, such as the so-called Forbush decreases, corotating decreases, long-lived, and multiple-dip cosmic-ray decreases.

4.2 Data and Analysis

High-speed solar-wind streams for the period 1996 – 2007 have been identified using the OMNI Web data base (omniweb.gsfc.nasa.gov) and tabulated giving information about some important parameters of the streams (see electronic supplement table in Gupta and Badruddin, 2010). We prepared a catalog for the extended period (2008 – 2011) based on the criteria adopted by Gupta and Badruddin (2010) [see Table 4.1]. To illustrate the parameters and symbols of this table, a typical compound stream is plotted (see Figure 4.1) along with the cosmic-ray intensity variations observed at the Oulu and Hermanus neutron monitors during the passage of the stream. To calculate $\Delta I/I$ [%], plotted in the top two panels, hourly counts were first averaged for the complete plotted period [x]. Then for each hour's count rate [x_i], the value $\frac{xi - x}{x}$ [%] is calculated and plotted as $\Delta I/I$ [%] as discussed in Chapter 2 in the section Data Analysis.

The two catalogs (see electronic supplementary material in Gupta and Badruddin (2010) and Table 4.1) together list 16 years of high-speed stream (HSS) data, which covers the complete solar cycle 23, the deep solar minimum between solar cycles 23 and 24, and some of the (increasing) portion of solar cycle 24. We used these

tabulated HSS of different speed, durations, and solar sources to study their effectiveness in modulating galactic cosmic rays.

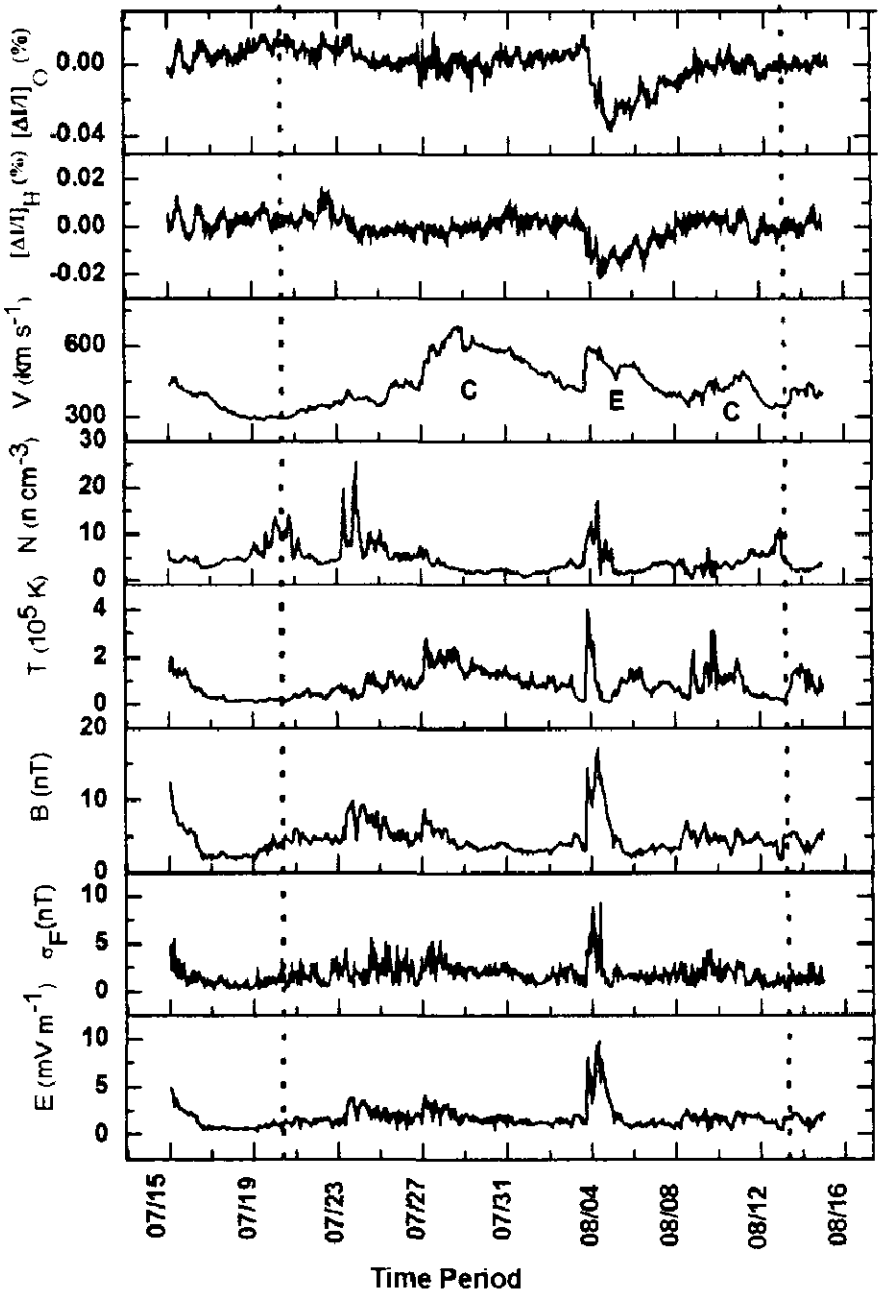

Figure 4.1 A typical compound high-speed stream caused by two coronal-hole associated streams (C) and a CME associated stream (E) observed between UT: 14:00, 20 July 2010 to UT 14:00, 12 August 2010. The dotted vertical lines on the left and right are the start and end times of the stream. We plot the temporal variation of various parameters: GCR-intensity variation recorded by Oulu neutron monitor $[\Delta I/I]_O$ (%), and Hermanus neutron monitor $[\Delta I/I]_H$ (%), the solar-wind velocity [V, km s^{-1}], plasma density [N, n cm^{-3}], plasma temperature [T, 10^5 K], interplanetary magnetic field [B, nT], standard deviation in field vector [σ_F, nT], and the electric field [E, mV m^{-1}] from 15 July 2010 to 14 August 2010.

We applied the method of superposed-epoch analysis and analyzed the cosmic-ray intensity data together with interplanetary plasma and field data. For this purpose we divided the HSS into convenient groups based on their i) speed, ii) durations, and iii) solar sources. We also studied the influence of individual streams in modulating the GCR intensity by grouping them into suitable GCR-effective groups of increasing range of GCR-intensity depressions produced by them.

4.3 Results and Discussion

4.3.1 GCR Effectiveness of High-Speed Streams of Different Speed

High-speed streams in the solar wind, as observed in near-Earth space, have velocities ranging from ≈ 400 km s^{-1} up to ≈ 1000 km s^{-1}. To study the effectiveness of HSS with such a wide range of speeds in modulating the GCR intensity, we divided them into five groups of streams of different velocity range: i) 400 – 500 km s^{-1}, ii) 501 – 550 km s^{-1}, iii) 551 – 600 km s^{-1}, iv) 601 – 650 km s^{-1}, and v) > 650 km s^{-1}. Observations show that during the passage of the HSS, the density [N] and temperature [T] of the solar-wind plasma also change. Thus these parameters [N and T] together with velocity [V] describe the physical conditions of solar-wind plasma during the passage of the HSS. We also considered the magnitude of magnetic-field vector [F, nT] attributable to the solar-wind plasma, fluctuations/turbulence in the field as indicated by standard deviations in magnetic field [σ_F, nT], and the interplanetary electric field [$E = FV$, mV m^{-1}] in addition to the solar-wind velocity [V, km s^{-1}] to study the GCR intensity modulation during the passage of the HSS.

To study of the effect of HSS-speed on the GCR-intensity modulation we performed a superposed-epoch analysis of hourly GCR intensity data as observed by neutron monitors: Oulu (Latitude = 64.05 N, Longitude = 25.47 E, cut-off rigidity R_c = 0.81 GV) and Hermanus (Latitude = 34.42 S, Longitude = 19.23 E, cut-off rigidity R_c = 4.58 GV) with different cut-off rigidities. Data of two neutron monitors were used to show that the observed variations are not local but global, with similar nature that differs in amplitude because of the different cut-off rigidity of the two locations. This analysis was performed for the arrival of HSS. The arrival time of the HSS is considered as the epoch (zero hour) for the analysis. The hourly data of neutron monitors, solar-wind velocity [V], interplanetary magnetic-field vector [F], standard

Table 4.1 A catalog of high-speed solar wind streams observed during 2008 – 2011.

Serial No.	Year	Start time DD/MMM/HH	End time DD/MMM/HH	Duration DD.HH	Stream association (a)	No. of stream sources	Shock (b)	Stream structure (c)	Shock arrival time (d) SSC DD/MMM/HH	Magnetic Cloud (e)	V_{max} [km s^{-1}] (f)	N_{max} [n cm^{-3}] (g)	T_{max} [10^5 K] (h)	B_{max} [nT] (i)
1	08	05 Jan:00	12 Jan:05	07.05	C	1	Y	S-C	04 Jan:23		706	40.7	4.09	15.9
2	08	12 Jan:06	24 Jan:11	12.05	C	1		C			710	13.0	2.92	9.1
3	08	24 Jan:13	27 Jan:12	02.23	C	1		C			550	09.6	2.74	8.9
4	08	31 Jan:08	07 Feb:02	06.18	C	1	Y	S-C	31 Jan:11		640	34.6	2.25	11.7
5	08	07 Feb:10	09 Feb:02	01.16	C	1		C			437	10.4	0.94	8.7
6	08	09 Feb:03	27 Feb:12	16.09	C-C	2		C2			725	23.2	3.81	16.9
7	08	27 Feb:13	07 Mar:21	09.08	C	1		C			768	21.1	5.28	10.5
8	08	07 Mar:22	26 Mar: 00	18.02	C-C-C	3	Y	S-C3	08 Mar:12		701	32.6	4.04	15.9
9	08	26 Mar:01	02 Apr:16	07.15	C	1	Y	S-C	26 Mar:10		676	23.5	3.56	9.5
10	08	02 Apr:17	16 Apr: 00	13.07	C-C-C	1	Y	C-S-C2	04 Apr:15		738	9.8	3.67	12.2
11	08	16 Apr:01	22 Apr:12	06.11	C	1	Y	S-C	15 Apr: 14		600	15.8	2.65	10.5
12	08	22 Apr: 13	30 Apr:15	08.02	C	1		C			654	17.6	5.22	11.8
13	08	30 Apr: 16	10 Apr:00	10.08	C	1	Y	C-S	30 Apr: 16		642	26.1	2.26	8.3
14	08	18 May:03	28 May:00	09.21	C	1		C			593	26.7	2.96	8.4
15	08	28 May 01	06 Jun:03	09.02	C	1	Y	S-C	28 May: 02		632	35.2	5.02	9.7
16	08	06 Jun:04	14 Jun:11	08.07	C	1		C			514	16.8	1.96	8.0
17	08	14 Jun:12	24 Jun:14	10.02	C-C	2	Y	S-C2	14 Jun: 12		754	37.9	4.97	14.8
18	08	24 Jun:15	04 Jul:08	10,17	C	1	Y	S-C	24 Jun: 20		641	19.8	3.20	13.4
19	08	04 Jul:09	09 Jul:01	04,16	C	1		C			413	17.4	1.54	9.1
20	08	09 Jul:02	20 Jul:11	11,09	C	1		C			697	15.5	3.30	14.6
21	08	20 Jul:12	31 Jul:23	11,11	C-C	2		C2			663	18.6	3.50	9.7
22	08	08 Aug:06	16 Aug:15	08,09	C	1	Y	S-C	08 Aug:23		645	30.2	4.68	18.3
23	08	16 Aug:16	24 Aug:10	07,18	C	1		C			626	22.9	3.66	9.7
24	08	02 Sep:19	13 Sep:17	10,22	C-C	1	Y	S-C2	03 Sep:16		622	20.5	2.96	14.8
25	08	14 Sep:04	23 Sep:08	09,04	C-E	1	Y	S-C-E	15 Sep: 19		583	39.5	2.86	11.6
26	08	30 Sep:11	08 Oct:19	08,08	C	1	Y	S-C	30 Sep: 13		705	9.9	3.35	8.2
27	08	11 Oct:05	17 Oct:10	06,05	C	1		C			548	32.1	3.75	13.5
28	08	28 Oct:01	05 Nov:18	08,17	C	1		C			705	15.2	3.60	13.8
29	08	6 Nov:07	14 Nov:12	08,05	C	1	Y	S-C	07 Nov: 04		573	29.1	2.74	11.9

Table 4.1 (*continued*)

30	08	14 Nov:13	22 Nov:01	07,12	E	1	Y	S-E	15 Nov:16	517	18.9	1.81	13.5
31	08	24 Nov:23	02 Dec:11	08,12	C	1	Y	S-C	24 Nov:23	648	74.9	3.89	21.7
32	08	02 Dec:12	21 Dec:19	19,07	E-C-C-E	4	Y	E-C2-S-E	16 Dec:12	567	24.4	2.62	10.7
33	08	21 Dec:20	30 Dec:02	08,16	C	1		C		556	25.3	2.58	11.5
34	08	31 Dec:03	08 Jan:05	08,02	C-C	2		C2		535	19.3	2.49	13.4
35	09	12 Jan:15	23 Jan:08	10,17	C-E	2		C-E		477	16.9	1.95	12.4
36	09	25 Jan:12	03 Feb:19	09,07	E-C-C	3	Y	E-S-C2	25 Jan:22	496	20.5	2.41	10.6
37	09	13 Feb:20	19 Feb: 05	05,09	C	1		C		581	50.7	3.25	15.9
38	09	19 Feb:06	03 Mar:02	11,20	C	1	Y	S-C	20 Feb:20	679	20.9	3.21	8.6
39	09	10 Mar:09	19 Mar: 13	09,04	C	1		C		567	21.9	2.99	18.4
40	09	19 Mar:21	03 Apr:06	14,09	C-C-C	3		C3		489	10.7	1.91	10.1
41	09	03 Apr:07	16 Apr: 09	13,02	C-C	2		C2		551	20.7	2.11	8.5
42	09	16 Apr:10	01 May:09	14,23	C-C	2	Y	C-S-C	24 Apr:03	536	27.0	2.02	11.1
43	09	02 May:09	13 May:14	11,05	C	1		C		508	16.3	2.02	7.1
44	09	27 May:23	23 Jun:02	26,03	C-E-C-C-C-C	6	Y	S-C-E-C4	28 May:05	434	29.8	1.53	10.1
45	09	24 Jun:02	09 Jul: 11	15,09	C-E	2		C-E		557	82.5	2.87	13.4
46	09	09 Jul:12	18 Jul: 06	08,18	C-C-E	3	Y	C-S-C-E	13 Jul:13	534	31.9	2.71	10.7
47	09	22 Jul: 01	30 Jul: 06	08,05	C	1		C		563	39.9	2.43	16.6
48	09	04 Aug:16	13 Aug: 18	09,02	C	1	Y	C-S	07 Aug:16	514	20.8	2.54	12.6
49	09	17 Aug:08	25 Aug: 19	08,11	C	1		C		559	16.5	2.64	11.8
50	09	28 Aug:22	03 Sep: 09	05,11	C	1	Y	S-C	30 Aug:02	471	12.7	1.26	12.3
51	09	03 Sep:10	08 Sep:03	04,17	C	1	Y	S-C	03 Sep: 16	484	19.3	1.47	8.3
52	09	13 Sep:11	20 Sep:10	06,23	C	1		C		460	27.4	1.38	8.2
53	09	20 Sep:11	25 Sep:22	05,11	C	1		C		460	15.0	1.38	9.4
54	09	25 Sep:23	07 Oct:22	11,23	C-E-C	3	Y	C-S-E-C	28 Sep:07	415	38.9	1.44	9.4
55	09	10 Oct:18	21 Oct: 05	10,11	C-C	2		C-S-C	11 Oct:00	436	48.5	1.68	12.2
56	09	21 Oct:06	04 Nov:09	14,03	C-E	2	Y	S-C-S-E	22 Oct:00 24 Oct:17	474	21.3	1.14	11.2
57	09	07 Nov:08	12 Nov:00	04,16	C-E	2	Y	S-C-E	08 Nov:10	442	24.8	1.72	9.7
58	09	18 Nov:17	05 Dec:06	16,13	C-C	2	Y	C-S-C	24 Nov:13	547	20.6	2.88	11.2
59	09	05 Dec:07	12 Dec:04	06,21	C-E	2	Y	S-C-E	05 Dec: 07	420	28.8	1.44	9.9
60	09	21 Dec:05	31 Dec:05	19,00	E-C-C-C	4	Y	S-E-C3	12 Dec: 20	427	29.1	1.58	9.4
61	10	11 Jan:01	20 Jan:08	09,07	C	1		C		512	33.8	2.91	11.9
62	10	20 Jan:09	29 Jan:18	09,09	C	1		C		509	34.2	3.06	15.5
63	10	29 Jan:19	06 Feb:07	07,12	C	1		C		559	13.8	2.39	9.8

Table 4.1 (*continued*)

64	10	16 Feb:14	27 Feb:09	10,19	C-C	2	Y	C-S-C	25 Feb:17		496	09.9	3.11	8.7
65	10	08 Mar:12	22 Mar:10	13,22	C-C-C	3		C3			552	16.2	3.49	9.2
66	10	24 Mar:08	20 Apr:07	25,23	C-E-E-C	4	Y	C-S-E-S-E-C-S	02 Apr:07 05 Apr:08 11 Apr:13	Y	783	25.7	7.59	20.2
67	10	28 Apr:16	10 May:08	11,16	C	1	Y	S-C	02 May:09		707	38.7	4.67	18.3
68	10	10 May:09	14 May:13	04,04	C-C	2		C2			408	14.0	21.3	8.3
69	10	16 May:19	24 May:16	07,21	C	1		C			510	37.2	3.23	13.0
70	10	25 May:03	09 Jun:18	15,15	C-C	2	Y	S-C2	28 May 03	Y	616	26.0	3.31	14.3
71	10	09 Jun:19	23 Jun:09	13,14	C-C-C	3		C3		Y	557	29.1	3.00	10.8
72	10	23 Jun:10	10 Jul:09	16,23	C	1	Y	S-C	29 Jun: 07		683	28.2	3.49	10.0
73	10	10 Jul:10	20 Jul:13	10,03	C	1		C			466	41.1	2.09	16.1
74	10	20 Jul:14	12 Aug:14	23,00	C-E-C	3	Y	C-S-E-S-C	03 Aug:18 04 Aug:10		691	25.0	3.77	17.0
75	10	22 Aug:23	05 Sep:13	13,14	C-C	2		C2			693	33.7	4.55	18.8
76	10	05 Sep:14	12 Sep:08	06,18	C-C	2		C2			501	19.0	1.85	8.7
77	10	15 Sep:23	23 Sep:00	09,01	C-C	2		C2			493	21.1	2.27	10.9
78	10	23 Sep:01	03 Oct:10	10,09	C-C	2		C2			620	19.3	2.39	12.2
79	10	04 Oct:17	15 Oct: 00	10,07	C	1		C			447	37.4	1.18	13.5
80	10	15 Oct:01	04 Nov:20	20,19	C-C	2	Y	C2-S	30 Oct:10		658	27.8	3.91	9.9
81	10	10 Nov:13	05 Dec:11	24,22	C-C-C-C	4	Y	S-C4	10 Nov:18		635	29.8	3.44	11.6
82	10	12 Dec:12	22 Dec: 06	09,18	C	1	Y	C-S	19 Dec:22		654	21.2	4.41	11.5
83	11	06 Jan:16	23 Jan: 16	17,00	C-C-C-C	4	Y	S-C4	06 Jan:17		635	53.1	2.58	13.8
84	11	31 Jan:12	14 Feb:03	13,15	E-C	2	Y	E-C-S	31 Jan:16		647	81.5	5.30	21.0
85	11	14 Feb:09	27 Feb:10	13,01	C-E	2		C-E	-		691	75.0	7.08	31.0
86	11	28 Feb:15	09 Mar:18	09,03	C	1		C	-		687	39.0	4.56	14.0
87	11	09 Mar:21	22 Mar: 05	12,08	C	1		C	-		599	24.9	2.88	13.8
88	11	22 Mar:10	27 Mar: 03	04,17	C	1		C	-		516	30.8	2.80	10.4
89	11	31 Mar:20	11 Apr: 05	10,09	C-C	2		C2	-	Y	650	15.9	4.97	15.4
90	11	11 Apr:06	17 Apr: 12	06,06	C	1		C	-		600	53.1	3.49	15.0
91	11	17 Apr:14	28 Apr: 14	11,00	C-C	2		C2	-		555	32.2	3.64	15.9
92	11	28 Apr:15	08 May: 01	09,10	C	1		C	-		703	13.8	7.07	17.3
93	11	09 May:03	21 May: 03	12,00	C-C	2		C2	-		596	32.3	3.86	11.0

Table 4.1 *(continued)*

94	11	21 May:04	04 Jun:16	14.12	C-C	2	C2	-		752	17.3	10.70	13.0
95	11	04 Jun:18	09 Jun:20	05.02	E-C-C	3	E-C2	-		556	56.9	4.10	23.6
96	11	09 Jun:21	29 Jun:16	19.19	C-C-C	3	C3	-		661	14.9	8.85	10.9
97	11	08 Jul:23	17 Jul:12	08.13	C	1	C	-		708	32.0	5.36	12.8
98	11	17 Jul:13	27 Jul:21	10.08	C-C	2	C2	-		731	09.7	3.58	10.4
99	11	28 Jul:04	04 Aug:04	07.00	C	1	C	-		686	16.2	5.37	14.1
100	11	04 Aug:10	13 Aug:14	09.04	C-C	2	C2	-		632	29.1	10.20	29.4
101	11	13 Aug:19	22 Aug:23	09.04	C	1	C	-		575	28.8	2.65	9.4
102	11	23 Aug:00	31 Aug:22	08.22	E-C	2	E-C	-		569	12.3	3.68	8.6
103	11	02 Sep:15	25 Sep:05	12.14	C-C-C	3	C-S-C-S-C	-		652	41.0	6.30	19.3
104	11	25 Sep:07	09 Oct. 14	14.07	C-C-C	3	C3	-		704	30.5	10.07	34.2
105	11	09 Oct:15	21 Oct: 17	12.02	C	1	C	-		480	19.3	2.45	8.4
106	11	23 Oct:14	29 Oct:05	05.15	C	1	C	-	Y	534	29.3	4.86	24.0
107	11	29 Oct:12	06 Nov:17	07.05	C	1	C	-		436	27.9	1.69	12.6
108	11	06 Nov:00	21 Nov:05	15.05	C-C	2	C2	-		464	22.2	2.62	9.8
109	11	21 Nov:11	07 Dec:05	15.18	C-C-E-C	4	C2-E-C	-		486	26.0	5.33	17.0
110	11	09 Dec:08	17 Dec:06	07.22	C	1	C	-		491	13.6	3.64	10.7
111	11	18 Dec: 01	27 Dec:06	09.05	C	1	C	-		418	27.2	1.46	9.7

Column: (a) C stands for stream associated with a coronal hole, E stands for stream associated with a coronal mass ejection. Multiple Cs and Es are used for compound streams associated with multiple coronal hole(s)/multiple mass ejection(s); (b) Y is used if shock(s) is (are) identified during a particular event, otherwise it is empty; (c) S stands for shock associated with streams and put in order of its arrival time. The symbols C2 and C3 indicate that the stream is due to two and three coronal hole streams in succession, respectively; (d) SSC stands for sudden storm commencement, (-) indicates that SSC data are not available; (e) Y is used if the stream has a magnetic cloud structure, otherwise empty; (f. g, h. i) the peak values of solar plasma/field parameters, solar-wind velocity [V_{max}], plasma density [N_{max}], plasma temperature [T_{max}], and magnetic field [B_{max}] during each streams.

deviation of vector magnetic field [σ_F], interplanetary electric field [E], solar-wind plasma density [N], and temperature [T] were analyzed. The results of the analysis showing the average behavior for the five speed-groups of the HSS are plotted in Figure 4.2. The influence of the HSS on GCR intensity is apparent because the intensity begins to decrease upon the arrival of the HSS. Although the temporal variations of GCR intensity correspond to temporal variations of the HSS speed, other solar-wind parameters (*e.g.* magnetic-field vector [F], field fluctuations represented by σ_F, and interplanetary electric field [E]) are also enhanced at the HSS arrival (see Figure 4.2).

Figure 4.2 shows the average behavior, both the temporal variations and the amplitudes of various parameters, during the passage of the five HSS speed-groups. However, it is clear from these figures that the GCR effectiveness (ability to depress the GCR intensity) of five HSS speed-groups are different (see also Table 4.2a – 4.2d). To study the GCR effectiveness of HSS in more detail, we determined the amplitude of the GCR-intensity depression caused by individual HSS. Then, adopting the criteria suggested by Kumar and Badruddin (2014a), we divided the GCR effectiveness into four groups, based on certain ranges of the GCR-intensity depressions. These GCR-effective groups are the so–called small (0.01 – 0.49 %), moderate (0.50 – 1.49 %), large (1.50 – 2.99 %), and very large (≥ 3.00 %) depressions, as observed at a mid-latitude neutron monitor. With this division of the GCR effectiveness into four categories, we made a comparative study of the GCR effectiveness of five HSS speed-groups. These results are tabulated in Table 4.2b. This table shows that not all of the HSS are GCR-effective. Although their relative contribution varies, most HSS of each speed group – A, B, C, D, and E (see Table 4.2b) are either small or moderately GCR effective. Another interesting observation from this table is that some of the HSS from each speed-group, from A up to E, are able to produce depressions with large and very large GCR effectiveness, although their number is small in some cases. This may be interpreted to indicate that the velocity of the HSS is not the only or the most effective parameter that decides the GCR effectiveness of individual HSS.

As can be seen from the superposed-epoch plots in Figure 4.2, the typical temporal profile of each HSS speed-group is such that the solar-wind velocity begins to

increase near zero hour, reaches a maximum speed after a certain time, and then begins to slowly decrease. Although the temporal profiles are different, the enhancements in other solar-wind parameters [F, σ_F, E, N, and T] also start near the zero hour, reach a maximum, and then decrease.

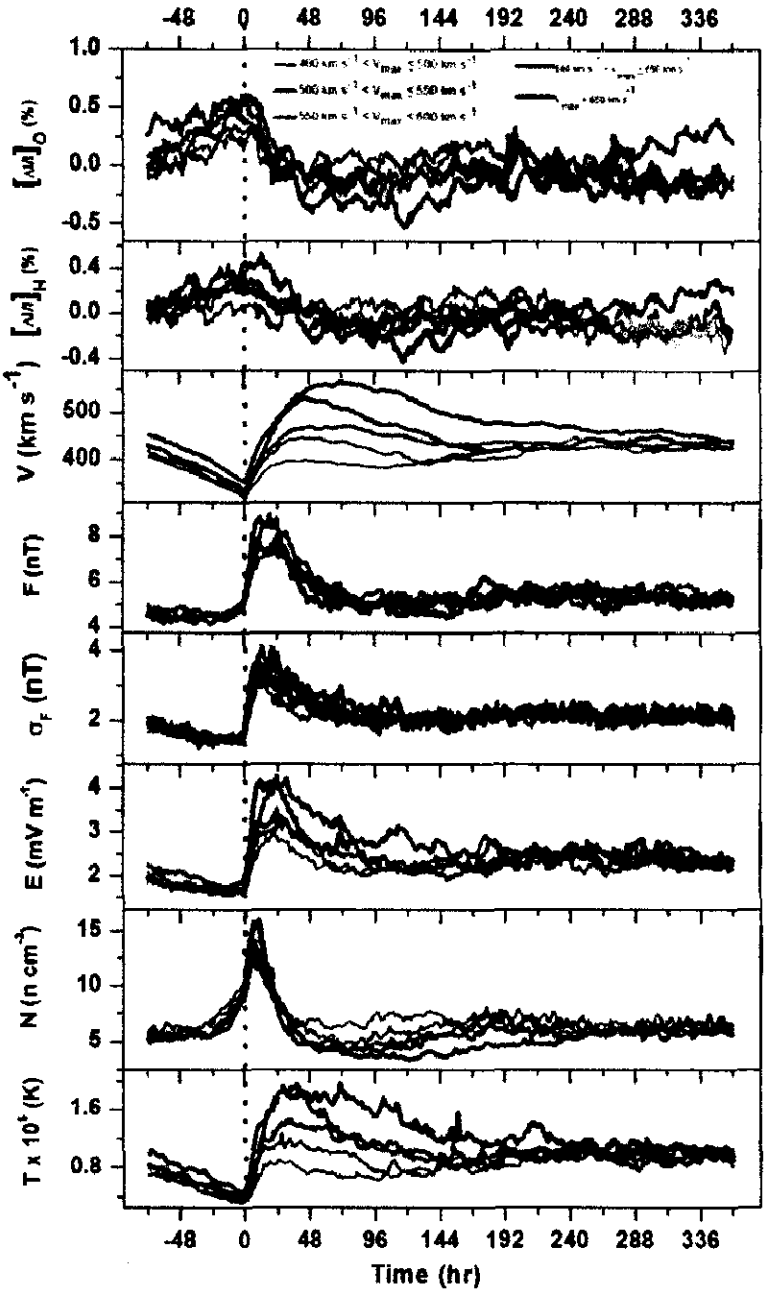

Figure 4.2 Superposed-epoch analysis results of the GCR-intensity variation recorded at Oulu NM $[\Delta I/I]_O$ (%), at Hermanus NM $[\Delta I/I]_H$ (%), the solar-wind velocity [V, km s^{-1}], interplanetary magnetic field vector [F, nT], standard deviation of magnetic field [σ_F, nT], electric field [E, mV m^{-1}], plasma density [N, n cm^{-3}], and the plasma temperature [T, 10^5 K] plotted for the arrival times of high-speed streams (zero hour) of the five categories based on the speed.

Table 4.2a Amplitudes and changes of various parameters obtained from averaged plots based on speed using superposed-epoch analysis.

Velocity interval [km s^{-1}]	No.	ΔI [%] Oulu	ΔI [%] Hrms	V_{max} [km s^{-1}]	ΔV [km s^{-1}]	F_{max} [nT]	ΔF [nT]	$\sigma_{F\,max}$ [nT]	$\Delta\sigma_F$ [nT]	E_{max} [mV m^{-1}]	ΔE [mV m^{-1}]	N_{max} [n cm^{-3}]	ΔN [n cm^{-3}]	T_{max} (10^5) [K]	ΔT (10^5) [K]
401 – 500	136	0.46	0.27	401	81	7.60	2.90	3.17	1.73	2.97	1.39	12.62	4.35	0.91	0.58
501 – 550	74	0.61	0.28	447	120	7.62	2.90	3.89	2.43	3.27	1.59	14.03	7.65	1.27	0.96
551 – 600	103	0.75	0.42	472	138	8.02	3.66	3.43	2.03	3.54	1.93	13.42	7.87	1.47	1.10
601 – 650	88	0.86	0.68	531	195	8.98	4.33	4.12	2.57	4.29	2.62	15.86	10.38	1.93	1.58
> 650	170	1.09	0.73	566	212	8.86	3.79	3.93	2.41	4.24	2.40	12.81	7.34	1.84	1.39

Table 4.2b Distribution [percent] of GCR effectiveness due to streams of five categories based on the speed.

Speed [km s^{-1}] range	Speed group	Total streams	GCR-effective streams	Number [%]			
				Small depressions [$0.01\% \le \Delta I \le 0.49\%$]	Moderate depressions [$0.5\% \le \Delta I \le 1.49\%$]	Large depressions [$1.5\% \le \Delta I \le 2.99\%$]	Very large depressions [$\Delta I \ge 3.0\%$]
401 – 500	A	136	104	50.0	35.6	11.5	2.9
501 – 550	B	74	61	41.0	45.9	11.5	1.6
551 – 600	C	103	81	29.6	51.9	11.1	7.4
601 – 650	D	88	74	27.0	47.3	18.9	6.8
> 650	E	170	137	30.7	38.7	15.3	15.3

Depressions in GCR-intensity also start near the zero hour (see Figure 4.2), reach a minimum level after some time, and then begin to increase (recover). It will be interesting, therefore, to determine whether the duration of the GCR-intensity decrease – from the start of the decrease around zero hour to when it reaches its lowest depression level – is the same as, or is different from the duration of increase in solar-wind parameters from the start of increase (around zero hour) to when it reaches its highest enhancement level. In other words, whether the time of minima of GCR decrease coincides with the time of maxima of solar-wind parameters [V, F, σ_F, E, N, and T] or if there is some time lag between the two. Table 4.2c shows that the lowest GCR depression is reached later than the maxima reached in the solar-wind parameters. In other words, there is some time lag between GCR-intensity minima and the solar-wind parameter maxima as seen in all of the HSS speed-groups. However, compared with other solar wind parameters, the lag is shorter with the velocity of the solar wind.

Table 4.2c Time lag/lead between the minima of GCR-intensity depression and corresponding maxima in interplanetary parameters for different HSS speeds.

Speed group	Speed interval [km s^{-1}]	Main phase [hrs]	$(\Delta t)_V$ [hrs]	$(\Delta t)_F$ [hrs]	$(\Delta t)_{\sigma F}$ [hrs]	$(\Delta t)_E$ [hrs]	$(\Delta t)_N$ [hrs]	$(\Delta t)_T$ [hrs]
A	401 – 500	41	+01	–22	–28	–22	–34	–31
B	501 – 550	40	+03	–20	–35	–15	–37	–17
C	551 – 600	81	–24	–48	–57	–48	–66	–40
D	601 – 650	77	–34	–56	–62	–52	–65	–47
E	>650	118	–49	–107	–95	–88	–114	–93

Although there are time lags between GCR-intensity minima and the maxima of solar-wind parameters, nevertheless the average temporal profiles of GCR-intensity variation and solar-wind parameters in all HSS speed-groups in general show opposite trends, *i.e.* when the GCR intensity decreases, the solar-wind parameters increase and *vice versa*. Therefore, it seems appropriate to search for the solar-wind parameter(s) that best follows the time profile of GCR intensity not only during the main phase, (start of decrease to minima) but also during the recovery phase. For this purpose, we

performed a linear regression and obtained correlation coefficients between GCR intensity and different solar-wind parameters, during the main and the recovery phase separately. Table 4.2d shows that the correlation of GCR intensity variation is in general better with the variation in solar-wind velocity, during main as well as the recovery phases. The scatter plot and linear fit during the main phase are shown in Figure 4.3. Another observation from this figure is that the decrease rate of GCR intensity with increase in solar-wind velocity is almost the same ($\approx 0.5 \times 10^{-2}$) due to the HSS irrespective of their speed-groups.

Table 4.2d Linear correlation coefficients [R] obtained from the linear correlation between the temporal variation of the GCR-intensity depressions and the corresponding parameters [V, F, σ_F, E, N, and T] during the main and recovery phases of the intensity-depression caused by different stream categories based on speed.

Speed group [km s^{-1}]	Value of R between ΔI and various parameters											
	During main phase						During recovery phase					
	V	F	σ_F	E	N	T	V	F	σ_F	E	N	T
401 – 500	−0.93	−0.27	0.39	−0.56	0.86	−0.80	−0.14	−0.29	−0.07	−0.27	−0.11	−0.05
501 – 550	−0.91	0.19	0.55	−0.51	0.85	−0.85	−0.80	−0.12	−0.14	−0.38	0.74	−0.52
551 – 600	−0.95	−0.14	−0.25	−0.55	0.77	−0.87	−0.64	0.34	−0.12	0.14	0.63	−0.40
601 – 650	−0.94	0.54	0.39	0.04	0.91	−0.62	−0.11	−0.38	−0.25	−0.42	−0.05	−0.32
> 650	−0.94	0.68	0.63	0.37	0.94	−0.67	−0.88	0.32	0.01	−0.64	0.82	−0.62

4.3.2 GCR Effectiveness of Different Duration HSS

From the survey of the HSS temporal profiles in the solar wind, it is clear that the duration of the HSS may be as short as $\lesssim$ two days and as long as half the solar rotation period or even longer ($\gtrsim$ 13.5 days) (see, *e.g.*, Lindblad, Lundstedt, and Larsson, 1989; Mavromichalaki and Vassilaki, 1998; Maris and Maris, 2005; Gupta and Badruddin, 2010; Xystouris, Sigala, and Mavromichalaki, 2014, and references therein). Thus it will be interesting to investigate how these HSS of such a wide range of durations modulate the GCR intensity, and whether the duration of HSS has any influence on the level of depression and temporal profile in GCR intensity.

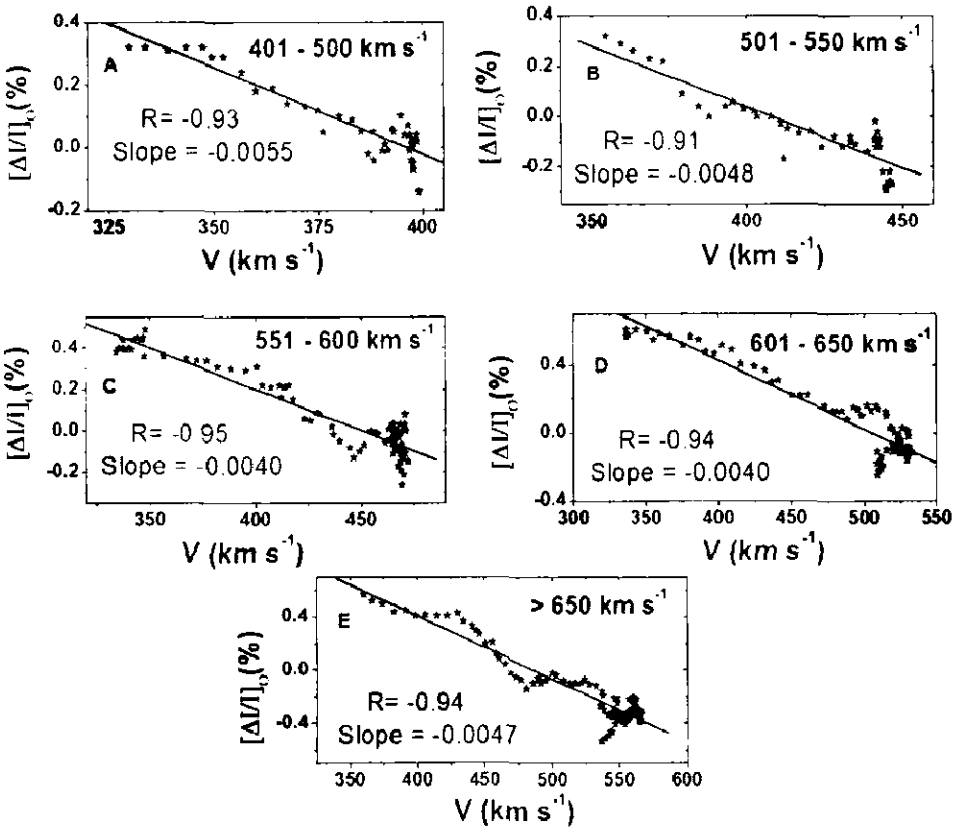

Figure 4.3 Relationship between the averaged temporal variation of the solar-wind velocity and the GCR-intensity depressions during the main phase of the intensity decrease caused by the five stream categories based on speed.

To study this we have grouped the HSS observed during 1996 – 2011 into five arbitrary duration-groups: group A (2 days < $\Delta t \leq$ 4.5 days), group B (4.5 days < $\Delta t \leq$ 7.5 days), group C (7.5 days < $\Delta t \leq$ 10.5 days), group D (10.5 days < $\Delta t \leq$ 13.5 days), and group E (Δt > 13.5 days). A superposed-epoch analysis of GCR intensity and solar-wind plasma/field parameters [V, F, σ_F, E, N, and T] with respect to arrival of different duration HSS groups of streams (A, B, C, D, and E) shows that the duration of the HSS influences both the amplitudes and the temporal profile of the GCR intensity variation (see Figure 4.4 and Table 4.3a).

We studied not only the average amplitudes and temporal profiles, based on superposed-epoch analysis, but also the GCR effectiveness of all five HSS duration groups (A, B, C, D, and E) by dividing the GCR effectiveness of individual streams into four categories: small, moderate, large, and very large GCR effectiveness. The results are presented in Table 4.3b. The GCR-effectiveness of each duration-group of

streams is not same; the relative number of the small, moderate, large, and very large effective streams is different for different duration-groups (see Table 4.3b for details).

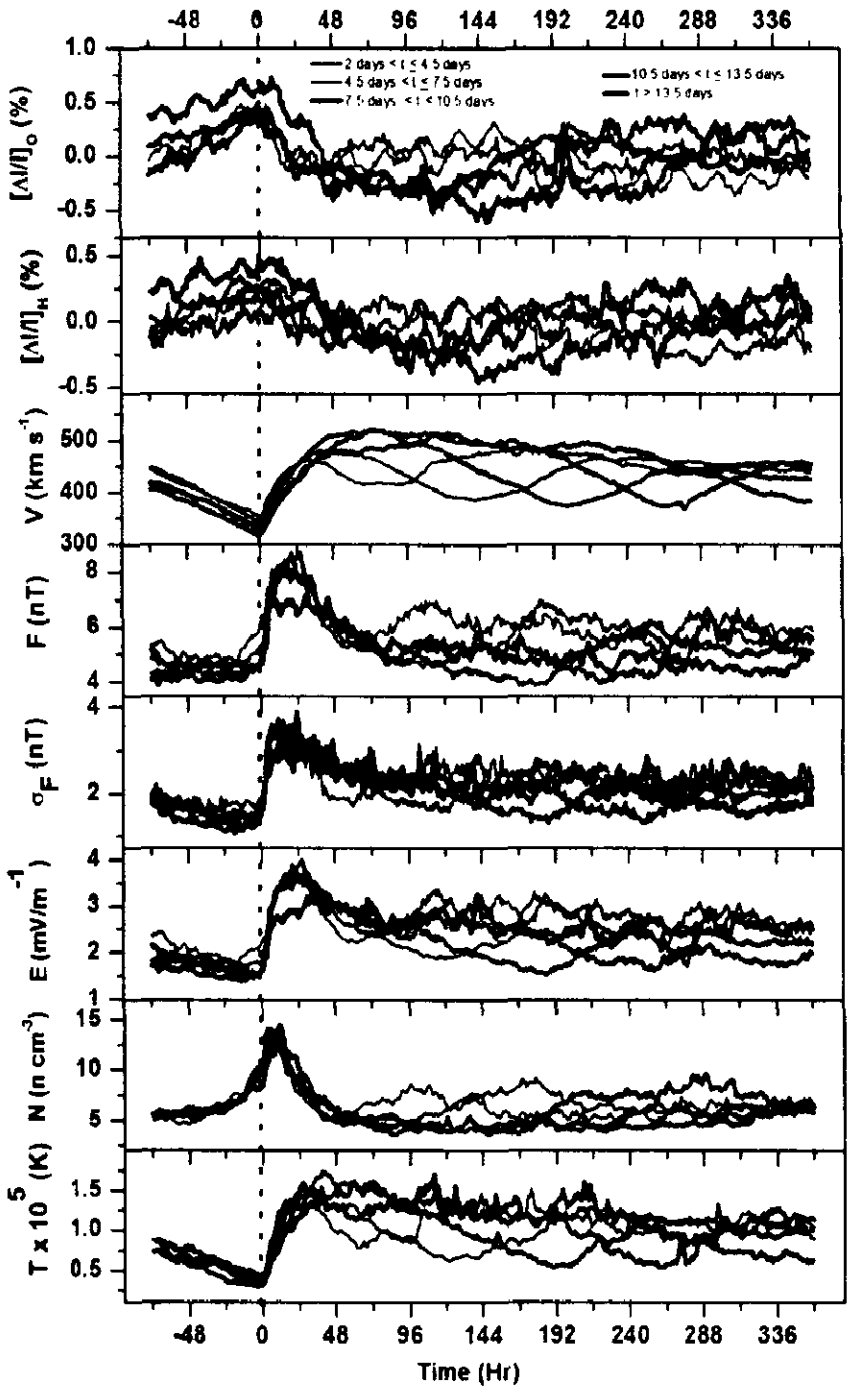

Figure 4.4 Superposed-epoch analysis results of the GCR-intensity variation recorded at Oulu NM NM $[\Delta I/I]_O$ (%), at Hermanus NM $[\Delta I/I]_H$ (%), the solar-wind velocity [V, km s^{-1}], interplanetary magnetic field vector [F, nT], standard deviation of magnetic field [σ_F, nT], electric field [E, mV m^{-1}], plasma density [N, n cm^{-3}], and the plasma temperature [T, 10^5 K] plotted for the arrival times of high-speed streams (zero hour) of the five categories based on the duration.

Table 4.3a Amplitudes and changes of various parameters obtained from averaged plots based on duration using superposed-epoch analysis.

Duration [t: days]	Duration group	No.	ΔI [%] Oulu	ΔI [%] Hrms	V_{max} [km s^{-1}]	ΔV [km s^{-1}]	F_{max} [nT]	ΔF [nT]	$\sigma_{F\,max}$ [nT]	$\Delta\sigma_F$ [nT]	E_{max} [mV m^{-1}]	ΔE [mV m^{-1}]	N_{max} [n cm^{-3}]	ΔN [n cm^{-3}]	T_{max} (10^5) K	ΔT (10^5) K
$2 \le t \le 4.5$	A	82	0.59	0.33	464	110	8.71	3.83	3.76	1.96	3.91	1.91	12.42	7.49	1.44	1.00
$4.5 < t \le 7.5$	B	181	0.67	0.41	482	140	8.27	3.27	3.60	2.10	3.74	2.00	13.35	7.85	1.54	1.15
$7.5 < t \le 10.5$	C	159	0.82	0.51	519	186	8.24	3.72	3.54	2.12	3.69	2.09	14.16	8.33	1.74	1.37
$10.5 < t \le 13.5$	D	77	0.84	0.49	521	192	8.72	4.17	3.88	2.43	3.99	2.45	14.34	8.91	1.61	1.22
$t > 13.5$	E	77	1.33	0.92	511	114	7.16	3.05	3.51	2.31	3.21	1.81	14.07	8.35	1.53	1.24

Table 4.3b Distribution (in percent) of GCR effectiveness due to streams of five categories based on the duration.

Duration range [days]	Group	Total Streams	GCR-effective streams	Number [%]			
				Small depressions [$0.01\% \le \Delta I \le 0.49\%$]	Moderate depressions [$0.5\% \le \Delta I \le 1.49\%$]	Large depressions [$1.5\% \le \Delta I \le 2.99\%$]	Very large depressions ($\Delta I \ge 3.0\%$)
$2 \le t \le 4.5$	A	82	57	49.1	35.1	12.3	3.5
$4.5 < t \le 7.5$	B	182	137	38.7	43.1	**11.7**	**6.5**
$7.5 < t \le 10.5$	C	157	136	25.0	49.3	**18.4**	**7.3**
$10.5 < t \le 13.5$	D	77	60	43.4	35.0	**13.3**	**8.3**
$t > 13.5$	E	77	67	32.8	14.8	10.5	14.9

As in the case of earlier groups based on the speed of HSS, we have also examined the time lag, if any, between the minima of the GCR-intensity depression and the maxima of solar-wind plasma/field parameters caused by five HSS duration-groups (see Table 4.3c). As in the case of speed-groups, there is in general some time lag between GCR-intensity minima and solar-wind parameter maxima during the HSS of all the duration groups; the GCR-intensity minima occur after solar-plasma/field maxima. However, the time lag is shorter between GCR minima and solar-wind velocity maxima than for other solar-wind parameters considered in this chapter. Another interesting feature Table 4.3c is that this time lag between GCR minima and solar-wind velocity-maxima is shortest for shorter-duration HSS groups (*e.g.* A, B, and C).

As discussed earlier for the case of speed-groups, in this case, the average temporal variation of GCR intensity also correlates better with temporal variation in solar-wind velocity than with other solar-wind plasma/field parameters (see Table 4.3d). This correlation is good not only during the main phase of the GCR-intensity decrease, but also during the recovery phase. The correlations between GCR intensity and solar-wind velocity for the main phase are shown in Figure 4.5 for all the five HSS duration-groups. However, as shown in these figures, the rate of GCR-intensity decrease with increase in solar-wind velocity is different for all duration-groups. Thus, it appears that some other factor(s) also contribute to the rate at which GCR-intensity decreases during the main phase.

4.3.3 GCR Effectiveness of HSS from Different Solar Sources

High-speed streams as observed in near-Earth space are not only generated by a stream from a coronal hole or a CME, but may also result from streams from multiple coronal holes, multiple CMEs, and both the coronal holes and CMEs (for details see Gupta and Badruddin, 2010). Moreover, the temporal evolution of these stream categories, as seen in the time profile of the solar-wind speed classified on the basis of sources(s) is different. Therefore, it is interesting to study the influence of these streams on the cosmic-ray intensity. To study this, we applied a superposed-epoch analysis to the GCR-intensity data. In addition to GCR-intensity data, we applied this analysis to simultaneous interplanetary plasma and field data [V, F, σ_F, E, N, and T].

Table 4.3c Time lag/lead between the minima of GCR-intensity depression and corresponding maxima in interplanetary parameters for different HSS duration.

Duration group	Duration interval [days]	Main phase [hrs]	$(\Delta t)_V$ [hrs]	$(\Delta t)_F$ [hrs]	$(\Delta t)_N$ [hrs]	$(\Delta t)_T$ [hrs]	$(\Delta t)_{\sigma F}$ [hrs]	$(\Delta t)_E$ [hrs]
A	$2 \le t \le 4.5$	40	−09	−19	−33	−16	−29	−20
B	$4.5 < t \le 7.5$	39	+05	−20	−36	−16	−33	−20
C	$7.5 < t \le 10.5$	75	−03	−60	−67	−33	−62	−42
D	$10.5 < t \le 13.5$	116	−42	−90	−105	−56	−93	−90
E	$t > 13.5$	135	−29	−134	−139	−104	−119	−113

On the basis of these average profiles, obtained by the superposed-epoch analysis, with reference to five sources-groups of streams, we compared the time profiles and amplitudes of GCR-intensity depressions caused by the five HSS source-groups as well as the time profiles of GCR-intensity with interplanetary parameter [V, F, σ_F, E, N, and T] during the passage of each group of streams.

Table 4.3d Linear correlation coefficients [R] obtained from the linear correlation between the temporal variation of the GCR-intensity depressions and the corresponding parameters [V, F, σ_F, E, N, and T] during the main and recovery phases of intensity-depression caused by different stream categories based on duration.

Duration groups	Value of R between ΔI and various parameters											
	During main phase						During recovery phase					
	V	F	σ_F	E	N	T	V	F	σ_F	E	N	T
$2 \le t \le 4.5$	−0.88	−0.34	0.07	−0.65	0.60	−0.81	−0.90	−0.44	0.27	−0.60	0.81	−0.64
$4.5 < t \le 7.5$	−0.94	0.38	0.60	−0.20	0.90	−0.84	−0.79	−0.33	−0.39	−0.64	0.74	−0.68
$7.5 < t \le 10.5$	−0.98	0.22	0.08	−0.38	0.93	−0.92	−0.96	−0.66	−0.86	−0.88	0.90	−0.92
$10.5 < t \le 13.5$	−0.90	0.43	0.24	0.08	0.84	−0.86	−0.92	−0.75	−0.76	−0.92	0.68	−0.90
$t > 13.5$	−0.94	0.85	0.78	0.23	0.95	−0.47	−0.42	−0.33	0.06	−0.46	0.42	−0.16

Based on the averaged values, we studied which of the interplanetary parameters best correlates with GCR intensity separately for the five streams classes. Another aim of this study is to determine which of the interplanetary parameters best correlates with the decrease amplitudes. Yet another purpose of this study is to discuss the time lag/lead between decrease amplitudes in the GCR intensity and the amplitudes of the corresponding interplanetary parameters caused by the five source-groups of streams, based on the average profiles obtained through the superposed-epoch analysis.

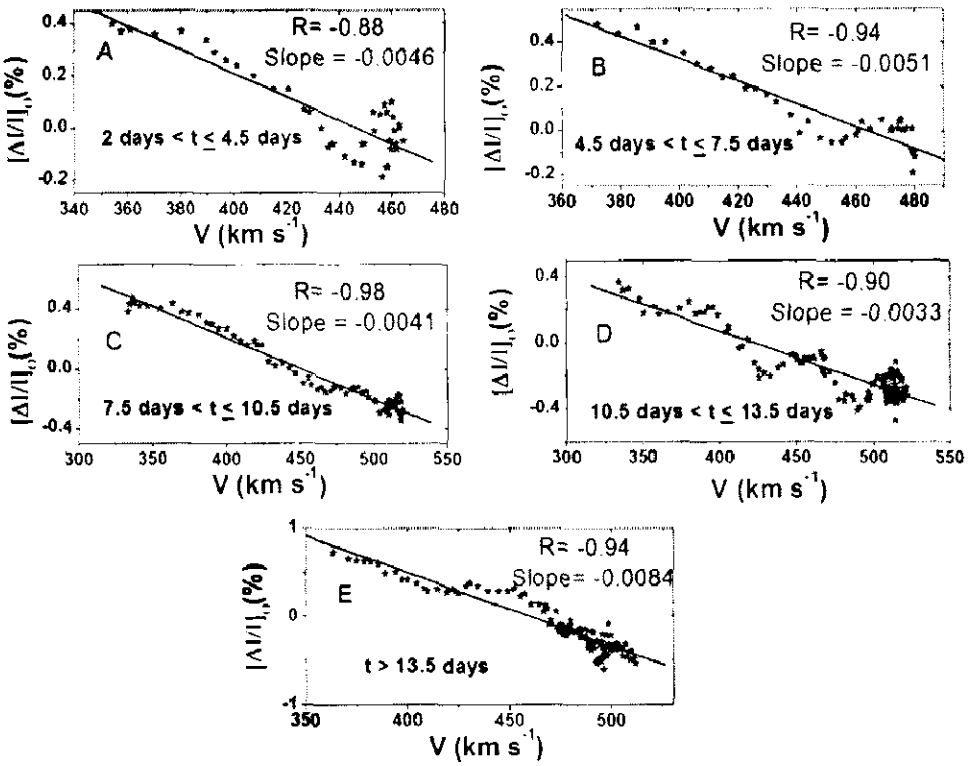

Figure 4.5 Relationship between the averaged temporal variation of the solar-wind velocity and the GCR-intensity depressions during the main phase of the intensity decrease caused by the five stream categories based on duration.

It is expected this study will provide further insight into the solar sources, interplanetary structures, solar plasma/field parameters, and the physical process that play an important role during short-term (≤ a solar rotation) intensity depressions during i) the passage of different classes of streams, ii) cosmic-ray depressions of different shapes and sizes (duration), iii) the passage of different types of interplanetary structures, and iv) the different nature of plasma and field fluctuations/variations.

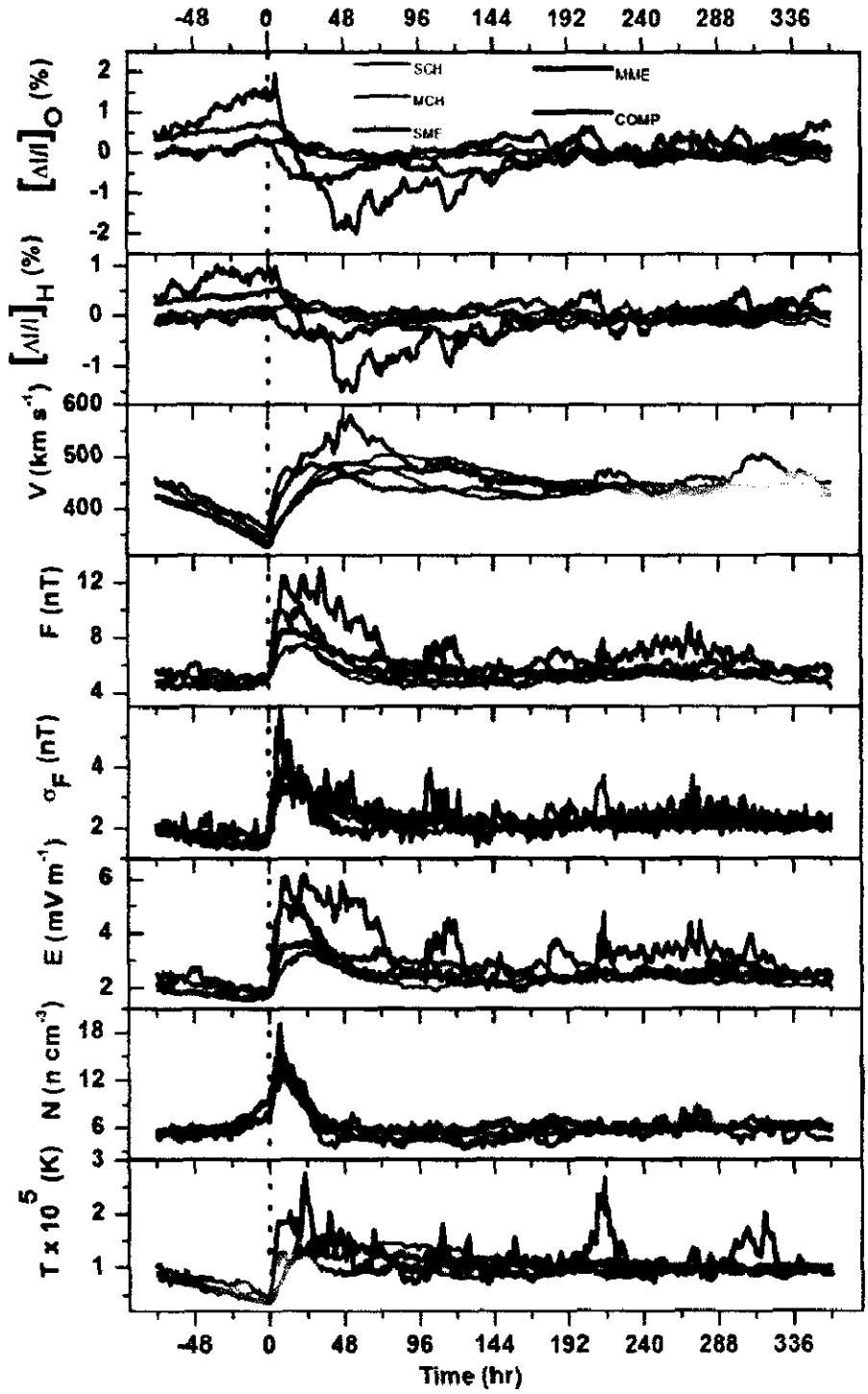

Figure 4.6 Superposed-epoch analysis results of the GCR-intensity variation recorded at Oulu NM $[\Delta I/I]_O$ (%), at Hermanus NM $[\Delta I/I]_H$ (%), the solar-wind velocity [V, km s^{-1}], interplanetary magnetic field vector [F, nT], standard deviation of magnetic field [σ_F, nT], electric field [E, mV m^{-1}], plasma density [N, n cm^{-3}], and the plasma temperature [T, 10^5 K] plotted for the arrival times of the high-speed streams (zero hour) of the five categories based on the stream sources.

In Figure 4.6, we have plotted the superposed-epoch results of solar-wind velocity [V, km s^{-1}], interplanetary (vector) magnetic field [F, nT], standard deviation of F [σ_F, nT], interplanetary electric field [E, mVm^{-1}], plasma density [N, n cm^{-3}], and temperature [T, K] along with the cosmic-ray intensity [%], with respect to arrival time (zero hour) of the five HSS source-groups, classified on the basis of their sources. The superposed hourly values of various parameters are shown for the HSS from (a) a single coronal hole, (b) more than one coronal hole, (c) a single coronal mass ejection, (d) more than one coronal mass ejection, and (e) coronal hole(s) and coronal mass ejection(s). These streams are referred to as (a) single CH, (b) multiple CH, (c) single ME, (d) multiple ME and (e) compound streams. The plots of Figure 4.6 lead us to conclude that, among the five groups of streams, multiple ME streams are on average the most effective, while the single CH groups of streams are least effective in modulating the GCR intensity. According to GCR effectiveness – in order of increasing depressions – the stream can be arranged as single CH, multiple CH, single ME, compound, and multiple ME (see Table 4.4a). The averaged amplitudes, obtained from Figure 4.6, for various parameters are also given in this table. In general, the amplitudes of these parameters are also higher for increasingly more GCR-effective groups of streams. In addition to amplitudes, the time profiles of these parameters are different for different type of streams.

As shown in Figure 4.6, the average depressions in the GCR intensity as well as time profiles during the passage of streams of different origin, divided into five source-groups, are different. These average time profiles correspond to all the 257 single CH streams, 114 multiple CH streams, 44 single ME streams, 20 multiple ME streams, and 135 compound streams identified during 1996 – 2011 in solar cycle 23 (see Gupta and Badruddin, 2010 and Table 4.1). However, it is known (*e.g.* Badruddin, 1997) that all the observed high-speed streams do not necessarily depress the GCR intensity, as observed by ground-based neutron monitor.

Therefore, we examined the GCR-intensity response for each individual identified streams. The GCR effectiveness of a stream, *i.e.* "the ability of the streams to depress the GCR intensity", is different for different stream categories. We found that for single CH 193/257 (≈ 75 %), multiple ME 93/114 (≈ 82 %), single ME 34/44 (≈ 77 %), multiple ME 18/20 (≈ 90 %) and compound streams 118/135 (≈ 88 %) are GCR

Table 4.4a Amplitudes and changes of various parameters obtained from averaged plots based on sources using superposed-epoch analysis.

Group Name	No.	ΔI [%] Oulu	ΔI [%] Hrms	V_{max} [km s^{-1}]	ΔV [km s^{-1}]	F_{max} [nT]	ΔF [nT]	$\sigma_{F\,max}$ [nT]	$\Delta\sigma_F$ [nT]	E_{max} [mV m^{-1}]	ΔE [mV m^{-1}]	N_{max} [n cm^{-3}]	ΔN [n cm^{-3}]	T_{max} (10^5) K	ΔT (10^5) K
SCH	257	0.45	0.26	489	151	7.44	2.59	3.76	1.96	3.91	1.91	12.65	6.65	1.59	1.22
MCH	114	0.50	0.38	505	172	7.60	3.07	3.60	2.10	3.74	2.00	13.15	7.36	1.61	1.24
SME	44	1.18	0.55	488	140	10.52	5.64	3.54	2.12	3.69	2.09	13.56	8.00	1.47	1.03
MME	20	3.84	2.45	546	184	13.07	8.15	3.88	2.43	3.99	2.45	19.03	13.46	2.74	2.28
COMP	135	1.30	1.12	475	148	8.58	3.52	3.51	2.31	3.21	1.81	14.98	8.76	1.33	0.98

Table 4.4b Distribution [in percent] of GCR effectiveness due to streams of five categories based on the sources.

Stream group	Total Streams	GCR-effective streams	Number [%]			
			Small depressions [$0.01\% \leq \Delta I \leq 0.49\%$]	Moderate depressions [$0.5\% \leq \Delta I \leq 1.49\%$]	Large depressions [$1.5\% \leq \Delta I \leq 2.99\%$]	Very large depressions [$\Delta I \geq 3.0\%$]
SCH	257	193	39.4	46.6	11.4	2.6
MCH	114	93	46.2	38.7	11.8	3.3
SME	44	34	41.2	38.2	11.8	8.8
MME	20	18	11.1	22.2	27.8	38.9
COMP	135	118	25.4	42.3	17.8	14.4

effective; they depress the intensity of varying amplitude. However, individual depressions due to these streams vary significantly; from less than 0.5 % up to more than 5 %.

To statistically compare the relative GCR effectiveness of different stream source categories with one another, as mentioned earlier, we divided the GCR-intensity depressions into four groups: small, moderate, large, and very large depressions. The results of this statistical distribution are summarized in Table 4.4b. This table shows that most of the GCR-effective streams produce either small or moderate depressions. However, although their number is relatively small, the majority of the multiple ME streams (67 %) produce large and very large depressions taken together. Compound streams also produce relatively more (32 %) depression of large and very large categories. The other three stream categories (single CH, multiple CH, and single ME) produce fewer (≤ 20 %) large and very depressions; only 14 % by single CH, 15 % by multiple CH and 20 % by single ME streams.

. In general, as is evident from the averaged superposed plots in Figure 4.6, not only the amplitudes, but also the temporal evolution of GCR-intensity variation caused by the different stream source categories is different. The temporal evolution of intensity variation may be broadly described as follows: depressions start at the arrival of streams, reach a minimum level after certain time, and then start recovering slowly toward the pre-decrease level. Interplanetary plasma and field parameters, as evident from Figure 4.6, begin to increase at the arrival of the stream, reach a maximum after a certain time, and then decrease to their pre-increase level after some time. Although, in general, GCR depression due to all five source-groups of streams starts at the arrival time of streams, the time the lowest in GCR depression does not appear to coincide with the time of maximum in plasma and field parameters. Thus, there appears to be a time lag/lead of several hours in the timings of minima/maxima of GCR intensity and interplanetary parameters. In general, interplanetary plasma/field parameters attain the peak earlier than the GCR-intensity minimum. These results for time lag/lead are summarized in Table 4.4c.

As evident from superposed plots of Figure 4.6 and Table 4.4a, not only do the timings of the maxima/minima of GCR intensity and individual interplanetary parameters minima/maxima differ from each other, but there also appears to be an

Table 4.4c Time lag/lead between the minima of GCR-intensity depression and corresponding maxima in interplanetary parameters for different HSS sources.

Source group	Source of structure	Main phase [hrs]	$(\Delta t)_V$ [hrs]	$(\Delta t)_F$ [hrs]	$(\Delta t)_{\sigma F}$ [hrs]	$(\Delta t)_E$ [hrs]	$(\Delta t)_N$ [hrs]	$(\Delta t)_T$ [hrs]
A	SCH	36	–01	–24	–32	–22	–41	–15
B	MCH	52	+25	–26	–25	–26	–45	–16
C	SME	48	–12	–19	–30	–31	–30	–22
D	MME	51	–02	–20	–47	–44	–48	–33
E	COMP	116	–47	–108	–111	–108	–112	–93

appreciable difference in temporal evolutions/variations of GCR intensity and individual interplanetary parameters. It is known from the GCR-intensity modulation models that solar-wind velocity, interplanetary magnetic-field strength and/or magnetic turbulence are effective interplanetary parameters in modulating the intensity of galactic cosmic rays.

Table 4.4d Linear correlation coefficients [R] obtained from the linear correlation between the temporal variation of the GCR-intensity depressions and corresponding parameters [V, F, σ_F, E, N, and T] during the main and recovery phases of intensity-depression caused by different streams categories.

Stream category	Value of R between ΔI and various parameters											
	During main phase						During recovery phase					
	V	F	σ_F	E	N	T	V	F	σ_F	E	N	T
SCH	–0.80	0.54	0.73	0.04	0.82	–0.73	–0.32	–0.27	–0.24	–0.42	0.04	–0.32
MCH	–0.96	–0.09	–0.28	–0.62	0.91	–0.88	–0.71	–0.07	–0.53	–0.58	0.52	–0.76
SME	–0.98	–0.74	–0.41	–0.74	0.08	0.75	–0.72	–0.50	0.06	–0.47	0.25	0.01
MME	–0.92	0.40	0.65	0.06	0.86	0.48	–0.66	–0.27	0.06	–0.40	0.30	0.13
COMP	–0.91	0.81	0.80	0.46	0.91	–0.61	–0.88	–0.02	-0.03	–0.53	0.73	–0.03

However, the relative effectiveness of individual parameters, out of these three, in influencing the decrease (main phase) and recovery time profiles is unclear. It is also

of interest to know which of these parameters is relatively more influential in deciding the amplitude of depressions caused by streams of different sources and associated interplanetary structures.

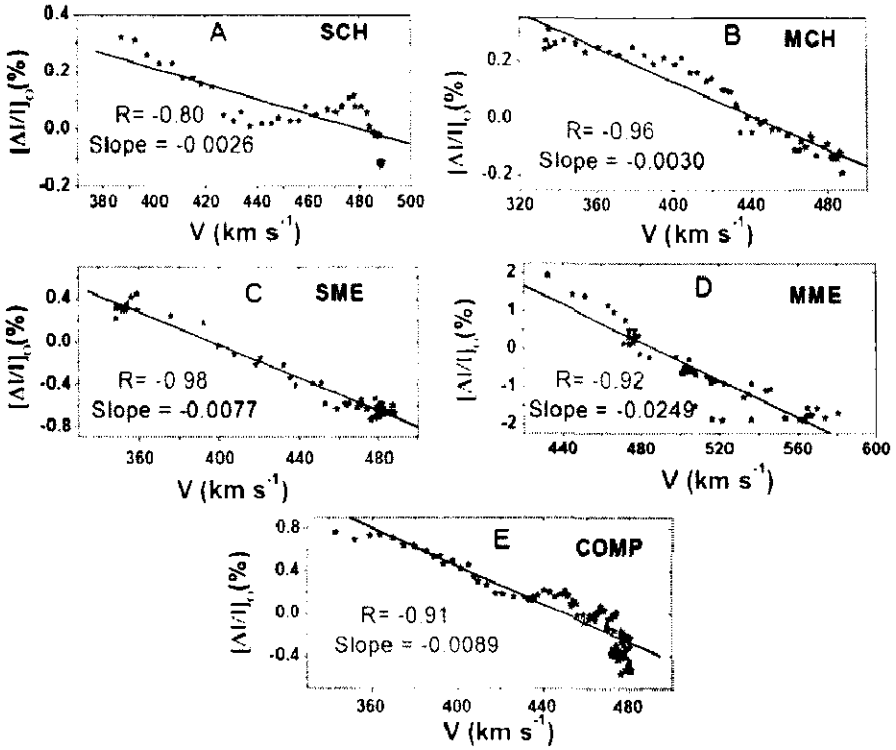

Figure 4.7 Relationship between the averaged temporal variation of the solar-wind velocity and the GCR-intensity depressions during the main phase of the intensity decrease caused by the five stream categories based on sources.

To determine the best interplanetary parameter whose temporal variation best corresponds to the time variation of GCR-intensity during i) main phase and ii) recovery phase, we performed a correlative analysis between the GCR-intensity evolution and the corresponding temporal evolutions of interplanetary parameters during the main and recovery phases of five streams categories (see Table 4.4d). The temporal variations of the GCR-intensity best follow the temporal evolution of solar-wind velocity during both the main (see Figure 4.7) and the recovery phase (see Table 4.4d).

4.3.4 GCR effectiveness of the HSS that are associated or are not associated with Shocks

We have presented results concerning the effects of HSS on GCR intensity by grouping them on the basis of i) speed, ii) duration, and iii) solar source(s). However, streams of varying speed, duration, and solar sources may or may not be associated with an interplanetary shock or sheath.

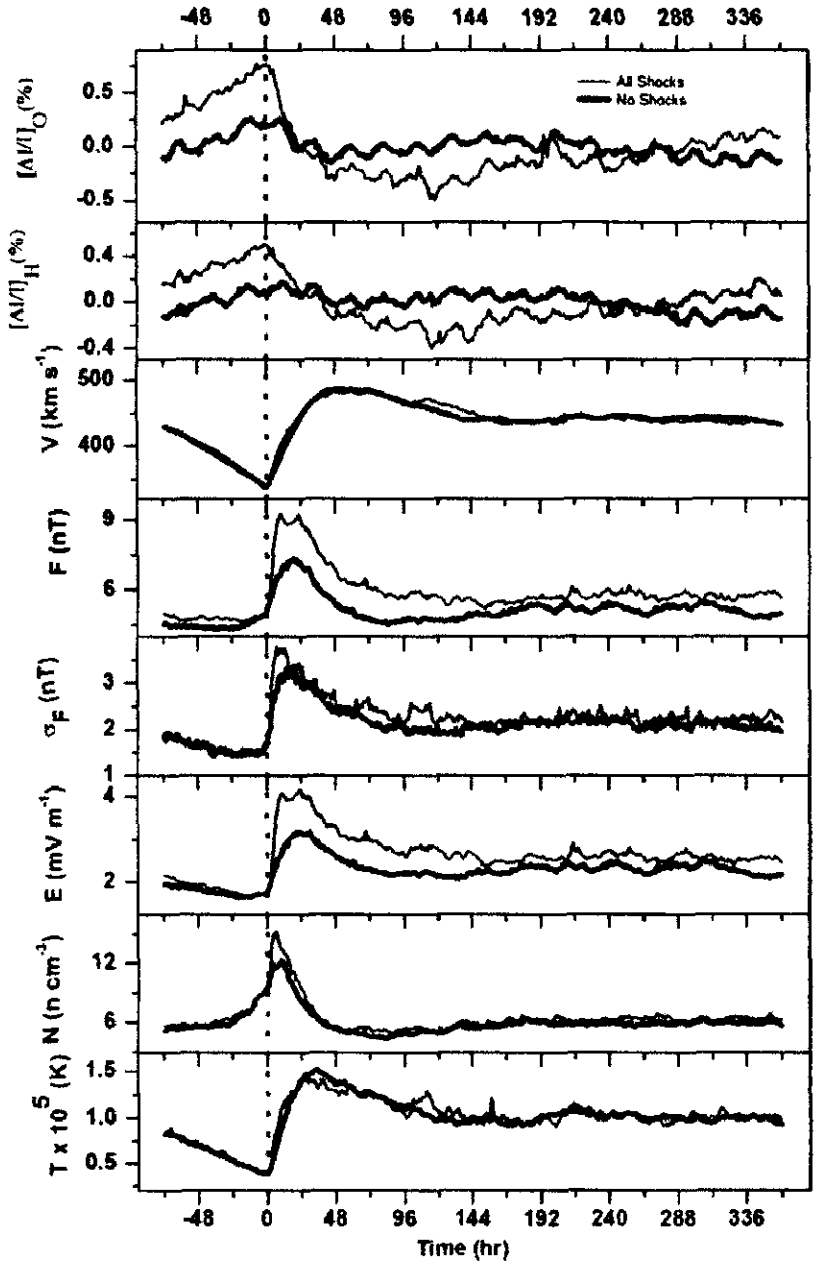

Figure 4.8 Superposed-epoch analysis results of the GCR-intensity variation recorded at Oulu NM $[\Delta I/I]_O$ (%), at Hermanus NM $[\Delta I/I]_H$ (%), the solar-wind velocity [V, km s^{-1}], interplanetary magnetic field vector [F, nT], standard deviation of magnetic field [σ_F, nT], electric field [E, mV m^{-1}], plasma density [N, n cm^{-3}], and the plasma temperature [T, 10^5 K] plotted for the arrival times of high-speed streams (zero hour) associated or not associated with a shock.

During their passage, shock-associated CMEs/magnetic clouds, in particular, have been found to be influential in sudden depressions observed in GCR intensity (*e.g.* see Badruddin, Yadav, and Yadav, 1986; Zhang and Burlaga 1988; Venkatesan and Badruddin, 1990; Cane, 2000; Badruddin, 2002; Richardson and Cane, 2011; Kumar and Badruddin, 2014a, and references therein). To study the relative GCR effectiveness of HSS that are associated or are not associated with shocks, we first divided all the HSS into two groups: those associated with shocks, and those not associated with shocks. The superposed-epoch plots of GCR intensity variation and simultaneous changes in solar-wind plasma/field parameters three days before and fifteen days after the arrival of shock-associated HSS and those not associated with shocks are shown in Figure 4.8. From these averaged temporal profiles obtained after subjecting the hourly data to superposed-epoch analysis we observe that the HSS associated with shocks are about three times more GCR effective than those not associated with shocks, even though the average enhancement in speed of the HSS in both the cases is equal. However, the enhancements in magnetic-field vector [ΔF] and enhancement in field fluctuation/turbulence [$\Delta\sigma_F$] are ≈ 1.5 times higher for shock-associated HSS than for HSS not associated with shocks (see Table 4.5a).

As far as the GCR effectiveness of individual stream is concerned, only 258/337 of HSS that are not-associated with a shock are GCR effective; about 90 % of these are in the small GCR-effective category or are moderately GCR effective. On the other hand, 196/235 of the HSS associated with shocks are GCR-effective, and a significant number of them (≈ 35%) are in the large or very large GCR-effective category (see Table 4.5b).

A statistical distribution of the HSS velocity by grouping individual stream speeds into suitable intervals is represented in Figure 4.9 in the form of histograms for the HSS (A) associated and (B) not associated with shocks. Gaussian-fit curves representing these distributions of V_{max} are also drawn. For comparison, these fitted curves are shown separately in Figure 4.10. It can be seen from these figures that the shapes of two curves representing V_{max} almost overlap, and the central-peak values of V_{max} are also similiar. However a similar statistical distribution of interplanetary magnetic-field vector [F_{max}], during individual HSS that are associated or are not-associated with shocks and the best-fit Gaussian curve shows a shift toward higher values in the distribution, and the central-peak value [x_c] of F_{max} and σ_{Fmax} in the fitted

curves is higher for the shock-associated HSS (see Figures 4.11, 4.12, 4.13, and 4.14).

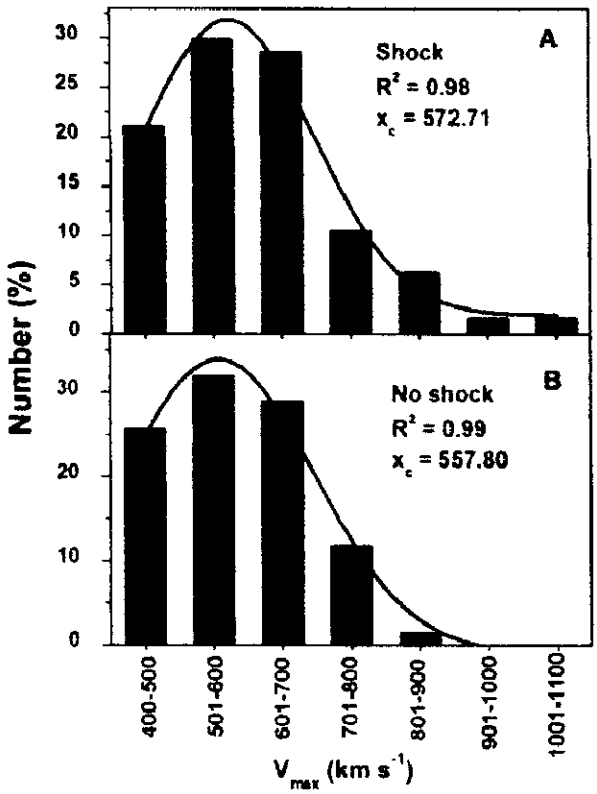

Figure 4.9 Frequency distribution of the highest speed [V_{max}, km s^{-1}] observed during the passage of high-speed streams associated or not associated with shocks.

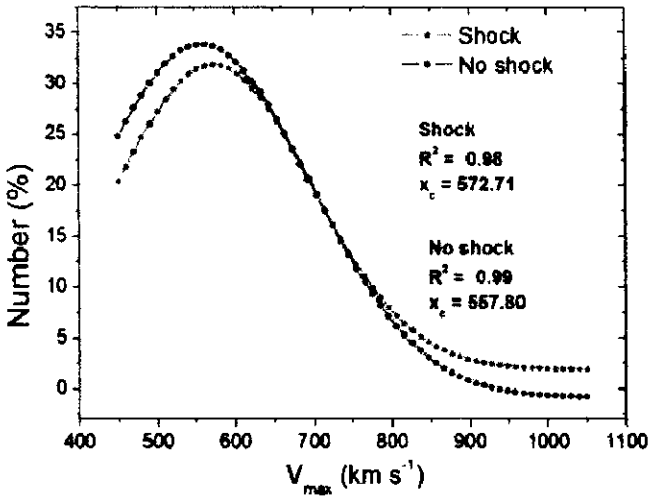

Figure 4.10 Gaussian best-fit curves representing the distribution of the highest speed [V_{max}] observed during the passage of HSS associated or not associated with shocks. Central peak values [x_c] obtained from the fits are also given.

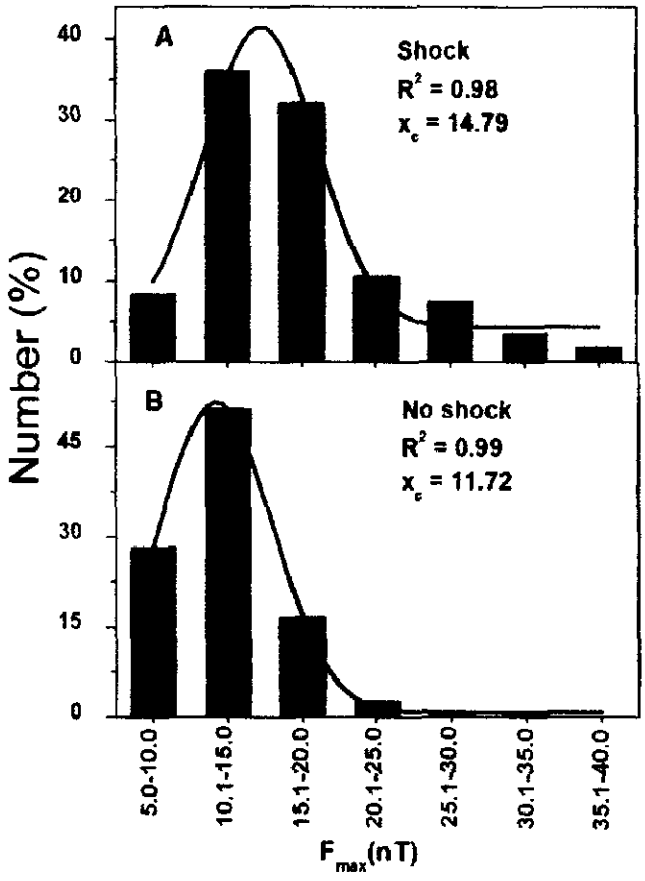

Figure 4.11 Frequency distribution of the strongest magnetic field [F_{max}, nT] observed during the passage of HSS associated or not associated with shocks.

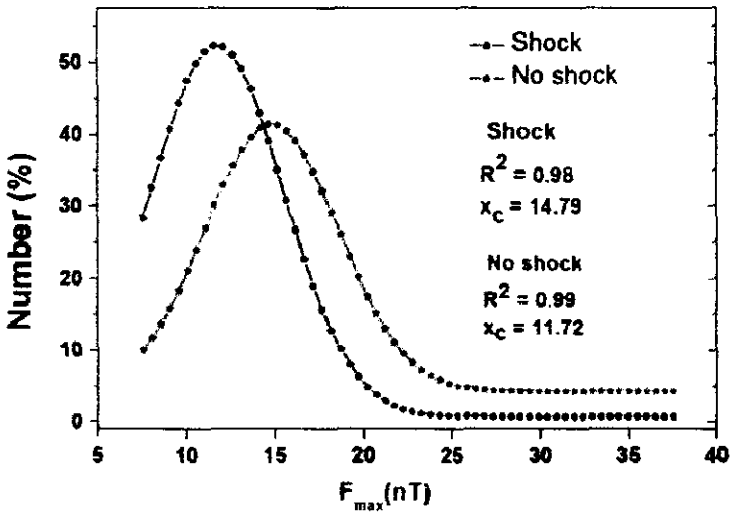

Figure 4.12 Gaussian best-fit curves representing the distribution of the strongest magnetic field [F_{max}] observed during the passage of HSS associated or not associated with shocks. Central peak values [x_c] obtained from the fits are also given.

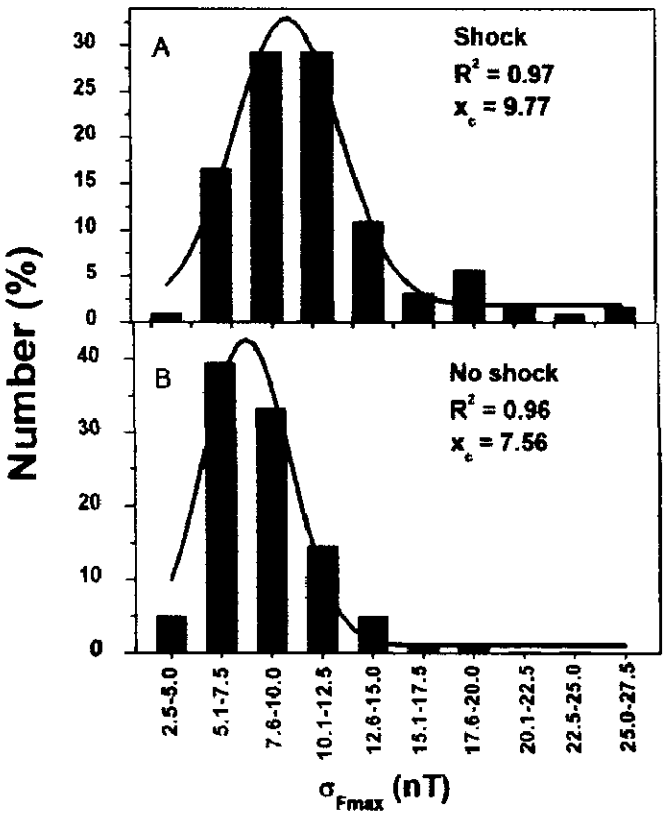

Figure 4.13 Frequency distribution of the highest standard deviation of the magnetic field [σ_{Fmax}, nT] observed during the passage of HSS associated or not associated with shocks.

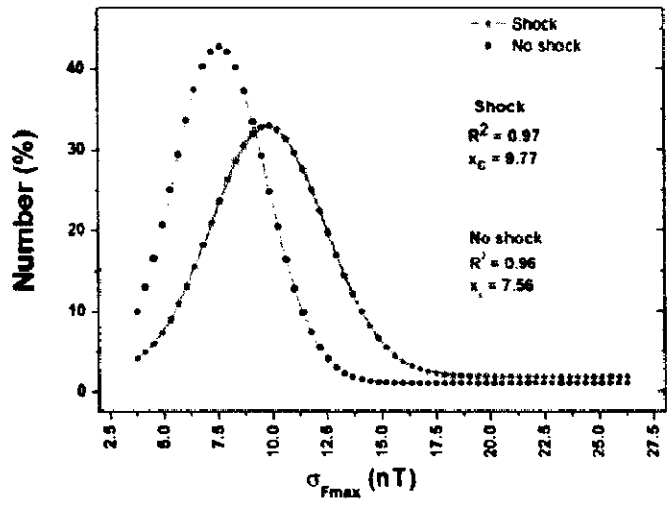

Figure 4.14 Gaussian best-fit curves representing the distribution of the highest standard deviation of the magnetic field [σ_{Fmax}] observed during the passage of HSS associated or not associated with shocks. Central peak values [x_c] obtained from the fits are also given

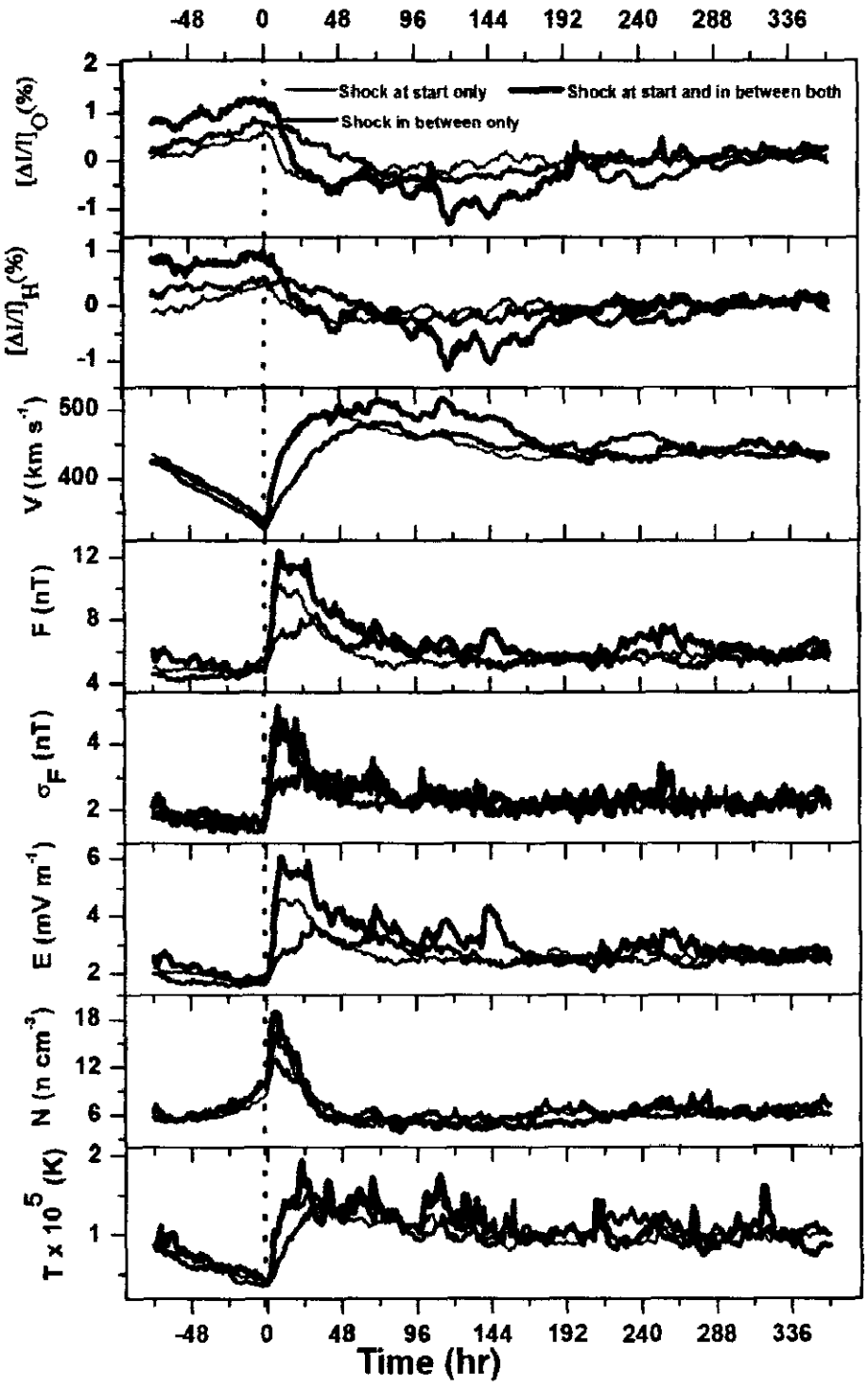

Figure 4.15 Superposed-epoch analysis results of the GCR-intensity variation recorded at Oulu NM $[\Delta I/I]_O$ (%), at Hermanus NM $[\Delta I/I]_H$ (%), the solar-wind velocity [V, km s^{-1}], interplanetary magnetic field vector [F, nT], standard deviation of magnetic field [σ_F, nT], electric field [E, mV m^{-1}], plasma density [N, n cm^{-3}], and the plasma temperature [T, 10^5 K] plotted for arrival time of the high-speed streams (zero hour) of three categories based on the arrival of shocks.

We have observed that HSS associated with a shock or sheath is more GCR effective than those not associated with such structures. However, it was realized that during the whole span of the HSS duration (from the start to returning to the pre-decrease level speed), shocks may occur at the beginning of the HSS, in between the start and the end of the HSS, and both at start and in between the HSS duration. It will be interesting to determine whether the GCR effectiveness of these three types of shock-associated HSS is the same or different and whether the temporal profiles of GCR intensity are similar or not for these three stream categories associated with shocks.

As shown in Figure 4.15, there are differences both in amplitudes and time profiles in these three cases. The intensity depression is greatest among the three cases when the shock occurs at the start and in between the start and the end of the HSS as well; depression also occurs for an extended period before it begins to recover. In this case, as well as in the case when there is a shock only at the start, the initial depression is faster than when the shock only occurs in between the start and the end of the HSS; in this later case the intensity depression progresses slowly to reach a minimum level and then recovery occurs. As regards the enhancements in solar-wind plasma/field parameters during the passage of these three HSS categories, on average, there are only small differences in velocity enhancements during the passage of the three HSS categories. However, enhancements in F and σ_F, are largest for a shock both at the start and in between the HSS, and the enhancements in these two parameters are smallest when a shock only occurs in between the start and the end of the HSS (see Table 4.5a). This again emphasizes the role of enhanced F and/or σ_F in influencing the depression amplitude.

From the study of GCR effectiveness of individual streams of the three shock-groups, we observe that their GCR effectiveness is distributed in small, moderate, large, and very large GCR-effective categories. However, ≈ 43 % of shock-group E HSS produce GCR depressions in the large or very large category, while the contributions of shock-group HSS C and D together are only ≈ 26 % and ≈ 38 % to these categories of GCR effectiveness (4.5b).

Table 4.5c Time lag/lead between the minima of GCR-intensity depression and corresponding maxima in interplanetary parameters caused by HSS that are associated or are not associated with shocks.

Shock group	Source of structure	Main phase [hrs]	$(\Delta t)_V$ [hrs]	$(\Delta t)_F$ [hrs]	$(\Delta t)_N$ [hrs]	$(\Delta t)_T$ [hrs]	$(\Delta t)_{\sigma F}$ [hrs]	$(\Delta t)_E$ [hrs]
A	All shocks	116	−68	−105	−109	−90	−108	−92
B	No shock	57	+4	−27	−36	−13	−32	−23
C	Shock only at start	45	+3	−34	−37	−19	−33	−34
D	Shock only in between	96	−20	−56	−83	−19	−67	−59
E	Shock start and in between both	119	−71	−109	−112	−96	−110	−109

Table 4.5d Linear correlation coefficients [R] obtained from linear correlation between temporal variation of the GCR-intensity depressions and the corresponding parameters [V, F, σ_F, E, N, and T] during the main and recovery phases of intensity depression due to different stream categories based on shock arrival time.

Structure group	Value of R between ΔI and various parameters											
	During main phase						During recovery phase					
	V	F	σ_F	E	N	T	V	F	σ_F	E	N	T
All shocks	−0.95	0.51	0.58	0.23	0.92	−0.55	−0.84	0.21	0.16	−0.41	0.71	**−0.21**
No shock	−0.88	−0.24	−0.32	−0.61	0.80	−0.81	−0.13	−0.16	−0.10	−0.20	−0.01	−0.11
Shock only at start	−0.98	−0.18	0.12	−0.43	0.70	−0.85	−0.87	−0.11	−0.14	−0.52	0.61	−0.67
Shock only in between	−0.92	0.02	−0.15	−0.55	0.89	−0.68	−0.82	−0.19	−0.04	−0.41	0.54	−0.19
Shock both at start and in between	−0.90	0.44	0.64	0.26	0.88	−0.35	−0.82	−0.04	0.06	−0.45	0.72	−0.24

The statistical distribution of the velocity [V_{max}] for three types of shock-associated HSS is as follows: (C) the shock observed at the beginning of the HSS, (D) the shock observed any time in between the HSS duration, and (E) the shock observed at the start as well as in between the HSS. This is shown in the form of a histogram in Figure 4.16. The distribution for type C and D HSS are similar, while the distribution shifts toward higher values of V_{max} for type E HSS. The best-fit Gaussian curves for the first two HSS types (C and D) almost overlap and the central-peak value of V_{max} is almost equal for these two. However, for the third category of shock-associated HSS, when the shock occurs both at the start and in between the start and the end of the HSS, the distribution is shifted towards higher V_{max} values. The central peak values for case E are also higher than in the other two cases (see Figure 4.17). However, the distribution of magnetic field [F_{max}] during the HSS of the three types (C, D, and E) shows a strong shift in distribution towards higher values for type E HSS compared with types C and D; both of these (type C and D) show a similar distribution (Figure 4.18). There is a large difference in the central-peak values of F_{max} for type E HSS as compared with HSS of type C and D; it is much higher for type E HSS (Figure 4.19). The shift in central peak value of σ_F is also observed to be strongest toward the higher side (see Figures 4.20 and 4.21).

The study of the time lag between GCR-intensity minimum and the interplanetary plasma/field parameter maximum based on the superposed plots shows that these time lags are different for different interplanetary parameters. However, comparatively, the time lag is smallest with solar-wind velocity maximum (see Table 4.5c), as was observed in earlier classifications.

We searched for the parameter that best correlates in the GCR-intensity variation both during the main and the recovery phase. This study was made during GCR-intensity modulation caused by i) all the HSS associated with shocks, ii) all the HSS not associated with shocks, iii) shock only at the start, iv) shock only in between the start and the end of the HSS, and v) shock both at the start and in between the start and the end of the HSS. Regardless of the HSS shock-group, the time variation of the GCR intensity best correlates with the time variation of the solar-wind velocity both during the main as well as during the recovery phase (see Table 4.5d).

A summary of the central peak values [xc] obtained from the Gaussian fit plots (see Figures 4.9 – 4.14 and Figures 4.16 – 4.21) for the distribution of V_{max}, F_{max}, and

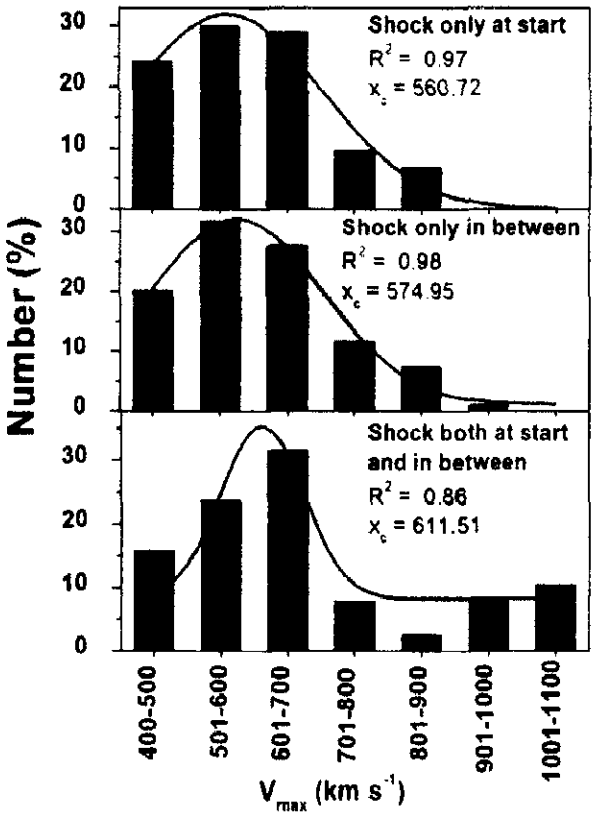

Figure 4.16 Frequency distribution of the highest speed [V_{max}, km s^{-1}] observed during the passage of different HSS categories based on the arrival time of shocks.

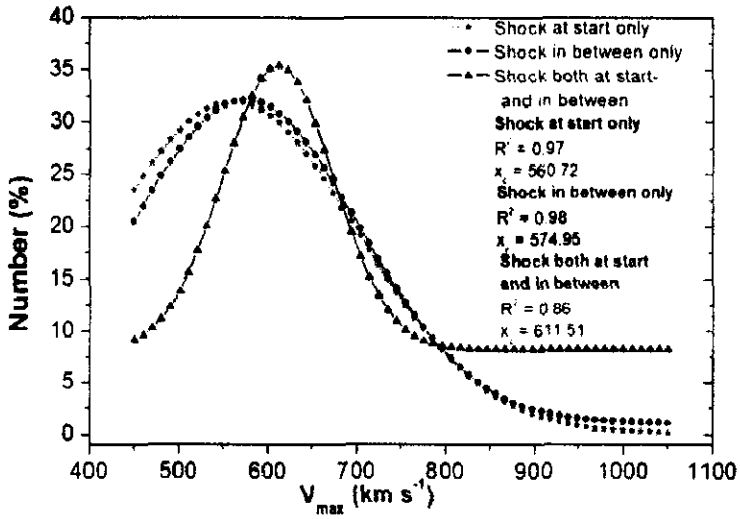

Figure 4.17 Gaussian best-fit curves representing the distribution of the highest speed [V_{max}] observed during the passage of different HSS categories based on the arrival of shocks. Central peak values [x_c] obtained from the fits are also given.

σ_{Fmax}, during the passage of various groups of HSS based on their shock association, are presented in Table 4.6.

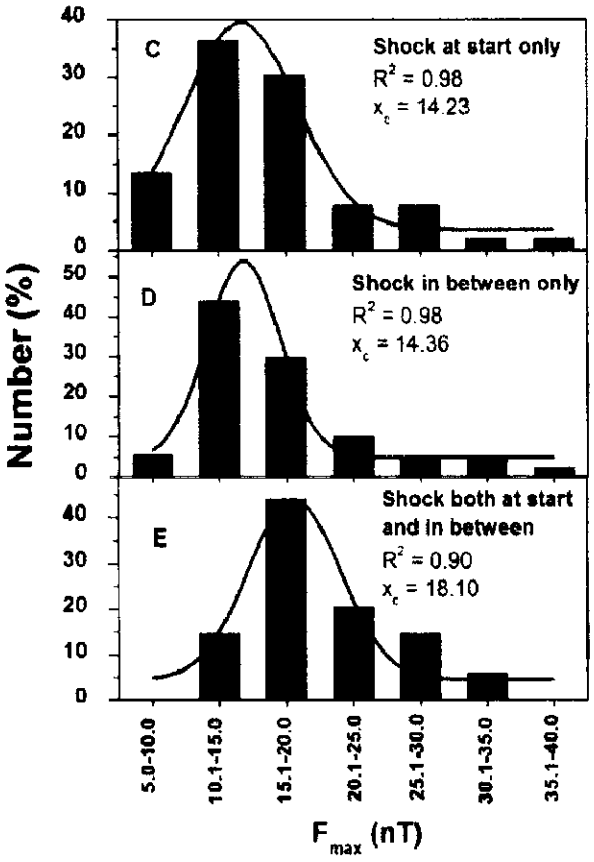

Figure 4.18 Frequency distribution of the strongest magnetic field [F_{max}, nT] observed during the passage of different HSS categories based on the arrival of shocks.

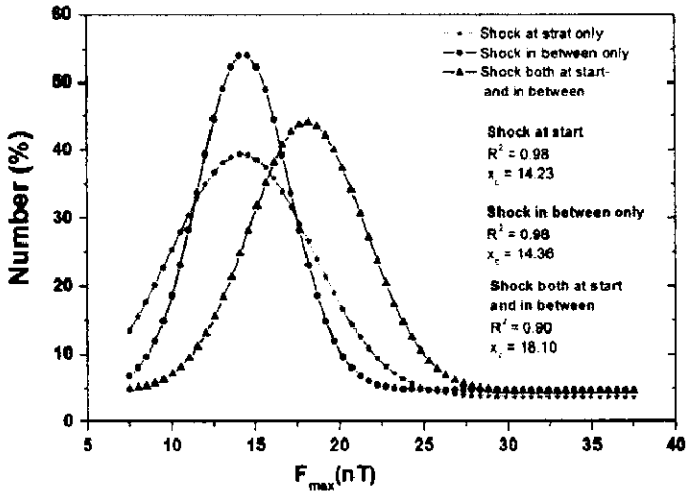

Figure 4.19 Gaussian best-fit curves representing the distribution of the strongest magnetic field [F_{max}] observed during the passage of different HSS categories based on the arrival of shocks. Central peak values [x_c] obtained from the fits are also given.

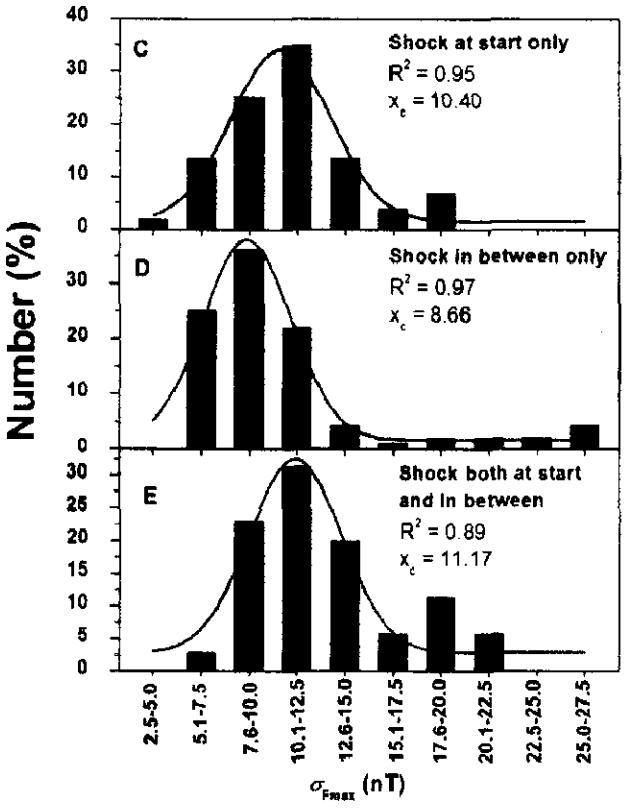

Figure 4.20 Frequency distribution of the highest standard deviation of the magnetic field [$\sigma_{F_{max}}$, nT] observed during the passage of different HSS categories based on the arrival of shocks.

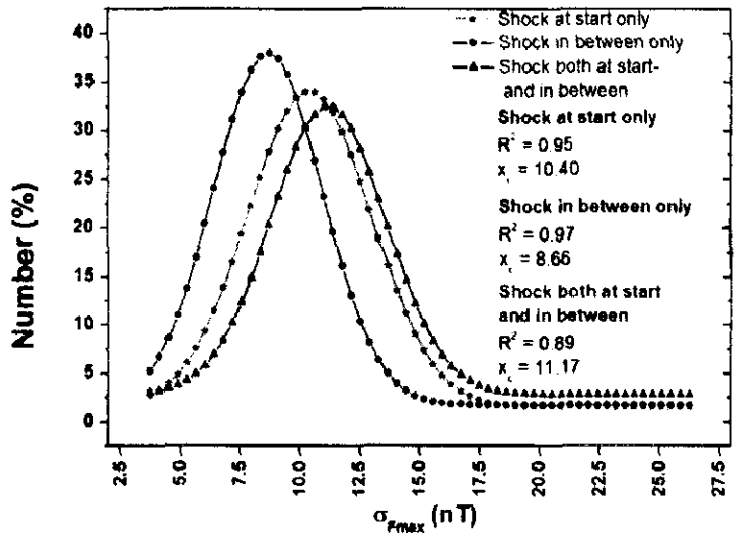

Figure 4.21 Gaussian best-fit curves representing the distribution of the highest standard deviation of the magnetic field [$\sigma_{F_{max}}$] observed during the passage of different HSS categories based on the arrival of shocks. Central peak values [x_c] obtained from the fits are also given.

Table 4.6 Central peak value [x_c] obtained from Gaussian fit [$y = y_0 + (A/w\sqrt{\pi/2})\ \exp(-2(x - x_c)^2/w^2)$] for the distribution of V_{max}, F_{max}, and σ_{Fmax} during the HSS passage grouped into five categories based on their shock association.

Shock group	HSS-association	Gaussian-fit parameter x_c for		
		V_{max} [km s^{-1}]	F_{max} [nT]	σ_{Fmax} [nT]
A	All Shock	572.71 ± 10.14	14.79 ± 0.34	9.77 ± 0.21
B	No Shock	557.80 ± 8.99	11.72 ± 0.07	7.56 ± 0.21
C	Shock only at start	560.72 ± 16.55	14.23 ± 0.37	10.40 ± 0.27
D	Shock only in between	574.95 ± 9.75	14.36 ± 0.37	8.66 ± 0.20
E	Shock both at start and in between	611.51 ± 17.62	18.10 ± 0.80	11.17 ± 0.40

The plot of the GCR intensity and the solar-wind velocity during the main phase of the intensity decrease obtained from the superposed results is shown in Figure 4.22. Although in general the correlation between the two parameters is good, the rate at which GCR-intensity decreases with the increase in solar-wind velocity is different for all five HSS shock-groups; this rate of decrease with increase in solar-wind velocity is lowest (0.21×10^{-2}) when no shock is associated with the HSS and it is highest (1.3×10^{-2}) when there is a shock at the start and in between (see Figure 4.22). This indicates that although the temporal variation of GCR intensity in general follows the temporal variation of solar-wind velocity, the decrease rate depends on other factors as well.

We have seen earlier that even though the enhancement in solar-wind velocity due to streams in certain cases is almost the same, the amplitude of the decrease is quite different. Therefore, to search for the parameter that best correlates with the decrease amplitude caused by HSS of different groups, we obtained scatter plots of GCR-intensity-decrease amplitude [ΔI] and enhancements in various plasma/field parameters [ΔV, ΔF, and $\Delta\sigma_F$]. These are shown in Figure 4.23. It shows that the correlation of ΔI with ΔV is poor, but is much better with ΔF and $\Delta\sigma_F$. This may be interpreted as meaning that not the speed of HSS, but the enhancements in F and σ_F are the more important factors in deciding the extent (amplitude) of the decrease during the passage of HSS, which emphasize the significant role of magnetic turbulence in GCR-intensity modulation by scattering cosmic-ray particles.

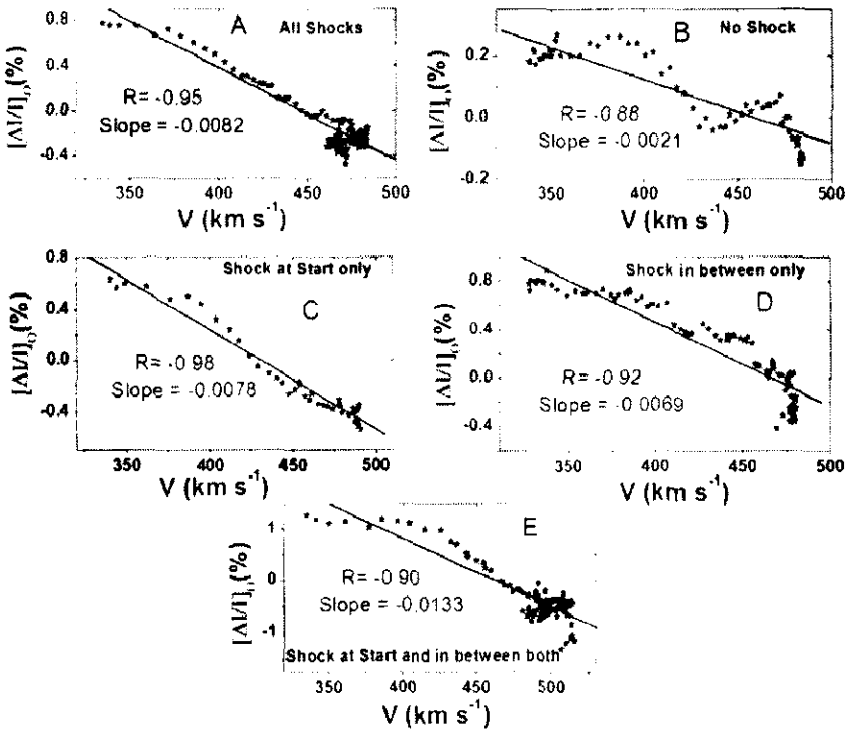

Figure 4.22 Relationship between the averaged temporal variation of the solar-wind velocity and the GCR-intensity depressions during the main phase of the intensity decrease caused by the five stream categories based on the arrival of shocks.

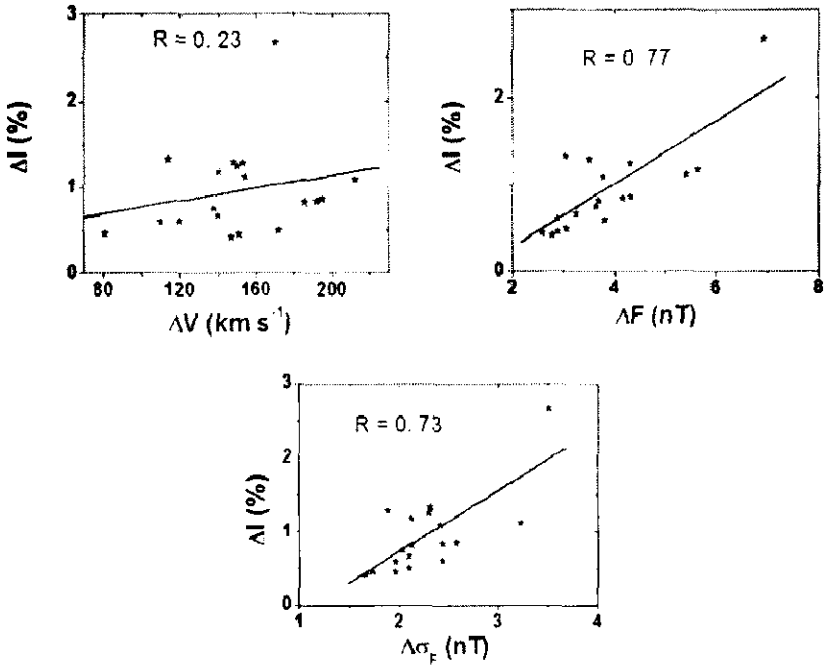

Figure 4.23 Relation between the amplitudes of the GCR-intensity decrease and enhancements in various parameters [ΔV, ΔF, and $\Delta\sigma_F$] obtained form average plots caused by streams grouped on the basis of different criteria (*i.e.* solar-wind speed, HSS duration, solar sources, and presence or absence of accompanying shocks).

4.4 Summary and Conclusions

- High-speed streams identified in interplanetary plasma and field data have a wide range of speeds. The durations of these streams are quite variable; the duration of longer streams is as much as ten times the duration of shorter streams. Individual streams, as observed in near-Earth space, are a consequence of flows caused by the coronal hole(s), coronal mass ejection(s) propagating interplanetary shock(s), and/or their superposed effects.
- Our study of the influence of the HSS velocity on the GCR-intensity variation showed that on average the GCR-intensity decreases at the arrival time of the stream with streams of higher speed, which produce more depressions. However, the streams of any speed-group are not all GCR effective, nor are all the streams of each group equally GCR effective. This supports the earlier conclusion that the velocity of the stream is not the only parameter that decides the GCR effectiveness of individual HSS. From the averaged time profile of the GCR intensity and solar-wind parameters [V, F, σ_F, E, N, and T], we observed that although after the HSS arrival all these solar-wind parameters increase and reach a maximum level, there are time lags between the maxima of these parameters and minima in GCR intensity; however, this time lag is least with V compared with the other solar-wind parameters [F, σ_F, E, N, and T]. Moreover, the temporal variation in V better follows (in anti-phase) the temporal variation in GCR intensity both during the main and the recovery phases.
- The duration of the stream influences the temporal profile of the GCR-intensity depressions, including the recovery of the GCR intensity; for a longer stream duration, the depression in intensity persists for a longer time. However, the streams of each duration-group are not all GCR effective, nor are they equally GCR effective; their individual GCR effectiveness is different, ranging from small, moderate, and large to very large. Similar to the average temporal behavior in individual speed-groups, the temporal variation of V better follows the temporal variation of the GCR intensity (in anti-phase) with minimum time lag compared with the other solar parameters. However, the decrease rate in GCR intensity with the increase in the solar-wind velocity is different for all speed-groups. This again indicates that some other factors

also influence the rate at which the GCR intensity decreases during the main phase.

- Sources of the individual HSS observed in near-Earth space were traced to the solar atmosphere as streams caused by i) a single coronal hole, ii) multiple coronal holes, iii) a single CME, iv) multiple CMEs, and v) a compound stream formed by coronal hole(s) and CME(s) (Gupta and Badruddin, 2010). The analysis of the GCR-intensity variations caused by these streams from different types of sources showed that although not all the streams from each group are GCR effective, on average, listed in order of increasing GCR effectiveness these are the streams from a single coronal hole, multiple coronal holes, a single CME, compound streams caused by coronal hole(s) and CME(s), and by multiple CMEs. Moreover, the relation between the variations of V and GCR intensity is better during both the main and the recovery phase. However, the intensity rate decrease with the increase in solar-wind velocity during the main phase is different for all five HSS source-groups; this rate is highest for multiple mass-ejection streams and lowest for streams from a single coronal hole.
- We divided all of the streams into two groups on the basis of their shock association, *i.e.* those associated and those not associated with a shock or sheath region. A superposed-epoch analysis of these two stream groups indicated that the HSS associated with shocks are about three times more GCR effective than those not associated with shocks, even though the enhancement in the average HSS speed in both cases is nearly equal. Moreover, we observed from these superposed plots that the enhancements in the magnetic field vector [ΔF] and also the enhancement in the field fluctuation/turbulence [$\Delta\sigma$F] are ≈1.5 times higher for shock-associated HSS than for HSS that are not associated with shocks. Furthermore, as regards the GCR effectiveness of individual streams, about 90 % of the HSS not associated with shocks are either moderately GCR effective or their GCR effectiveness is small. On the other hand, for a significant number of streams associated with shocks (≈35 %), the GCR effectiveness is either large or very large. However, during the whole duration of the HSS, shocks may occur at i) the beginning of the HSS, ii) in between the start and the end of the HSS, and iii) both at the start and in between the HSS span. The analysis of the GCR intensity together with the

solar-wind parameters showed that both amplitude and temporal profiles of the GCR-intensity variations were different in these three cases. Out of these three cases, the intensity depression was strongest when the shock occurred both at the start of the HSS and in between the start and the end of the HSS. In this case, as well as in the case when the shock only occurred at the start, the initial depression was faster than for an HSS where the shock only occurred in between the start and the end of the HSS. For the average variations in solar-wind parameters the difference in velocity enhancements in the three cases is small; however, enhancements in F and σ_F were highest when a shock occurred at the start and in between the start and the end of the HSS. We furthermore note that regardless of the HSS shock group, for all five groups, the temporal variation of GCR intensity best follows the temporal variation of solar-wind velocity (in antiphase) both during the main and during the recovery phase of the GCR-intensity variation, as also observed for the groupings mentioned above. However, the decrease rate in GCR intensity with the increase in solar-wind velocity during the main phase is lowest for the no-shock group of the HSS, and this rate is highest for the shock-group when the shock occurs at the start and in between the start and the end of the HSS.

- A correlation analysis between the amplitudes of GCR intensity [ΔI] obtained for different categorization of streams and corresponding amplitudes in solar plasma and field parameters, particularly enhancements in velocity [ΔV], magnetic-field vector [ΔF], and field-vector standard deviation [$\Delta\sigma$F], showed that the correlation between ΔI and ΔV is poor, but it is much better with ΔF and $\Delta\sigma$F. This again emphasizes the role of the enhanced and turbulent magnetic field in producing larger amplitude depressions in the GCR intensity, such as Forbush decreases.

****

Chapter 5

SUMMARY AND CONCLUSIONS

This last chapter presents the summary of the research work carried out in this thesis and conclusions drawn from the study of influence of different structures/features of solar wind on the cosmic-ray intensity.

On the basis of results of our analysis of the cosmic-ray intensity together with interplanetary plasma and field parameters during the passage of ICMEs, CIRs and High-speed solar-wind streams (HSS) of solar cycle 23, and in the light of discussions presented in previous Chapters, the following conclusions have been drawn.

- More than 200 ICMEs were detected during the period 1996 – 2009 (solar cycle 23). Survey of the response of individual ICMEs on GCR intensity was done. Based on this survey, we classified the GCR response (depressions) in five groups; quiet ($\Delta I \approx 0.0$), small ($\Delta I \approx -0.01$ to -0.49 %); moderate ($\Delta I \approx -0.50$ to -1.49 %); large ($\Delta I \approx -1.50$ to -2.99 %); and very large (ΔI larger than -3.00 %). Nearly half (48.4 %) of the total ICMEs, identified in the near-Earth interplanetary plasma/field data, either do not produce any depression in GCR intensity (17.3 %) or produce 'small' depressions of less than 0.5 % (31.1 %). The rest of the ICMEs either produce the so-called moderate (27.3 %), large (11.8 %), or very-large (12.5 %) depressions in GCR intensity.
- The average GCR-intensity depression profile due to the four groups of GCR effective ICMEs (small, moderate, large, and very large) with successively increasing depressions start at the arrival of ICME-related disturbance, with a relatively sharper decrease at first up to a few hours, followed by a slower decrease until minimum intensity is reached. Subsequently recovery starts, reaching the pre-decrease level in a much longer time (a few days).
- It is found from the frequency distribution of plasma/field parameter (speed, magnetic-field vector, and electric fields) that the distribution of these parameters, their peak values, and the spread of frequency distribution shift successively towards the higher side from the quiet, small, moderate, large, to very large group of GCR effective ICMEs.
- From statistical analysis of five groups of GCR-effective ICMEs (quiet, small, moderate, large, and very large) associated/not associated with different structures/features, we found that "large" and "very large" depressions together are much larger (37.3 %) due to shock-associated ICMEs than those not associated with shocks (11.9 %). Similarly a larger number of large and very large depressions in GCR intensity are associated with ICMEs with BDE rather than to non-BDE ICMEs, magnetic clouds rather than to ICMEs having

another than the magnetic-cloud structure, and ICMEs due to halo ICMEs rather than due to non-halo ICMEs.

- The central-peak values, full width at half maximum, and their products obtained from Gaussian fits to distributions of different parameters [V_{max}, F_{max}, and E_{max}] due to shock, BDE, MC, and halo ICMEs are larger than those not associated with these structures/features.
- ICMEs associated with shocks/BDEs/MCs/halo-CMEs are 1.5 to 4 times more GCR-effective and have larger enhancements in plasma/field parameters than those due to ICMEs not associated with these structures/features respectively.
- From the best-fit linear relation between averaged GCR-intensity depressions [%] and maximum values of magnetic [F_{max}] and electric fields [E_{max}], we found that GCR intensity decreases at the rate of ≈ 0.40 % per unit increase in vector magnetic field [nT] and ≈ 0.50 % per unit increase in electric field [mV m^{-1}].
- An exponential fit to the recovery of GCR intensity reveals that the characteristic recovery time is much larger for shock/BDE/MC/halo-CME-associated ICMEs than those not associated with these structures/features.
- ICMEs are found to be more GCR effective as compared to CIRs, even though the enhancement in solar-wind velocity due to CIRs is larger than the enhancements in solar-wind velocity due to CIRs is larger than the enhancement due to ICMEs. However, the average amplitudes of interplanetary magnetic and electric field vectors are larger during the passage of ICMEs. In addition to amplitudes, the time profiles of GCR intensity depressions are also different due to these two interplanetary structures in agreement with earlier findings.
- The average amplitude of GCR intensity depression for ICMEs is ~ 1.5% as compared for CIRs which is ~ 0.5% and the ratio of intensity depression due to shock-associated CIRs to non-shock CIRs is about 2.5.
- The GCR intensity depression in general starts at the arrival of ICMEs, whether associated with shocks or not; however depression is much larger due to shock-associated ICMEs in agreement with previous studies, emphasizing the importance of shock/sheath region in transient modulation of GCRs.

- The CIRs with forward shock are more effective in depressing the GCR intensity than those not associated with shock although the time profiles of GCR intensity in two cases are almost similar; slow depression to a minimum and a long and slow recovery.
- At the arrival of stream interface within CIRs, a further decrease in GCR intensity generally to takes place.
- From the average plots obtained from superposed-epoch analysis, the time variation of GCR intensity due to ICMEs, during the main (decrease) phase, is found to be better correlated with time variation of magnetic field vector. However time variation of solar-wind velocity better correlates with GCR intensity during this phase, in case of decrease due to CIRs. During the recovery phase, the temporal variation of GCR intensity is found to be better correlated with simultaneous variations in solar-wind velocity, during the recovery of decrease both due to ICMEs as well CIRs.
- The amplitude of depression is maximum for the case of shock-associated ICMEs, a fast-decrease starts at the arrival of disturbance and minimum intensity is reached within ~ 18 hours. Sudden enhancement in F and σ_F at the beginning and σ_F remaining enhanced till about the same duration emphases the important role of enhanced and turbulent magnetic field in such decreases through the scattering of cosmic rays by the enhanced and turbulent field region.
- Our study of the influence of the HSS speed/duration on the GCR-intensity variation showed that on average the GCR-intensity decreases at the arrival time of the stream with streams of higher speed/duration, which produce more depressions. However, the streams of any speed or duration group are not all GCR effective, nor are all the streams of each group equally GCR effective. From the averaged time profile of the GCR intensity and solar-wind parameters [V, F, σ_F, E, N, and T], we observed that although after the HSS arrival all these solar-wind parameters increase and reach a maximum level, there are time lags between the maxima of these parameters and minima in GCR intensity; however, this time lag is least with V compared with the other solar-wind parameters [F, σ_F, E, N, and T]. Moreover, the temporal variation in

V better follows (in anti-phase) the temporal variation in GCR intensity both during the main and the recovery phases.

- The analysis of the GCR-intensity variations caused by the streams from different types of sources (a single coronal hole, multiple coronal holes, a single CME, multiple CMEs, and a compound stream formed by coronal hole(s) and CME(s)) showed that although not all the streams from each group are GCR effective, on average, listed in order of increasing GCR effectiveness these are the streams from a single coronal hole, multiple coronal holes, a single CME, compound streams caused by coronal hole(s) and CME(s), and by multiple CMEs. Moreover, the relation between the variations of V and GCR intensity is better during both the main and the recovery phase. However, the intensity rate decrease with the increase in solar-wind velocity during the main phase is different for all five HSS source-groups; this rate is highest for multiple mass-ejection streams and lowest for streams from a single coronal hole.
- The HSS associated with shocks are about three times more GCR effective than those not associated with shocks, even though the enhancement in the average HSS speed in both cases is nearly equal. Moreover, we observed from these superposed plots that the enhancements in the magnetic field vector [ΔF] and also the enhancement in the field fluctuation/turbulence [$\Delta\sigma$F] are $\approx$ 1.5 times higher for shock-associated HSS than for HSS that are not associated with shocks. Furthermore, as regards the GCR effectiveness of individual streams, about 90 % of the HSS not associated with shocks are either moderately GCR effective, or their GCR effectiveness is small. On the other hand, for a significant number of streams associated with shocks ($\approx$ 35 %), the GCR effectiveness is either large or very large. However, during the whole duration of the HSS, shocks may occur at i) the beginning of the HSS, ii) in between the start and the end of the HSS, and iii) both at the start and in between the HSS span. The analysis of the GCR intensity together with the solar-wind parameters showed that both amplitude and temporal profiles of the GCR-intensity variations were different in these three cases. Out of these three cases, the intensity depression was strongest when the shock occurred both at the start of the HSS and in between the start and the end of the HSS. In this

case, as well as in the case when the shock only occurred at the start, the initial depression was faster than for an HSS where the shock only occurred in between the start and the end of the HSS. For the average variations in solar-wind parameters the difference in velocity enhancements in the three cases is small; however, enhancements in F and σ_F were highest when a shock occurred at the start and in between the start and the end of the HSS. We furthermore note that regardless of the HSS shock group, for all five groups, the temporal variation of GCR intensity best follows the temporal variation of solar-wind velocity (in antiphase) both during the main and during the recovery phase of the GCR-intensity variation, as also observed for the groupings mentioned above. However, the decrease rate in GCR intensity with the increase in solar-wind velocity during the main phase is lowest for the no-shock group of the HSS, and this rate is highest for the shock-group when the shock occurs at the start and in between the start and the end of the HSS.

- A correlation analysis between the amplitudes of GCR intensity [ΔI] obtained for different categories of streams and corresponding amplitudes in solar plasma and field parameters, particularly enhancements in velocity [ΔV], magnetic-field vector [ΔF], and field-vector standard deviation [$\Delta\sigma$F], showed that the correlation between ΔI and ΔV is poor, but it is much better with ΔF and $\Delta\sigma_F$. This again emphasizes the role of the enhanced and turbulent magnetic field in producing larger amplitude depressions in the GCR intensity, such as Forbush decreases.
- We found that whether it is CME, CIR, or HSS, the amplitude of GCR intensity depression is much more when shock/sheath region is formed ahead of these structures/features. Moreover, the magnetic-field vector amplitude/enhancements and/or turbulence in it (represented by σ_F) best correlate with the amplitude of depression. These results emphasize the importance of enhanced and turbulent magnetic field in depressing the GCR intensity through the scattering of GCRs by the enhanced and turbulent magnetic field region.

****

BIBLIOGRAPHY

Abbrescia, M., Aiola, S., Antolini, R., Avanzini, C., Baldini, F.R., Bencivenni, G., *et al.*: 2011, *Eur. Phys. J. Plus.* **126**, 61.

Abhayankar, K.P.: 1977, *Bull. Astron. Soc. India*, **5**, 40.

Alanko, H.K., Usoskin, I.G., Marsula, K., Kovoltsov, G.A.: 2007, *J. Geophys. Res.* **112**, A08101.

Alves, M.V., Echer, E., Ganzalez, W.D.: 2011, *J. Atmos. Sol. Terr. Phys.* **73**, 1380.

Ananth, A.G., Venkatesan, D.: 1993, *Solar Phys.* **143**, 373.

Arunbabu, K.P., Antia, H.M., Dugad, S.R., Gupta, S.K., Hayashi, Y., Kawakami, S., *et al*: 2013, *Astron. Astrophys.* **555**, A139.

Aslam, O.P.M., Badruddin: 2014, *Solar Phys.* **289**, 2247.

Augusto, C.R.A., Kopkinen, V., Navia, C.E., Tsui, K.H., Shigueoka, H., Fauth, A.C., *et al.*: 2012, *Astrophys. J.* **759**: 143.

Axford, W.I.: 1962, *J. Geophys. Res.* **67**, 3791.

Badruddin: 1997, *Astrophys. Space Sci.* **246**, 171.

Badruddin: 1998, *Planet Space Sci.* **46**, 1015.

Badruddin: 2000, *Nuovo Cimento*, **C23**, 217.

Badruddin: 2002, *Solar Phys.* **209**, 195.

Badruddin: 2006, *Astron. Astrophys.* **27**, 209.

Badruddin, Singh, Y.P.: 2009, *Planet. Space Sci.* **57**, 318.

Badruddin, Venkatesan, D., Zhu, B.Y.: 1991, *Solar Phys.* **134**, 203.

Badruddin, Yadav, R.S., Yadav, N.R.: 1986, *Solar Phys.* **105**, 413. .

Badruddin, Yadav, R.S., Yadav, N.R., Agrawal, S.P.: 1985, In: Jones, F.C., Admas, J., Mason, G.M. (eds.) *Proc. 19th Int. Cosmic Ray Conf. La Jolla*, **5**, NASA conference Publication 2376, 258.

Balogh, A., Gonzalez-esparza, J.A., Forsyth, R.J., Burton, M.E., Goldstein, B.E., Smith, E.J.: 1995, *Space Sci. Rev.* **72**, 171.

Barouch, E., Burlaga, L.F.: 1975, *J. Geophys. Res.* **80**, 449.

Basu, S., Antia, H.M.: 2008, *Physics Reports*, **457**, 217.

Bazilevskaya, G.A., Cliver,E.W., Kovaltsov, G.A.: Ling, A.G., Shea, M.A.; Smart, D.F., *et al.*: 2014, *Space Sci. Rev.* **186**, 409.

Belov, A., Abunin, A., Abunina, M., Eroshenko, E., Oleneva, V., Yanke, V., *et al.*: 2014, *Solar Phys.* **289**, 3949.

Blanco, J.J., Catalan, E., Hidalgo, M.A., Medina, J., Garcia, O. Rodriguez-Pacheco, J.: 2013, *Solar Phys.* **284**, 167.

Boella, G., Gervasi, M., Mariani, S., Rancoita, P.G., Usoskin, I.G.: 2001, *J. Geophys. Res.* **106**, 29355.

Burlaga, L.F.: 1971, *Space Sci. Rev.* **12**, 600.

Burlaga, L.F.: 1983, *Proc. 18th Int. Cosmic Ray Conf.* **12**, 21.

Burlaga, L.F.:1995, *Interplanetary Magnetohydrodynamics*. New York, U.S.A.: Oxford University Press.

Burlaga, L.F., Behannon, K.W.: 1982, *Solar Phys.* **81**, 181.

Burlaga, L.F., King, J.A.: 1979, *J. Geophys. Res.* **84**, 663.

Burlaga, L.F., Sittler, E., Mariani, F., Schwenn, R.: 1981 *J. Geophys. Res.* **86**, 6673.

Burlaga, L.F., Klein, L., Sheeley Jr., N.R., Michels, D.J., Howard, R.A., Koomen, M.J., *et al.*: 1982, *Geophys. Res. Lett.*, **9**, 1317.

Burlaga, L.F., McDonald, F.B., Goldstein, M.L., Lazarus, A.J.: 1985, *J. Geophys. Res.* **90**, 12027.

Cane, H.V.: 1993, *J. Geophys. Res.* **98**, 3509.

Cane, H.V.: 2000, *Space Sci. Rev.* **93**, 55.

Cane, H.V., Richardson, I.G.: 2003, *J. Geophys. Res.* **108**, 1156.

Cane, H.V., Reames, D.V., von Rosenvinge, T.T.: 1988, *J. Geophys. Res.* **93**, 9555.

Cane, H.V., Richardson, I.G., von Rosenvinge, T.T.: 1996, *J. Geophys. Res.* **101**, 21561.

Cane, H.V., Richardson I.G., Wibberenz, G.: 1997, *J. Geophys. Res.* **102**, 7075.

Charbonneau, P.: 2014, *Ann. Rev. Astron. Astrophys.* **52,** 251.

Cheng, A.F., Sarris, E.T., Dadopoulos C.: 1990 , *Astrophys. J.* **350**, 413.

Chowdhury, P., Dwivedi, B.N., Ray, P.C.: 2011, *New Astron.* **16**, 430.

Chree, C.: 1912, *Philos. Trans. Royal Soc. London,* A **212**, 75.

Cliver, E.W., Ling, A.G.: 2001, *Astrophys. J. Lett.* **551**, L189.

Connelly, J.N., Bizzarro, M., Krot, A.N., Nordlund, Å., Wielandt, D., Ivanova, M.A.: 2012, *Science*, **338**, 651.

Cremades, H., Bothmer, V.: 2004, *Astron. Astrophys.* **422**, 307.

Cremades, H., Bothmer, V., Tripathi, D.: 2006, *Adv. Space Res.* **38**, 461.

Dorotovic, I., Kudela, K., Lorenc, M., Rybansky, M.: 2008, *Solar Phys.*, **250**, 339.

Duggal, S. P., Pomerantz, M. A.: 1978, *Geophys. Res. Lett.* **5**, 625.

Dumbovic, M., Vrsnak, B., Calagovic, J., Karlica, M.: 2011, *Astron. Astrophys.* **531**, A91.

Dumbovic, M., Vrsnak, B., Calagovic, J., Zupar, R.: 2012, *Astron. Astrophys.* **548**, A28.

Echer, E., Gonzalez, W.D., Alives, M.V.: 2006, *Space Weather* **4**, S06001.

Erdelyi, R., Ballai, I.: 2007, *Astron. Nachr*, **328**, 726.

Fahr, H.J., Fichtner, H.: 1991, *Space Sci. Rev.* **58**, 193.

Farrugia, C.J., Berdichevsky, D.B.: 2004, *Ann. Geophys.* **22**, 3679.

Feldman, W.C., Asbridge, J.R., Bame, S.T., Gosling, J.T.: 1976, *J. Geophys. Res.* **81**, 5054.

Feldman, U., Schuhle, U., Widing, K.G., Laming, J.M.: 1998, *Astrophys. J.* **505**, 999.

Fisk, L.A.: 1980, In: Pepin, R.O., Eddy, J.A., Merrill, R.B. (eds.) *Proc. Conf. Ancient Sun*, New York and Oxford, Pergamon Press, 103.

Fisk, L.A.: 1996, *J. Geophys. Res.* **101**, 15,547.

Forbush, S.E.: 1937, *Phys. Rev.* **31**, 1108.

Forbush, S.E., Pomerantz, M.A., Duggal, S.P., Tsao, C.H.: 1983, *Solar Phys.* **82**, 113.

Forman, M.A., Gleeson, L.J.: 1975, *Astrophys. Space Sci.* **32**, 77.

Gallagher, P.T., Phillips, K.J.H., Harra-Murnion, L.K., Baudin, F., Keenan, F.P.: 1999, *Astron. Astrophys.* **348**, 251.

Gleeson, L.J., Axford, W.I.: 1968, *Astrophys. J.* **154**, 1011.

Gopalswamy, N.: 2004, In: Giannina, P., Steven, T.S. (eds.) *Astrophys. Space Sci. Librabry*, **317**, Kluwer Academic Publishers, Dordrecht, The Netherlands, 201.

Gopalswamy, N.: 2006, *Astron. Astrophys.* **27**, 243.

Gopalswamy, N.: 2006, *Sun and Geosphere*, **1**, 020000.

Gopalswamy, N., Yashiro, S., Akiyama, S.: 2007, *J. Geophys. Res.* **112**, A06112.

Gopalswamy, N., Hanaoka, Y., Kosugi, T., Lepping, R.P., Steinberg, J.T., Plunkett, S.: 1998, *Geophys. Res. Lett.* **25**, 2485.

Gopalswamy, N., Lara, A., Yashiro, S., Kaiser, M.L., Howard, R.A.: 2001, *J. Geophys. Res.* **106**, 29207.

Gopalswamy, N., Lara, A., Yashiro, S., Nunes, S., Howard, R. A.: 2003, In: Wilson, A. (ed.) *Proc. ESA Publications Division*, 403.

Gosling, J.T.: 1990, In: Russel, C.T., Priest, E.R., Lee, L.C. (eds.) *Physics of Magnetic Flux Ropes, Geophys. Monogr. Ser.* **58**, AGU, Washington, 343.

Gosling, J.T.: 1992, In: Svestka, Z., Jackson, B.V., Machado, M.E. (eds.) *Proc. Colloquium No. 133 of the International Astronomical Union*, Springer Verlag 258.

Gosling, J.T.: 1993, *J. Geophys. Res.* **98**, 18937.

Gosling, J.T.: 1996, *Ann. Rev. Astron. Astrophys.* **34**, 35.

Gosling, J.T., Pizzo, V.: 1999, *Space Sci. Rev.* **89**, 21.

Gosling, J.T., Hildner, E., Macqueen, R.M., Munro, R.H., Poland, A.I., Ross, C.L.: 1975, *Solar Phys.* **40**, 439.

Gosling, J.T., Asbridge, J.R., Bame, S.J., Feldman, W.C.: 1978, *J. Geophys. Res.* **83**, 1401.

Gosling. J.T., Baker, D.N., Bame, S.J., Feldman, W.C., Zwickl, R.D., Smith, E.J.: 1987, *J. Geophys. Res.* **92**, 8519.

Gupta, V., Badruddin: 2009, *Astrophys. Space Sci.* **312**, 185.

Gupta, V., Badruddin: 2010, *Solar Phys.* **264**, 165.

Hall, D.L., Duldig, M.L., Humble, J.E.: 1996, *Space Sci. Rev.* **78**, 401.

Hansteen, V.H., Leer, E., Holzer, T.E.: 1997, *Astrophys. J.* **482**, 498.

Heber, B.: 2013, *Space Sci. Rev.* **176**, 265.

Heber, B., Potgieter, M.S.: 2006, *Space Sci. Rev.* **127**, 117.

Heber, B., Fichner, H., Scherer, K.: 2006, *Space Sci. Rev.* **125**, 81.

Hess, V.F., Demmelmair, A.: 1937, *Nature* **140**, 316.

Howard, R., Michels, D. Jr. N., Koomen, M.: 1982, *Astrophys. J. Lett.* **263**, L101.

http://voyager.jpl.nasa.gov

Hundhausen, A.J.: 1972, *Coronal Expansion and Solar Wind*, Springer-Verlag, Berlin.

Hundhausen, A.J, Gosling, J.T.: 1976, *J. Geophys. Res.* **81**, 1436.

Hundhausen, A.J., Sawyer, C.B., House, L., Illing, R.M.E., Wagner, W.J.: 1984, *J. Geophys. Res.* **89**, 2639.

Iucci, N., Parisi, M., Storini, M., Villoresi, G.: 1979a, *Nuovo Cimento* **2C**, 1.

Iucci, N., Parisi, M., Storini, M., Villoresi, G.: 1979b, *Nuovo Cimento* **2C**, 421

Iucci, N., Parisi, M., Signorini, C., Storini, M., Villoresi, G.: 1989, *Astron. Astrophys. Suppl.* **81**, 367.

Jian, L.K., Russell, C.T., Luhmann, J.G.: 2011, *Solar Phys.* **274**, 321.

Jian, L., Russel, C.T., Luhmann, J.G., Skoug, R.M.: 2006a, *Solar Phys.*, **239**, 393.

Jian, L., Russell, C.T., Luhmann, J.G., Skoug, R.M.: 2006b, *Solar Phys.* **239**, 337.

Jokipii, J.R., Parker, E.N.: 1969, *Astrophys. J.* **155**, 777.

Jokipii, J.R., Parker, E.N.: 1970, *Astrophys. J.* **160**, 735.

Jokipii, J.R.; Levy, E.H.; Hubbard, W.B.: 1977, *Astrophys. J.* **213**, 861.

Jordan, A.P., Spence, H.E., Blake, J.B., Shaul, D.N.A.: 2011, *J. Geophys. Res.* **116**, A11103.

Kahler, S.W., Reames, D.V.: 1991, *J. Geophys. Res.* **96**, 9419.

Kallenrode, M.B.:1998, *Space Physics*, Springer-Verlag Berlin.

Kane, R.P.: 1977, *J. Geophys. Res.* **82**, 561.

Kane, R.P.: 2010, *Ann. Geophys.* **28**, 479.

Kane, R.P.: 2014, *Solar Phys.* **289**, 2669.

Kennel, C.F., Blandford, R.D., Coppi, P.: 1989, *J. Plasma Phys.* **42**, 299.

Kim, R.S., Gopalswamy, N., Cho, K.S., Moon, Y.J., Yashiro, S.: 2013, *Solar Phys.* **284**, 77.

Klein, L.W., Burlaga, L.F.: 1982, *J. Geophys. Res.* **87**, 613.

Kota, J.: 2013, *Space Sci. Rev.* **176**, 391.

Kota, J., Jokipii, J.R.: 1983, *Astrophys. J.* **265**, 573.

Krieger, A.S., Timothy, A.F., Roelof, E.C.: 1973, *Solar Phys.* **29**, 505.

Kudela, K.: 2012, In: Lazar, M. (ed.) *Exploring the Solar Wind*, Intech, Rijeka, 285.

Kudela, K.: 2013, *J. Phys.: Conf. Series*, **409**, 012017.

Kudela, K., Brenkus, R.: 2004, *J. Atmos. Sol. Terr. Phys.* **66**, 1121.

Kudela, K., Storini, M.: 2005, *J. Atmos. Solar-Terr. Phys.* **67**, 907.

Kudela, K., Storini, M., Hofer, M.Y., Belov, A.: 2000, *Space Sci. Rev.* **93**, 153.

Kumar, A., Badruddin: 2014a, *Solar Phys.* **289**, 2177.

Kumar, A., Badruddin: 2014b, *Solar Phys.* **289**, 4267.

Lada, C.J.: 2006, *Astrophys. J. Lett.* **640**, L63.

Laster, H., Lenchek, A.M., Singer S.F.: 1962, *J. Geophys. Res.* **67**, 2639.

Laurenza, M., Vecchio, A., Storini, M., Carbone, V.: 2012, *Astrophys. J.* **749**, 167.

LeRoux, J.A., Potgieter, M.S.: 1991, *Astron. Asrtophys.* **243**, 531.

LeRoux, J.A., Potgieter, M.S.: 1995, *Astrophys. J.* **442**, 847.

Lepping, R.P., Berdichevsky, D.B. Wu, C.C.: 2006, *Ann. Geophys.* **24**, 215.

Lepping, R.P., Burlaga, L.F., Tsurutani, B.T., Ogilvie, K.W., Lazarus, A.J., Evans, D.S., Klein, L.W.: 1991, *J. Geophys. Res.* **96**, 9425.

Lindblad, B.A., Lundstedt, H., Larsson, B.: 1989, *Solar Phys.* **120**, 145.

Lindermann, F.A.: 1919, *Phil, Mag.* **38**, 669.

Liu, Y., Richardson, J.D., Belcher, J.W., Kasper, J.C. Skoug, R.M.: 2006, *J. Geophys. Res.* **111**, A09108.

Lockwood, J.A.: 1971, *Space Sci. Rev.* **12**, 658.

Lockwood, J.A., Webber, W.R., Debrunner, H.: 1991, *J. Geophys. Res.* **96**, 11587.

Lockwood, J.A., Webber, W.R., Jokipii, J.R.: 1986, *J. Geophys. Res.* **91**, 2851.

Ma, L.H., Han, Y.B., Yin, Z.Q.: 2009, *Solar Phys.* **255**, 187.

Marcz, F.: 1992, *Planet. Space Sci.* **40**, 979.

Maris, O., Maris, G.: 2005, *Adv. Space Res.* **35**, 2129.

Marubashi, K.: 1986, *Adv. Space Res.* **6**, 335.

Marubashi, K.: 1997, In: Crooker, N., Joselyn, J., Feynman, J. (eds.) Washington,D.C.: American Geophys. Union, *Geophys. Monogr.* **99**, 147.

Mavromichalaki, H., Vassilaki, A.: 1998, *Solar Phys.* **183**, 181.

Mavromichalaki, H., Preka-Papadema, P., Liritzis, I., Petropoulos, B., Kurt, V.: 2003, *New Asrton.* **8**, 777.

McComas, D.J., Gosling, J.T., Winterhalter, D., Smith, E.J.: 1988, *J. Geophys. Res.* **93**, 2519.

Modzelewska, R., Alania, M.V.: 2012, *Adv. Space Res.* **50**, 716.

Morishita, I., Nagashima, K., Sakakibara, S., Munakata, K.: 1990, *Proc. 21st Int. Cosmic Ray Conf.* **6**, 217.

Morrison, P: 1954, *Phys. Rev.* **95**, 646.

Morrison, P: 1956, *Phys. Rev.* **101**, 1397.

Mustajab, F., Badruddin: 2013, *Planet. Space Sci.* **82**, 43.

Nagashima, K., Sakakibara, S., Fujimoto, K., Tatsuoka, R., Morishita, I.: 1990, *Nuovo Cim.* **13C**, 551.

Nishida, A.: 1982, *J. Geophys. Res.* **87**, 6003.

Oh, S.Y., Yi, Y.: 2009, *J. Geophys. Res.* **114**, A11102.

Oh, S.Y., Yi, Y.: 2012, *Solar Phys.*, **280**, 197.

Oh, S.Y., Yi, Y., Kim, Y.H.: 2008, *J. Geophys. Res.* **113**, A01103.

Osherovich, V., Burlaga, L.F.: 1997, In: Crooker, N., Joslyn, J.A., Feynman, J. (eds.) *Geophys. Monogr. Ser.*, AGU, Washington DC, **99**, 157.

Owens, M.J., Forsyth, R.J.: 2013, *Living Rev. Solar Phys.* lrsp-2013–5.

Parker, E.N.: 1958, *Astrophys. J.* **128**, 664.

Parker, E.N.: 1964, *Astrophys. J.* **139**, 72.

Parker, E.N.: 1965, *Planet. Space Sci.* **13**, 9.

Patzold, M., Bird, M.K., Vollad, H., Levy, G.S., Seidel, B.L., Stelzried, C.T.: 1987, *Solar Phys.* **109**, 91.

Pizzo, V.: 1978, *J. Geophys. Res.* **83** (A12), 5563.

Potgieter, M.S.: 1995, *Adv. Space Res.* **16**, 191.

Potgieter, M.S.: 1998, *Space Sci. Rev.* **83**, 147.

Potgieter, M.S.: 2013, *Living Rev. Solar Phys.* lrsp-2013–3.

Potgieter, M.S.: 2014, *Adv. Space Res.* **53**, 1415.

Quenby, J.J., Mulligan, T., Blake, J.B., Mazur, J.E., Shaul, D.: 2008, *J. Geophys. Res.* **113**, A10102.

Rao, U.R.: 1972, *Space Sci. Rev.* **12**, 719.

Reames, D.V., Kahler, S.W., Tylka, A.J.: 2009, *Astrophys. J. Lett.*, **700**, L199.

Richardson, I.G.: 2004, *Space Sci. Rev.* **111**, 267.

Richardson, I.G., Cane, H.V.: 2010, *Solar Phys.* **264**, 189.

Richardson, I.G., Cane, H.V.: 2011, *Solar Phys.* **270**, 609.

Richardson, I.G., Cane, H.V., Wibberenz, G.: 1999, *J. Geophys. Res.* **104**, 12549.

Richardson, I.G., Wibberenz, G., Cane, H.V.: 1996, *J. Geophys. Res.* **101**, 13483.

Rosenbauer, H., Schwenn, R., Marsch, E., Meyer, B., Miggenrieder, H., Montgomery, M.D., *et al.*: 1977, *J. Geophys.* **42**, 561.

Sabbah, I.: 2000, *Can. J. Phys.* **78**, 293.

Sabbah, I., Kudela, K.: 2011, *J. Geophys. Res.* **116**, A04103.

Sabbah, I., Rybansky, M.: 2006, *J. Geophys. Res.* **111**, A01105.

Sanderson, T.R., Beeck, J., Marsden, R.G., Tranquille, C., Wenzel, K.P., McKibben, R.B., *et al.*: 1990, *Proc. 21st Int. Cosmic Ray Conf.* **6**, 251.

Sarabhai, V.: 1963, *J. Geohpys. Res.* **68**, 1555.

Sarris, E.T., Dodopoulos, C., Venkatesen, D.: 1989, *Solar Phys.* **120**, 153.

Schwenn, R.: 2006, *Living Rev. Solar Phys.* **3**, 2.

Sheeley Jr. N., Howard, R.A., Michels, D.J., Koomen, M.J., Schwenn, R., Muhlhauser, K.H., *et al.*: 1985, *J. Geophys. Res.* **90**, 163.

Simpson, J.A.: 1954, *Phys. Rev.* **94**, 426.

Singh, Y.P., Badruddin: 2006, *J. Atmos. Solar-Terr. Phys.* **68**, 803.

Singh, Y.P., Badruddin: 2007a, *J. Geophys. Res.* **112**, A05101.

Singh, Y.P., Badruddin: 2007b, *J. Geophys. Res.* **112**, A02101.

Smith, E.J., Tsurutani, B.T., Rosenberg R.L.: 1978, *J. Geophys. Res.* **83**, 717.

Sonett, C., Colburn, D., Davis, L., Smith, E., Coleman, P.: 1964, *Phys. Rev. Lett.* **13**, 153.

Storini, M.: 1990, *Nuovo Cimento*, **13C**, 103.

Strauss, R.D., Potgieter, M.S., Ferreira, S.E.S.: 2012, *Adv. Space Res.* **49**, 392.

Subramanian, P., Antia, H.M., Dugad, S.R., Goswami, U.D., Gupta, S.K., Hayashi, Y., *et al.*: 2009, *Astron. Astrophys.* **494**, 1107.

Synder, C.W., Neugebauer, M.: 1963, *Proc. 18th Int. Cosmic Ray Conf.* **1**, 210.

Taniuti, T.A.: 1962, *Progress Theoretical Phys.* **28**, 756.

Tobias, S.M.: 2005, In: Soward, A.M. (ed.) *Fluid Dynamics and Dynamos in Astrophyics and Geophysics*, CRC Press, 193.

Tousey, R., Bartoe, J.D.F., Bohlin, J.D., Brueckner, G.E., Purcell, J.D., Scherrer, V.E., *et al.*: 1973, *Solar Phys.* **33**, 265.

Usoskin, I.G., Braun, I., Gladysheva, O.G., HöRandel, J.R., JäMséN, T. Kovaltsov G.A. *et al*: 2008, *J. Geophys. Res.* **113**, A07102.

Venkatesan, D., Badruddin: 1990, *Space Sci. Rev.* **52**, 121.

Venkatesan, D., Shukla, A.K., Agrawal, S.P.: 1982, *Solar Phys.* **81**, 375.

Venkatesan, D., Badruddin, Ananth, A.G., Pillai, S.: 1992, *Solar Phys.* **137**, 345.

Wang, Y., Zhang, J.A.: 2008, *Astrophys. J.*, **680**, 1516.

Watermann, J., Wintoft, P., Sanahuja, B., Saiz, E., Poedts, S., Palmroth, M., *et al.*: 2009, *Space Sci. Rev.* **147**, 233.

Wawrzynczak, A., Alania, M. V.: 2010, *Adv. Space Res.* **45**, 622.

Webb, D.F., Howard, T.A.: 2013, *Living Rev. Solar Phys.* lrsp-2013–3.

Webber, W.R., Lockwood, J.A.: 1988, *J. Geophys. Res.* **93**, 8735.

Wibberenz, G., LeRoux, J.A., Potgieter, M.S., Bieber, J.W.: 1998, *Space Sci. Rev.* **83**, 309.

Wilson, R.M., Hildner, E.: 1984, *Solar Phys.* **91**, 169.

Wilson, R.M., Hildner, E.: 1986, *J. Geophys. Res.* **91**, 5867.

Wimmer-Schweingruber, R.F., von Steiger, R., Paerli, R.: 1999, *J. Geophys. Res.* 104, 9933.

Woolfson, M.: 2000, *Astron. Geophys.* **41**, 12.

Wu, C.C.:1990, *J. Geophys. Res.* **95**, 8149.

Xystouris, G., Sigala, E., Mavromichalaki, H.: 2014, *Solar Phys.* **289**, 995.

Yu, X.X., Lu, H., Le, G.M., Shi, F.: 2010, *Solar Phys.* **263**, 223.

Zhang, G., Burlaga, L.F.: 1988, *J. Geophys. Res.* **93**, 2511.

Zhang, J., Richardson, I.G., Webb, D.F., Gopalswamy, N., Huttunen, E., Kasper, J.C., *et al.*: 2007, *J. Geophys. Res.* **112**, A10102.

Zhao, X.P., Webb, D.F.: 2003, *J. Geophys. Res.* **108**, 1234.

****